Georgia Institute of Technology
Daniel Guggenheim
School of Aerospace Engineering

CCL Report 2009-02-1

Hybrid LES of Detonations in Reacting Multi-Phase Mixtures

Suresh Menon and Franklin Génin

Computational Combustion Laboratory
School of Aerospace Engineering
Georgia Institute of Technology
270 Ferst Drive
Atlanta, Georgia 30332-0150
http://www.ccl.gatech.edu

20090410038

Sponsored by: *Air Force Office of Scientific Research*
Contract Number: *FA9550-06-1-0056*
Date: *February 28, 2009*

AFRL-SR-AR-TR-09-0117

REPORT DOCUMENTATION PAGE

The public reporting burden for this collection of information is estimated to average 1 hour per response, including the time for reviewing instructions, searching existing data sources, gathering and maintaining the data needed, and completing and reviewing the collection of information. Send comments regarding this burden estimate or any other aspect of this collection of information, including suggestions for reducing the burden, to Department of Defense, Washington Headquarters Services, Directorate for Information Operations and Reports (0704-0188), 1215 Jefferson Davis Highway, Suite 1204, Arlington, VA 22202-4302. Respondents should be aware that notwithstanding any other provision of law, no person shall be subject to any penalty for failing to comply with a collection of information if it does not display a currently valid OMB control number.

PLEASE DO NOT RETURN YOUR FORM TO THE ABOVE ADDRESS.

1. REPORT DATE *(DD-MM-YYYY)* 28-02-2009	**2. REPORT TYPE** Final Report	**3. DATES COVERED** *(From - To)* December 1 2005 - November 30 2008

4. TITLE AND SUBTITLE

HYBRID LES OF DETONATIONS IN REACTING MULTI-PHASE MIXTURES

5a. CONTRACT NUMBER

FA9550-06-1-0056

5b. GRANT NUMBER

5c. PROGRAM ELEMENT NUMBER

6. AUTHOR(S)

Suresh Menon and Franklin Genin

5d. PROJECT NUMBER

5e. TASK NUMBER

5f. WORK UNIT NUMBER

7. PERFORMING ORGANIZATION NAME(S) AND ADDRESS(ES)

School of Aerospace Engineering
Georgia Institute of Technology
Atlanta, GA 30332

8. PERFORMING ORGANIZATION REPORT NUMBER

CCL-TR-2009-02-1

9. SPONSORING/MONITORING AGENCY NAME(S) AND ADDRESS(ES)

AFOSR/NL
4015 Wilson Blvd,
Arlington, VA 22203
Dr. Fariba Fahroo

10. SPONSOR/MONITOR'S ACRONYM(S)

AFOSR/NM

11. SPONSOR/MONITOR'S REPORT NUMBER(S)

12. DISTRIBUTION/AVAILABILITY STATEMENT

Unlimited, Unclassified

13. SUPPLEMENTARY NOTES

14. ABSTRACT

A Large-Eddy Simulation (LES) methodology adapted to the resolution of high Reynolds number turbulent flows in supersonic conditions was proposed and developed. A novel numerical scheme was designed, that switches from a low-dissipation central scheme for turbulence resolution to a flux difference splitting scheme in regions of discontinuities. A state-of-the-art closure model was extended in order to take compressibility effects and the action of shock / turbulence interaction into account. The proposed method was validated and employed for the study of shock / turbulent shear layer interaction as a mixing-augmentation technique, and highlighted the efficiency in mixing improvement after the interaction, but also the limited spatial extent of this turbulent enhancement. A second study focused on the injection of a sonic jet normally to a supersonic crossflow. The validity of the simulation was assessed by comparison with experimental data, and the dynamics of the interaction was examined. The sources of vortical structures were identified, with a particular emphasis on the impact of the flow speed onto the vortical evolution.

15. SUBJECT TERMS

Large Eddy Simulation, hybrid shock capturing, compressible turbulence, shock-shear interactions

16. SECURITY CLASSIFICATION OF:			**17. LIMITATION OF ABSTRACT**	**18. NUMBER OF PAGES**	**19a. NAME OF RESPONSIBLE PERSON**
a. REPORT	**b. ABSTRACT**	**c. THIS PAGE**			Suresh Menon
Unclassified	Unclassified	Unclassified	UU	166	**19b. TELEPHONE NUMBER** *(Include area code)* 404-894-9126

Standard Form 298 (Rev. 8/98)
Prescribed by ANSI Std. Z39.18

TABLE OF CONTENTS

LIST OF TABLES iv

LIST OF FIGURES v

SUMMARY ix

I INTRODUCTION 1

- 1.1 Turbulence in Compressible Flows . . . 2
  - 1.1.1 Compressible Turbulence . . . 2
  - 1.1.2 Shock / Turbulence Interaction . . . 6
- 1.2 Numerical Simulation of Compressible Turbulent Flows . . . 7
  - 1.2.1 Numerical Issues in Supersonic Turbulent Flows Computations 8
  - 1.2.2 Turbulence Modeling for Compressible and High-Speed Flows 11
- 1.3 Present Study . . . 12

II GOVERNING EQUATIONS AND MODELING 15

- 2.1 The Navier-Stokes Equations . . . 15
- 2.2 Governing Equations for LES . . . 18
  - 2.2.1 Spatial Filtering and Favré Averaging . . . 19
  - 2.2.2 Filtering the Navier-Stokes Equations . . . 19
- 2.3 Closure Model for the LES Equations . . . 21
  - 2.3.1 Derivation of the k^{sgs} Closure Model . . . 23
  - 2.3.2 Evaluation of the Model Coefficients . . . 26
    - 2.3.2.1 Nominal Values of the Closure Coefficients . . . 26
    - 2.3.2.2 Dynamic Evaluation of the Closure Coefficients . . 27
  - 2.3.3 Realizability Conditions . . . 33

III COMPUTATIONAL METHODS 35

- 3.1 Numerical Integration . . . 35
  - 3.1.1 Finite Volume Method . . . 35
  - 3.1.2 McCormack Time Integration . . . 36

3.2 A Hybrid Scheme for Supersonic Turbulent Flows 36

3.3 A Central Scheme for Turbulent Flows 39

  3.3.1 A 2nd Order Accurate Method - the Original McCormack Scheme 39

  3.3.2 A 4th Order Extension to the McCormack Scheme 40

3.4 A Flux-Difference Splitting Scheme for Discontinuity Capturing . . . 41

  3.4.1 Interface Reconstruction 42

    3.4.1.1 MUSCL Interpolation 42

    3.4.1.2 Monotonicity of the Reconstructed States 45

    3.4.1.3 Flattening Procedure 47

  3.4.2 A Class of Approximate Riemann Solvers - HLL· 48

    3.4.2.1 The 2-waves HLL Riemann Solver 49

    3.4.2.2 Restoration of the Middle Wave - the HLLC Riemann Solver 51

    3.4.2.3 A Hybrid Riemann Solver - HLLC/E 55

3.5 Verification of the Upwind Scheme 56

  3.5.1 One-Dimensional Tests 57

  3.5.2 Two-Dimensional Cases 63

3.6 Assessment and verification of the hybrid methodology 68

  3.6.1 Assessment of the Hybrid Scheme Parameters 68

  3.6.2 Simulation of a Richtmyer-Meshkov Instability 69

  3.6.3 Shu-Osher Interaction 71

  3.6.4 Shock / Vortex Interaction 74

3.7 Other Computational Issues 76

  3.7.1 Viscous Fluxes 76

  3.7.2 Time-Step Determination 77

  3.7.3 Boundary Conditions 78

  3.7.4 Parallelization 81

IV SIMULATION OF SHOCK / TURBULENCE INTERACTION 82

4.1 Initial Field of Isotropic Turbulence 83

4.2 Direct Simulations of Shock / Isotropic Turbulence Interaction . . . 85
4.3 LES of Shock / Isotropic Turbulence Interaction 94
4.4 LES of Shock / Turbulent Shear Layer Interaction 99

V SONIC JET IN SUPERSONIC CROSS-FLOW 109

5.1 Configuration and Parameters for the JICF Study 112
5.2 Comparisons with Experiments 113
5.3 Time-Averaged Flow Features 117
5.4 Unsteady Features and Flow Dynamics 124
5.5 Computational Performance and Model Analysis 131
5.6 Conclusion of the Jet in Crossflow Dynamical Study 136

VI CONCLUSION AND RECOMMENDATIONS 138

6.1 Conclusion 138
6.2 Recommendations for Future Work 140

REFERENCES 142

LIST OF TABLES

3.1 Initial conditions for the left and right states in the one-dimensional tests used to validate the shock-capturing methodology. 60

3.2 Parameters used in the one-dimensional tests used to validate the shock-capturing methodology. 60

5.1 Experimental parameters for the jet in cross flow experiment of Santiago and Dutton [1997]. 112

5.2 Numerical parameters for two jets in crossflow simulation: (a) freestream Mach number $M = 2$ and (b) jet to freestream momentum ratio $J = 5$. 117

LIST OF FIGURES

1.1 Schematic of the energy balance for compressible turbulence 3

2.1 Representation of the subgrid and sub-testscale regions in a model turbulent energy spectrum, and modeling assumptions for the dynamic procedure of Germano et al. [1990]. 28

2.2 Representation of the subgrid and testscale regions in a model turbulent energy spectrum, and modeling assumptions for the LDKM. . . . 29

3.1 Schematic representing the curvilinear grid spacing definitions, from Nelson [1997]. 41

3.2 Region defining second order TVD schemes (shaded in grey). 44

3.3 Characteristic curves for the Monotonized central (MC), minmod (MM) and superbee (SB) limiters. 44

3.4 Characteristic curves for the van Leer (VL) and van Albada (VA) limiters. 45

3.5 Schematic illustrating the gradient violation during the reconstruction procedure. 46

3.6 (x, t) diagram of an approximate Riemann problem evolution with two characteristic waves. 49

3.7 (x, t) diagram of an approximate Riemann problem evolution with three characteristic waves. 52

3.8 Pressure profiles for M=5.2 normal shock with a Calorically perfect gas EOS. 58

3.9 $C_p(T)$ for a thermally perfect gas, and pressure profiles for M=5.2 normal shock. 58

3.10 Computational grid for oblique shock calculations (left) and pressure contours for $M_{in} = 5$ and a ramp angle of 15°. 59

3.11 Results of test cases T1 and T2 for the validation of the upwind methodology. 61

3.12 Results of test cases T3 and T4 for the validation of the upwind methodology. 62

3.13 Results of test cases T5 and T6 for the validation of the upwind methodology. 62

3.14 Schematic of the perturbed grid used in the odd-even test. 63

3.15 Results of the odd-even test case using the HLLE, Roe, HLLC, TSRS and HLLC/E Riemann solvers. 64

3.16 Isolines of the temperature field for the carbuncle test case using the HLLE Riemann solver. 65

3.17 Isolines of the temperature field for the carbuncle test case using contact-preserving Riemann Solvers and the HLLC/E hybrid Riemann solver. 65

3.18 Radii of the blast wave fronts as a function of time for the case of planar, cylindrical and spherical Blast waves. 66

3.19 Sedov's point explosion problem: pressure profiles of the one-dimensional reference and two-dimensional simulations. 67

3.20 Schematic of the Richtmyer-Meshkov Instability problem. 69

3.21 Richtmyer-Meshkov Instability simulation at an early stage of the interaction. (a) density field, (b) mass fractions product and (c) switch function. 70

3.22 Richtmyer-Meshkov Instability simulation at a late stage of the interaction. (a) density field, (b) mass fractions product and (c) switch function. 71

3.23 Density profile at the final time for the Shu-Osher shock / entropy wave interaction for coarse and medium resolutions. 72

3.24 Evolution of the density for the Shu-Osher shock / entropy Wave interaction using different schemes. 73

3.25 Evolution of the density for the Shu-Osher shock / entropy Wave interaction for fine resolution. 74

3.26 Angular variations of the pressure field in the shock / vortex interaction problem. 76

4.1 Temporal evolution of the Velocity skewness and turbulent Mach number in the simulation of isotropic decaying turbulence. 84

4.2 Schematic of the shock / Isotropic turbulence interaction configuration. 85

4.3 Longitudinal and transverse Reynolds stress profile in the direct simulation of the shock / isotropic turbulence interaction problems, with normal Mach numbers of 1.29, 2.0 and 3.0. 87

4.4 Longitudinal and transverse Reynolds stress profile in the direct simulation of the shock / isotropic turbulence interaction problems using the hybrid methodology, the flux-difference splitting and the Piecewise Parabolic Method, for normal Mach numbers of 1.29, 2.0 and 3.0. . . 88

4.5 Velocity spectra for the $M = 1.29$, $M = 2.0$ and $M = 3.0$ shock / isotropic turbulence interaction. 90

4.6 Profiles of the ratios between LES and DNS cells volumes for the shock / isotropic turbulence interaction problem. 91

4.7 *a – priori* estimate of the subgrid stresses for the LDKM and DSM models for the shock / isotropic turbulence interaction problem. . . . 92

4.8 Profiles of the k^{sgs} budget in $M = 1.29$ and $M = 3.0$ shock / isotropic turbulence interactions 93

4.9 Profiles of Reynolds stresses from the LES calculations, and comparisons with the filtered DNS fields, for the $M = 1.29$, $M = 2.0$ and $M = 3.0$ shock / isotropic turbulence cases. 95

4.10 Velocity spectra of the filtered DNS field and of the LES field for the $M = 1.29$, $M = 2.0$ and $M = 3.0$ shock / isotropic turbulence cases. . 97

4.11 Dynamic coefficients profiles for the shock / isotropic turbulence interactions. 98

4.12 Schematic of the base Mixing layer configuration. 100

4.13 Iso-surface of the Q-criterion for the base mixing layer and the shocked mixing layer. 102

4.14 Mixing Layer growth rate for the reference and shock mixing layers. . 103

4.15 Normalized variances for the base mixing layer. 104

4.16 Normalized variances for the shocked mixing layer. 105

4.17 Total pressure profiles for the reference and shocked mixing layers. . . 106

4.18 Profiles of the LDKM closure coefficients for the reference mixing layer. 107

4.19 Profiles of the LDKM closure coefficients for the shocked mixing layer. 108

5.1 Schematics of the supersonic JICF interaction. 110

5.2 Profiles of mean axial and transverse velocities in the centerplane at four locations downstream of the injection and comparison with experimental data. 114

5.3 Profiles of fluctuating axial and transverse velocities in the centerplane at four locations downstream of the injection, and comparison with experimental data. 115

5.4 Contours of Reynolds stresses in two cross-planes downstream of the injection ($x/d = 3.0$ and $x/d = 5.0$). Comparison between experimental (left) and numerical (right) results. 116

5.5 Energy spectra at three locations of the centerplane of the reference jet in crossflow configuration. 118

5.6 Pressure field, temperature gradient contours and streamlines in the centerplane for the three JICF cases. 119

5.7 Vortical structures in the JICF configuration represented by the iso-contours of Q variable 120

5.8 Average velocity vectors at five cross sections downstream of the injector for the reference JICF. 122

5.9 Contours of the average injected mass flux for two vertical planes for the reference JICF. 123

5.10 Iso-surface of $Q = 10^8 s^{-2}$ highlighting the hanging vortices for the three JICF cases. 123

5.11 Iso-surface of $Q = 10^8 s^{-2}$ and streamlines from the upper boundary layer. 124

5.12 Large scale structures for the reference JICF. 125

5.13 Contours of temperature gradients magnitude and of Mach number field for the reference JICF. 126

5.14 Contours of the temperature gradients magnitude in the $x/d = 0$ cross-plane at $t = 8\mu s$ of the reference JICF. 127

5.15 Iso-surface of the passive scalar injected from the jet colored by the vorticity magnitude. 129

5.16 Visualization of an instantaneous windward vortex by superposing the iso-contour of the passive scalar and of positive Q. 130

5.17 Closure coefficient contours for case A of the JICF - Instantaneous and time-averaged fields. 132

5.18 Profiles of mean axial and transverse velocities in the centerplane at four locations downstream of the injection. Comparison of different closure models 134

5.19 Profiles of fluctuating axial and transverse velocities in the centerplane at four locations downstream of the injection, and comparison with experimental data. 135

5.20 Contours of time averaged k^{sgs} for the simulation of Case A using $LDKM_{NCC}$ and LDKM. 136

SUMMARY

The interaction of shock waves with turbulent regions can have a strong impact on the flow evolution, and shock induced heating can trigger ignition, combustion and turbulent flame propagation. The numerical resolution of multi-phase, turbulent reacting flow is of fundamental importance but remains a very challenging problem. The capture of strong discontinuities, typical of high-speed flows, requires the use of shock-capturing schemes, which are not adapted to the resolution of turbulent structures due to their intrinsic dissipation. On the other hand, low-dissipation schemes are unable to resolve shock fronts and other sharp gradients without creating high amplitude numerical oscillations. Furthermore, the nature of turbulence in high-speed flows differs from its incompressible behavior, and, in the context of Large-Eddy Simulation, the subgrid closure must be adapted to the modeling of compressibility effects and shock waves on turbulent flows. The developments described in the present report are two-fold. First, a state of the art closure approach for LES is extended to model subgrid turbulence in compressible flows. The energy transfers due to compressible turbulence and the diffusion of turbulent kinetic energy by pressure fluctuations are assessed and integrated in the Localized Dynamic k^{sgs} model. Second, a hybrid numerical scheme is developed for the resolution of the LES equations and of the model transport equation, which combines a central scheme for turbulent resolutions to a shock-capturing method. A smoothness parameter is defined and used to switch from the basc smooth solver to the upwind scheme in regions of discontinuities.

It is shown that the developed hybrid methodology permits a capture of shock / turbulence interactions in direct simulations that agrees well with other reference simulations, and that the LES methodology effectively reproduces the turbulence evolution and physical phenomena involved in the interaction. This numerical approach is then employed to study a problem of practical importance in high-speed mixing. The interaction of two shock waves with a high-speed turbulent shear layer as a mixing augmentation technique is considered. It is shown that the levels of turbulence are increased through the interaction, and that the mixing is significantly improved in this flow configuration. However, the region of increased mixing is found to be localized to a region close to the impact of the shocks, and that the statistical levels of turbulence relax to their undisturbed levels some short distance downstream of the interaction. The present developments are finally applied to a practical configuration relevant to scramjet injection. The normal injection of a sonic jet into a supersonic crossflow is considered numerically, and compared to the results of an experimental study. A fair agreement in the statistics of mean and fluctuating velocity fields is obtained. Furthermore, some of the instantaneous flow structures observed in experimental visualizations are identified in the present simulation. The dynamics of the interaction for the reference case, based on the experimental study, as well as for a case of higher freestream Mach number and a case of higher momentum ratio, are examined. The classical instantaneous vortical structures are identified, and their generation mechanisms, specific to supersonic flow, are highlighted. Furthermore, two vortical structures, recently revealed in low-speed jets in crossflow but never documented for high-speed flows, are identified during the flow evolution.

CHAPTER I

INTRODUCTION

There is a renewed interest in the research community in high altitude and high-speed flight. Advanced designs for supersonic and hypersonic vehicles still require significant developments, particularly in the field of propulsive systems. Ramjet engines, in which the incoming air flow speed is decreased to subsonic speed relative to the engine, can be efficiently used for M = 3 to 5 flight regimes, but beyond these speeds, alternate propulsion systems are required. The Supersonic Combustion ramjet (or scramjet) engine, where the incoming airflow is decelerated but remains supersonic within the engine, is one of the most promising propulsion options. The study of mixing and combustion processes in supersonic environment has thus been the topic of on-going research. A review of scramjet propulsion (Curran and Murthy [2000]) highlights the different programs in Japan, Russia, Germany, France and the United States, including their specific and complementary aspects.

Studies of high-speed mixing have been, for the most part, experimental. Progress in high-speed imaging and acquisition systems have permitted the development of sophisticated methods that provide qualitative and quantitative evaluations of supersonic velocity (supersonic PIV, LDV) and scalar fields (Planar Laser Scattering, Planar Laser-Induced Fluorescence, CARS thermometry). These campaigns are however limited by the lack of modularity and the high cost associated with the experimental rigs. The development of high accuracy, low cost, dynamic numerical simulations, on the other hand, could make Computational Fluid Dynamics (CFD) a complementary tool for preliminary design purposes, as insights into the physics involved in fundamental configurations and in specific geometries could be gained. To be operational, such a numerical tool should be able to simulate high-speed flows reliably, at reasonable computational cost.

Turbulence in such engines is of fundamental importance, as fast mixing of fuels and oxidizers is a requirement to an efficient and stable combustor. Turbulence in compressible flows differs from its incompressible counter-part, and an accurate numerical approach should account for these changes. The developments presented in the present report focus on the development of a novel numerical methodology for accurate low-cost calculations of high-speed turbulent flows. To better understand the challenges associated with this development, we first review the physics of compressible turbulence, from the early observations and interpretations to the current knowledge. We then present an overview of the challenges encountered during the design of high-fidelity numerical schemes for the numerical resolutions of high-speed turbulent flows.

1.1 Turbulence in Compressible Flows

1.1.1 Compressible Turbulence

Turbulence is present in most flows of practical interest and has a strong impact on their evolution. The seemingly random fluctuations in pressure, velocity, etc. can significantly change the dynamics of a system, increasing the drag over a body and generating noise, but also leading to high levels of mixing. Turbulence has for these reasons been the focus of a large body of research, involving theoretical, analytical, experimental and, more recently, numerical works. Despite the chaotic nature of turbulence, reliable predictions can be made for many simple, fundamental configurations. However, due to the large span of time- and length- scales involved, the complexity of the flow equations, and the variability in experimental and numerical studies, the fundamental physics of turbulence is not yet fully understood, and remains a very active and prolific area of research.

Most of the early studies have concentrated on simpler incompressible flows, that is, flows with little fluctuations in density associated with pressure fluctuations. The simplifications brought to the governing equations from the incompressible assumption facilitate theoretical and analytical derivations. Furthermore, experimental studies are often limited to low-speed incompressible conditions. Yet, the quest for increased flight speeds has been a major motivation for aeronautical developments, and the study of compressible turbulent flows has become necessary as flight speed has indeed increased. The characterization of high-speed compressible and turbulent flows is an effort that has combined analytical studies to experimental observations. A turbulent flow is called compressible when a significant amount of density fluctuations is formed in response to perturbations in the pressure field (Lele [1994]), and these density variations are associated with local velocity divergence. Kovásznay [1953] carried out a small perturbation analysis of the Navier-Stokes equations and showed that a field of turbulence could be essentially decomposed into three modes of fluctuations: vorticity, acoustic and entropy modes. In first order analysis, these modes are decoupled. However, higher order analyses show that mode coupling occurs, and that any two modes can interact through non-linearities and generate all three modes (Chu and Kovásznay [1958]). Furthermore, the turbulent velocity is characterized as the superposition of a solenoidal (non-divergent) component, and a dilatational (irrotational) part obtained from a Helmholtz decomposition. The first contribution is found in incompressible flows, whereas the second component is typical of compressible flows. Their energetic behaviors are very different in nature. The vortical structures of the solenoidal field interact through non-linearities and viscous forces, and form the well-known energy cascade. The dilatational field is an ondulatory and propagative mode, where kinetic energy is exchanged with the energy contained in the thermodynamics fluctuations. The energy balance in compressible turbulence is then more complex than in the incompressible case as new physical phenomena arise. The turbulent production and solenoidal dissipation (hereafter noted P and ϵ_s respectively) are the main actors of the energy budget in incompressible turbulent flows. The new energy transfers, highlighted in Fig. 1.1, come from the dissipation

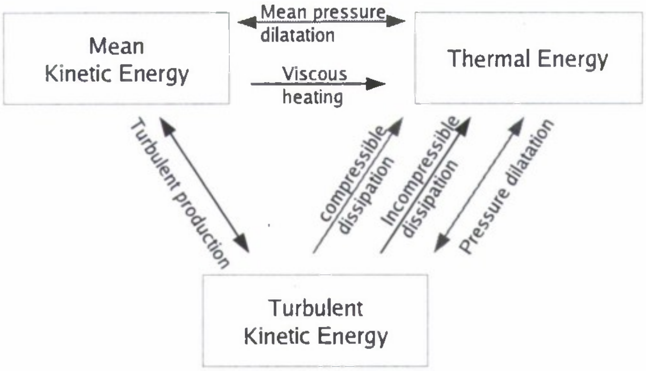

Figure 1.1: Transfers between mean kinetic energy, turbulent kinetic energy and thermal energy (adapted from Ristorcelli [1997]).

of compressible turbulence by the dilatational dissipation (ϵ_d) of turbulent kinetic energy and by the pressure dilatation correlation ($< pd >$). These decompositions have been employed in Rapid Distortion Theories and Linear Interaction Analyses in order to gain insight in the fundamental processes of compressible turbulence. This analytical work is however limited to fundamental, homogeneous flows, and cannot be applied to general and practical configurations.

These modal decompositions are also often used in the interpretation of experimental results. Multiple experimental studies have focused on high-speed shear layers and their deviation from the incompressible behavior. The skin friction coefficients in a high-speed boundary layer and the mixing layer growth rate were found affected by the free-stream velocity / Mach number. Two types of compressible turbulent flows have been identified: those affected by the variations in the *mean* thermodynamics fields, and those that contain small scale fluctuations in thermodynamics variables that interact with the turbulent structures. High-speed boundary layers were found to be mostly affected by the large density/temperature gradients within the layer. If properly scaled (e.g., van Driest [1951]), these high flows could be directly related to the incompressible boundary layers. Morkovin [1962] postulated that the acoustic mode was negligibly small in a typical non-hypersonic boundary layer, and that the entropy mode was also negligible for adiabatic flows. Small scale fluctuations in the thermodynamics field would then be associated with the velocity fluctuations through an isentropic process. The vortical mode of fluctuations is dominant, and the turbulent structures are comparable to their incompressible counter-parts (Bradshaw [1977], Friedrich and Bertolotti [1997]). From that perspective, compressible turbulence plays little role in the physics of supersonic boundary layers.

Turbulent mixing layers, on the other hand, were found to be strongly affected by the flow compressibility. Experiments have shown that the mixing layers growth rate is reduced as the levels of compressibility are increased (Brown [1974], Papamoschou and Roshko [1988]). Also, the turbulent structures in the flow are changed in high speed flows: the turbulent shear stress decreases, and the normal stress anisotropy increases in increasingly compressible mixing layers. Furthermore, the (reduced) growth rate is a visible and easily measurable quantity. Parameterizations of the effects of compressibility on spatial mixing layers have been obtained, that relate the ratio of the compressible to the incompressible growth rates to a quantification of the level of compressibility in the shear layer. The convective Mach number (M_c, defined from the velocity difference and the average speeds of sound in the two streams, Papamoschou and Roshko [1988]), and other parameters (Slessor et al. [2000]) have been proposed as a measure of the compressibility levels, leading to a fairly good collapse of well-documented experimental data of growth rate reduction onto a single curve (Barone et al. [2006]). Another motivation for the study of high speed mixing layers lies in the practical implications of the reduced growth rate: mixing is of fundamental interest for high-speed propulsion systems, where fuel / oxidizer mixing is of great importance. For these reasons, this configuration is an ideal candidate for the study of compressible turbulence in practical flows, and has been the focus of many studies, but the actual impact of compressible turbulence could not be estimated.

A new look into the fundamentals of compressible turbulent dynamics has emerged with the development of highly accurate computational techniques and the direct numerical simulations of isotropic turbulent and homogeneous shear flows. The objective of the early studies was the characterization and quantification of the compressible energy transfers, reviewed earlier, then regarded as the main cause for the shear layer growth rate reduction. More particularly, the increasing impact of the dilatational dissipation with compressibility was primarily suspected, and many researchers have studied its evolution, eventually leading to scaling laws and models for ϵ_d. Zeman [1990] attributed the most part of the dilatational dissipation to the appearance of *shocklets* in the flow. These regions of localized compressions (shocks in regions of strong dilatational velocity fields, which satisfy the Rankine-Hugoniot relations) have been observed in direct simulations of two-dimensional shear layers, and found to strongly impact the mixing layer developments. From an assumed probability density function of the occurrence of shocklets, Zeman [1990] proposed a simple modeling expression for the dilatational dissipation in this analytical work, relating ϵ_d linearly to ϵ_s, with a exponential dependence on the square of turbulent Mach number M_t (defined as the Mach number based on the rms velocity of the turbulent kinetic energy). Another closure for the dilatational dissipation was derived by Sarkar based on DNS simulations of isotropic compressible turbulence (Sarkar et al. [1989]) and homogeneous shear flows (Sarkar [1992]). Again, a linear scaling between solenoidal and dilatational dissipations was found, with a proportionality factor depending on M_t^2. The other compressible energy transfer, the pressure dilatation correlation, has also been regarded as a major means of turbulence modification in compressible flows. Acoustic modes, amplified through pressure-dilatation, were believed to lead to acoustic losses, hence reducing the levels of turbulent kinetic energy in the flow. Again, many researchers have studied the structural form of this energy transfer, and several models have been proposed (Zeman [1990], Taulbee and Van Osdol [1991], Sarkar [1992], El Baz [1992]).

These models successfully reproduced a decrease in the mixing layer growth rate, but failed to capture the changes in the mixing layer turbulent statistics, and deteriorated the simulations of high-speed boundary layers. Their physical relevance was questionable. The presence of shocklets has not been confirmed in experiments and three-dimensional numerical simulations unless relatively high Mach numbers (well above the lowest Mach numbers showing compressibility effects) are considered (Vreman [1997], Rossmann et al. [2002], Fu and Li [2006]). Furthermore, the effective dissipation due to these features, when present, is found to be at most a few percent of the overall dissipation (Lele [1994], Vreman [1997]). These early models were found not to represent the physics of energy transfers in fully developed compressible turbulence, but rather modeled the evolution of flows away from acoustic equilibrium.

More insight into the development of supersonic mixing layers has been gained later from analytical results, Rapid Distortion Theory studies and DNS studies of compressible mixing layers. The principal modes of instability change as the convective Mach number is increased. The two-dimensional, most unstable modes of incompressible mixing layers (Michalke [1964], Pierrehumbert and Widnall [1982], Metcalfe et al. [1987]) are found to persist for convective Mach numbers up to $M_c = 0.6$, though the growth rate of the wave decreases as the Mach number is increased. After $M_c = 0.6$, the most unstable mode of the mixing layer has been found to be three-dimensional, with further decrease in the instability growth rate (Sandham and Reynolds [1991]). These trends persist in the non-linear regimes (Lele [1994]). It has been shown that the pressure strain correlation, which re-distributes the turbulent kinetic energy between the different components of the turbulent stresses, decreased with the convective Mach number, hence increasing the shear stress anisotropy (Sarkar [1995], Simone et al. [1997]). The turbulent production is then reduced, and the turbulent kinetic energy within the mixing layer decreases. Modifications in turbulent behavior for compressible mixing layers is found to be mostly of a structural nature.

At the same time, a more fundamental understanding of compressible turbulence has been gained from analytical and spectral studies. Fundamental studies have shown that the solenoidal velocity field in isotropic turbulence is not strongly affected by the levels of compressibility. The spectral representation of the solenoidal energy shows a persisting $k^{-5/3}$ behavior in the inertial range, unless high values of the turbulent Mach number are considered ($M_t = \mathcal{O}(1)$, Lele [1994], Bataille et al. [1997]). Furthermore, the amount of dilatational energy remains relatively small for moderate values of the turbulent Mach number. It has also been shown that the dilatational dissipation scales as M_t^4, and inversely to the Reynolds number in the limit of small turbulent Mach numbers (Ristorcelli [1997], Fauchet and Bertoglio [1999]). The pressure-dilatation is related to the departure from equilibrium in the turbulent energy budget (balance between production and dissipation), and can accordingly play a non-negligible role in out-of-equilibrium flows. The energy losses due to acoustic radiation were, however, found to represent a rather small portion of the turbulent kinetic energy production in many cases (Lele [1994], Dussauge [2001]), unable to represent alone the turbulent kinetic energy reduction. Finally, it should be noted that high values of M_t are not likely to be encountered in configurations of practical interest, unless hypersonic speeds are considered (Ristorcelli and Blaisdell [1997], Ristorcelli [1997], Dussauge [2006]), leading to a "weakly compressible nature of turbulence" (Ristorcelli and Blaisdell [1997]). The small M_t developments described here are valid for a large range of practical configurations.

Overall, it is seen that turbulence in high-speed flows is mostly solenoidal, with little contributions from the dilatational components of the velocity field. Furthermore, the universal scales of the solenoidal component of the velocity are not affected by the presence of compressible turbulence, and still show an *incompressible behavior*. Scalings of the dilatational dissipation and pressure-dilatation correlation show that the former is negligibly small for most cases of practical turbulent flows (small M_t, large Reynolds number), whereas the latter can play a role in out-of-equilibrium flows, and should be considered in the turbulent energy budget. The most important impact of compressibility on the turbulent behavior resides in the modification of the Reynolds stresses caused by the reduced pressure strain rate correlation.

1.1.2 Shock / Turbulence Interaction

The findings presented earlier have highlighted the very low levels of compressible (dilatational) velocity in many practical configurations. The changes in compressible turbulent flows have been found to be mostly of a structural nature. These results are valid for flows with small bulk dilatation, that is, when the length-scales of the turbulent fluctuations are comparable or smaller than the characteristic length-scales of the pressure fluctuations. The presence of strong compressions, typical of supersonic flows, changes the considerations presented earlier, and lead to a different evolution of the turbulent statistics.

Interactions of shocks with shear flows occur in many high-speed flow situations such as external aerodynamics of transonic, supersonic and hypersonic vehicles or internal flows in scramjets. Such interactions can have a strong impact on the flow evolution, increasing turbulent mixing, but also increasing losses and surface drag and/or heat transfer depending upon the strength of the shock. Many studies of shock / turbulence interactions have been conducted, both numerically and experimentally (see Andreopoulos et al. [2000] for a review), and physical insights have been gained from the studies of simple test cases, such as the interaction of shocks with isotropic and/or homogeneous turbulence, studied experimentally (e.g., Jacquin et al. [1993], Honkan and Andreopoulos [1992], Barre et al. [1996], Agui et al. [2005]) and numerically using high-order shock capturing methods (e.g., Lee et al. [1993], Hannappel and Friedrich [1995], Lee et al. [1997], Mahesh et al. [1997], Jamme et al. [2002, 2005]) and, more recently, using a shock-fitting method (Sesterhenn et al. [2005]).

It has been shown that shock / turbulence interactions generally lead to an amplification of all components of the turbulent stresses, and consequently of the turbulent kinetic energy. In the case of shock / isotropic turbulence interactions, linear analysis shows that the stream-wise component of the stress is the most amplified for a mean flow Mach number of $M \leq 2$, and that the trend is reversed afterward. As the mean flow Mach number is further increased, the amplification factors saturate at $M \approx 3$ (Lee et al. [1997]).

A more detailed observation of the turbulence evolution behind the shock shows that the transverse fluxes decrease first in the post-shock region as a consequence of the compression, while the streamwise stress is directly amplified In response to the incoming fluctuations in velocity and thermodynamics, the shock front corrugates and oscillates around its mean position. This phenomenon leads to the generation of pressure and dilatational velocity fluctuations behind the front. The acoustic potential energy created from this corrugation *feeds* the Reynolds stresses: evanescent acoustic waves amplify the levels of turbulence further downstream of the interaction (Lee et al. [1993, 1997], Jamme et al. [2002]). This energy transfer occurs over a short region behind the shock, and amplifies mostly the dilatational velocity field, hence increasing the level of compressible turbulence. The non-linear coupling between solenoidal and dilatational modes leads to a redistribution of the energy, leaving downstream a field of homogeneous and mostly solenoidal turbulence.

The amplification of the turbulent stresses behind the shock was found to be dependent on the shape of the initial energy spectrum of the incoming turbulent fields, its thermodynamic state and its level of compressible turbulence (Lele [1994], Hannappel and Friedrich [1995]). Lee et al. [1997] demonstrated that the physics of the interaction shock / turbulence actually had only little dependence on the initial spectrum, but much stronger correlation was found for the other parameters. Linear analysis and direct simulations showed that thermodynamic and entropy fluctuations were reduced through the interaction, even more so as the Mach number was increased. Correlations between streamwise velocity and temperature fluctuations of the initial turbulent field were found to influence the anti-correlation of vortical and acoustic modes in the post-shock region, and impact the level of stress amplification. A positive correlation between streamwise velocity and temperature fluctuations reduces the stresses amplification factor and increases the transverse characteristic length-scales, while a strongly negative correlation results in an essentially opposite trend (Mahesh et al. [1997], Jamme et al. [2002]), significantly impacting the interaction of shock waves with turbulent boundary layers.

1.2 Numerical Simulation of Compressible Turbulent Flows

Simulations of supersonic turbulent flows are a somewhat recent effort. Most of the early numerical schemes were found either too dissipative to perform turbulent studies, or incompatible with the strong variations found in compressible turbulent flows. Besides fundamental studies, the resolution of practical configurations in compressible environment by Reynolds Averaged Navier Stokes (RANS) or Large-Eddy Simulations (LES) suffered from the same inadequacy of the computational methods, and from the absence of closure models adapted to high-speed turbulent flows. The challenges that need to be faced to develop a reliable LES methodology for the simulation of compressible turbulent flows are two-fold: first, the resolution of turbulent flows requires highly accurate non-dissipative schemes. Second, the practical simulations of turbulent flows cannot be performed exactly for full-scale configurations, and modeled equations have to be solved for this flows. The relevance of the results depends on the accuracy of the modeling method adopted.

1.2.1 Numerical Issues in Supersonic Turbulent Flows Computations

A proper computational methodology requires highly accurate numerical schemes that permit the capture of flow discontinuities such as shocks and contact discontinuities, as well as the resolution of turbulent structures. This is a challenging task, as the self-steepening nature of shock waves requires a dissipative scheme to enable their capture with reduced unphysical oscillations, whereas a low-dissipation is desired for the accurate resolution of turbulent fields. The techniques developed for the resolution of the hydrodynamics equations, where crisp discontinuity capturing is desired, are presented first. The second part reviews the development of algorithms for the studies of turbulent flows in supersonic environments, where, in addition to shock-capturing properties, a low dissipation is desired.

- Upwind schemes for the resolution of supersonic flows

Until 1959, most numerical approaches were based on the expansion of the governing equations into Taylor series to obtain a finite difference approximation to the governing equations. Implicitly, the functions discretized are assumed continuous with continuous derivatives. This assumption is certainly not true in supersonic flows, where shocks and contact discontinuities are part of the flow. Many researchers have developed directionally biased numerical methods to handle physical discontinuities. Even then, most schemes were found to be dispersive, which led to high amplitude non-physical oscillations in the regions of the discontinuities.

Godunov [1959] first recognized that this assumption of continuous functions could be relaxed by resolving the Euler equations in a finite volume framework (while most studies until then were using finite difference), and resolving a Riemann problem for every interface. Getting an evaluation of the fluxes through the exact solution of the non-linear problem relaxed the assumption of continuous variables. This method, which allowed the non-dispersive resolution of flows with discontinuities was applied, and, to some extent, further developed in the following years. In the beginning of the 1970's, fundamental studies on the mathematical formulation of upwind schemes for the resolution of systems of hyperbolic equations were conducted (Lax [1972], van Leer [1973]), which later led to the development of more accurate, more stable and less dissipative methods. Among the first such contributions, and maybe one of the most influential, was the Monotone Upstream Centered Schemes for Conservation Laws (MUSCL) approach of van Leer [1973, 1974, 1979], where a higher order reconstruction of the physical field was achieved, while preserving the *monotonicity* of the solution.

Further developments of upwind schemes followed in the 1980's, based on the previous studies. Colella and Woodward extended the order of the reconstruction method, and developed the high-order and very accurate Piecewise Parabolic Method (Colella and Woodward [1984]). A framework was devised by Harten et al. [1987], for which an arbitrary order of accuracy can be achieved by adapting the stencil for the reconstruction to an adapted smoothness parameter. This scheme, based on the Total Variation Bounding condition and called Essentially Non Oscillatory (ENO) scheme, has been further extended by Liu et al. [1994b] to the Weighted Essentially Non Oscillatory (WENO) schemes, resulting in sharper resolutions of the discontinuities.

The developments conducted during that decade also included the design of approximate Riemann solvers needed for the closure of these upwind schemes. Exact Riemann solvers suffer from prohibitive costs. Researchers have started defining approximate solvers that satisfy acceptable accuracy, while significantly reducing the simulation's cost. The approximate Riemann solvers of Osher and Chakravarthy [1983], Roe (Roe [1981]), Harten-Lax-vanLeer (Harten et al. [1983]), the Two-Shock Riemann Solver and the Adaptive Non iterative Riemann Solver (Toro [1999]) are among the most commonly used. These schemes are referred to as Flux Difference Splitting (FDS) methods. Other shock-capturing methods have been addressed, such as the Flux Vector Splitting (FVS) techniques. Most of the FVS approaches, often used in external aerodynamics simulations, are based on the FVS of Steger and Warming [1981], or on the FVS method of van Leer [1982]. These methods are very appealing due to their great simplicity and computational efficiency. However, their excessive dissipation has led researchers towards the development of new schemes, that combine the simplicity/cost advantages of FVS methods, and the accuracy of FDS methods, by splitting the treatment of the inviscid equations into pressure-based fluxes and convection-based fluxes, leading to the Advection Upstream Splitting Method (AUSM) class of schemes (Liou and Steffen [1993]). The diffusion of these methods remains small and viscous flows can be correctly captured. Finally, the shock-fitting techniques have raised a recent interest. Their basis is the treatment of shock waves as propagating discontinuities, resolved with the dynamic Rankine-Hugoniot relations and the integration of this discontinuity to the global resolution. Their inclusion in general three-dimensional simulations is however complex and prohibitively expensive.

- Hybrid numerical schemes for the study of compressible turbulence in supersonic flows

The study of compressible turbulent flows using Direct Numerical Simulation (DNS) and LES can be performed using a wide variety of schemes. Central schemes, Padé differencing, compact schemes or spectral methods are commonly used in such studies. Their use for simulations where strong gradients are present is, however, inadequate, and alternate approaches are required. Upwind methods with very fine resolutions, such that the inherent numerical dissipation does not dominate the turbulent behavior, have been successfully employed in the past. High resolution simulations of compressible turbulence, for instance, have been performed using ENO/WENO schemes (Ladeinde et al. [1996], Martin [2006]), or the Piecewise Parabolic Method (PPM) (Mirin et al. [1999]). Such simulations are, however, not always feasible. Lee et al. [1997] showed in a DNS study of shock / turbulence interaction that the use of a sixth-order ENO scheme throughout the domain significantly dissipates the turbulent energy of the flow.

Hybrid schemes have been proposed for the resolution of high-speed viscous problem in the context laminar flow simulations and/or under-resolved DNS studies, where schemes developed to capture flow discontinuities were found to be too dissipative and to artificially increase boundary layer thicknesses and other viscous properties of the flow. One of the first examples of hybrid schemes was proposed by Harten and Zwas [1972], blending a Lax-Wendroff method and a Lax-Friedrichs approach, Harten [1978] later revisiting this methodology and replacing the Lax-Friedrichs scheme with a first order upwind approach. These formulation, though capable of capturing some of the important flow physics, were found to strongly depend on the shock detection formulation, and lack universality. The numerical scheme presented by Jameson et al. [1981] can be seen as a hybrid methodology, where a central scheme with second-order artificial dissipation, for shock capturing purpose, is blended with a central scheme with fourth-order artificial dissipation for smooth flow resolution.

The development of hybrid methodologies switching explicitly between different fluxes evaluations has gained popularity in the studies of high-speed turbulent flows from a DNS stand-point. Some studies have been conducted using *primitive*, non self-adapting hybrid schemes, in which the stationary properties of the flow were used to arbitrarily separate the regions where upwind schemes are used from those where central/spectral/compact schemes are used (Lee et al. [1997], Mahesh et al. [1997]). For instance, for the resolution of shock / turbulence interaction by DNS, Lee et al. [1997] used a sixth-order ENO shock-capturing scheme only in the mean-flow direction, over a relatively short region surrounding the mean shock location, defined offline, and used a Padé scheme over the remaining cells, and for all cells in the transverse directions to minimize dissipation effects.

Hybrid schemes, where two different flux computations are employed in different regions of the domain, are currently being developed for similar applications. A dynamic switching procedure is usually associated with these schemes. The local smoothness of the flow is evaluated and used to determine the scheme to employ. Many of these hybrid schemes use compact schemes for the capture of the turbulent structures in the flow, as these schemes show a spectral-like resolution. Furthermore, using low-pass spatial filtering techniques, these methods have been applied to curvilinear grids. However, compact schemes are poorly suited to the resolution of transonic to supersonic flows, creating high amplitude, unphysical oscillations, and much work has been devoted to the stabilization of these schemes in shock-containing flows, spanning from artificial diffusion (Cook and Cabot [2004], Kawai and Lele [2008]) to the application of adaptive filters, reducing the accuracy in close shock regions only (Visbal and Gaitonde [2005]). In the context of hybrid methods, these compact schemes have been combined to TVD (Rizzetta et al. [2001]), ENO (Adams and Shariff [1996]) or WENO (Pirozzoli [2002], Ren et al. [2003]) schemes and have been found well suited to simple canonical flows. However, extension to complex (practical) geometries and parallelization of such codes is difficult (Hill and Pullin [2004]), and the computational cost of these schemes is rather high, which makes such schemes unadapted to full scale simulations.

Alternatively, hybrid schemes that employ classical central schemes for the resolution of the smooth regions in the flow have been proposed (Vreman [1997], Hill and Pullin [2004], Kim and Kwon [2005], Fryxell and Menon [2005]). Their low cost, good accuracy and applicability in complex domains make them suitable candidates for practical applications. Furthermore, their adaptability to body-conforming grids permits the development of methods valid in practical geometries.

1.2.2 Turbulence Modeling for Compressible and High-Speed Flows

Turbulent flows are entirely described by the Navier-Stokes equations, which involve a very large range of time- and length- scales. Direct Numerical Simulations of compressible flows can be performed for fundamental configurations, and can provide valuable insights into the physics and processes of canonical flows. Their extension to arbitrary, realistic flows of interest is not yet feasible, as the computational resources required increase significantly as the simulated Reynolds number is increased. Practical, full-scale geometries usually involve very high Reynolds numbers, orders of magnitude larger than what is currently achievable with DNS. The universality of the small scales of turbulence has been exploited to reduce the computational requirements. A scale separation permits one to distinguish the geometry-dependent energetic scales, which require an exact resolution, from the universal scales, which can be modeled from theoretical and analytical considerations, or from experimental observations.

In this context, statistical averages of the turbulent motions are commonly used. Reynolds-Averaged Navier-Stokes (RANS) simulations permit a capture of the time-averaged fields of the flow, and can provide detailed information on some physical features and processes in a complex environment, provided an accurate turbulence model is used. The entire spectrum of turbulent statistics (in time and space) must be accounted for in the models used in these simulations. Furthermore, the dynamics of the system is lost. Many applications are strongly affected by the unsteadiness of the physical processes, and cannot be captured correctly by time-averaged methodologies. Large Eddy Simulations are an alternative approach to RANS for the simulation of turbulent flows. There, the universality of turbulence at the small length-scales is exploited. The large scales are explicitly resolved, and their interaction with the small scales modeled. The temporal evolution of the flow is explicitly solved. A proper modeling of the small (*subgrid*) scales is required in this approach.

Most numerical studies of high-speed flows are based on models developed for incompressible flows and include some compressibility corrections derived from some of the early work described earlier. The dilatational dissipation model of Sarkar [1991] is often used in practical models (Delarue and Pope [1997], Oevermann [2000], Park and Mahesh [2007]) This scaling relates the compressible dilatation to the solenoidal dissipation as:

$$\epsilon_d = \alpha_d \left({M_t}^2 + \mathcal{O}(M_t^4) \right) \epsilon_s \tag{1.1}$$

As reviewed earlier, this model does not reflect the correct physics of compressible dilatation, but it is still used as it is successful in capturing the reduced growth rate of compressible mixing layers. The actual variations of the dilatational dissipation for relevant aerodynamics applications was shown by Ristorcelli [1997] and Shao and Bertoglio [1996] to scale as:

$$\epsilon_d = \frac{{M_t}^4}{Re_l} \epsilon_s \tag{1.2}$$

with an inverse proportionality to the Reynolds number (Re_l). From these considerations, the dilatational dissipation is expected to play an important role only in the context of high M_t and low-Reynolds number compressible flows. Several models for the pressure-dilatation have also been proposed. Sarkar [1991] conducted a scaling analysis based on the decomposition of the pressure field into contributions of incompressible and purely compressible components, and found from DNS studies of isotropic compressible turbulence (Sarkar [1991]) and compressible shear flows (Sarkar [1992]) that the pressure-dilatation scales as:

$$< pd >= -\alpha_1 P M_t + \alpha_2 \epsilon_s M_t^2 + \alpha_3 S_{kk} k M_t^2 \qquad (1.3)$$

where S_{kk} represents the flow dilatation. This model is still used in some RANS applications (Calhoon et al. [2006], Fasel et al. [2006]) In practical aerodynamics flows, this correlation was found from asymptotic analysis to be a function of the departure from equilibrium of the turbulent kinetic energy budget. Ristorcelli [1997] found that:

$$< pd > \propto M_t^2 \left(\frac{Sk}{\epsilon}\right)^2 [P - \epsilon] \qquad (1.4)$$

where S is the rate of strain and k the turbulent kinetic energy. This model has been integrated in second order moment closure models to model the isotropic part of the pressure strain correlations (Adumitroaie et al. [1999]). Other studies have closed the pressure-dilatation correlation by explicitly tracking the density and/or pressure variance in the simulation (Taulbee and Van Osdol [1991], Durbin and Zeman [1992], Yoshizawa [1995], Hamba [1996]).

Many models have been proposed and employed to account for the influence of the dilatational turbulence on the flow evolution. Most of the early models have been derived from direct simulations, where arbitrary levels of compressibility were used for initial conditions, and did not represent the physics of well-developed compressible turbulent flows. Other models have been suggested where the energetic transfers are not modeled directly, but require the resolution of (multiple) additional equations within the flow, leading to higher levels of complexity and modeling uncertainties. Models that integrate the analytical scalings of the compressible energetic transfers have not yet been proposed for simple, energetic closure approaches.

1.3 Present Study

The goal of the present study is to develop a computationally efficient Large-Eddy Simulation methodology adapted to the resolution of high-speed turbulent flows for practical applications. To achieve this goal, two objectives have been identified and addressed. The first objective consists in developing a numerical method that satisfies the constraints imposed by the simulations of turbulence in high-speed flow. Regions of strong discontinuities have to be captured as a part of the solution, so that the methodology can be applied to general flows with propagating waves. In that sense, a locally dissipative scheme must be employed. Away from discontinuities, the scheme must be adapted to the resolution of smooth flows dominated by turbulent structures, reducing the amount of intrinsic dissipation. A hybrid numerical scheme is developed and presented in this study, that combines a fourth-order central scheme to a flux-difference splitting approach for shock-capturing purpose. A switching procedure based on an evaluation of the local flow smoothness is used to combine these two numerical schemes.

The second objective is to extend a state of the art closure approach to properly model the relevant physical features that arise in supersonic compressible turbulence. A model adapted to the resolution of high-speed turbulent flow must integrate the modes of energy transfer typical of compressible turbulence. Furthermore, the energy budget in shock / turbulence interactions must be modeled correctly. As reviewed earlier, the level of compressible turbulence in practical flows is small compared to the incompressible contribution. The extension of a low-compressibility model to include compressibility effects is justified. The Localized Dynamic k^{sgs} Model (LDKM) is extended in the current study to model the pressure-dilatation correlation, important in non-equilibrium flows, and the diffusion of turbulent energy by pressure fluctuations, which plays an important role in shock / turbulence interactions. Based on the analytical scalings described earlier, the dilatational dissipation is found negligible in the problems of practical interest, where typical Reynolds numbers are high and the turbulent Mach number low. This mode of energy transfer is neglected in the present developments. The structural changes of the turbulent features with compressibility are captured through the dynamic evaluation of the closure model.

The LES methodology developed during the present study is validated against fundamental studies of canonical flows and practical applications of interest. Notably, a re-examination of the shock / turbulence interaction is performed in the context of DNS, to assess the performance of the hybrid methodology, and is repeated using the LES methodology to show the proper capture of the physical phenomena involved in this problem. This study is then extended to the analysis of the physics involved in a shock-induced mixing enhancement technique. Furthermore, the simulation of a configuration relevant to scramjet injections is performed. The classical configuration of a sonic jet injection into a supersonic cross-flow is used to highlight the compressible closure performance, and a study of dynamical behavior of the problem, with a particular emphasis on the dynamics of the turbulence evolution, is performed.

This report summarizes the key developments and results obtained in the course of this project. Chapter 2 presents the mathematical modeling used in the present for the simulations of compressible turbulent fluid flow. The chapter opens with a description of the Navier-Stokes equations for a compressible flow, followed by a derivation of the LES equations that result from a filtering operation. The unclosed terms that result from the filtering operation and require modeling are then highlighted. This chapter is closed by presenting the modeling approach adopted for this study, including the modeling of the compressible terms, specific to the present development.

The second developmental aspect of this work is presented in Chap. 3. This chapter presents a hybrid framework that permits the combination of two schemes with different characteristics, in order to capture supersonic turbulent flows. A low-dissipation scheme, adapted to the resolution of turbulent flows away from shocks is associated to an upwind method for discontinuity-capturing purpose. A detailed description of the two numerical schemes integrated in this framework is provided. In particular, the shock-capturing scheme developed and implemented for the resent study is given in detail.

Chapter 4 presents the testing, validation and application of the presented LES methodology to problems of shock / turbulence interactions. Direct simulations of shock / isotropic turbulence are presented first and compared to reference data. This fundamental configuration is used to validate the numerical approach, and to highlight the importance of some closure terms in an *a priori* study of the closure model. This study is then repeated from an LES perspective, showing the proper capture of the turbulent evolution with the developed LES methodology. Application to a more practical case of shock / turbulent shear layer interaction is then considered. A high-speed mixing layer is simulated with and without shocks interactions, highlighting the impact of the shocks on the shear layer evolution, and the localized enhancement of the mixing efficiency due to the turbulence amplification through the interaction.

In Chap. 5, the relevance of this approach is demonstrated by applying it to a practical scramjet configuration. The numerical set-up reproduces the experimental study of a sonic jet in supersonic cross-flow, considered as a potential injection method in scramjet designs. Results show a good capture of the physical processes and demonstrate the applicability of the proposed hybrid LES approach to practical supersonic flow modeling and design problems. The influence of the compressible closure on the flow features is reported. Furthermore, the time-accurate resolution of this interaction permits a capture of the flow dynamics and an identification of the time-averaged and instantaneous vortical structures is presented.

Chapter 6 closes this report by summarizing the different developments performed in this work, highlighting their relevance and range of applicability, and finally closing with a few recommendations for future work.

CHAPTER II

GOVERNING EQUATIONS AND MODELING

In the present chapter, the governing equations for LES of compressible turbulent flows and the closure strategy developed for this study are presented. First, the more general Navier-Stokes equations are described. The filtering operation is presented next, the LES equations are obtained and the unclosed terms identified. Finally, the model used to evaluate these subgrid terms is presented.

2.1 The Navier-Stokes Equations

The Navier-Stokes equations can be used to entirely describe any compressible turbulent flow, in the continuum regime, and in the absence of external forces, MHD effects, etc. These equations express the conservation of mass, momentum, energy and species densities, and read:

$$\frac{\partial \rho}{\partial t} + \frac{\partial \rho u_i}{\partial x_i} = 0 \tag{2.1}$$

$$\frac{\partial \rho u_i}{\partial t} + \frac{\partial}{\partial x_j}\left[\rho u_i u_j + P\delta_{ij} - \tau_{ij}\right] = 0 \tag{2.2}$$

$$\frac{\partial \rho E}{\partial t} + \frac{\partial}{\partial x_i}\left[\left(\rho E + P\right) u_i + q_i - u_j \tau_{ij}\right] = 0 \tag{2.3}$$

$$\frac{\partial \rho Y_k}{\partial t} + \frac{\partial}{\partial x_i}\left[\rho Y_k \left(u_i + V_{i,k}\right)\right] = 0 \quad k = 1, ..., N_s \tag{2.4}$$

Here, ρ is the density, $(u_i)_{i=1,2,3}$ is the velocity vector in Cartesian coordinates, P is the pressure, and Y_k is the mass fraction for species k. Also, N_s represents the total number of species in the flow. The total energy is noted E, and τ_{ij}, q_i and $V_{i,k}$ are the stress tensor, the heat flux vector and the species diffusion velocity respectively. The total energy is the sum of internal energy (e) and kinetic energy:

$$E = e + \frac{1}{2} u_k u_k, \tag{2.5}$$

where the internal energy is the sum of the contributions from all species:

$$e = \sum_{k=1}^{N_s} Y_k e_k \tag{2.6}$$

where e_k corresponds to the $k-th$ species sensible energy.

This system of equations remains unclosed until an equation of state (EOS) is defined to relate the thermodynamics variables together. Furthermore, expressions for the stress tensor, the heat flux and the species diffusion velocity are required.

- Equation Of State

It is assumed in the present study that the gases under consideration obey to the perfect gas EOS. Introducing the temperature T, this EOS can be expressed as:

$$P = \rho R T \tag{2.7}$$

Here, R is the universal gas constant per unit mass. With $\mathcal{R}_u$ the universal gas constant per mole, R is given by:

$$R = \mathcal{R}_u \sum \frac{Y_k}{MW_k} \tag{2.8}$$

where MW_k is the molar weight of the $k-th$ species. With this EOS, it can be shown that the internal energy is a function of the temperature only, so that the $k-th$ species sensible energy is expressed as:

$$e_k = e_k^0 + \int_{T_0}^{T} C_{v,k}(T')dT' \tag{2.9}$$

where $C_{v,k}(T)$ is the specific heat at constant volume for the $k-th$ species and e_k^0 is the reference energy evaluated at a reference temperature T_0. Let us also define, for convenience, the enthalpy as $h = e + P/\rho$. The sensible enthalpy of a given species k can then be written as:

$$h_k = h_k^0 + \int_{T_0}^{T} C_{p,k}(T')dT' \tag{2.10}$$

where $C_{p,k}(T)$ is the specific heat at constant pressure for the $k-th$ species and is related to $C_{v,k}(T)$:

$$C_{p,k}(T) = C_{v,k}(T) + \frac{\mathcal{R}_u}{MW_k} \tag{2.11}$$

If the specific heats are assumed independent of temperature, a calorically perfect gas (CPG) is considered, and it is customary in this case to define the ratio of specific heats γ as:

$$\gamma_k = \frac{C_{p,k}}{C_{v,k}} \tag{2.12}$$

The EOS is then fully defined with Eqn. 2.11 and 2.12. This closure is appropriate to fundamental studies or simulations of practical flows with low temperatures and/or flows with small temperature variations. However, when higher variations in the temperature field are expected, one must resort to a more advance EOS. A thermally perfect gas (TPG) has temperature-dependent specific heats, and is well adapted to the simulations of practical flows under moderate conditions of pressure and temperature, that is, away from the critical thermodynamics condition. In the present study, despite the presence of strong compressive waves, the physical conditions are far from the critical points and the conditions of validity of the perfect gas EOS are satisfied. The specific heats temperature dependence are obtained from experimental measurements and curve-fitting (Gordon and McBride [1994]).

- Definition of the stress tensor

The fluids simulated here are assumed to be Newtonian: the stresses are proportional to the local rate of strain. Mathematically, this is expressed as:

$$\tau_{ij} = \mu \left(\frac{\partial u_i}{\partial x_j} + \frac{\partial u_j}{\partial x_i} \right) + \lambda \, \frac{\partial u_k}{\partial x_k} \, \delta_{ij} \tag{2.13}$$

where μ is the viscosity coefficient, assumed to be a function of temperature only. Again this assumption is acceptable for the pressure and temperature ranges considered in the present study. For gases, the viscosity is an increasing function of temperature, and different models exist to describe this dependence (White [1991]). Sutherland's *law* for the viscosity is given by:

$$\mu = \mu_0 \left(\frac{T}{T_0} \right)^{3/2} \frac{T_0 + S}{T + S}, \tag{2.14}$$

where μ_0, T_0 are species-specific reference values and S a constant. The dependence is sometimes given as a power-law function,

$$\mu = \mu_0 \left(\frac{T}{T_0} \right)^{n} \tag{2.15}$$

where the exponent n depends on the fluid composition, but usually takes values close to 0.7.

The remaining constant in Eqn. 2.13, λ, is the *bulk* viscosity. Following Stokes' hypothesis, it is assumed that the stress tensor is traceless, so that the bulk viscosity is related to μ as $\lambda = -2/3\,\mu$. Finally, the stress terms are given by

$$\tau_{ij} = 2\mu \left(S_{ij} - \frac{1}{3} S_{kk} \delta_{ij} \right) \tag{2.16}$$

where S_{ij} is the rate of strain tensor:

$$S_{ij} = \frac{1}{2} \left(\frac{\partial u_i}{\partial x_j} + \frac{\partial u_j}{\partial x_i} \right) \tag{2.17}$$

- Definition of the heat flux vector

The heat flux vector has contributions from the thermal conduction and from the flux of sensible enthalpy due to species diffusion. Fourier's law is used to relate the thermal conduction to the local temperature gradient. The expression for the heat flux vector is:

$$q_i = -\kappa \frac{\partial T}{\partial x_i} + \rho \sum_{1}^{N_s} Y_k h_k V_{i,k} \tag{2.18}$$

For the range of conditions considered in this study, the thermal conductivity κ, is also a function of the temperature only. Correlations of the type of Sutherland's law or of the power law dependence can be used. A Prandtl number (Pr) can be used to relate κ to μ. The Prandtl number is defined as:

$$Pr = \frac{C_p \mu}{\kappa} \tag{2.19}$$

and is assumed constant in the present study ($Pr = 0.72$).

- Definition of the species diffusion velocities

The species diffusion velocities, $V_{i,k}$, are modeled using a Fickan diffusion approximation. This closure reads:

$$V_{i,k} = -\frac{D_k}{Y_k} \frac{\partial Y_k}{\partial x_i} \tag{2.20}$$

The diffusion coefficient D_k depends on species k, the other species in the environment and the static pressure and temperature. Here, these coefficients are obtained from a constant Lewis number (Le) assumption, where the Lewis number is:

$$Le = \frac{\kappa}{\rho C_p D_k} \tag{2.21}$$

With the equation of state and the expressions for the stress tensor, the heat flux vector and the species diffusion velocity, the Navier-Stokes equations are closed and can be solved *exactly* through Direct Numerical Simulation (DNS). In this context, accurate simulations of turbulent processes should capture all the relevant scales of motion, from the largest, scaling with the outer dimensions of the configuration, down to the smallest scales of the flow, of the order of the Kolmogorov scale. This separation of scales increases as the Reynolds number is increased. As a consequence, the discretization requirements grow rapidly as the simulated Reynolds number is increased. As an illustration, Kaneda et al. [2003] performed a simulation of a $Re_\lambda = 1200$ isotropic turbulent field, which required a resolution of 4096^3 grid points. This Reynolds number, probably about as high as we can get today through DNS, is still far from what is reached in full-scale configurations. DNS does not appear as a viable solution to the current industrial and/or practical needs in computer simulations of fluid flows.

2.2 Governing Equations for LES

The separation of scales in high-Reynolds number turbulent flows, and the universality of the small scales, as first envisioned by Kolmogorov, are widely accepted characteristics of a turbulent flow. The Large Eddy Simulation equations are obtained by spatially filtering the Navier-Stokes equations, in order to separate the large, geometry-dependent scales from the small, universal scales. LES methods rely on the assumption that the universal small scales and their interaction with the large scales can be modeled, whereas the large energy containing scales need to be explicitly solved. In the present section, a spatial filter is applied to the Navier Stokes equations, and the Favré-filtered LES equations are presented. All *subgrid*, unclosed terms are explicitly identified.

2.2.1 Spatial Filtering and Favré Averaging

The separation between large and small scales is obtained by applying a spatial filter to the governing equations. Let $G(\mathbf{x}, \mathbf{x}')$ be the mathematical description of the filter Kernel used for this operation, where $\mathbf{x}$ and $\mathbf{x}'$ are position vectors. Then, variable f is filtered into $\overline{f}$ as:

$$\overline{f}(\mathbf{x}, t) = \int_{\Omega} f(\mathbf{x}', t)\ G(\mathbf{x}, \mathbf{x}') d^3\ \mathbf{x}' \tag{2.22}$$

where Ω represents the entire domain. In the current implementation, the filter used is a top-hat filter kernel. Practically, G is the product of three one-dimensional filters:

$$G(\mathbf{x} - \mathbf{x}') = \prod_{i=1}^{3} g_i(x_i - x_i') \tag{2.23}$$

where x_i is the $i-th$ computational coordinate, and g_i's are one-dimensional top-hat filters that read:

$$g_i(x_i - x_i') = \begin{cases} \frac{1}{\Delta_i}, & |x_i - x_i'| < \frac{\Delta_i}{2} \\ 0, & \text{otherwise} \end{cases} \tag{2.24}$$

Δ_i is the local one-dimensional filter size in the $i-$direction. The global filter size Δ is obtained from the one-dimensional filter sizes as $\Delta = (\Delta_1 \Delta_2 \Delta_3)^{1/3}$. For the current LES methodology, the one-dimensional filter sizes are based on the local grid spacings, and Δ is a measure of the local grid cell size.

Let us also define the *mass-weighted* filtered variable, or *Favré-filtered* variable. This alternate averaging procedure is often performed for the study of compressible flows as it significantly reduces the number of unclosed terms that result from the filtering operation, and is adopted in the present study. $\widetilde{f}$ is the Favré-filtered variable f defined by:

$$\widetilde{f} = \frac{\overline{\rho f}}{\overline{\rho}} \tag{2.25}$$

where ρ is the local fluid density.

2.2.2 Filtering the Navier-Stokes Equations

The spatial filter described above can be reduced to a function of $\mathbf{x} - \mathbf{x}'$, the relative position in space, and can thus commute with both temporal and spatial partial derivatives. The application of the filter to the Navier-Stokes equations is hereafter presented.

- Mass conservation

The equation for mass conservation reads:

$$\frac{\partial \rho}{\partial t} + \frac{\partial \rho u_i}{\partial x_i} = 0 \tag{2.26}$$

Using the commutativity of the filter with the derivatives, the filtered continuity equation reads:

$$\frac{\partial \overline{\rho}}{\partial t} + \frac{\partial \overline{\rho u_i}}{\partial x_i} = 0 \tag{2.27}$$

Finally, in terms of Favré-filtered variables, this equation reduces to:

$$\frac{\partial \overline{\rho}}{\partial t} + \frac{\partial \overline{\rho}\widetilde{u}_i}{\partial x_i} = 0 \tag{2.28}$$

- Momentum conservation

The governing equation for the momentum is obtained by following the same steps as for the continuity equation: the exact equation is filtered, and the commutativity of the filter with the derivatives is called. Finally, Favré-filtering is used. The governing equation for momentum reads:

$$\frac{\partial \overline{\rho}\widetilde{u}_i}{\partial t} + \frac{\partial}{\partial x_j}\left[\overline{\rho}\widetilde{u_i u_j} + \overline{P}\delta_{ij} - \overline{\tau_{ij}}\right] = 0 \tag{2.29}$$

This relation is strictly equivalent to the following:

$$\frac{\partial \overline{\rho}\widetilde{u}_i}{\partial t} + \frac{\partial}{\partial x_j}\left[\overline{\rho}\widetilde{u}_i\widetilde{u}_j + \overline{P}\delta_{ij} + \tau_{ij}^{sgs} - \overline{\tau_{ij}}\right] = 0 \tag{2.30}$$

so that the convective term in the equation above can be treated from the resolved field, and the subgrid stress $\tau_{ij}^{sgs} = \overline{\rho}(\widetilde{u_i u_j} - \widetilde{u}_i\widetilde{u}_j)$ is introduced. τ_{ij}^{sgs} is related to the correlation of the fluctuating velocities u_i and u_j at scales smaller than the filtering dimension (the local grid size). Hence, such terms are called *subgrid* terms and denoted using an *sgs* superscript.

- Energy conservation

The exact total energy equation is filtered into:

$$\frac{\partial \overline{\rho}\widetilde{E}}{\partial t} + \frac{\partial}{\partial x_j}\left[\overline{\rho}\left(\widetilde{u_j E}\right) + \overline{u_j P} + \overline{q_j} - \overline{u_i \tau_{ji}}\right] = 0 \tag{2.31}$$

which again is strictly equal to:

$$\frac{\partial \overline{\rho}\widetilde{E}}{\partial t} + \frac{\partial}{\partial x_j}\left[\overline{\rho}\widetilde{u}_j\widetilde{E} + \widetilde{u}_j\overline{P} + \overline{q_j} - \widetilde{u}_i\overline{\tau_{ji}} + H_j^{sgs} + \sigma_j^{sgs}\right] = 0 \tag{2.32}$$

where the terms H_j^{sgs} and σ_j^{sgs} correspond to $H_j^{sgs} = \overline{\rho}\left(\widetilde{E u_j} - \widetilde{E}\widetilde{u}_j\right) + \left(\overline{u_j P} - \overline{P}\widetilde{u}_j\right)$, and $\sigma_j^{sgs} = -(\overline{u_i \tau_{ij}} - \widetilde{u}_i\overline{\tau_{ij}})$.

- Species density conservation

Filtering the equations that govern the species conservation leads to the following relations:

$$\frac{\partial \overline{\rho}\widetilde{Y}_k}{\partial t} + \frac{\partial}{\partial x_i}\left[\overline{\rho}\left(\widetilde{Y_k u_i} + \widetilde{Y_k V_{i,k}}\right)\right] = 0 \tag{2.33}$$

Re-arrangement of those terms leads to:

$$\frac{\partial \overline{\rho}\widetilde{Y}_k}{\partial t} + \frac{\partial}{\partial x_i}\left[\overline{\rho}\left(\widetilde{Y}_k\widetilde{u}_i + \widetilde{Y}_k\widetilde{V}_{i,k}\right) + Y^{sgs}_{i,k} + \theta^{sgs}_{i,k}\right] = 0 \tag{2.34}$$

where the terms noted $Y^{sgs}_{i,k}$ and $\theta^{sgs}_{i,k}$ correspond to $Y^{sgs}_{i,k} = \overline{\rho}\left(\widetilde{u_iY_k} - \widetilde{u}_i\widetilde{Y}_k\right)$, and $\theta^{sgs}_{i,k} = \overline{\rho}\left(\widetilde{V_{i,k}Y_k} - \widetilde{V}_{i,k}\widetilde{Y}_k\right)$

- Equation of state

The perfect gas EOS is used throughout this study. Filtering this equation leads to:

$$\begin{aligned} \overline{P} &= \overline{\rho R T} = \overline{\rho}\widetilde{RT} \\ &= \overline{\rho}\widetilde{R}\widetilde{T} + \overline{\rho}\mathcal{R}_u T^{sgs} \end{aligned} \tag{2.35}$$

where T^{sgs} is the sum of the subgrid species-temperature correlations.

$$T^{sgs} = \sum \frac{\widetilde{Y_kT} - \widetilde{Y}_k\widetilde{T}}{MW_k} \tag{2.36}$$

2.3 Closure Model for the LES Equations

From the initial conditions and the time integration of Eqn. 2.28, 2.30, 2.32 and 2.34, the variables $\overline{\rho}$, $\widetilde{u}_i$, $\widetilde{E}$ and $\widetilde{Y}_k$ are known. The filtered continuity equation is fully closed. The other governing equations are unclosed and all the subgrid and filter terms in these equations require some evaluations or modeling. The total energy being the sum of a kinetic and an internal contribution, the Favré averaged total energy $\widetilde{E}$ is given by:

$$\begin{aligned} \widetilde{E} &= \widetilde{e} + \tfrac{1}{2}\widetilde{u_k u_k} \\ &= \widetilde{e} + \tfrac{1}{2}\widetilde{u}_k\widetilde{u}_k + \tfrac{1}{2}\left(\widetilde{u_k u_k} - \widetilde{u}_k\widetilde{u}_k\right) \\ &= \widetilde{e} + \tfrac{1}{2}\widetilde{u}_k\widetilde{u}_k + k^{sgs} \end{aligned} \tag{2.37}$$

Here, k^{sgs} denotes the un-resolved, or *subgrid* part of the kinetic energy. The filtered internal energy is given by:

$$\widetilde{e} = \sum_{k=1}^{N_s} \widetilde{Y}_k e^0_{f,k} + \sum_{k=1}^{N_s} \widetilde{Y}_k \int_{T_0}^{\widetilde{T}} C_{V,k}(T)dT + \sum_{k=1}^{N_s} E^{sgs}_k \tag{2.38}$$

Provided that E^{sgs}_k is evaluated, the Favré filtered temperature can be obtained. The filtered stress tensor in the momentum equation is computed in analogy to the unfiltered Navier-Stokes equations as follows:

$$\overline{\tau_{ij}} = 2\mu(\widetilde{T})\left(\widetilde{S}_{ij} - \frac{1}{3}\widetilde{S}_{kk}\delta_{ij}\right) \tag{2.39}$$

where $\widetilde{S_{ij}}$ represents the rate of filtered strain. Similarly, the filtered heat flux vector and the filtered species diffusion velocity are computed as:

$$\overline{q_j} = -\kappa(\widetilde{T})\frac{\partial \widetilde{T}}{x_j} + \overline{\rho}\sum \widetilde{Y}_k h_k(\widetilde{T})\widetilde{V_{i,k}} + q_j^{sgs} \tag{2.40}$$

$$\widetilde{V_{i,k}} = -\frac{D_k}{\widetilde{Y}_k}\frac{\partial \widetilde{Y}_k}{\partial x_i} \tag{2.41}$$

All the *subgrid-scale* terms, denoted with a *sgs* superscript, are unclosed, and therefore, require specific modeling. These terms are:

$$\tau_{ij}^{sgs} = \overline{\rho}\,(\widetilde{u_i u_j} - \widetilde{u}_i\widetilde{u}_j) \tag{2.42}$$

$$H_i^{sgs} = \overline{\rho}\left(\widetilde{Eu_i} - \widetilde{E}\widetilde{u}_i\right) + \left(\overline{u_i P} - \widetilde{u}_i\bar{P}\right) \tag{2.43}$$

$$\sigma_i^{sgs} = (\overline{u_j\tau_{ij}} - \widetilde{u}_j\overline{\tau_{ij}}) \tag{2.44}$$

$$Y_{i,k}^{sgs} = \overline{\rho}\left(\widetilde{u_i Y_k} - \widetilde{u}_i\widetilde{Y}_k\right) \tag{2.45}$$

$$\theta_{i,k}^{sgs} = \overline{\rho}\left(\widetilde{V_{i,k}Y_k} - \widetilde{V}_{i,k}\widetilde{Y}_k\right) \tag{2.46}$$

$$q_{i,k}^{sgs} = \overline{\rho}\left(\widetilde{h_k Y_k V}_{i,k} - \widetilde{h}_k\widetilde{Y}_k\widetilde{V_{i,k}}\right) \tag{2.47}$$

$$T^{sgs} = \sum_{k=1}^{N_s}(\widetilde{Y_k T} - \widetilde{Y}_k\widetilde{T})/MW_k \tag{2.48}$$

$$E_k^{sgs} = \widetilde{Y_k e_k(T)} - \widetilde{Y}_k e_k(\widetilde{T}) \tag{2.49}$$

It should be noted that, in the expressions for $\theta_{i,k}^{sgs}$, $q_{i,k}^{sgs}$ and E_k^{sgs}, the repeated index k does not imply summation. The closure strategy to model the subgrid terms is presented next.

An eddy-viscosity type closure is adopted in this study. The eddy viscosity, ν_t, is evaluated using a characteristic length-scale, provided by the local grid size $\overline{\Delta}$, and a characteristic subgrid velocity, obtained from the subgrid kinetic energy k^{sgs}, so that $\nu_t = c_\nu\overline{\Delta}\sqrt{k^{sgs}}$. The unclosed terms in the momentum equation, the subgrid stresses τ_{ij}^{sgs}, are then closed as:

$$\tau_{ij}^{sgs} = -2\overline{\rho}\nu_t\left(\widetilde{S}_{ij} - \frac{1}{3}\widetilde{S}_{kk}\delta_{ij}\right) + \frac{2}{3}k^{sgs}\delta_{ij} \tag{2.50}$$

The two unclosed terms in the energy equation, H_i^{sgs} and σ_i^{sgs} are modeled together:

$$H_i^{sgs} + \sigma_i^{sgs} = -(\overline{\rho}\nu_t + \mu)\frac{\partial k^{sgs}}{\partial x_i} - \frac{\overline{\rho}\nu_t c_p}{Pr_t}\frac{\partial \widetilde{T}}{\partial x_i} + \widetilde{u}_j\tau_{ij}^{sgs} \tag{2.51}$$

The subgrid diffusion of species mass fractions, $Y_{i,k}^{sgs}$, is also modeled using an eddy-diffusivity assumption, as:

$$Y_{i,k}^{sgs} = -\frac{\overline{\rho}\nu_t}{Sc_t}\frac{\partial \widetilde{Y}_k}{\partial x_i} \tag{2.52}$$

The diffusions due to subgrid fluctuations in species diffusion velocity, $\theta_{i,k}^{sgs}$ and $q_{i,k}^{sgs}$, are neglected in the present study. All simulations in this study are non-reactive, and the impact of these diffusion terms is expected to be small. Also, T^{sgs} and E_k^{sgs} are usually found to be very small (Fureby and Moller [1995], Veynante and Poinsot [1996]), and will be neglected in the present study as well. The determination of the local value of the subgrid kinetic energy k^{sgs} is needed for the evaluation of the eddy viscosity, and is described next.

2.3.1 Derivation of the k^{sgs} Closure Model

The subgrid kinetic energy is obtained using a transport equation model. The exact governing equation for the subgrid kinetic energy is hereafter derived, and the different contributions to the evolution of k^{sgs} are identified.

- Filtering of the Total Kinetic Energy Equation

The non-filtered equation for the kinetic energy is obtained from the Navier-Stokes equations by multiplying the $i-$ momentum equation by u_i:

$$u_i\frac{\partial \rho u_i}{\partial t} + u_i\frac{\partial \rho u_i u_j}{\partial x_j} + u_i\frac{\partial P\delta_{ij}}{\partial x_j} - u_i\frac{\partial \tau_{ij}}{\partial x_j} = 0 \tag{2.53}$$

Applying the chain rule, and calling the mass conservation Eqn. 2.1, it is straightforward to show that:

$$\frac{\partial \rho K}{\partial t} + \frac{\partial \rho u_j K}{\partial x_j} + u_i\frac{\partial P\delta_{ij}}{\partial x_j} - u_i\frac{\partial \tau_{ij}}{\partial x_j} = 0 \tag{2.54}$$

where $K = 1/2(u_i u_i)$ is the kinetic energy per unit mass. Filtering the previous equation, and using Favré-filtering, the governing equation for $\widetilde{K}$ reads:

$$\frac{\partial \overline{\rho}\widetilde{K}}{\partial t} + \frac{\partial \overline{\rho}\widetilde{u_j K}}{\partial x_j} + \overline{u_i\frac{\partial P\delta_{ij}}{\partial x_j}} - \overline{u_i\frac{\partial \tau_{ij}}{\partial x_j}} = 0 \tag{2.55}$$

- Deriving the Resolved Kinetic Energy Equation

The governing equation for the resolved kinetic energy is obtained similarly. Multiplying the filtered momentum equation, Eqn. 2.30, by the filtered velocity $\widetilde{u}_i$, gives:

$$\widetilde{u}_i\frac{\partial \overline{\rho}\widetilde{u}_i}{\partial t} + \widetilde{u}_i\frac{\partial \overline{\rho}\widetilde{u}_i\widetilde{u}_j}{\partial x_j} + \widetilde{u}_i\frac{\partial}{\partial x_j}\left[\overline{P}\delta_{ij} + \tau_{ij}^{sgs} - \overline{\tau_{ij}}\right] = 0 \tag{2.56}$$

Again, using chain rules and the filtered equation for mass conservation, Eqn. 2.28, the equation for $\widetilde{K}_{res} = \frac{1}{2}\widetilde{u}_i\widetilde{u}_i$ is reached:

$$\frac{\partial \overline{\rho}\widetilde{K}_{res}}{\partial t} + \frac{\partial \overline{\rho}\widetilde{u}_j\widetilde{K}_{res}}{\partial x_j} + \widetilde{u}_i\frac{\partial}{\partial x_j}\left[\overline{P}\delta_{ij} + \tau_{ij}^{sgs} - \overline{\tau_{ij}}\right] = 0 \tag{2.57}$$

- Deriving the Subgrid Kinetic Energy Equation

The un-resolved kinetic energy, k^{sgs}, is the subgrid part of the filtered total kinetic energy: $k^{sgs} = \widetilde{K} - \widetilde{K}_{res}$. Subtracting Eqn. 2.57 from Eqn. 2.55 gives:

$$\begin{aligned} \frac{\partial \overline{\rho} k^{sgs}}{\partial t} + \frac{\partial \overline{\rho}\left(\widetilde{u_j K} - \widetilde{u_j}\widetilde{K}_{res}\right)}{\partial x_j} &+ \left(\overline{u_i \frac{\partial P \delta_{ij}}{\partial x_j}} - \widetilde{u}_i \frac{\partial \overline{P} \delta_{ij}}{\partial x_j}\right) - \left(\overline{u_i \frac{\partial \tau_{ij}}{\partial x_j}} - \widetilde{u}_i \frac{\partial \overline{\tau_{ij}}}{\partial x_j}\right) \\ &- \widetilde{u}_i \frac{\partial \tau_{ij}^{sgs}}{x_j} = 0 \end{aligned} \tag{2.58}$$

The second term in this last equation can be re-arranged into:

$$\frac{\partial \overline{\rho}\left(\widetilde{u_j K} - \widetilde{u_j}\widetilde{K}_{res}\right)}{\partial x_j} = \frac{\partial \overline{\rho} \widetilde{u}_j k^{sgs}}{\partial x_j} + \frac{\partial \overline{\rho}\left(\widetilde{u_j K} - \widetilde{u}_j \widetilde{K}\right)}{\partial x_j} \tag{2.59}$$

so that the convective term for k^{sgs} is obtained. Chain rules are used to re-arrange the contributions that involve the pressure and the stress tensor, and the final form of the k^{sgs} equation reads:

$$\frac{\partial}{\partial t} \overline{\rho}\, k^{sgs} + \frac{\partial}{\partial x_i}\left(\overline{\rho}\, \widetilde{u}_i k^{sgs}\right) = \mathcal{T}_{k^{sgs}} + pd_{k^{sgs}} + P_{k^{sgs}} - D_{k^{sgs}} \tag{2.60}$$

where the different contributions to the k^{sgs} evolution equation have been re-cast: $\mathcal{T}_{k^{sgs}}$ represents the diffusion of k^{sgs}, $pd_{k^{sgs}}$ is the pressure dilatation correlation, and $P_{k^{sgs}}$ and $D_{k^{sgs}}$ are the production and dissipation of k^{sgs} respectively. Their exact expressions are given by:

$$\mathcal{T}_{k^{sgs}} = -\frac{\partial}{\partial x_i}\left(\left(\overline{\rho}\widetilde{K\, u_i} - \overline{\rho}\, \widetilde{K} \widetilde{u}_i - \widetilde{u}_j \tau_{ij}^{sgs}\right) + \left(\overline{u_i P} - \widetilde{u}_i \overline{P}\right) - \left(\overline{u_j \tau_{ij}} - \widetilde{u}_j\ \overline{\tau_{ij}}\right)\right) \tag{2.61}$$

$$pd_{k^{sgs}} = \overline{P \frac{\partial u_i}{\partial x_i}} - \overline{P} \frac{\partial \widetilde{u}_i}{\partial x_i} \tag{2.62}$$

$$P_{k^{sgs}} = -\tau_{ij}^{sgs} \frac{\partial \widetilde{u}_j}{\partial x_i} \tag{2.63}$$

$$D_{k^{sgs}} = \left(\overline{\tau_{ij} \frac{\partial u_i}{\partial x_j}} - \overline{\tau_{ij}} \frac{\partial \widetilde{u}_i}{\partial x_j}\right) \tag{2.64}$$

This equation requires modeling since diffusion, dissipation and pressure-dilatation correlation cannot be readily evaluated. The diffusion due to subgrid fluctuations in kinetic energy, subgrid fluctuations in viscous stress, and subgrid fluctuations in pressure all contribute to the global diffusion of k^{sgs} and each require proper modeling. The first contribution (often referred to as the triple velocity correlation) and the second are modeled using a gradient diffusion model. First, the subgrid stress work is modeled by:

$$-\frac{\partial - \left(\overline{u_i \tau_{ij}} - \widetilde{u}_i\ \overline{\tau_{ij}}\right)}{\partial x_i} = \frac{\partial}{\partial x_i}\left(\mu \frac{\partial k^{sgs}}{\partial x_i}\right) \tag{2.65}$$

Second, the subgrid transport of subgrid kinetic energy is modeled by:

$$-\frac{\partial\left(\overline{\rho}\widetilde{K u_i} - \overline{\rho}\,\widetilde{K}\widetilde{u}_i - \widetilde{u}_j \tau_{ij}^{sgs}\right)}{\partial x_i} = \frac{\partial}{\partial x_i}\left(\overline{\rho}\frac{\nu_t}{\sigma_K}\frac{\partial k^{sgs}}{\partial x_i}\right) \tag{2.66}$$

where σ_K is a model constant.

The diffusion due to subgrid pressure fluctuations is often neglected in LES of flow where compressibility effects are small. This approximation might be acceptable in low Mach number flows. However, as will be seen later, this contribution is fundamental in the context of shock / turbulence interactions, and requires modeling. Following the eddy-viscosity formulation used in the present study, this term is closed as:

$$\overline{u_i P} - \widetilde{u}_i \overline{P} = \overline{\rho}\widetilde{R}(\widetilde{u_i T} - \widetilde{u}_i \widetilde{T}) = -\frac{\overline{\rho}\nu_t \widetilde{R}}{\sigma_P}\frac{\partial \widetilde{T}}{\partial x_i} \tag{2.67}$$

Noting that this diffusion term is directly related to the subgrid diffusion of enthalpy in the governing equation for the energy conservation, the closure coefficient σ_P is taken to be the same, that is, the turbulent Prandtl number Pr_t. The global model for the diffusion of subgrid kinetic energy reads:

$$\mathcal{T}_{k^{sgs}} = \frac{\partial}{\partial x_i}\left[\left(\frac{\overline{\rho}\nu_t}{\sigma_k} + \mu\right)\frac{\partial k^{sgs}}{\partial x_i} + \frac{\overline{\rho}\nu_t \widetilde{R}}{Pr_t}\frac{\partial \widetilde{T}}{\partial x_i}\right] \tag{2.68}$$

For high Reynolds number flows, the dissipation of turbulent kinetic energy occurs mostly at the small scales. Its expression is universal and depends on the energy transfer rate within the inertial range. In compressible flows, however, the dissipation of turbulent kinetic energy has contributions from the solenoidal and the dilatational fields. Most models for the compressible part of the dissipation evaluate this term as a function of the solenoidal contribution, with a dependence on the turbulent Mach number, as reviewed earlier. The analytical work of Ristorcelli [1997] and Fauchet and Bertoglio [1998] showed that the actual dependence is on M_t^4, which remains small for most flows of practical concern. Furthermore, the relation between solenoidal and compressible dissipation scales as the inverse of the Reynolds number. The contribution of the compressible part is then very small compared to the solenoidal part, and is therefore neglected in the present model. By analogy with the Kolmogorov concept of energy cascade, and assuming that the cutoff scale lies within the inertial range, the dissipation of subgrid kinetic energy is assumed to be entirely determined by the characteristic turbulent velocity scale (based on k^{sgs}) and the characteristic length-scale (the local grid cell size), so that:

$$D_{k^{sgs}} = \overline{\rho}c_\epsilon (k^{sgs})^{3/2}/\overline{\Delta} \tag{2.69}$$

The last unclosed term in the governing equation for k^{sgs} is the pressure dilatation correlation. Here again, this term is often neglected in simulations where compressibility is not expected to play a major role, but does require a proper modeling in the context of high-speed flow simulations. The study of Ristorcelli [1997] shows that this term varies with M_t^2, and depends on the departure from equilibrium, that is, the difference between production and dissipation of turbulent energy. The present closure formulation uses this scaling analysis to model the pressure dilatation correlation as:

$$pd_{k^{sgs}} = \alpha_{pd} M_t^{sgs2} \left(\frac{\overline{\rho}\widetilde{S}k^{sgs}}{D_{k^{sgs}}} \right)^2 (P_{k^{sgs}} - D_{k^{sgs}}) \tag{2.70}$$

where M_t^{sgs2} is the turbulent Mach number based on k^{sgs}, and $\widetilde{S}$ is related to the total strain rate:

$$\widetilde{S}^2 = \frac{1}{2}\widetilde{S}_{ij}\widetilde{S}_{ij} \tag{2.71}$$

The final form of the evolution equation for the subgrid kinetic energy used here is finally obtained as:

$$\begin{aligned} \frac{\partial}{\partial t}\overline{\rho}\, k^{sgs} + \frac{\partial}{\partial x_i}\left(\overline{\rho}\, \widetilde{u}_i k^{sgs}\right) &= \frac{\partial}{\partial x_i}\left[\left(\overline{\rho}\nu_t + \mu\right) \frac{\partial k^{sgs}}{\partial x_i} + \frac{\overline{\rho}\nu_t \widetilde{R}}{Pr_t}\frac{\partial \widetilde{T}}{\partial x_i} \right] \\ &\quad - \left(1 + \alpha_{pd} M_t^{sgs2} \left(\frac{\overline{\rho}\widetilde{S}k^{sgs}}{D_{k^{sgs}}} \right)^2 \right) \left(\tau_{ij}^{sgs} \frac{\partial \widetilde{u}_j}{\partial x_i} + \overline{\rho} c_\epsilon \frac{(k^{sgs})^{3/2}}{\overline{\Delta}} \right) \end{aligned} \tag{2.72}$$

2.3.2 Evaluation of the Model Coefficients

2.3.2.1 Nominal Values of the Closure Coefficients

The closure for the LES equation and for the k^{sgs} equation is now complete, and uses six closure coefficients, $(c_\nu, c_\epsilon, \sigma_k, Pr_t, Sc_t, \alpha_{pd})$. Nominal values for c_ν and c_ϵ can be obtained from theoretical considerations. The dissipation coefficient can be determined from an assumed model turbulent spectrum. The Pao energy spectrum (Pao [1965]) is a good approximation for the energy spectral distribution at high Reynolds numbers of isotropic flows:

$$E(\kappa) = \alpha \epsilon^{\frac{2}{3}} \kappa^{-\frac{5}{3}} exp(-\frac{3}{2}\alpha(\kappa\eta)^{\frac{4}{3}}) \tag{2.73}$$

where α is the Kolmogorov constant ($\alpha \approx 1.5$), η the Kolmogorov scale and ϵ the total dissipation. This model spectrum contains both inertial and dissipative ranges. Considering κ_c the cut-off wavenumber, given by $\kappa_c = \pi/\overline{\Delta}$ (see, e.g. Pope [2000]), the subgrid kinetic energy is:

$$k^{sgs} = \int_{\kappa_c}^{\infty} \alpha \epsilon^{\frac{2}{3}} \kappa^{-\frac{5}{3}} exp(-\frac{3}{2}\alpha(\kappa\eta)^{\frac{4}{3}}) d\ \kappa \tag{2.74}$$

Assuming that the cutoff length-scale is well within the inertial, far from the dissipative scales, so that $\overline{\Delta}/\eta >> 1$, or in other form, $\kappa_c\eta << 1$, the exponential term remains very close to 1, and k^{sgs} is approximated as:

$$k^{sgs} = \int_{\kappa_c}^{\infty} \alpha \epsilon^{\frac{2}{3}} \kappa^{-\frac{5}{3}} d\kappa = \left(\frac{3\alpha}{2} \right)^{3/2} \frac{\epsilon^{2/3}}{\kappa_c^{2/3}} \tag{2.75}$$

so that the total dissipation is related to the subgrid kinetic energy:

$$\epsilon = \left(\frac{2}{3\alpha}\right)^{3/2} (k^{sgs})^{3/2} \kappa_c = 0.931 \frac{(k^{sgs})^{3/2}}{\overline{\Delta}} \tag{2.76}$$

The spectrum of dissipation is obtained from the energy spectrum as $D(\kappa) = 2\nu\kappa^2 E(\kappa)$. Its integration between κ_c and ∞ gives $\epsilon_{k^{sgs}}$:

$$\epsilon^{sgs} = 2\nu \int_{\kappa_c}^{\infty} \alpha\epsilon^{\frac{2}{3}} \kappa^{-\frac{5}{3}} \kappa^2 exp(-\frac{3}{2}\alpha(\kappa\eta)^{\frac{4}{3}}) d\ \kappa = \epsilon\ exp(-\frac{3}{2}\alpha(\kappa_c\eta)^{\frac{4}{3}}) \tag{2.77}$$

Again, the exponential term is assumed to be fairly close to 1, so that the dissipation of subgrid kinetic energy is given by $\epsilon^{sgs} \approx \epsilon = 0.931\frac{(k^{sgs})^{3/2}}{\overline{\Delta}}$.

Spectral closure theories (Kraichnan [1976]) can be used to evaluate the eddy viscosity formulation as $\nu_t = 0.441\alpha^{-3/2}\sqrt{E(\kappa_c)\kappa_c^{-1}}$. With the Pao energy spectrum and the expression for the total dissipation obtained earlier, one gets:

$$\nu_t = 0.261\sqrt{\alpha\left(\frac{0.931(k^{sgs})^{3/2}}{\overline{\Delta}}\right)^{2/3} \kappa_c^{-\frac{8}{3}} exp(-\frac{3}{2}\alpha(\kappa_c\eta)^{\frac{4}{3}})} \tag{2.78}$$

The exponential factor is again neglected, and since $\kappa_c = \pi/\overline{\Delta}$, the eddy viscosity can be evaluated:

$$\begin{aligned} \nu_t &= \tfrac{0.261\sqrt{\alpha 0.931^{2/3}}}{\pi^{4/3}}\sqrt{k^{sgs}\overline{\Delta}} \\ &= 0.067\sqrt{k^{sgs}\overline{\Delta}} \end{aligned} \tag{2.79}$$

This evaluation of the closure coefficients leads to $c_\nu = 0.067$ and $c_\epsilon = 0.931$. This constant coefficients closure has been frequently used, and shows good results in many cases. It should be noted however that these coefficients have been evaluated for a given assumed spectrum, with the assumption of a very high Reynolds number flow. In particular, Lesieur and Métais [1996] discuss the scalings for spectral closures, and point out that a spectrally averaged eddy viscosity along with the constraint of subgrid-scale kinetic energy dissipation being equal to ϵ could lead to an expression for the eddy viscosity as $\nu_t = 2/3\alpha^{-3/2}\sqrt{E(\kappa_c)\kappa_c^{-1}}$. c_ν would then be evaluated as 0.101, highlighting some of the uncertainties in the determination of the closure coefficient for subgrid terms in physical space.

2.3.2.2 *Dynamic Evaluation of the Closure Coefficients*

In general, it can be expected that the values for the closure coefficients depend on the configuration, and vary in both space and time. They should then be computed as a part of the solution. The k^{sgs} closure model presented here has been extended in order to evaluate dynamically these coefficients as a function of the local flow properties. This method, the localized Dynamic k^{sgs} Model (LDKM) was originally developed for the simulation of incompressible flows by Kim and Menon [1995]. The formulation of the dynamic model is hereafter presented.

The concept of dynamic modeling, introduced by Germano et al. [1990], is based on an explicit filtering of the exact filtered equations and of the model formulation,

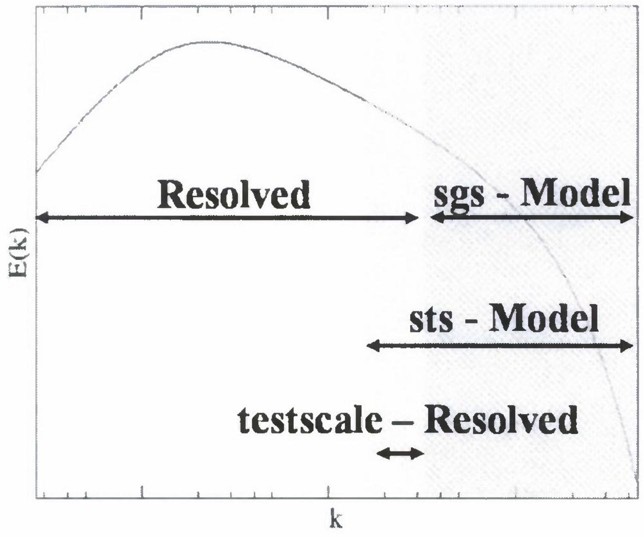

Figure 2.1: Representation of the subgrid and sub-testscale regions in a model turbulent energy spectrum, and modeling assumptions for the dynamic procedure of Germano et al. [1990].

and is schematically illustrated in Fig. 2.1. Noting $\widehat{f}$ the explicitly filtered variable f, and dropping the density for clarity, the filtered subgrid stress leads to:

$$\widehat{\tau_{ij}^{sgs}} = \widehat{\widetilde{u_i u_j}} - \widehat{\widetilde{u}_i \widetilde{u}_j} \tag{2.80}$$

which is re-arranged into:

$$\widehat{\tau_{ij}^{sgs}} = \underbrace{\left(\widehat{\widetilde{u_i u_j}} - \widehat{\widetilde{u}}_i \widehat{\widetilde{u}}_j\right)}_{\tau_{ij}^{sts}} - \underbrace{\left(\widehat{\widetilde{u}_i \widetilde{u}_j} - \widehat{\widetilde{u}}_i \widehat{\widetilde{u}}_j\right)}_{\mathcal{L}_{ij}} \tag{2.81}$$

The first term on the right hand side of this equation resembles a subgrid stress, but for a filter at a new level, hereafter referred to as sub-testscale level, and τ_{ij}^{sts} is the sub-testscale stress. The second term is called the Leonard stress, and is directly computable from the resolved field. Assuming that the subgrid stress is modeled as $\tau_{ij}^{sgs} = f\left(\widetilde{S}_{ij}, \overline{\Delta}\right)$, then [1] :

$$\widehat{\overbrace{f\left(\widetilde{S}_{ij}, \overline{\Delta}\right)}} = \left(\widehat{\widetilde{u_i u_j}} - \widehat{\widetilde{u}}_i \widehat{\widetilde{u}}_j\right) - \left(\widehat{\widetilde{u}_i \widetilde{u}_j} - \widehat{\widetilde{u}}_i \widehat{\widetilde{u}}_j\right) \tag{2.82}$$

Furthermore, modeling the sub-testscale stress with the same closure approach, one

---

[1] The $\widehat{\overbrace{(\;)}}$ symbol is used here to denote the application of the test-filter, as the *hat* symbol cannot be sufficiently extended to cover the whole expression.

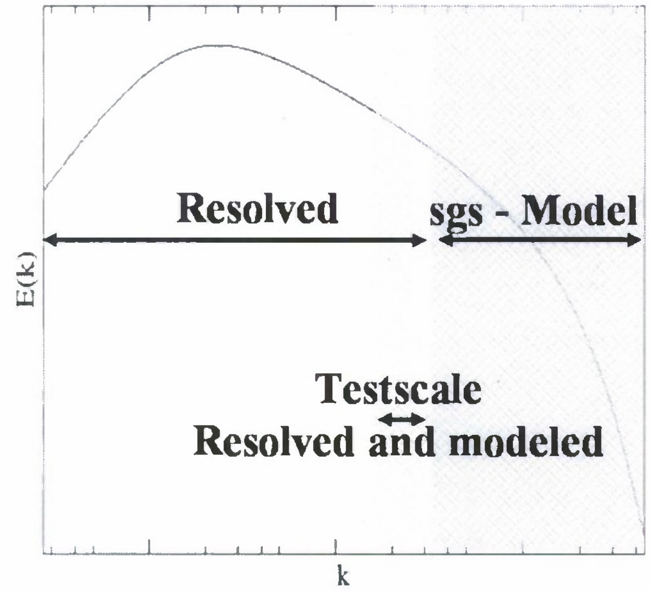

Figure 2.2: Representation of the subgrid and testscale regions in a model turbulent energy spectrum, and modeling assumptions for the LDKM.

gets:

$$\widehat{\overbrace{f\left(\widetilde{S}_{ij},\overline{\Delta}\right)}} = f\left(\widehat{\widetilde{S}}_{ij},\widehat{\Delta}\right) - \left(\widehat{\widetilde{u}_i\widetilde{u}_j} - \widehat{\widetilde{u}}_i\widehat{\widetilde{u}}_j\right) \tag{2.83}$$

The closure coefficient that appears in the function $f(.,.)$ can be obtained, assuming it is constant within the explicit filtering. This method was first applied to the dynamic Smagorinsky model (DSM), but the method was found ill-posed, as a division with an un-bounded denominator was involved in the final expression for the Smagorinsky coefficient. Stabilization of this model required averaging over the homogeneous directions of the flow. This dynamic model showed improved predictions compared to the constant coefficients Smagorinsky model. Extension of this method to other closure models has been performed. It should be noted that a Dynamic k^{sgs} Model (DKM) has been developed using the same principle as in the DSM, but again, the method for computing the closure coefficient in the momentum equation was still performing a division with a denominator that could reach zero. This issue was again circumvented by averaging the coefficient along directions of homogeneity.

The LDKM method has been developed in a truly localized fashion, without any need for averaging. Rather than considering that the model used for τ_{ij}^{sgs} could be extended to the modeling of τ_{ij}^{sts}, a similarity between the testscale Leonard stress $\mathcal{L}_{ij}$ and τ_{ij}^{sgs} is assumed, as illustrated in Fig. 2.2. It should be noted that such a relation has been experimentally observed and reported by Liu et al. [1994a]. Considering the

Favre averaged testscale Leonard stress (the density is now included for completeness):

$$\mathcal{L}_{ij} = \widehat{\bar{\rho}} \left(\frac{\widehat{\bar{\rho}\tilde{u}_i\tilde{u}_j}}{\widehat{\bar{\rho}}} - \frac{\widehat{\bar{\rho}\tilde{u}_i}}{\widehat{\bar{\rho}}} \frac{\widehat{\bar{\rho}\tilde{u}_j}}{\widehat{\bar{\rho}}} \right) \tag{2.84}$$

The testscale resolved kinetic energy is then given by the trace of the Leonard stress tensor:

$$k^{test} = \frac{1}{2}\frac{\mathcal{L}_{kk}}{\widehat{\bar{\rho}}} = \frac{1}{2} \left(\frac{\widehat{\bar{\rho}\tilde{u}_k\tilde{u}_k}}{\widehat{\bar{\rho}}} - \frac{\widehat{\bar{\rho}\tilde{u}_k}}{\widehat{\bar{\rho}}} \frac{\widehat{\bar{\rho}\tilde{u}_k}}{\widehat{\bar{\rho}}} \right) \tag{2.85}$$

The similarity in form between Leonard stress at the testscale level and subgrid stress tensor can then be expressed mathematically as:

$$\mathcal{L}_{ij} = -2c_\nu \sqrt{k^{test}}\widehat{\bar{\rho}}\widehat{\Delta} \left(\frac{\widehat{\bar{\rho}\tilde{S}_{ij}}}{\widehat{\bar{\rho}}} - \frac{1}{3}\frac{\widehat{\bar{\rho}\tilde{S}_{kk}}}{\widehat{\bar{\rho}}}\delta_{ij} \right) + \frac{1}{3}\mathcal{L}_{kk}\delta ij \tag{2.86}$$

or, identically:

$$\mathcal{L}_{ij} = -2c_\nu \sqrt{k^{test}}\widehat{\Delta} \left(\widehat{\bar{\rho}\tilde{S}_{ij}} - \frac{1}{3}\widehat{\bar{\rho}\tilde{S}_{kk}}\delta_{ij} \right) + \frac{2}{3}\widehat{\bar{\rho}}k^{test}\delta_{ij} \tag{2.87}$$

$\mathcal{L}_{ij}$, k^{test} and $\widehat{\bar{\rho}\tilde{S}_{ij}}$ can be computed from the resolved fields of velocity and density. c_ν remains the only unknown in this equation. The closure coefficient is however over-specified, as six independent equations are obtained from this relation. The redundancy is removed using the least-square method proposed by Lilly [1992]. The testscale stress tensor model error tensor E_{ij} is defined as:

$$E_{ij} = \mathcal{L}_{ij} + 2c_\nu \sqrt{k^{test}}\widehat{\Delta} \left(\widehat{\bar{\rho}\tilde{S}_{ij}} - \frac{1}{3}\widehat{\bar{\rho}\tilde{S}_{kk}}\delta_{ij} \right) - \frac{1}{3}\mathcal{L}_{kk}\delta ij \tag{2.88}$$

This tensor represents the differences between exact subtest-scale stresses and modeled stresses. A minimization of the *r.m.s.* error is enforced. Mathematically, this consists in ensuring that the derivative of $E_{ij}E_{ij}$ with respect to the model coefficient c_ν is zero. This expression reads:

$$\frac{\partial E_{ij}E_{ij}}{\partial c_\nu} = 4\mathcal{M}_{ij}\mathcal{L}'_{ij} + 8c_\nu\mathcal{M}_{ij}\mathcal{M}_{ij} = 0 \tag{2.89}$$

where:

$$\mathcal{L}'_{ij} = \mathcal{L}_{ij} - \frac{1}{3}\mathcal{L}_{kk}\delta_{ij} \tag{2.90}$$

and

$$\mathcal{M}_{ij} = \sqrt{k^{test}}\widehat{\Delta} \left(\widehat{\bar{\rho}\tilde{S}_{ij}} - \frac{1}{3}\widehat{\bar{\rho}\tilde{S}_{kk}}\delta_{ij} \right) \tag{2.91}$$

Finally, the expression for c_ν is obtained:

$$c_\nu = -\frac{\mathcal{M}_{ij}\mathcal{L}'_{ij}}{2\mathcal{M}_{ij}\mathcal{M}_{ij}} \tag{2.92}$$

The evaluation of the coefficient c_ν requires a division, but the denominator is a well-defined non-zero quantity. Consequently, this dynamic formulation is stable, and can be applied in a truly localized manner. It is also worth noting that, even though $\mathcal{M}_{ij}$ appears at both numerator and denominator, the tensorial notation $\mathcal{M}_{ij}\mathcal{M}_{ij}$ implies a distributive multiplication, hence it is not possible to cancel $\mathcal{M}_{ij}$ out of the numerator and denominator. It is also worth noting that an evaluation of the model coefficient based on the production of k^{test} from exact and modeled Leonard stresses leads to the same formulation of the closure coefficient. The two production terms are:

$$\mathcal{L}_{ij}^{filter}\frac{\widehat{\bar{\rho}\widetilde{S_{ij}}}}{\widehat{\bar{\rho}}} = \mathcal{L}_{ij}^{model}\frac{\widehat{\bar{\rho}\widetilde{S_{ij}}}}{\widehat{\bar{\rho}}} \tag{2.93}$$

which give:

$$\mathcal{L}_{ij}\widehat{\bar{\rho}\widetilde{S_{ij}}} = \left(-2c_\nu\sqrt{k^{test}}\widehat{\Delta}\;\left(\widehat{\bar{\rho}\widetilde{S}_{ij}} - \frac{1}{3}\widehat{\bar{\rho}\widetilde{S}_{kk}}\delta_{ij}\right) + \frac{1}{3}\mathcal{L}_{kk}\delta_{ij}\right)\widehat{\bar{\rho}\widetilde{S_{ij}}} \tag{2.94}$$

So that:

$$c_\nu = \frac{\mathcal{L}'_{ij}\widehat{\bar{\rho}\widetilde{S_{ij}}}}{-2\mathcal{M}_{ij}\widehat{\bar{\rho}\widetilde{S_{ij}}}} \tag{2.95}$$

Noting that both $\mathcal{L}'_{ij}$, appearing in the numerator, and $\mathcal{M}_{ij}$ in the denominator are traceless, it is strictly equivalent to replace $\widehat{\bar{\rho}\widetilde{S_{ij}}}$ in the previous expression by $\widehat{\bar{\rho}\widetilde{S_{ij}}} - \widehat{\bar{\rho}\widetilde{S_{kk}}}\delta_{ij}$. Then,

$$c_\nu = \frac{\mathcal{L}'_{ij}\left(\widehat{\bar{\rho}\widetilde{S}_{ij}} - \frac{1}{3}\widehat{\bar{\rho}\widetilde{S}_{kk}}\delta_{ij}\right)}{-2\mathcal{M}_{ij}\left(\widehat{\bar{\rho}\widetilde{S}_{ij}} - \frac{1}{3}\widehat{\bar{\rho}\widetilde{S}_{kk}}\delta_{ij}\right)} \tag{2.96}$$

Multiplying both numerator and denominator by $\sqrt{k^{test}}\widehat{\Delta}$, one gets exactly the relation:

$$c_\nu = -\frac{\mathcal{M}_{ij}\mathcal{L}'_{ij}}{2\mathcal{M}_{ij}\mathcal{M}_{ij}} \tag{2.97}$$

In order to determine the closure coefficient for the dissipation of k^{sgs}, the governing equation for k^{test} is used. Its derivation is very similar to the derivation of the k^{sgs} governing equation, and reads:

$$\frac{\partial}{\partial t}\bar{\rho}\,k^{test} + \frac{\partial}{\partial x_i}\left(\widehat{\bar{\rho}\widetilde{u}_i k^{test}}\right) = \mathcal{T}_{k^{test}} + pd_{k^{test}} + P_{k^{test}} - D_{k^{test}} \tag{2.98}$$

where the expression for the diffusion, pressure-dilatation correlation, production and dissipation at the testscale level are fully expressed as functions of the resolved variables and of the subgrid stresses only. In particular, the production of k^{test} is $P_{k^{test}} = -\mathcal{L}_{ij}\widehat{\bar{\rho}\widetilde{S_{ij}}}/\widehat{\bar{\rho}}$, and its dissipation is given by:

$$D_{k^{test}} = \widehat{\overbrace{(\overline{\tau_{ij}} - \tau_{ij}^{sgs})\frac{\partial\widetilde{u_j}}{\partial x_i}}} - \widehat{\overbrace{(\overline{\tau_{ij}} - \tau_{ij}^{sgs})}}\,\frac{1}{\widehat{\bar{\rho}}}\,\bar{\rho}\widehat{\frac{\partial\widetilde{u_j}}{\partial x_i}} \tag{2.99}$$

Under the similarity assumption, the dissipation of k^{test} is modeled with the same formulation as the dissipation of k^{sgs}, $D_{k^{test}} = \widehat{\overline{\rho}}c_\epsilon(k^{test})^{3/2}/\widehat{\Delta}$, where again, only the closure coefficient remains unknown. With the following notation:

$$\widetilde{\Sigma_{ij}} = 2\left(\widetilde{S_{ij}} - \frac{1}{3}\widetilde{S_{kk}}\delta_{ij}\right) \tag{2.100}$$

the difference between filtered and subgrid stresses is given by:

$$\overline{\tau_{ij}} - \tau_{ij}^{sgs} = \mu_{eff}\widetilde{\Sigma_{ij}} - \frac{2}{3}\overline{\rho}k^{sgs}\delta_{ij} \tag{2.101}$$

where $\mu_{eff} = \mu + \mu_t$. μ_{eff} is assumed to be constant over the width of the explicit filter. The expression for the dissipation coefficient c_ϵ is given by:

$$c_\epsilon = \frac{\widehat{\Delta}}{\widehat{\overline{\rho}}\left(k^{test}\right)^{\frac{3}{2}}}\left(\frac{\mu_{eff}}{\widehat{\overline{\rho}}}\left[\widehat{\overline{\rho}}\,\widehat{\widetilde{\Sigma_{ij}}\frac{\partial\widetilde{u}_j}{\partial x_i}} - \widehat{\widetilde{\Sigma_{ij}}}\;\overline{\rho}\widehat{\frac{\partial\widetilde{u}_j}{\partial x_i}}\right] - \frac{2}{3}\left[\overline{\rho}\widehat{k^{sgs}\frac{\partial\widetilde{u}_k}{\partial x_k}} - \widehat{\overline{\rho}k^{sgs}}\frac{\partial\widehat{\widetilde{u}}_k}{\partial x_k}\right]\right) \tag{2.102}$$

In compressible flows, the closure for the energy equation plays a fundamental role, as strong variations in the energy / temperature fields are associated with the compressibility of the flow. The turbulent Prandtl number, used to close the energy equation, has been shown in experimental and DNS studies to vary spatially and temporally for a given turbulent flow. Furthermore, the statistical average of Pr_t has been found to be flow-dependent. It is generally found that Pr_t remains of the order of unity. Chambers et al. [1985] report an average turbulent Prandtl number $Pr_t = 0.4$ in an experimental study of turbulent mixing layers, with spatial variations between 0.3 and 0.6. Using direct simulations of decaying incompressible isotropic turbulence, Moin et al. [1991] showed that Pr_t could be assumed approximately constant, $Pr_t \approx 0.4$, but that compressibility could significantly impact the theoretical value of this closure coefficient which varies between 0.25 and 0.6. Also, Pham et al. [2007] studied the evolution of a turbulent thermal plume using both DNS and LES, and showed variations of Pr_t between 0.2 and 0.7. It appears clearly from these exact evaluations of Pr_t that assuming a constant value for this closure model can be a rather limiting approach.

In the present work, the dynamic evaluation of the closure coefficients is extended to the local computation of the turbulent Prandtl number, using the same similarity assumptions as for the other closure coefficients. At the testscale level, the expression for the temperature and velocity correlation, n_i, can be computed exactly from the resolved field.

$$n_i = \frac{\widehat{\overline{\rho}\widetilde{u}_i\widetilde{T}}}{\widehat{\overline{\rho}}} - \frac{\widehat{\overline{\rho}\widetilde{u}_i}}{\widehat{\overline{\rho}}}\frac{\widehat{\overline{\rho}\widetilde{T}}}{\widehat{\overline{\rho}}} \tag{2.103}$$

Using the same modeling assumption as in the subgrid term case, the testscale velocity temperature correlation is given by:

$$\frac{\widehat{\overline{\rho}\widetilde{u}_i\widetilde{T}}}{\widehat{\overline{\rho}}} - \frac{\widehat{\overline{\rho}\widetilde{u}_i}}{\widehat{\overline{\rho}}}\frac{\widehat{\overline{\rho}\widetilde{T}}}{\widehat{\overline{\rho}}} = \frac{c_\nu\sqrt{k^{test}}\widehat{\Delta}}{\widehat{\overline{\rho}}Pr_t}\widehat{\overline{\rho}\frac{\partial\widetilde{T}}{\partial x_i}} \tag{2.104}$$

Pr_t is the only unknown of this system of three independent equations. Again, the over-specification is solved using a least-square method to minimize the error vector. Solving for the inverse of the Prandtl number, the following expression is obtained:

$$1/Pr_t = -\frac{d_i n_i}{d_i d_i} \tag{2.105}$$

where

$$d_i = \frac{c_\nu \sqrt{k^{test}}\widehat{\Delta}}{\widehat{\overline{\rho}}} \widehat{\overline{\rho}\frac{\partial \widetilde{T}}{\partial x_i}} \tag{2.106}$$

The formulation of the model for the pressure-dilatation correlation is given in Eqn. 2.70. Again, the similarity assumption is made between subgrid and testscale pressure dilatation in order to evaluate the closure coefficient α_{pd}. $pd_{k^{test}}$ can be expressed as:

$$pd_{k^{test}} = \widehat{\overline{P}\frac{\partial \widetilde{u}_i}{\partial x_i}} - \frac{\widehat{\overline{P}}}{\widehat{\overline{\rho}}} \widehat{\overline{\rho}\frac{\partial \widetilde{u}_i}{\partial x_i}} \tag{2.107}$$

The model associated with this expression reads:

$$pd_{k^{test}} = \alpha_{pd} M_t^{test^2} \left(\frac{\widehat{\overline{\rho}\widetilde{S}}k^{test}}{D_{k^{test}}} \right)^2 (P_{k^{test}} - D_{k^{test}}) \tag{2.108}$$

A single scalar expression is obtained for the closure coefficient:

$$\alpha_{pd} = \frac{\widehat{\overline{P}\frac{\partial \widetilde{u}_i}{\partial x_i}} - \widehat{\overline{P}}/\widehat{\overline{\rho}}\, \widehat{\overline{\rho}\frac{\partial \widetilde{u}_i}{\partial x_i}}}{M_t^{test^2} \left(\frac{\widehat{\overline{\rho}\widetilde{S}}k^{test}}{D_{k^{test}}} \right)^2 (P_{k^{test}} - D_{k^{test}})} \tag{2.109}$$

It should be noted that the denominator depends on the departure from equilibrium at the testscale level. If the production of k^{test} balances the dissipation, the formulation is found ill-posed. The pressure dilatation correlation is expected to be relatively small in most case, reaching 10% of the dissipation in non-equilibrium flow configurations. This is used to bound the value of α_{pd} and prevent divergent values of the modeled pressure-dilatation correlation.

The other coefficients σ_k and Sc_t could also be evaluated dynamically, if needed using a similar strategy. However, the impact of the σ_k is small compared to other terms in the governing equation for k^{sgs}, and is therefore, assumed to be constant ($\sigma_k = 1$). The turbulent Schmidt number is taken to be equal to 0.9. This latter approximation is acceptable for simulations where species play a passive role.

2.3.3 Realizability Conditions

Vreman et al. [1994] showed that if a positive semi-definite filter, such as the top-hat filter, is used within an LES formulation, the subgrid stresses have to be positive semi-definite. These conditions, referred to as the *realizability* constraints, were found to be satisfied by the LDKM formulation most of the time during the computation of well resolved turbulence (Nelson and Menon [1998]). However, the strong and very localized variations induced by shocks can make this property difficult to satisfy over certain regions of the flow. An explicit enforcement of the realizability constraints is performed in this study. The realizability constraint is given by:

$$\begin{array}{rcl} \tau_{11}^{sgs}, \tau_{22}^{sgs}, \tau_{33}^{sgs} & \geq & 0 \\ |\tau_{12}^{sgs}|^2 & \leq & \tau_{11}^{sgs}\tau_{22}^{sgs} \\ |\tau_{23}^{sgs}|^2 & \leq & \tau_{22}^{sgs}\tau_{33}^{sgs} \\ |\tau_{13}^{sgs}|^2 & \leq & \tau_{11}^{sgs}\tau_{33}^{sgs} \\ \det\left[\tau_{ij}^{sgs}\right] & \geq & 0. \end{array} \tag{2.110}$$

With the closure adopted in the present study, the three intermediate relations are re-arranged to show:

$$\tau_{12}^{sgs2} + \tau_{13}^{sgs2} + \tau_{23}^{sgs2} \leq \tau_{11}^{sgs}\tau_{22}^{sgs} + \tau_{11}^{sgs}\tau_{33}^{sgs} + \tau_{22}^{sgs}\tau_{33}^{sgs} \tag{2.111}$$

Noting that $\tau_{ij}^{sgs} = -2\overline{\rho}\nu_t\widetilde{\Sigma}_{ij} + 2/3\overline{\rho}k^{sgs}\delta_{ij}$, one can re-write the previous relation as:

$$\begin{array}{rcl} (2\overline{\rho}\nu_t)^2(\widetilde{\Sigma}_{12}^2 + \widetilde{\Sigma}_{13}^2 + \widetilde{\Sigma}_{23}^2) & \leq & (2\overline{\rho}\nu_t)^2(\widetilde{\Sigma}_{11}\widetilde{\Sigma}_{22} + \widetilde{\Sigma}_{11}\widetilde{\Sigma}_{33} + \widetilde{\Sigma}_{22}\widetilde{\Sigma}_{33}) \\ & - & \frac{2}{3}(\overline{\rho}k^{sgs}2\overline{\rho}\nu_t)(\widetilde{\Sigma}_{11} + \widetilde{\Sigma}_{22} + \widetilde{\Sigma}_{33}) \\ & + & 3\frac{4}{9}\overline{\rho}^2k^{sgs2} \end{array} \tag{2.112}$$

The trace of the tensor $\widetilde{\Sigma}_{ij}$ is 0. Hence, the second term on the right hand side of the equation given above can be canceled out. The first term can be re-expressed as:

$$\widetilde{\Sigma}_{11}\widetilde{\Sigma}_{22} + \widetilde{\Sigma}_{11}\widetilde{\Sigma}_{33} + \widetilde{\Sigma}_{22}\widetilde{\Sigma}_{33} = \frac{1}{2}\underbrace{(\widetilde{\Sigma}_{11} + \widetilde{\Sigma}_{22} + \widetilde{\Sigma}_{33})}_{=0}{}^2 - \frac{1}{2}(\widetilde{\Sigma}_{11}^2 + \widetilde{\Sigma}_{22}^2 + \widetilde{\Sigma}_{33}^2) \tag{2.113}$$

The equation given above can then be formulated:

$$(\nu_t)^2(\widetilde{\Sigma}_{12}^2 + \widetilde{\Sigma}_{12}^2 + \widetilde{\Sigma}_{23}^2 + \frac{1}{2}(\widetilde{\Sigma}_{11}^2 + \widetilde{\Sigma}_{22}^2 + \widetilde{\Sigma}_{33}^2)) \leq \frac{1}{3}k^{sgs2} \tag{2.114}$$

Given that ν_t is given by $\nu_t = c_\nu\sqrt{k^{sgs}}\Delta$, one can get an upper bound for the c_ν coefficient as:

$$c_\nu \leq \frac{\sqrt{k^{sgs}}}{\sqrt{3}\ \widetilde{S}\ \overline{\Delta}} \tag{2.115}$$

where $\widetilde{S}$ is the strain rate magnitude defined earlier. These constraints are explicitly enforced everywhere.

CHAPTER III

COMPUTATIONAL METHODS

As reviewed earlier, the computational resolution of turbulence in high-speed flows is a challenging task, as it requires a numerical scheme that combines a fine capture of the turbulent structures in the flow with low inherent dissipation, and a shock-capturing capability, to resolve all discontinuities in the flow as a part of the solution. In order to allow for such simulations, a hybrid scheme is developed in the present study that switches dynamically and locally between two numerical schemes in different regions of the flow. The McCormack scheme will be first presented, and its extension to fourth order spatial accuracy will be examined. The shock capturing methodology developed and implemented in the framework of this hybrid approach is described afterwards. Finally, the smoothness sensor used to assess the numerical switch is described.

3.1 Numerical Integration

3.1.1 Finite Volume Method

The governing equations described in Chap. 2 can be written in the following form:

$$\frac{\partial Q}{\partial t} + \frac{\partial F_x}{\partial x} + \frac{\partial F_y}{\partial y} + \frac{\partial F_z}{\partial z} = S \tag{3.1}$$

where Q is the vector of conserved state variables, F_x, F_y and F_z represent the fluxes in the x, y and z direction respectively. and the vector S contains all the source terms. A finite volume approach is used in the current study ; the governing equations are integrated over a control volume V (a computational cell), delimited by a surface Σ, as follows:

$$\iiint_V \frac{\partial Q}{\partial t} dV + \iiint_V \left(\frac{\partial F_x}{\partial x} + \frac{\partial F_y}{\partial y} + \frac{\partial F_z}{\partial z}\right) dV = \iiint_V S dV \tag{3.2}$$

With Green's theorem, the previous relation is re-expressed as:

$$\frac{\partial Q}{\partial t} + \frac{1}{V} \oint_\Sigma (F_x\, n_x + F_y\, n_y + F_z\, n_z)\, d\Sigma = S \tag{3.3}$$

where Q and S are averaged over the volume of integration, F over the cell interfaces, and (n_x, n_y, n_z) are the normalized Cartesian components of the elemental surface normal vector.

In the structured framework adopted here, any computational cell of coordinates (i, j, k) is delimited by 6 interfaces $(\Sigma_l)_{l=1..6}$ located at $(i \pm 1/2, j, k)$, $(i, j \pm 1/2, k)$, and $(i, j, k \pm 1/2)$. Noting more generally $F_l = F_x n_x + F_y n_y + F_z n_z$ the corresponding fluxes evaluations, the increment in the cell-centered variable Q is computed as:

$$dQ = -\frac{dt}{V} \sum_{l=1,..6} (F_l \; \Sigma_l) + S \; dt \tag{3.4}$$

3.1.2 McCormack Time Integration

The time integration is performed using a two-stage Runge-Kutta method. As will be presented later, the fluxes evaluation in the McCormack method differ during the two stages of the time-integration. For this reason, the two stages are often called *predictor* and *corrector*, and their formulation is given by:

$$\begin{array}{lcll} Q^{(\star)} & = & Q^{(n)} + dQ^{(n)} & (Predictor) \\ Q^{(n+1)} & = & \frac{1}{2} \left[Q^{(n)} + Q^{(\star)} + dQ^{(\star)} \right] & (Corrector), \end{array} \tag{3.5}$$

Here, $dQ^{(n)}$ and $dQ^{(\star)}$ are the increments in state variables, obtained as in Eqn. 3.4, based on the variables $Q^{(n)}$ and $Q^{(\star)}$ respectively. This results in an explicit methodology with second order accuracy in time. This time integration, originally chosen as a part of the McCormack scheme, is applied to both the central and the upwind schemes presented hereafter. The spatial accuracy of the overall scheme is determined by the accuracy in the evaluation of the fluxes at the cell interfaces. The smooth flow solver will be presented first, for both second and fourth order spatial accuracies, followed by a description of the upwind shock-capturing flux computation.

As mentioned above, the scheme used here is explicit. The increments computed at a given sub-iteration are based on the field at that sub-iteration. The superscripts in $Q^{(n)}$ or $Q^{(\star)}$ are redundant, and are dropped in the following description of the schemes for clarity. Also, the numerical schemes hereafter described are used to evaluate the fluxes at the interfaces. The flux at a given $i + 1/2$ interface is determined from the cell variables of varying i's, but for fixed j and k. In order to simplify the notations, only the index corresponding the i location will be kept, j and k being implicitly fixed. Furthermore, it should be noted that the extension of the computational operations described for the i-direction to the other two directions is straightforward, the indices i, j and k being essentially interchangeable.

3.2 A Hybrid Scheme for Supersonic Turbulent Flows

In order to evaluate the state variable increment in Eqn. 3.4, the fluxes at the cell interfaces must be evaluated. In order to capture both the discontinuities in the flow and allow for the resolution of the turbulent features, a hybrid framework has been developed. The flux evaluation is given by:

$$F_{i+1/2} = \lambda_{i+1/2} F^s_{i+1/2} + \left(1 - \lambda_{i+1/2}\right) F^u_{i+1/2} \tag{3.6}$$

where F^s is the flux obtained using a low-dissipation scheme adapted to the resolution of turbulent flows, presented in Sec. 3.3, whereas F^u is evaluated from a shock-capturing scheme, described in Sec. 3.4. Rather than blending the two schemes, the current hybrid methodology switches between them. The switch variable $\lambda_{i+1/2}$ is then given as a Heaviside step function, according to an evaluation of the smoothness of the local flow-field, used to determine which scheme is appropriate.

Several sensors can be found in the literature. In self-adjusting artificial diffusions, an explicit diffusive term is integrated to the governing equations, and its strength is dynamically computed from some characteristics of the flow variations. Harten and Zwas [1972] suggested the following self-adjusting parameter for shock-capturing:

$$\theta_{i+1/2} = \kappa \left[\frac{|\phi_{i+1} - \phi_i|}{\max_j |\phi_{j+1} - \phi_j|} \right]^m \tag{3.7}$$

where κ and m are user-dependent constants, and ϕ a variable that characterizes the discontinuity. The denominator captures the largest jump in the flow. These coefficients were found to strongly depend on the configuration, the presence and strength of the shocks within the simulation. More recently, the Jameson artificial dissipation (Jameson and Baker [1983]) was designed to stabilize central schemes in shock regions, and has been widely used. Its basis consists in evaluating the curvature of the pressure field and to compare it to the average pressure value:

$$S_i = \frac{P_{i+1} - 2P_i + P_{i-1}}{P_{i+1} + 2P_i + P_{i-1}} \tag{3.8}$$

Identically, Lapidus [1967] described an artificial dissipation method where the artificial viscosity is a function of the velocity divergence. These artificial diffusion methods modify the governing equation in order to stabilize the numerical scheme. The concept of blending and/or switching between two numerical schemes with dispersive and dissipative natures is somewhat more recent.

Several hybrid schemes based on ENO and WENO scheme for shock-capturing have been presented. The design of the switching functions has varied from author to author. Adams and Shariff [1996], Pirozzoli [2002] have used a switching formulation based solely on the gradients in the flow. Let $s_{i+1/2}$ be the gradient in fluxes at a given interface $i + 1/2$:

$$s_{i+1/2} = \frac{F_{i+1} - F_i}{\Delta x_{i+1/2}} \tag{3.9}$$

A spatial location in the flow was considered non-smooth in the study of Adams and Shariff [1996] if the following conditions were satisfied:

1. The modulus of the gradient times grid spacing is larger than a certain threshold $s_{i+1/2}\Delta x_{i+1/2} > \alpha$
2. The gradient attains a local maximum $|s_{i-1/2}| < |s_{i+1/2}| > |s_{i+3/2}|$.

The more dissipative, shock handling scheme is applied to the three surrounding interfaces, $(i - 1/2), (i + 1/2), (i + 3/2)$ if these two conditions are satisfied. Hill and

Pullin [2004] suggested a switch based on the smoothness factor computed in the context of WENO schemes to define the weight coefficients of the scheme. Later, Hill et al. [2006], Pantano et al. [2007] used a hybrid scheme that integrated a slightly different smooth flow solver, and changed to a Jameson-type sensor, (Eqn. 3.8) based on both pressure and density fields.

Other smoothness sensors are described in the literature that intend to identify shock waves within the computation field. Ducros et al. [1999] described a sensor based on the physical observation that, unless very high levels of compressible turbulence are expected in the flow, the turbulent structures are essentially vortical, and the bulk dilatation of the flow is associated with shock waves. The following expression:

$$\frac{||\vec{\nabla} \cdot \vec{U}||}{||\vec{\nabla} \cdot \vec{U}|| + ||\vec{\nabla} \times \vec{U}||} \tag{3.10}$$

quantifies the levels of compression and was combined to a Jameson sensor for shock detection.

In the present study, not only shocks, but all discontinuities need to be captured with the upwind method. Three types of discontinuities found in supersonic flows need to be detected, namely the contact discontinuities, sharp flame fronts and shock waves. The central scheme employed in the present study, and described in Sec. 3.3, can efficiently resolve gradients in the flow, but generates numerical oscillations in regions where flow gradients change rapidly. Accordingly, the sensor retained for the present implementation is based on the curvature of both the pressure and the density fields, sufficient to ensure the detection of all three types of discontinuities. The generic formulation of the smoothness parameter for variable ϕ ($\phi = P$ or $\phi = \rho$) is given by:

$$S_{\phi,i} = \begin{cases} \frac{|\phi_{i+1}-2\phi_i+\phi_{i-1}|}{|\phi_{i+1}-\phi_i|+|\phi_i-\phi_{i-1}|} - S_\phi^{th} & if\ |\phi_{i+1} - 2\phi_i + \phi_{i-1}| \geq \epsilon_\phi \phi_i \\ -S_\phi^{th} & otherwise \end{cases} \tag{3.11}$$

This formulation of $S_{\phi,i}$ permits a quantification of the changes in flow gradients rather than an identification of the gradients alone. For the present study, the coefficients ϵ_P and ϵ_ρ are taken to be equal to 0.05 and 0.1 respectively. The threshold values for the pressure and density switches, S_P^{th} and S_ρ^{th} are equal to 0.5 and 0.25 respectively. These coefficients were found from numerical experimentations to yield accurate simulations of turbulent flows in the presence of shocks and/or density interfaces. These sensors identify the regions where the pressure and/or density fields show rapid variations and where these variables show significant gradients. This permits to only capture the *heads* and *feet* of the discontinuities. The switch function $\lambda_{i+1/2}$ is then defined as:

$$\lambda_{i+1/2} = \begin{cases} 1 & if\ max(S_{P,i}, S_{P,i+1}, S_{\rho,i}, S_{\rho,i+1}) \leq 0 \\ 0 & otherwise \end{cases} \tag{3.12}$$

3.3 A Central Scheme for Turbulent Flows

The numerical scheme employed for the resolution of the turbulent structures should have a small intrinsic dissipation in order to capture the evolution of the fluctuations at the right rate. As reviewed in Chap. 1, several schemes have been employed in the context of DNS and LES. Compact schemes, for instance, have been found to have a quasi-spectral behavior, and are as such well adapted to turbulent studies. The high computational cost associated with these schemes, the poor behavior in gradient regions and the complexity in the scheme formulation for highly stretched and skewed grid make them poorly suited to practical studies. The focus of the present study being the development of a numerical methodology for complex geometries, the smooth flow solver integrated in the present hybrid method uses central differencing. High order central schemes have a low dissipation, permit a capture of turbulent structures and have grid-conforming capability.

3.3.1 A 2nd Order Accurate Method - the Original McCormack Scheme

In order to reduce numerical dissipation, the use of central schemes is preferred. Purely central schemes are, however, found to be unstable. Many researchers have developed modified central schemes with limiters and/or artificial dissipation to stabilize these numerical methods (*e.g.* Jameson and Baker [1983]). The method of MacCormack [1969] does not add any explicit diffusion to a central scheme, but rather uses the two stages of the time integration method to get a built-in dissipation within the scheme. To do so, the fluxes at the cell interfaces are computed using alternatively backward and forward differencing in the predictor / corrector sequence. This combination results in a central differencing method over the entire time integration. The numerical fluxes at the interfaces are obtained from the interpolated state variables. Noting $Q^+_{i+\frac{1}{2}}$ the interpolated state variable at the interface from backward extrapolation, and correspondingly $Q^-_{i+\frac{1}{2}}$ the result of the forward extrapolation, the fluxes are computed as:

$$F^s_{i+\frac{1}{2}} = F\left(Q^\pm_{i+\frac{1}{2}}\right) \tag{3.13}$$

In the original McCormack method, first order extrapolations are used at each step of the sequence. The neighboring cell centers are alternatively used to get the interface fluxes as:

$$\begin{aligned} Q^+_{i+\frac{1}{2}} &= Q_{i+1} \\ Q^-_{i+\frac{1}{2}} &= Q_i \end{aligned} \tag{3.14}$$

This formulation yields second order accuracy in space and time (hereafter noted $\mathcal{O}(2,2)$). The combination of first-order extrapolation within the predictor/corrector sequence leads to a higher-order scheme. The backward / forward sequence is alternated in order to prevent directional bias over the simulation.

3.3.2 A 4th Order Extension to the McCormack Scheme

Higher order schemes are better suited to the computations of turbulent flows. The original McCormack scheme having shown good accuracy for many practical problems of aerodynamics and turbulence, its predictor / corrector method is a good candidate for the design of higher order methods. Gottlieb and Turkel [1976] studied general forms of fourth-order accurate schemes with Richtmyer and McCormack time integration methods. They proposed an extension of the basic $\mathcal{O}(2,2)$ McCormack scheme to $\mathcal{O}(2,4)$ accuracy, by defining the fluxes based on the extrapolation:

$$\begin{aligned} Q^{+}_{i+\frac{1}{2}} &= \tfrac{1}{6}\left(7\,Q_{i+1} - Q_{i+2}\right) \\ Q^{-}_{i+\frac{1}{2}} &= \tfrac{1}{6}\left(7\,Q_{i} - Q_{i-1}\right) \end{aligned} \tag{3.15}$$

Nelson [1997] showed that this scheme really is $\mathcal{O}(2,3)$, due to the relation that exists between time-step and computational grid spacing, and developed a method that truly is fourth order in space. The computation of the fluxes (method hereafter called N24 scheme) is obtained from:

$$\begin{aligned} Q^{+}_{i+\frac{1}{2}} &= \tfrac{1}{6}\left(2\,Q_{i} + 5\,Q_{i+1} - Q_{i+2}\right) \\ Q^{-}_{i+\frac{1}{2}} &= \tfrac{1}{6}\left(2\,Q_{i+1} + 5\,Q_{i} - Q_{i-1}\right) \end{aligned} \tag{3.16}$$

Here again, alternating the backward / forward sequence is used to prevent persistent directional bias.

A stability analysis of the fourth-order extension to the McCormack scheme shows that the N24 scheme is unconditionally unstable for the resolution of the linear advection equation. It is further shown that the highest order that can be achieved with the McCormack methodology that ensures conditional stability is third order spatial accuracy. This theoretical analysis, based on the resolution of the simplified advection equation is of fundamental importance, but no conclusion can be made on the behavior of the scheme for the practical resolution of the Navier-Stokes equations. This system of equations is far more complex and non-linear. Furthermore, the presence of viscous forces stabilizes the practical simulations. Stable fourth-order schemes may be obtained within the McCormack formulation for the advective-diffusive equation with specific restrictions on the grid Reynolds number. In practice, very weak numerical oscillations are observed in simulations of turbulent flows using the N24 scheme. The method used here differs from the original scheme of Nelson [1997], but reduces the amount of numerical oscillations and keeps its fourth order accuracy:

$$\begin{aligned} Q^{+}_{i+\frac{1}{2}} &= -\tfrac{5}{18}Q_{i+2} + \tfrac{7}{6}Q_{i+1} + \tfrac{1}{9}Q_{i-1} \\ Q^{-}_{i+\frac{1}{2}} &= -\tfrac{5}{18}Q_{i-1} + \tfrac{7}{6}Q_{i} + \tfrac{1}{9}Q_{i+2} \end{aligned} \tag{3.17}$$

The formulation is extended to non-uniform grid spacings. Following the notations of Nelson [1997], as represented in Fig. 3.1, the spacing between the cell center and the interface at $i+1/2$ is noted $\Delta_i^{(1)}$, the spacing between cell center i and cell center

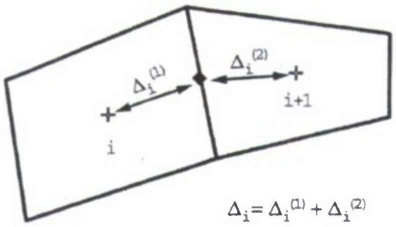

Figure 3.1: Schematic representing the curvilinear grid spacing definitions, from Nelson [1997].

$i+1$ is Δ_i. Grid stretching in the previous extrapolation procedure is accounted for as:

$$\begin{aligned}
Q^{+}_{i+\frac{1}{2}} &= -\tfrac{5}{9}\left(\frac{\Delta^{(1)}_{i+1}}{\Delta_{i+1}}\right)Q_{i+2} + \tfrac{1}{9}\left(7 + 5\frac{\Delta^{(1)}_{i+1}}{\Delta_{i+1}} + 2\frac{\Delta^{(1)}_{i}}{\Delta_i}\right)Q_{i+1} \\
&\quad + \tfrac{2}{27}\left(2 - 3\frac{\Delta^{(1)}_{i}}{\Delta_i} + \frac{\Delta^{(1)}_{i-1}}{\Delta_{i-1}} - \frac{\Delta_i}{\Delta_{i-1}}\right)Q_i + \tfrac{2}{27}\left(1 - \frac{\Delta^{(1)}_{i-1}}{\Delta_{i-1}} + \frac{\Delta_i}{\Delta_{i-1}}\right)Q_{i-1} \\
Q^{-}_{i+\frac{1}{2}} &= -\tfrac{5}{9}\left(1 - \frac{\Delta^{(1)}_{i-1}}{\Delta_{i-1}}\right)Q_{i-1} + \tfrac{1}{9}\left(14 - 5\frac{\Delta^{(1)}_{i-1}}{\Delta_{i-1}} - 2\frac{\Delta^{(1)}_{i}}{\Delta_i}\right)Q_i \\
&\quad + \tfrac{2}{27}\left(3\frac{\Delta^{(1)}_{i}}{\Delta_i} - \frac{\Delta_i + \Delta^{(1)}_{i+1}}{\Delta_{i+1}}\right)Q_{i+1} + \tfrac{2}{27}\left(\frac{\Delta_i + \Delta^{(1)}_{i+1}}{\Delta_{i+1}}\right)Q_{i+2}
\end{aligned} \tag{3.18}$$

The evaluation of $Q^{\pm}_{i+1/2}$ is used to evaluate the fluxes at the interface according to Eqn. 3.13.

3.4 A Flux-Difference Splitting Scheme for Discontinuity Capturing

Shocks and contact discontinuities are common features of supersonic flows and require proper resolution. Central schemes such as the fourth-order scheme described previously, are dispersive in nature, and create numerical oscillations around steep gradients, strongly affecting the flow and leading to unphysical values in the computed field. The upwind method required in the hybrid framework must be of dissipative nature, and to capture strong gradients as a part of the solution. A flux difference splitting has been chosen and implemented for the current study, and is hereafter described. This approach fulfills the shock-capturing requirement, and has a rather low computational cost and a body-conforming capability. A higher-order method is achieved by the use of a Monotone Upstream Centered Schemes for Conservation Laws (MUSCL) re-construction technique. The resolution of the Riemann problem is performed using an approximate Riemann solver, leading to the evaluation of the interface fluxes.

3.4.1 Interface Reconstruction

In flux difference splitting (FDS) methods, every cell interface is considered as a sharp separation between a left and a right state with different properties. The first step in FDS consists in re-constructing this Riemann problem.

3.4.1.1 MUSCL Interpolation

The interpolation used in the current scheme uses the MUSCL approach of van Leer [1979], in which the flow variables are assumed to have piecewise-linear variations. The left and right states for a given interface are evaluated as:

$$\begin{aligned} U^L_{i+1/2} &= U_i + \tfrac{\epsilon(1-\xi_i)}{4}\left[(1-\kappa)\,\Delta^+_{i-1/2}(U) + (1+\kappa)\,\Delta^-_{i+1/2}(U)\right] \\ U^R_{i+1/2} &= U_{i+1} - \tfrac{\epsilon(1-\xi_{i+1})}{4}\left[(1+\kappa)\,\Delta^+_{i+1/2}(U) + (1-\kappa)\,\Delta^-_{i+3/2}(U)\right] \end{aligned} \tag{3.19}$$

where first order piecewise constant extrapolation is used if $\epsilon = 0$, and higher order is obtained for $\epsilon = 1$. The coefficient ξ_i is computed from the flattening operation and will be described later. The value for κ drives the order of the interpolation. Third order spatial accuracy is obtained for $\kappa = 1/3$. All other values lead to a second order interpolation. $\kappa = 1$ corresponds to a central differencing scheme, whereas $\kappa = -1$ is a purely upwind interpolation.

van Leer [1979] introduced the concept of monotonicity in the interpolation procedure: the evaluation of the states at the cell interface should not create new extrema in the field. To enforce this condition, *limiters* are applied to the interpolation of $\Delta^{\pm}_{i-1/2}(U)$. The interpolation technique uses the following differencing:

$$\begin{array}{lr} \multicolumn{2}{c}{\Delta_{i+1/2}(U) = U_{i+1} - U_i} \\ \Delta^+_{i+1/2}(U) = \Delta_{i+1/2}(U)\phi(r^+_{i+1/2}) & r^+_{i+1/2} = \frac{\Delta_{i+3/2}(U)}{\Delta_{i+1/2}(U)} \\ \Delta^-_{i+1/2}(U) = \Delta_{i+1/2}(U)\phi(r^-_{i+1/2}) & r^-_{i+1/2} = \frac{\Delta_{i-1/2}(U)}{\Delta_{i+1/2}(U)} \end{array} \tag{3.20}$$

where ϕ is the so-called limiter. The interpolation reads then:

$$\begin{aligned} U^L_{i+1/2} &= U_i + \tfrac{\epsilon(1-\xi_i)}{4}\left[(1-\kappa)\,\phi(r^+_{i-1/2})(U_i - U_{i-1}) + (1+\kappa)\,\phi(r^-_{i+1/2})(U_{i+1} - U_i)\right] \\ U^R_{i+1/2} &= U_{i+1} - \tfrac{\epsilon(1-\xi_{i+1})}{4}\left[(1-\kappa)\,\phi(r^-_{i+3/2})(U_{i+2} - U_{i+1}) + (1+\kappa)\,\phi(r^+_{i+1/2})(U_{i+1} - U_i)\right] \end{aligned} \tag{3.21}$$

Noting that $r^+_{i-1/2} = 1/r^-_{i+1/2}$, the overall procedure can be re-arranged into:

$$\begin{aligned} U^L_{i+1/2} &= U_i + \tfrac{\epsilon(1-\xi_i)}{4}\left[(1-\kappa)\,\phi(r^+_{i-1/2}) + (1+\kappa)\,\phi(\tfrac{1}{r^+_{i-1/2}})r^+_{i-1/2}\right](U_i - U_{i-1}) \\ U^R_{i+1/2} &= U_{i+1} - \tfrac{\epsilon(1-\xi_{i+1})}{4}\left[(1-\kappa)\,\phi(r^-_{i+3/2}) + (1+\kappa)\,\phi(\tfrac{1}{r^-_{i+3/2}})r^-_{i+3/2}\right](U_{i+2} - U_{i+1}) \end{aligned} \tag{3.22}$$

Several limiters have been developed and used in the past. Five limiters have been identified and implemented for the current development, namely:

- Minmod Limiter

This limiter might be most common one. It can be expressed as:

$$\phi_{mm}(r) = max\left[0, min(r, 1)\right] \tag{3.23}$$

- Superbee Limiter

$$\phi_{sb}(r) = max\left[0, min(2r, 1), min(r, 2)\right] \tag{3.24}$$

The Minmod and Superbee limiters are actually part of a class of limiters described by Sweby:

$$\begin{gathered} \phi_{\beta}(r) = max\left[0, min(\beta r, 1), min(r, \beta)\right] \\ 1 \leq \beta \leq 2 \end{gathered} \tag{3.25}$$

where the minmod corresponds to $\beta = 1$ and the superbee corresponds to $\beta = 2$.

- Monotonized Central Limiter

$$\phi_{mc}(r) = max\left[0, min(2r, 2, \frac{1+r}{2})\right] \tag{3.26}$$

- Van Leer Limiter

$$\phi_{vl}(r) = \frac{|r| + r}{1 + r} \tag{3.27}$$

- Van Albada Limiter

$$\phi_{va}(r) = \frac{r^2 + r}{1 + r^2} \tag{3.28}$$

All these limiters satisfy a symmetry condition:

$$\frac{\phi(r)}{r} = \phi\left(\frac{1}{r}\right) \tag{3.29}$$

The relation expressed in eqn. 3.22 is simplified for a symmetric limiter to:

$$\begin{aligned} U^L_{i+1/2} &= U_i + \tfrac{\epsilon(1-\xi_i)}{2}\phi(r^+_{i-1/2})(U_i - U_{i-1}) \\ U^R_{i+1/2} &= U_{i+1} - \tfrac{\epsilon(1-\xi_{i+1})}{2}\phi(r^-_{i+3/2})(U_{i+2} - U_{i+1}) \end{aligned} \tag{3.30}$$

showing that the dependence on κ of the original interpolation procedure is lost when symmetric limiters are used. The implication of this property is that the order of the reconstruction depends on the local variations of the interpolated variable, and on the limiter used for the interpolation.

A scheme is said to be Total Variation Diminishing (TVD) if the total variation of the solution is diminishing as the simulation progresses. Limiters that satisfy the TVD condition lead to a monotonic scheme (Harten [1983]). The limiters used in the MUSCL technique ensure a second order TVD property if their descriptive functions lie in the region described in Fig. 3.2. The implemented limiters are shown in Fig. 3.3 and 3.4. Among the limiters that have been implemented, superbee is found to be the

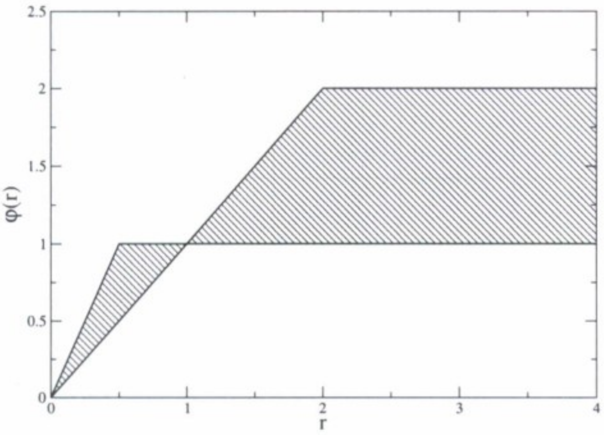

Figure 3.2: Region defining second order TVD schemes (shaded in grey).

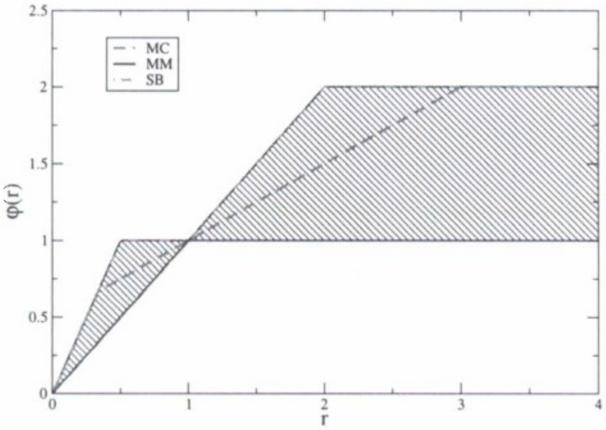

Figure 3.3: Characteristic curves for the Monotonized central (MC), minmod (MM) and superbee (SB) limiters.

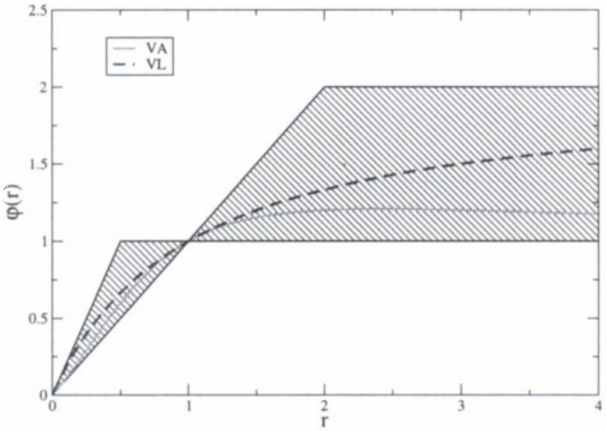

Figure 3.4: Characteristic curves for the van Leer (VL) and van Albada (VA) limiters.

most anti-diffusive. It is often considered *over compressive*, i.e., it tends to produce artificial compression and thus to sharpen profiles into discontinuities. Minmod is the least compressive option, and provides a great amount of numerical dissipation. More details about the design, the use, and the limitations of the limiters can be found in reference books on CFD (see, *e.g.* Hirsch [1997], Tannehill et al. [1997])

The reconstruction, Eqn. 3.30 is then fully defined, and can be applied to various sets of variables (Berthon [2005]). In the present work, the operation is performed on the primitive variables $(\overline{\rho}, \tilde{u}_i, \overline{P}, \overline{\rho_k})$. These variables are often used in this context, as they permit a crisp capture of the discontinuities, at a very small computational cost.

3.4.1.2 Monotonicity of the Reconstructed States

The monotonicity of each reconstructed variable is ensured in the method described previously by the use of TVD limiters. However, a global monotonicity of the interpolation procedure requires more attention.

- Conserving the Sign of the Gradients through the Interface

The monotonicity of the solution is enforced by:

$$\begin{aligned} max(U_i, U_{i+1}) \geq U^l_{i+\frac{1}{2}} \geq min(U_i, U_{i+1}) \\ max(U_i, U_{i+1}) \geq U^r_{i+\frac{1}{2}} \geq min(U_i, U_{i+1}) \end{aligned} \qquad (3.31)$$

Conservation of the sign of variations across the interface is however not ensured by this method. The configuration shown in Fig. 3.5 shows that the results of the reconstruction procedure can satisfy the monotonicity condition expressed in Eqn. 3.31 and violate the global variations of the interpolated variable: $U_{i+1} - U_i < 0$ and $U^R_{i+1/2} - U^L_{i+1/2} > 0$. The satisfaction of this extra monotonicity constraint is checked

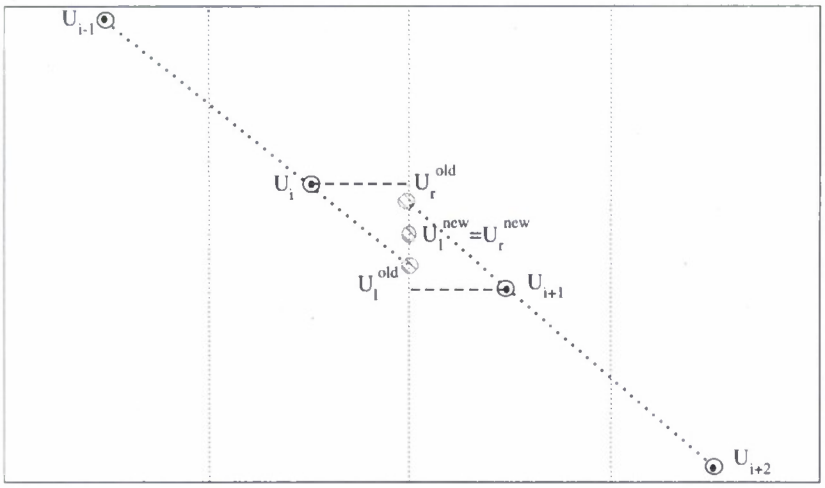

Figure 3.5: Schematic illustrating the gradient violation during the reconstruction procedure.

and enforced in the current procedure. Violation of this condition is corrected by setting:

$$U^{L,new}_{i+\frac{1}{2}} = \frac{1}{2}(U^{L,old}_{i+\frac{1}{2}} + U^{R,old}_{i+\frac{1}{2}}) \qquad U^{R,new}_{i+\frac{1}{2}} = U^{L,new}_{i+\frac{1}{2}} \tag{3.32}$$

It should be noted that the initial reconstructed field, $U^{L,old}_{i+\frac{1}{2}}$ and $U^{R,old}_{i+\frac{1}{2}}$, satisfy by construction the monotonicity expressed in Eqn. 3.31. This correction ensures that $U^{L,new}_{i+\frac{1}{2}}$ and $U^{R,new}_{i+\frac{1}{2}}$ also satisfy this property.

- Monotonicity of secondary variables

The interpolation is performed on a selected set of variables. In the present case, as mentioned earlier, the primitive variables are used for reconstruction. Other variables are needed for the Riemann solver resolution and flux computation. The left and right states of the temperature are required, for the evaluation of the speed of sound and the evaluation of the total energy. Temperature is re-computed from the interpolated field, rather than extrapolated itself. The monotonicity of this secondary variable:

$$max(T_i, T_{i+1}) > T^L_{i+\frac{1}{2}} > min(T_i, T_{i+1}) \tag{3.33}$$

is strictly enforced through modifications of the pressure interpolation if needed.

- Monotonicity of the species mass fractions

The MUSCL reconstruction is applied to the species densities, and the mass fractions are recomputed on each side of the interface. This operation requires special attention. The values of the limiters for the different species are likely to differ if the procedure is performed independently on each one of the species. The resulting set of mass fraction on a given side of the interface does not satisfy mass conservation, namely:

$$\sum_{k=1}^{N_s} Y_k^{L/R} \neq 1 \tag{3.34}$$

A re-normalization of the mass fraction at the interface has often been used in the past (Fryxell et al. [1989], Plewa and Müller [1999]). This method unfortunately leads to non-monotonic field of species mass fractions. The method adopted in the present study consists in reducing the order of the interpolation of the species to the *most limiting* reconstruction. For the species densities, the reconstruction reads:

$$\begin{aligned} \rho^l_{k,i+\frac{1}{2}} &= \rho_{k,i} + \tfrac{\epsilon(1-\xi_i)}{2} \underbrace{\min}_{k=0..N_s} \left(\phi\left(r^+_{i-1/2}(\rho_k)\right)\right)(\rho_{k,i} - \rho_{k,i-1}) \\ \rho^r_{k,i+\frac{1}{2}} &= \rho_{k,i+1} - \tfrac{\epsilon(1-\xi_{i+1})}{2} \underbrace{min}_{k=0..N_s} \left(\phi\left(r^-_{i+3/2}(\rho_k)\right)\right)(\rho_{k,i+2} - \rho_{k,i+1}) \end{aligned} \tag{3.35}$$

where $k = 0$ refers to the reconstruction of the total density.

3.4.1.3 Flattening Procedure

Colella and Woodward [1984] showed that post-shock oscillations were found in the resolution of strong shocks using shock-capturing schemes. This instability of the numerical scheme is related to the self-steepening property of the shocks. Colella and Woodward [1984] have found that reducing the order of the reconstruction in regions of steep and strong pressure gradients could eliminate these perturbations. The flattening method described in this reference is implemented in the current formulation to evaluate the coefficient ξ_i in Eqn. 3.22, employing the same coefficients. A cell is identified as being part of a shock wave if the following two conditions are satisfied

$$d_{P,i} = \frac{|P_{i+1} - P_{i-1}|}{min(P_{i+1}, P_{i-1})} - \frac{1}{3} > 0 \tag{3.36}$$

$$d_{u,i} = u_{i+1} - u_{i-1} < 0 \tag{3.37}$$

The shock thickness is then measured by relating the pressure gradient across two cells to the gradient across four cells,

$$S_{p,i} = \frac{P_{i+1} - P_{i-1}}{P_{i+2} - P_{i-2}} \tag{3.38}$$

$$\widetilde{\xi_i} = max\left[0, min\left(1, 10(S_{p,i} - 0.75)\right)\right] \tag{3.39}$$

Finally, the limiting factor ξ_i in the reconstruction procedure, Eqn. 3.30 is then defined as:

$$\xi_i = \begin{cases} max(\widetilde{\xi_i}, \widetilde{\xi_{i+1}}), & if P_{i+1} - P_{i-1} < 0 \\ max(\widetilde{\xi_i}, \widetilde{\xi_{i-1}}), & otherwise \end{cases} \tag{3.40}$$

With this description of the flattening method, the reconstruction procedure for the left and right states of the interface is now complete. The numerical fluxes are then obtained from these states using a Riemann solver. The next section describes the Riemann solver developed for the current study.

3.4.2 A Class of Approximate Riemann Solvers - HLL·

A brief description of the *HLL* Riemann solver family is given hereafter. The HLL approximate Riemann solvers have first been developed by Harten, Lax and van Leer (Harten et al. [1983]), by expressing a hyperbolic system of conservation laws in integrand form. From an initial interface separating two constant states, it is assumed that N waves can be formed from the characteristics evolution of the system, separating $N+1$ constant-properties regions. The knowledge of the jump relation through the waves and the wave-speeds permits to obtain a closed form expression for the intermediate states, and the associated fluxes. Harten et al. [1983] carried a full derivation for a two-waves problem, leaving the wave-speeds as sole unknowns to the solver, and have given a mathematical description for the 3-waves problem.

The 2-waves formulation for the resolution of the Euler equations (with wave-speeds expressions given by Einfeldt [1988], Einfeldt et al. [1991], thus called *HLLE*) has been proven robust and adequate for shocks and rarefactions, but appears as very dissipative for contact discontinuities. Toro et al. [1994] proposed a correction to the derivation of this solver, in order to *add* the missing contact wave (thus called *HLLC*), whose wave-speed was estimated by an approximation of the particle velocity in the intermediate region. The formulation is closed by expressing the jump conditions across all wave obtained from the exact Riemann solver for the Euler equations. This formulation was further studied by Batten et al. [1997], who related the averaged intermediate state to the HLLE evaluation, thus leading to an easy, but yet robust, 3-waves Riemann solver. It should be noted that this 3-waves solver does not follow the original work of Harten *et al*, as the intermediate wave speed is estimated from the 2-wave solver as a correction, and does not reduce to a single-wave problem in the physical limit of an isolated discontinuity. Linde [2002] derived a 3-waves Riemann solver (often referred to as the *HLLL*, of the HL^3 Riemann solver) that follows the original framework of Harten et al. [1983]. The basis of this formulation is more general than for the HLLC solver, as no assumption is made on the equations solved. The intermediate wave strength and jump conditions are determined from an entropy-minimizing procedure. This alternate $3 - waves$ solver can be used for the resolution of any hyperbolic system of equations. In particular, it has been shown (Gurski [2005]) that the HLLC formulation is a specific case of the more general HLLL formulation for the resolution of hydrodynamics problems. The increased complexity of this solver is adapted to complex governing equations (Miyoshi and Kusano [2005]), but is not justified in the resolution of hydrodynamics flows, where the HLLC solver is found to yield accurate and robust solutions. The derivation that will be hereafter presented focuses on the 2-waves formulation of the original HLL method and its HLLC extension.

The Riemann solver developed for this study uses a combination of the HLLE

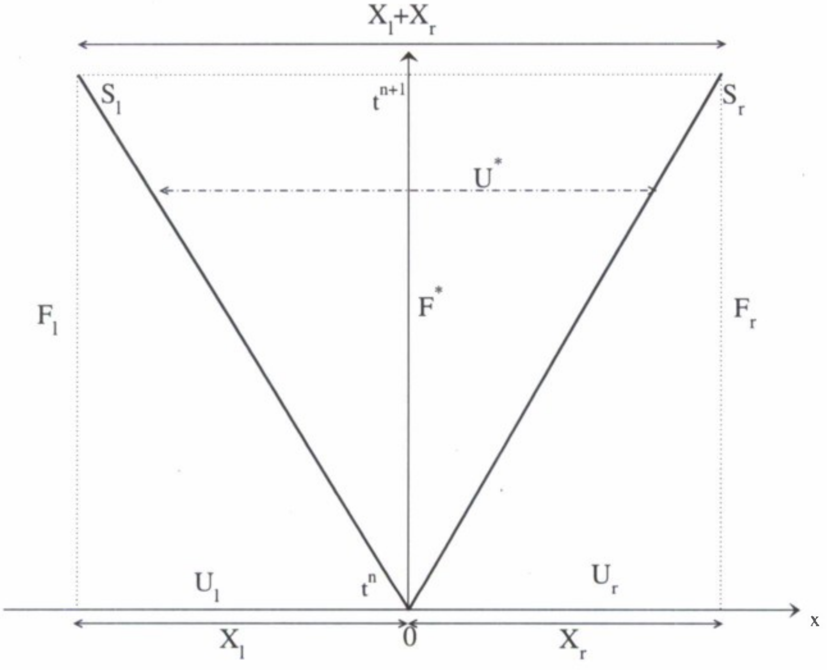

Figure 3.6: (x, t) diagram of an approximate Riemann problem evolution with two characteristic waves.

and HLLC solvers, in order to reduce the instabilities associated to contact-resolving solvers. The simpler 2-waves HLLE will be described hereafter. Following this derivation, the wave-speeds estimates, and the modifications that lead to the HLLC solver are given.

3.4.2.1 The 2-waves HLL Riemann Solver

The derivation of this solver is based on the assumption that an initial one-dimensional discontinuity gives rise to 2 waves, a left-moving wave (of Eulerian speed S^L), and a right-moving one (of Eulerian speed S^R). A typical (x,t) diagram for a subsonic case is given in Fig. 3.6. The integral form of the Euler equations (see, *eg*, Toro [1999]), reads:

$$\oint [Udx - F(U)dt] = 0 \tag{3.41}$$

where, noting $q = \vec{V} \cdot \vec{n} = un_x + vn_y + wn_z$ the interface normal velocity amplitude, U and $F(U)$ are given by:

$$U = \begin{bmatrix} \rho \\ \rho u \\ \rho v \\ \rho w \\ \rho E \\ \rho k^{sgs} \\ \rho Y_k \end{bmatrix}, \quad F = \begin{bmatrix} \rho q \\ \rho u q + P n_x \\ \rho v q + P n_y \\ \rho w q + P n_z \\ (\rho E + P) q \\ \rho k^{sgs} q \\ \rho Y_k q \end{bmatrix} \tag{3.42}$$

Let T be the local time step, $T = t^{n+1} - t^n > 0$. Note that, in all cases, $S^L < S^R$. Let us first treat the case where $S^L > 0$, which corresponds to a supersonic flow from left to right. The S^L wave would lie on the right of the interface, and the flux at $x = 0$, $F^\star$, is then obviously given by $F(U^L)$. Similarly, if $S^R < 0$, the flow is supersonic, from right to left, and $F^\star$ is given by $F(U^R)$.

Now, let us examine the case where $S^L \leq 0 \leq S^R$. The lengths X_l, X_r can then be expressed as $X_l = -TS^L$ and $X_r = TS^R$. Expressing the integral form of the Euler equations on the system in Fig. 3.6 gives:

$$\begin{gathered} \int_0^{-X_l} U(x,0)dx - \int_0^T F\big(U(X_l,t)\big)dt + \int_{-X_l}^{X_r} U(x,T)dx \\ - \int_T^0 F\big(U(X_r,t)\big)dt + \int_{X_r}^0 U(x,0)dx = 0 \end{gathered} \tag{3.43}$$

Assuming piecewise constant variables, and hence, piecewise constant fluxes, the previous relation can be re-written as:

$$\begin{gathered} U^L.\big(S^L T\big) - F^L.\big(T\big) \\ +U^\star.\big((S^R - S^L)T\big) - F^R.\big(-T\big) + U^R.\big(-S^R T\big) = 0 \end{gathered} \tag{3.44}$$

relation that, after re-arrangement, leads to:

$$U^\star = \frac{F^L - S^L U^L - (F^R - S^R U^R)}{S^R - S^L} \tag{3.45}$$

This shows that once (U^L, U^R) is known from the reconstruction procedure, and once the wave-speeds (S^L, S^R) are estimated, the variables in the $\star$-region are fully defined.

The integral relation applied across a given $k-$wave, $k = L/R$, results in the Rankine-Hugoniot relations that read:

$$\begin{aligned} F^\star &= F^L + S^L \left(U^\star - U^L\right) \\ F^\star &= F^R + S^R \left(U^\star - U^R\right) \end{aligned} \tag{3.46}$$

From these 2 relations, one can eliminate $U^\star$ in order to determine $F^\star$ as:

$$F^\star = \frac{S^R F^L - S^L F^R + S^L S^R (U^R - U^L)}{S^R - S^L} \tag{3.47}$$

Thus, the flux evaluated at the $i+1/2$ interface from the 2-waves HLL Riemann solver reads:

$$F_{i+1/2}^{HLLE} = \begin{cases} F^L & if \quad 0 \leq S^L \\ F^\star & if \quad S^L \leq 0 \leq S^R \\ F^R & if \quad S^R \leq 0 \end{cases} \tag{3.48}$$

Once an evaluation of the wave-speeds (S^L, S^R) is provided, the HLL Riemann solver is fully defined. Several wave-speeds estimates can be found in the literature (Davis [1988], Einfeldt [1988], Einfeldt et al. [1991], Toro [1999]), leading to schemes of different robustness and dissipation. In the present development, the wave-speeds are estimated following the work of Einfeldt (HLLE), as:

$$S^L = min\left[q^L - c^L, \breve{q} - \breve{c}\right] \quad S^R = max\left[q^R + c^R, \breve{q} + \breve{c}\right] \tag{3.49}$$

where $\breve{q}$ refers to the Roe-averaged contravariant velocity, and c is the speed of sound. The Roe-averaged variables are obtained from:

$$\breve{U} = \begin{bmatrix} \breve{\rho} \\ \breve{u} \\ \breve{v} \\ \breve{w} \\ \breve{H} \\ \breve{k}^{sgs} \\ \breve{Y}_k \end{bmatrix} = \frac{1}{\sqrt{\rho^L} + \sqrt{\rho^R}} \left(\sqrt{\rho^L} \begin{bmatrix} \sqrt{\rho^L \rho^R} \\ u^L \\ v^L \\ w^L \\ H^L \\ k^{sgs\ L} \\ Y_{k,l} \end{bmatrix} + \sqrt{\rho^R} \begin{bmatrix} \sqrt{\rho^L \rho^R} \\ u^R \\ v^R \\ w^R \\ H^R \\ k^{sgs\ R} \\ Y_{k,r} \end{bmatrix} \right) \tag{3.50}$$

The speed of sound $\breve{c}$ is not directly obtained from this procedure and is re-computed from the Roe-averaged variables $\breve{c} = f(\breve{h}, \breve{\rho}, \breve{Y}_k)$. These wave-speeds are related to the characteristic wave propagation speeds on each side of the interface. It should be noted that, for the present LES calculations, the eigenvalues of the governing equations are not modified by the governing equation for k^{sgs}. The estimates given can be used for the filtered Navier-Stokes equations.

This solver has proven to be robust and accurate for hypersonic calculations and shock capturing purposes. Its assumption of double wave is however limiting, and the consequent numerical smearing of contact discontinuities, shear waves, etc... makes it unsuitable for viscous and turbulent calculations. An extension of this scheme has been developed and presented by Toro et al. [1994], where the middle wave in the Riemann problem is taken into account in the derivation of the fluxes. This extended Riemann solver is named HLLC (C standing for Contact), and its derivation is given in the next section.

3.4.2.2 Restoration of the Middle Wave - the HLLC Riemann Solver

It is assumed for the derivation of the HLLC solver that a given interface separating two states gives rise to three waves, of speed S^L for the left moving wave, S^R for the right moving wave, and $S^\star$ for the contact wave. These discontinuities separate constant states of the fluid. S^L separates U^L from $U^{L\star}$, $S^\star$ is the interface between $U^{L\star}$ and $U^{R\star}$, while S^R separates $U^{R\star}$ from U^R. This assumption of thin interfaces is

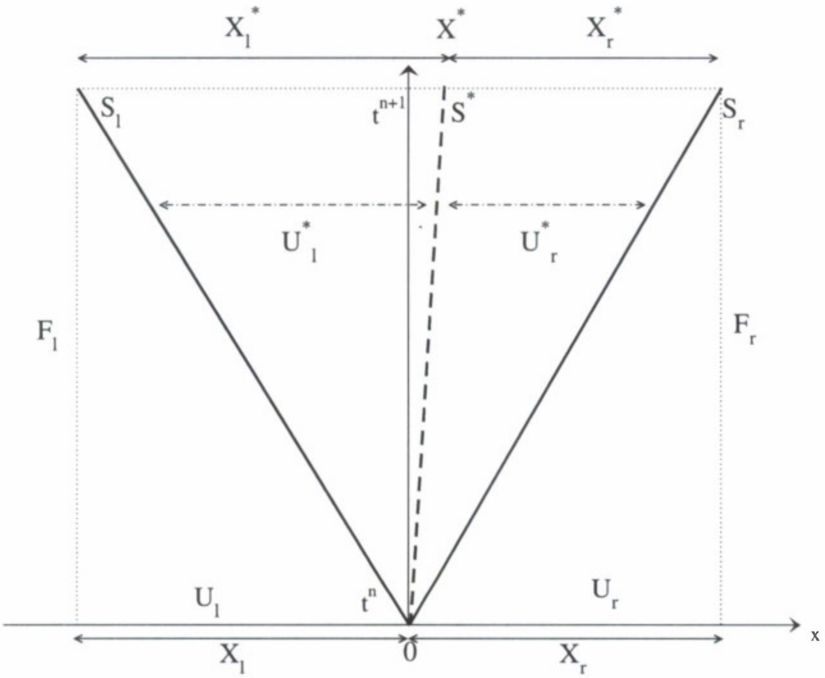

Figure 3.7: (x, t) diagram of an approximate Riemann problem evolution with three characteristic waves.

justified for both shocks and contact discontinuities, and is an approximation in the case of rarefactions. A typical representation of a subsonic system is shown in Fig. 3.7.

Let T be the local time step, $T = t^{n+1} - t^n > 0$. Note that, in all cases, $S^L < S^\star < S^R$. Similarly to the HLL solver, the case of a supersonic flow from left to right, where $S^L > 0$, leads to a flux at $x = 0$ given by $F(U^L)$. Again, if $S^R < 0$, the flux is given by $F(U^R)$. Now, let us examine the case when $S^L \leq 0 \leq S^R$. The lengths X_l and X_r can then be expressed as $X_l = -TS^L$ and $X_r = TS^R$ respectively, and similarly, $X^{L\star} = T(S^\star - S^L)$, $X_r^\star = T(S^R - S^\star)$. The Euler equations in integral form, Eqn. 3.41, can be applied to the system represented in Fig. 3.7, leading to the relation:

$$\begin{aligned} &\int_0^{-X_l} U(x,0)dx - \int_0^T F\big(U(X_l,t)\big)dt + \int_{-X_l}^{X^\star} U(x,T)dx \\ + \quad &\int_{X^\star}^{X_r} U(x,T)dx - \int_T^0 F\big(U(X_r,t)\big)dt + \int_{X_r}^0 U(x,0)dx = 0 \end{aligned} \tag{3.51}$$

With the same assumptions of piecewise constant variables and piecewise constant fluxes as in the derivation of the HLL solver, the previous relation can be re-written as:

$$\begin{aligned} &U^L.\big(S^LT\big) - F^L.\big(T\big) + U^{L\star}.\big((S^\star - S^L)T\big) \\ + \quad &U^{R\star}.\big((S^R - S^\star)T\big) - F^R.\big(-T\big) + U^R.\big(-S^RT\big) = 0 \end{aligned} \tag{3.52}$$

relation that, after re-arrangement, leads to:

$$(S^\star - S^L)U^{L\star} + (S^R - S^\star)U^{R\star} = F^L - S^LU^L - (F^R - S^RU^R) \tag{3.53}$$

This relation relates the left and right $\star$-variables together, and is often called the consistency condition. Note that assuming a unique $\star$−state, so that $U^{L\star} = U^{R\star}$ recovers the Consistency Condition of the *HLL* solver, Eqn. 3.45.

The integral applied around a control volume surrounding a given k−wave leads to:

$$U^k.(S^kT) - F^k.(T) - U^{k\star}.(-S^kT) + F^{k\star}.(T) = 0 \tag{3.54}$$

so that the corresponding Rankine-Hugoniot relations across the k−wave, $k = L/R$, are recovered, and read:

$$\begin{aligned} F^{L\star} &= F^L + S^L\left(U^{L\star} - U^L\right) \\ F^{R\star} &= F^R + S^R\left(U^{R\star} - U^R\right) \end{aligned} \tag{3.55}$$

Identically, the Rankine-Hugoniot relation across the $\star$-wave reads:

$$F^{L\star} = F^{R\star} + S^\star\left(U^{L\star} - U^{R\star}\right) \tag{3.56}$$

The relations 3.53, 3.55 and 3.56 give 4 relations for 4 unknowns ($F^{L\star}$, $F^{R\star}$, $U^{L\star}$, and $U^{R\star}$). It is however straightforward to show that they are not linearly independent. An assumption has to be made on the intermediate states in order to solve this system of equations.

Toro et al. [1994] closed the relation by assuming that the intermediate wave had the same properties as a contact discontinuity. Its propagation speed is then assumed identical to the particle velocity in the $\star$−region, and this wave retains the initial discontinuity in the passive scalar field. This also implies that both convective velocities and pressures have to match across the interface. Mathematically, those assumption are expressed by:

$$\begin{gathered} (\vec{V}^{L\star} \cdot \vec{n} = q^{L\star}) = (\vec{V}^{R\star} \cdot \vec{n} = q^{R\star}) = S^\star \\ P^{L\star} = P^{R\star} \\ \phi^{L\star} = \phi^L \ , \ \phi^{R\star} = \phi^R \end{gathered} \tag{3.57}$$

where ϕ is any passive scalar advected by the fluid ($\phi = k^{sgs}, Y_k, ...$). Note that the component of the velocity transverse to the interface, $\phi^k = \vec{V}^k - \left(\vec{V}^k \cdot \vec{n}\right)\vec{n} = \vec{V}^k - S^\star\vec{n}$, $k = L/R$ is a passive scalar for this one-dimensional problem. As mentioned in Toro [1999], all of these conditions are exactly satisfied by a contact discontinuity computed from an exact Riemann solver.

With these assumptions, one can re-write the four first elements of the vectorial equation expressed in Eqn. 3.53, as:

$$(S^\star - S^L)\overbrace{\begin{bmatrix}\rho^{L\star}\\ \rho^{L\star}u^{L\star}\\ \rho^{L\star}v^{L\star}\\ \rho^{L\star}w^{L\star}\end{bmatrix}}^{U^{L\star}} + (S^R - S^\star)\overbrace{\begin{bmatrix}\rho^{R\star}\\ \rho^{R\star}u^{R\star}\\ \rho^{R\star}v^{R\star}\\ \rho^{R\star}w^{R\star}\end{bmatrix}}^{U^{R\star}} = S^R\overbrace{\begin{bmatrix}\rho^{R}\\ \rho^{R}u^{R}\\ \rho^{R}v^{R}\\ \rho^{R}w^{R}\end{bmatrix}}^{U^{R}} - S^L\overbrace{\begin{bmatrix}\rho^{L}\\ \rho^{L}u^{L}\\ \rho^{L}v^{L}\\ \rho^{L}w^{L}\end{bmatrix}}^{U^{L}} + \underbrace{\begin{bmatrix}\rho^L q^L\\ \rho^L q^L u^L + P^L n_x\\ \rho^L q^L v^L + P^L n_y\\ \rho^L q^L w^L + P^L n_z\end{bmatrix}}_{F^L} - \underbrace{\begin{bmatrix}\rho^R q^R\\ \rho^R q^R u^R + P^R n_x\\ \rho^R q^R v^R + P^R n_y\\ \rho^R q^R w^R + P^R n_z\end{bmatrix}}_{F^R} \tag{3.58}$$

By assumption, $q^{k\star} = S^\star$ for both $k = L/R$. Projecting the vectorial momentum equation on the directional unit vector gives, along with the first relation, the following set of two equations:

$$\begin{gathered}\rho^{L\star}(S^\star - S^L) + \rho^{R\star}(S^R - S^\star) = \rho^R(S^R - q^R) - \rho^L(S^L - q^L)\\ \underbrace{\left[\rho^{L\star}(S^\star - S^L) + \rho^{R\star}(S^R - S^\star)\right]}\, S^\star = P^L - P^R + \rho^R q^R(S^R - q^R) - \rho^L q^L(S^L - q^L)\end{gathered} \tag{3.59}$$

Replacing the under-braced term in the last equation by the right-hand side of the first equation above leads to:

$$S^\star = \frac{P^R - P^L + \rho^L q^L(S^L - q^L) - \rho^R q^R(S^R - q^R)}{\rho^L(S^L - q^L) - \rho^R(S^R - q^R)} \tag{3.60}$$

Equation 3.55 is closed and the expressions for all $\star$-variables are obtained. One can write the first four relations, for continuity and momentum:

$$\underbrace{\begin{bmatrix}\rho^{k\star}S^\star\\ \rho^{k\star}S^\star u^{k\star} + P^{k\star}n_x\\ \rho^{k\star}S^\star v^{k\star} + P^{k\star}n_y\\ \rho^{k\star}S^\star w^{k\star} + P^{k\star}n_z\end{bmatrix}}_{F^{k\star}} = \underbrace{\begin{bmatrix}\rho^k q^k\\ \rho^k q^k u^k + P^k n_x\\ \rho^k q^k v^k + P^k n_y\\ \rho^k q^k w^k + P^k n_z\end{bmatrix}}_{F^k} + S^k\left(\underbrace{\begin{bmatrix}\rho^{k\star}\\ \rho^{k\star}u^{k\star}\\ \rho^{k\star}v^{k\star}\\ \rho^{k\star}w^{k\star}\end{bmatrix}}_{U^{k\star}} - \underbrace{\begin{bmatrix}\rho^{k}\\ \rho^{k}u^{k}\\ \rho^{k}v^{k}\\ \rho^{k}w^{k}\end{bmatrix}}_{U^{k}}\right) \tag{3.61}$$

the first relation leads directly to an expression for the density in the *star* region:

$$\rho^{k\star} = \rho^k \frac{S^k - q^k}{S^k - S^\star} \tag{3.62}$$

Again, multiplying the second relation by n_x, the third by n_y and the last by n_z, adding those three relations, and using the expression for $\rho^{k\star}$ given in Eqn. 3.62 leads directly to:

$$P^{k\star} = P^k + \rho^k(q^k - S^k)(q^k - S^\star) \tag{3.63}$$

Note that the relation expressed in Eqn. 3.63 is valid for both $k = L/R$, and satisfies $P^{L\star} = P^{R\star}$. Let us define β^k, α^k and ω^k as:

$$\begin{aligned} \beta^k &= \tfrac{S^\star - q^k}{S^k - S^\star} \\ \alpha^k &= \beta^k + 1 \\ \omega^k &= -\beta^k (q^k - S^k) \end{aligned} \tag{3.64}$$

The state vectors $U^{k\star}$ can then be expressed as:

$$U^{k\star} = \alpha^k U^k + \begin{bmatrix} 0 \\ \rho^k \omega^k n_x \\ \rho^k \omega^k n_y \\ \rho^k \omega^k n_z \\ \frac{P^\star S^\star - P^k q^k}{(S^k - S^\star)} \\ 0 \\ 0 \end{bmatrix} \tag{3.65}$$

With these relations, the evaluation of the wave-speeds provides the description of all states in the Riemann problem under consideration. It is then possible to describe the fluxes at $i + 1/2$ interface. The general expression for these fluxes is given by:

$$F_{i+1/2}^{HLLC} = \begin{cases} F^L & if \quad 0 \leq S^L \\ F^{L\star} = F^L + S^L (U^{L\star} - U^L) & if \quad S^L \leq 0 \leq S^\star \\ F^{R\star} = F^R + S^R (U^{R\star} - U^R) & if \quad S^{L\star} \leq 0 \leq S^R \\ F^R & if \quad S^R \leq 0 \end{cases} \tag{3.66}$$

The HLLC Riemann solver is then fully defined, and only the wave-speeds are needed to close its expression. The estimates detailed in Eqn. 3.49 for the HLLE solver are used for the evaluation of S^L and S^R, whereas $S^\star$ is defined through relation 3.60.

3.4.2.3 A Hybrid Riemann Solver - HLLC/E

Two Riemann solvers of the HLL- framework have been described earlier. The HLLE considers a 2−waves evolution to the Riemann problem constructed at the cell interfaces. Such Riemann solvers are called non-contact-preserving, as the intermediate wave, the contact discontinuity, is ignored. The improvement brought to this solver by the HLLC solver is the restoration of this wave in the problem. The latter solver if less diffusive, and improves greatly the results in computations of viscous problems.

Solvers that simulate 3−waves problems are known to suffer from instabilities in shock regions. The odd-even decoupling and carbuncle phenomena can lead to the creation of oscillations in the post-shock regions, and to the deformation of shock fronts. The HLLC solver is no exception. 2−waves solver do not suffer from these instabilities.

In order to reduce the instabilities that can occur in shock regions, Quirk [1994] suggested to switch to a non-contact-preserving solver within shocks thickness. It was however found that the instabilities come from the use of contact-preserving solvers in the directions transverse to the shock front. The hybrid solver designed for the present study uses this observation to combine HLLC and HLLE as follows. The hybrid solver returns the flux evaluation of the HLLC solver by default, but reverts to the HLLE fluxes if a shock is detected in the direction transverse to the direction of computation. Shock detection is performed following the method given in Eqn. 3.36 and 3.37.

$$F^{u}_{i+1/2} = \begin{cases} F^{HLLE}_{i+1/2} & if\ (d_{P,j} < 0\ and\ d_{u,j} < 0)\ or\ (d_{P,k} < 0\ and\ d_{u,k} < 0) \\ F^{HLLC}_{i+1/2} & otherwise \end{cases} \tag{3.67}$$

The MUSCL interpolation / HLLC/E Riemann solver approach is fully described. This scheme is adapted to the resolution of aerodynamic flows with TPG equation of state, and can be used on curvilinear grids. The performance of this scheme on classical test-cases is reported in Sec. 3.5.

The presentation of the upwind scheme completes also the description of the hybrid scheme developed in the present study. A verification of this hybrid methodology on classical and fundamental test cases is presented in App. 3.6. Also, verification of the scheme is presented through direct numerical simulations of shock / isotropic turbulence interactions in Chap. 4.

3.5 Verification of the Upwind Scheme

The capture of physical discontinuities is essential for the numerical simulations of supersonic turbulent flows. A shock-capturing methodology has been developed to achieve this goal, and its description is given in Chap. 3. The method implemented is based on flux difference splitting, as these methods yield robust and accurate resolutions of shock waves and discontinuities, and have limited dissipation. However, Riemann solvers, whether they are exact or approximate, have known instabilities and limitations. The manifestations of these flaws are well-documented.

The proposed upwind solver is designed to show a reduced sensitivity to theses instabilities. The reconstruction of the Riemann problem uses a flattening procedure which prevents under-resolved strong shocks within a computation. Also, the hybrid Riemann solver HLLC/E switches to a non-contact preserving solver in the regions transverse to shock front. All these methods are included to reduce the instabilities, and the aptitude of this scheme in practical simulations will be presented hereafter.

- Unphysical Values

Approximate Riemann solvers that are based on linearized estimates of the flux differences can lead to unphysical approximations of the total density or of the internal energy ($\rho < 0,\ e < 0$) in rarefactions. A consequence is the computation of "rarefaction shocks", an unphysical discontinuity computed within a rarefaction fan. A few entropy fixes have been advised and implemented that fix this specific failure (see Kermani and Plett [2001] for a comparison of the most common entropy fixes). For very strong rarefaction computations (near-vacuum states), entropy fixes are not sufficient to prevent the Riemann solver from computing unphysical solutions. HLL solvers do not suffer from this instability, do not suffer from such instabilities. This property of positivity preservation will be demonstrated later.

- Post-Shock Oscillations

Classical Riemann solvers along with a higher order reconstructions show an instability when a shock is propagating at low grid speeds, that is, when the shock propagation speed is small within the frame of reference of the computation. This phenomenon, first reported by Colella and Woodward [1984] was shown to be the consequence of the self-steepening properties of the shocks. The cure designed in this reference paper, the flattening procedure, is implemented in the present formulation in order to reduce such instabilities.

- Odd-Even Decoupling and Carbuncle Phenomenon

The carbuncle phenomenon is an instability the arises in hypersonic computations, when stagnation points create recirculation regions behind bow shocks. The curved shock is incorrectly captured, and small kinks form along the shock front. This phenomenon has been identified in blunt body calculations, and has been analytically analyzed (Pandolfi and D'Ambrosio [2001], Svetsov [2001], Chauvat et al. [2005]). Most accurate upwind methods suffer from this instability (Roe scheme, AUSM-M, Osher scheme, etc...), whereas flux vector splitting and non-contact preserving methods do not show this instability.

The odd-even instability occurs when shock fronts propagate with the main front aligned with the grid. This instability is triggered by small numerical round-off errors which grow into strong oscillations (Quirk [1994]). Again, this instability is found in many Riemann solver, more particularly, in exact Riemann solvers. And once again, non-contact preserving solvers do not seem affected by this perturbation.

The hybrid solver presented in Chap. 3 was specifically designed to minimize all these perturbations. But, as the robustness of the solver should not be detrimental to the accuracy of the resolution, the following verification study shows that the upwind method is not subject to strong instabilities and remains accurate.

3.5.1 One-Dimensional Tests

The ability of the shock-capturing methodology to capture shocks is tested first. Two particular aspects are considered: first, the ability to capture shock waves at their right propagation speed is tested. This study is performed over a one-dimensional domain, since the Rankine-Hugoniot relations are essentially expressed in one-dimensional form. The second test focuses on the capture of oblique shocks. Here, the extension to multi-dimensional problems over curvilinear grids is tested. Also, the amount of post-shock oscillations can be quantified.

The very first case is that of a normal shock on a one-dimensional grid. Different Mach numbers have been tested, and all simulations lead to the same conclusions. The case of $M = 5.2$ is hereafter presented. A $0.1m$ long domain is discretized

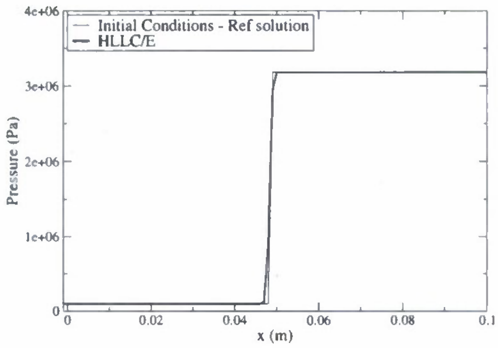

Figure 3.8: Pressure profiles for M=5.2 normal shock with a Calorically perfect gas EOS.

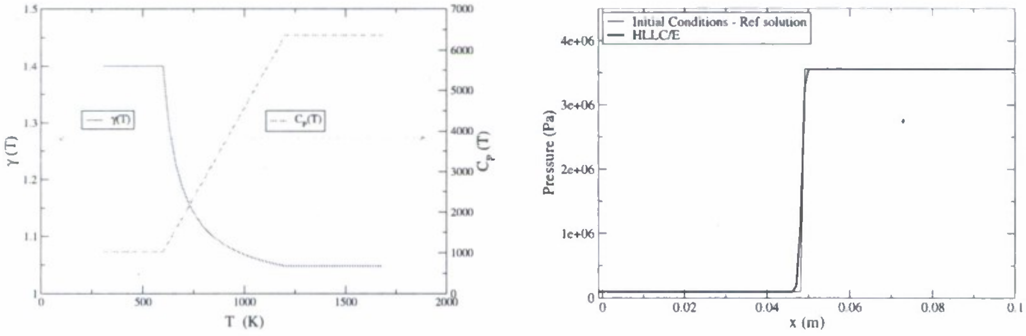

(a) CPG

(b) TPG

Figure 3.9: $C_p(T)$ for a thermally perfect gas, and pressure profiles for M=5.2 normal shock.

using 100 grid cells. Initial conditions are given by $(P, T, M)_l = (101325., 300., 5.2)$ from 0. to $0.05m$, and the steady Rankine-Hugoniot relations are used for the initial jump conditions, leading to $(P, T, M)_r = (3179578.5, 1859.1257, 0.4125191924)$ for a calorically perfect gas with a specific heat ratio $\gamma = 1.4$. Supersonic inflow is used at the left boundary, while a subsonic characteristics-based non-reflecting outflow is used at the right boundary. The flow properties reach a stationary state for this problem, and the stationary pressure profile is shown in Fig. 3.5.1. The shock is crisply captured, with two cell *in* the shock thickness. The Rankine Hugoniot jump relations are correctly captured, and the propagation speed comes out correctly. A second test was performed using an arbitrary thermally perfect gas. The dependence of the specific heat at constant pressure is represented in Fig. 3.9(a), and the pressure profile obtained at stationary state is shown in Fig. 3.9(b). Here again, the Rankine-Hugoniot relations are recovered in the simulation, and the shock is captured over two cells.

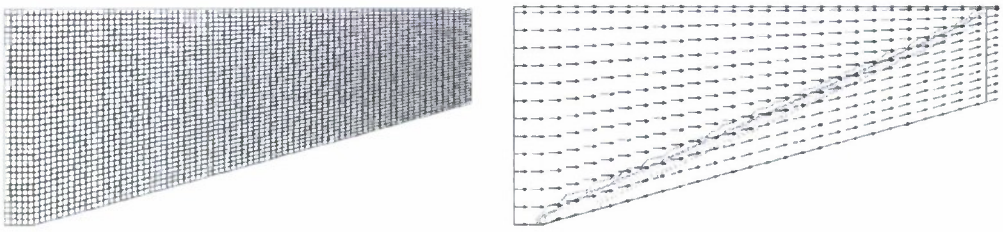

(a) Computational grid (b) Pressure contours

Figure 3.10: Computational grid for oblique shock calculations (left) and pressure contours for $M_{in} = 5$ and a ramp angle of 15°.

The performance of the upwind on skewed grid is tested by simulating supersonic flows over ramps. The capture of oblique shocks is of fundamental importance for practical applications. The simulations performed here consist in a two-dimensional channel with an inclined lower wall, as represented in Fig. 3.10(a). The domain is discretized using 80 × 36 grid cells. Supersonic inflow and outflow are used at the left and right boundaries respectively, whereas the top and bottom boundaries use symmetry conditions. The angle of the ramp at the bottom wall has been varied between 5° and 25°, and three different inflow Mach numbers were tested: $M_{in} = 2$, $M_{in} = 5$ and $M_{in} = 10$. This test was conducted for calorically perfect gases ($\gamma = 1.4$). The accuracy of the simulation was assessed by comparing the shock angle from the computation to the theoretical values (see, *e.g.* Anderson [2003]). A typical flow-field is presented in Fig. 3.10(b). All shock angles were captured accurately, with less than 3% error on the shock angles. Small oscillations in the pressure field are obtained close to the head of the ramp, which quickly dampen further downstream. The present shock-capturing methodology efficiently captures shock waves at the right propagation speed and performs well on skewed curvilinear grids.

A series of test cases for shock-capturing schemes have been proposed in the literature. These tests have been designed to assess the capacity of different numerical schemes in resolving fundamental features of supersonic flows, as well as some particularly challenging configurations. A compilation of such tests is reported in Liska and Wendroff [2003], and are repeated using the present shock-capturing formulation. These tests, denoted $T1$ to $T7$, are performed over a one-dimensional domain. They are all based on the physical evolution of an initial interface into a complex flow. All cases have a domain that extends from 0 to 1, except case T7 which has a domain extending from 0.1 to 0.6. The parameters for these tests are given in tables 3.1 and 3.2. The initial physical states at the left and right of the discontinuity are given in table 3.1. In table 3.2, x_0 represents the physical location of the initial interface, T is the total physical time of computation. A calorically perfect gas EOS is used in all cases. The specific heat ratio of the gases, γ, depends on the problems and is reported in table 3.2. Also, the boundary conditions used in these problems are either supersonic inflows (i in table 3.2), or supersonic outflows (o in table 3.2).

Table 3.1: Initial conditions for the left and right states in the one-dimensional tests used to validate the shock-capturing methodology.

test	ρ_l	u_l	p_l	ρ_r	u_r	p_r
T1	1	0.75	1	0.125	0	0.1
T2	1	-19.59745	1000	1	-19.59745	0.01
T3	1	-2	0.4	1	2	0.4
T4	1.4	0.1	1	1	0.1	1
T5	1	1	10^{-6}	1	-1	10^{-6}

Table 3.2: Parameters used in the one-dimensional tests used to validate the shock-capturing methodology.

test	x_0	T	γ	resolution	left boundary	right boundary
T1	0.3	0.2	1.4	100	i	o
T2	0.8	0.012	1.4	200	o	i
T3	0.5	0.15	1.4	100	o	o
T4	0.5	2	1.	100	i	o
T5	0.5	1	2/3	100	i	i

A last test $T6$ was performed, where the evolution of two initial interfaces is simulated. This *interacting blast wave* problem was first considered by Colella and Woodward [1984], and is a particularly stringent configuration to simulate. For this case, the physical domain extends from 0 to 1. The left and right boundaries are treated as symmetry boundaries. $(\rho, u, p) = (1, 0, 1000)$ between $x = 0$ and $x = 0.1$, $(\rho, u, p) = (1, 0, 0.01)$ for $0.1 \leq x \leq 0.9$, and $(\rho, u, p) = (1, 0, 100)$ between $x = 0.9$ and $x = 1$. The physical time for this simulation is of 0.0038.

All the results presented hereafter are compared to the results of high resolution simulations performed using a Piecewise Parabolic Method (PPM). Tests $T1$ and $T2$ are variations on the classical shock tube test case of Sod. In $T1$, the initial interface forms a right-moving shock, a left-moving rarefaction fan, and an intermediate contact discontinuity. Specifically, the rarefaction fan contains as sonic point, a physical feature that some linearized solver cannot resolve correctly. With the current scheme, all waves are correctly captured at their right speed. The expansion is continuous, and the capture of an unphysical *rarefaction shock* does not occur. Furthermore, the dissipation applied to the sharp waves is relatively small: the shock is captured over three cells, and the contact spreads over four cells. The latter is mostly dissipated from the initial stage of the development.

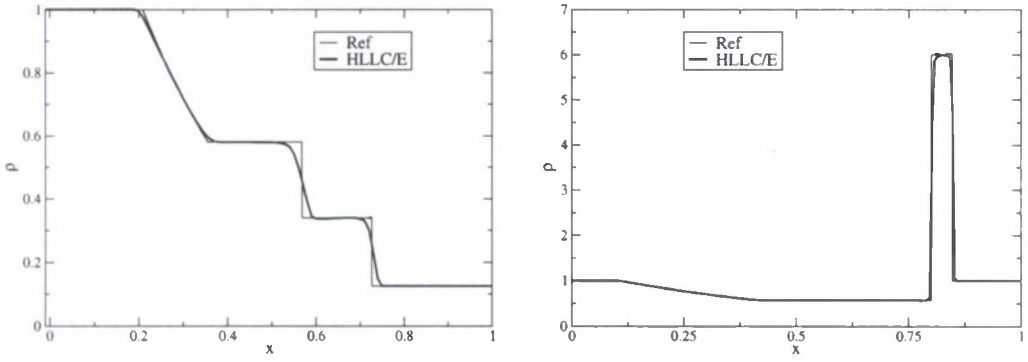

(a) T1

(b) T2

Figure 3.11: Results of test cases T1 and T2 for the validation of the upwind methodology.

Case $T2$ is a variation where the contact discontinuity is stationary in the course of the simulation. The peak in density is correctly simulated, with minimal dissipation. Again, the shock is resolved over three cells, while four cells are needed for the strong contact discontinuity.

The test case in $T3$ evolves into a near-vacuum state in the center of the domain. Both the pressure and the density reach values close to 0, but the internal energy remains relatively high. The HLLC/E scheme is able to capture this phenomenon without unphysical values for the internal energy. The lowest temperatures, formed at the center of the domain, are however not fully captured.

$T4$ tests the ability to capture slowly moving contact discontinuities. This configuration is difficult to resolve properly, as the slow motion tends to dissipate the density front. In the current simulation, eight cells are necessary to resolve this jump in density. The amount of dissipation is for this case significant, but comparable to other state of the art numerical schemes (Liska and Wendroff [2003]).

Test $T5$ is the classical test case of *Noh*, where two infinite strength shocks propagate outwards from the center of the domain. This test shows that, even very strong shocks are captured at their right propagation speed, and that the fronts are resolved over three points. The use of the flattening procedure smears slightly the shock fronts, but permits the resolution of the problem with minimal post-shock oscillations. The state at the center of the domain should be strictly constant. A dip in the density profile remains from the formation of the shocks. But apart from this impact of the initial conditions, the physics of this test problem is well captured.

The interacting blast waves problem is particularly intricate to resolve. The simulations of the shock fronts crossing can lead to a strong dissipation of the intermediate region. The scheme used here captures most of the structures correctly, and recovers the blast propagation speed after their interaction. The amplitude of the strongest wave is however under-estimated by the current methodology.

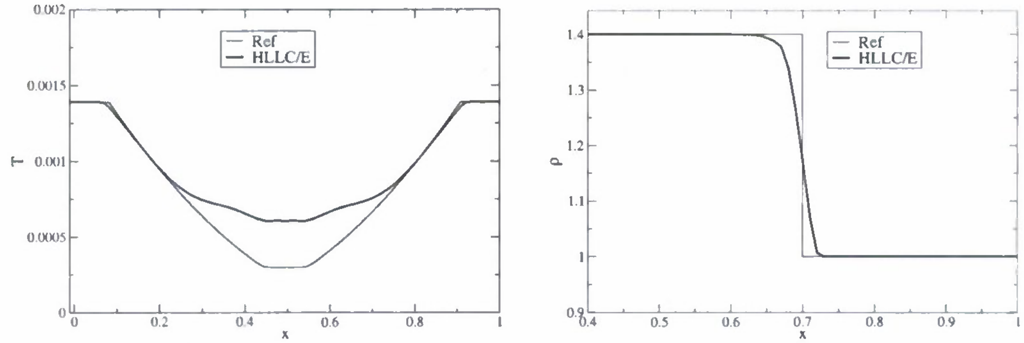

(a) T3 (b) T4

Figure 3.12: Results of test cases T3 and T4 for the validation of the upwind methodology.

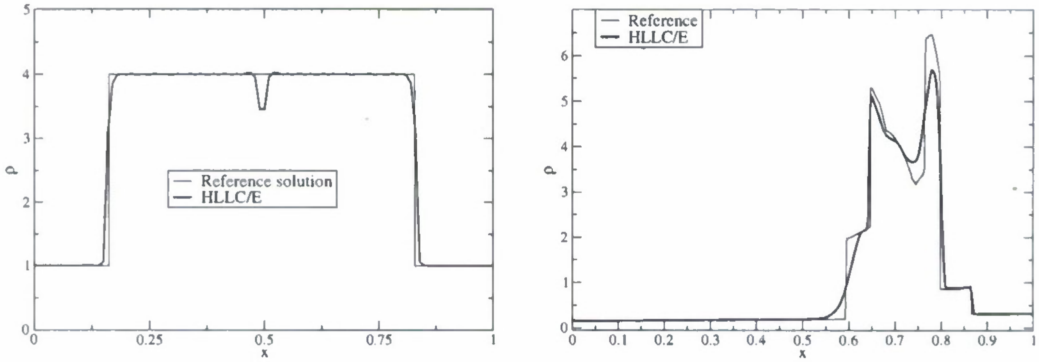

(a) T5 (b) T6

Figure 3.13: Results of test cases T5 and T6 for the validation of the upwind methodology.

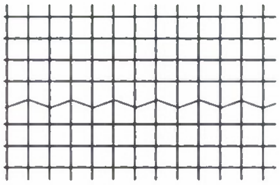

Figure 3.14: Schematic of the perturbed grid used in the odd-even test.

These one-dimensional tests have shown that the current scheme correctly captures the shock fronts and their propagation speeds, with reduced dissipation. The contact discontinuity are smeared over a few cells, but their behavior is otherwise well simulated. The performance in strong rarefactions is not as good as for the other tests. Such configurations are however not important for the type of applications considered in the present study. Overall, this shock-capturing method is adapted to the capture of discontinuities in supersonic flows, and compares overall well to other numerical techniques (presented in Liska and Wendroff [2003]).

3.5.2 Two-Dimensional Cases

The good performance of the shock-capturing methodology for fundamental one-dimensional problems has been presented. The extension to multi-dimensional transient problems can be problematic for several reasons: the instabilities reviewed at the beginning of this appendix arise in multi-dimensional problems only. Also, the capture of shock propagations at the right speed is fundamental in one-dimension. The capture of shock propagation in arbitrary directions in a multi-dimensional problem is somehow more challenging. A review of the scheme performance on test cases triggering the instabilities is given first. The resolution of spherically propagating shocks are presented after.

The behavior of the hybrid solver on the odd-even decoupling is studied in a test-case adapted from Quirk [1994] and Liska and Wendroff [2003]. The problem follows the same initialization as test case *T*8 of Sec. 3.5.1 on a two-dimensional grid: $(x, y) \in (0, 1)x(0, 0.125)$. 800×10 grid cells are used to discretize this problem, and the grid is uniform except at the centerline where a very small perturbation is generated. The spacing in the y-direction being $\Delta y = 0.0125$, the amplitude of the perturbation is $2\ 10^{-7}$ and the formulation of the y-components at the centerlines reads:

$$Y_{CL} = Y_{mid} + (-1)^i 10^{-7} \tag{3.68}$$

A sketch of the resulting grid, where the perturbation has been amplified for clarity, is represented in Fig. 3.5.2 The test case has been run using five different solvers: the Two-Shock Riemann Solver (TSRS) and the solver of Roe with Harten-Hyman entropy correction have been considered along with the HLLC, HLLE and HLLC/E. In all cases, the MUSCL reconstruction used a monotonized central limiter and flattening. The computational fields of density right before the interaction of the two blast waves is showed in Fig. 3.15. The top figure obtained with HLLE shows the

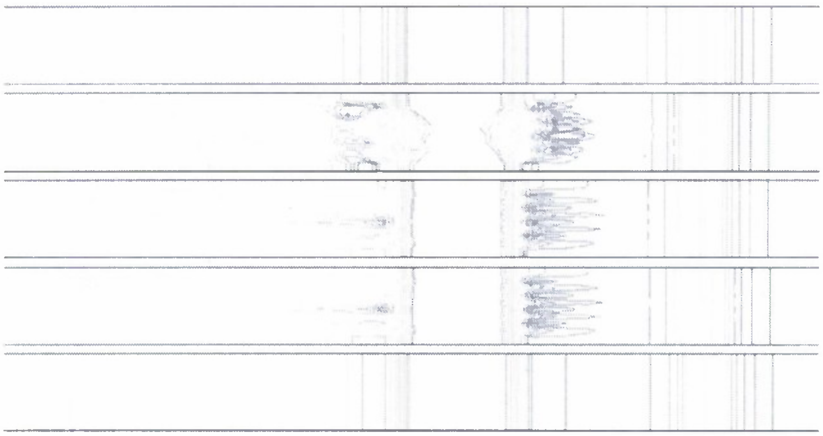

Figure 3.15: Results of the odd-even test case using several Riemann solvers: HLLE, Roe, HLLC, TSRS and HLLC/E solvers respectively.

physical phenomena correctly: at the left of the domain, a right-moving shock is followed by an expansion fan, and on the opposite side, a weaker, left-moving shock is followed by another rarefaction fan. This problem is essentially one-dimensional in nature. The HLLC, Roe and TSRS solvers are contact-preserving, and develop the instability early in the course of the simulation. Before the interaction, the blast fronts are strongly distorted. Not only do the post-shock regions show high amplitude oscillations, but also do the main fronts show distortion. The HLLC/E solver switches to the non-contact preserving in the direction transverse to the shock and dissipates the small instabilities quickly. The figure shows an essentially one-dimensional flow. Quantitatively, the maximum vertical velocities during the course of the simulations have been recorded. The maximum horizontal velocity varies between 13 and 32. The HLLC and TSRS get vertical velocities of 3.03 and 3.01 respectively, whereas the Roe solver predictions show vertical velocities as high as 8.45. The HLLC/E solver results in vertical velocities $\mathcal{O}(10^{-7})$. The hybrid solver seems to successfully minimize the odd-even instability.

A second test-case is the classical blunt body in hypersonic flow, which triggers the carbuncle phenomenon. A Mach 10 flow over a circular rod is simulated. The gas is calorically perfect, with $\gamma = 1.4$, and the rod has a circular cross-section. $80x160$ grid cells are used to solve this problem. Figure 3.5.2 shows the temperature isolines for the carbuncle problem using the HLLE Riemann solver. The stagnation region is correctly captured, and no deformation of the leading shock is observed. The use of more accurate Riemann solvers that do not neglect the middle wave leads to improper captures of the curved shock, as seen in Fig. 3.17. The Roe solver is the most sensitive to this instability, and results in the formation of a very strong shock deformation. The whole interaction is changed. The other Riemann solvers are also subject to the instability. Kinks are formed along the main shock front which lead to slip lines in the post-shock regions. The flow-field is perturbed by the instability. The hybrid solver reduces the impact of the instability, an are showing a slight instability as well. It is

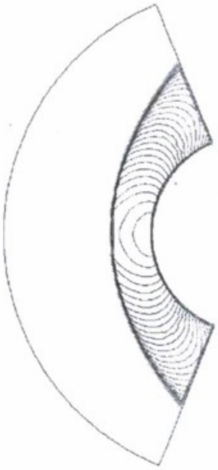

Figure 3.16: Isolines of the temperature field for the carbuncle test case using the HLLE Riemann solver.

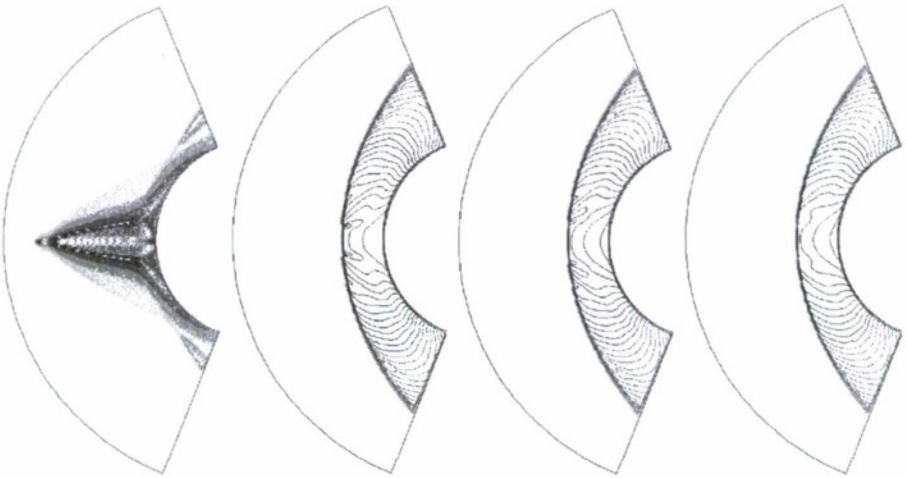

(a) Roe (b) HLLC (c) TSRS (d) HLLC/E

Figure 3.17: Isolines of the temperature field for the carbuncle test case using contact-preserving Riemann Solvers and the HLLC/E hybrid Riemann solver.

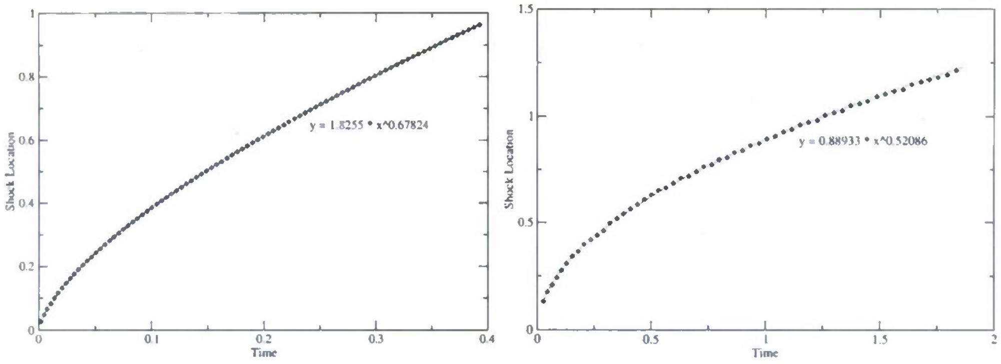

(a) Planar blast

(b) Cylindrical blast

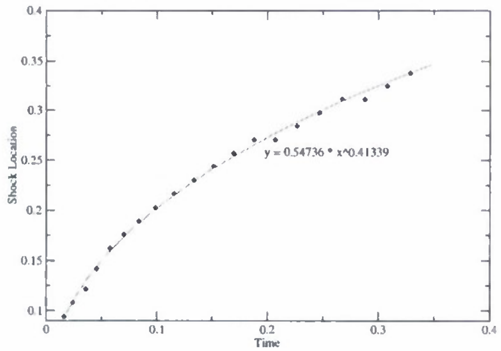

(c) Spherical blast

Figure 3.18: Radii of the blast wave fronts as a function of time for the case of planar, cylindrical and spherical Blast waves.

apparent that the HLLC/E case suppresses almost completely this instability.

The last test presented here is the point source explosion of Sedov. In this problem, the far-field of an explosive charge is considered to reach a self-similar state. Sedov [1959] quantified the normalized profiles behind the outgoing blast waves, and showed that the radius of the outwards-going follows $R(t) \propto t^{2/(n+2)}$, where $n = 1$ for a planar explosion, $n = 2$ for a cylindrical one, and $n = 3$ for a circular explosion. The following simulations have been performed. The initialization consists in an initial radius of $8.5dx$, where dx is the spacing of the uniform grid, of high pressure, set to 19.73. The outer environment is composed of fluid at rest, at a pressure of 10^{-5}. The density is set to 1 everywhere. The fluid is made of a calorically perfect gas with $\gamma = 1.4$. $128x1x1$ grid cells were used for the planar case, $128x128x1$ grid cells for the cylindrical case, and $128x128x128$ for the circular case.

The temporal evolution of the radii of the blast waves was collected for all cases, and are presented in Fig. 3.18. Curve-fits to these profiles show that their evolutions follow closely the analytical result of Sedov [1959]. Furthermore, the resolution of a cylindrical or spherical phenomenon on a Cartesian grid usually leads to a-symmetric solutions, as, from a numerical stand point, the propagation speed in the direction aligned with the cells and in the transverse directions is not identical. The extension of the one-dimensional hydrodynamic solver to multi-dimensional simulations should minimize this type of errors. Figure 3.19 shows the normalized pressure distribution versus radius for every point in the domain. The reference data have been obtained from a high-resolution one-dimensional study. The shock is captured over two to three cells. Furthermore, the scattering of the data is smaller than one grid cell of the two-dimensional grid, highlighting the very small anisotropy obtained in the resolution of this cylindrical problem on a Cartesian grid, hence showing the appropriateness of the extension of the upwind scheme to multi-dimensional simulations. Due to the coarseness of the two-dimensional grid compared to the one-dimensional reference simulation, the field of the coarser simulation is filtered on the grid, and *averaged* over the cell volume, so that the pressure peak is not fully recovered.

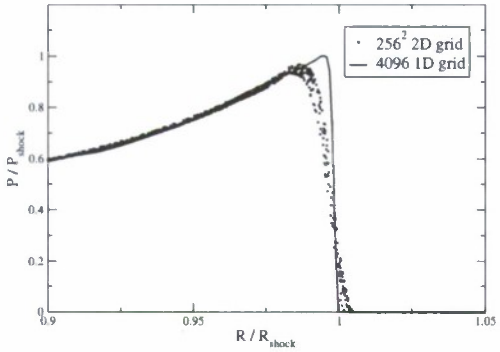

(a)

Figure 3.19: Sedov's point explosion problem: pressure profiles of the one-dimensional reference and two-dimensional simulations.

The results of these different verification studies have shown that the shock-capturing methodology developed here can efficiently capture discontinuities in supersonic flows, and that its extension to multi-dimensional problems is adequate. Shocks and contact are captured at their right propagation speeds. Smearing of the contacts has been observed, in good agreement with other state of the art numerical methods for supersonic flows. The sensitivity of the scheme to classical instabilities has been shown to be considerably reduced by the hybrid Riemann solver. This numerical method does not perform very well for very strong rarefactions, but such features are not found in the typical applications this method is intended for.

3.6 Assessment and verification of the hybrid methodology

The hybrid numerical methodology described in Sec. 3.2 is designed to detect discontinuities in the flow through the evaluation of the flow smoothness, Eqn. 3.11. The numerical scheme employed to compute the interface flux reverts to a shock capturing method if the smoothness exceeds a threshold value, see Eqn. 3.12. The values for the noise factors and thresholds have been set from numerical experiments of typical flows of interest, and are hereafter described. The smoothness of the pressure field is evaluated in order to distinguish pressure oscillations due to acoustic fields from pressure jumps associated with shocks. The density field on the other hand, can be related to species gradients, contact discontinuities, flame fronts or shocks. This knowledge of typical flow conditions is used to assess the numerical scheme coefficients.

The proposed approach is validated over a series of tests. The classical Shu-Osher testcase considers in a simplified one-dimensional configuration the interaction between a shock and a field of turbulence. The capture of this problem requires a good capture of the shock wave and a reduced dissipation of the turbulent field. Second, the interaction of a vortex tube with a normal shock is examined. The problem involves the generation of acoustic pulses (requiring smooth resolution) caused by the shock front deformation.

3.6.1 Assessment of the Hybrid Scheme Parameters

Gradients in the pressure field can be caused by multiple physical phenomena (coherent structures formation, reaction, explosion, etc...). Their evolution can be either isentropic (rarefaction fan, acoustic wave, compression fan) or anisentropic (shock wave). Acoustic waves that involve relatively high pressure gradients steepen into propagating shocks due to the non-linearities of the Euler equations. Compression fans turn into shock waves due to the self-steepening characteristic of the pressure field. As a consequence, even rather small pressure gradients need to be detected by the smoothness parameter. $\epsilon_P = 0.05$ is found to permit a correct distinction between acoustic waves and self-steepening or shock waves. With the shock capturing method employed here, the resolution of a shock wave front extends over two to three cells. The curvature of the pressure peaks at the head and foot of the shock wave, and the smoothness factor has been found relatively insensitive to the value of the threshold coefficient. For the present study, $S_P^{th} = 0.5$ has been chosen, but no significant difference in the flow resolution was observed when using $S_P^{th} = 0.2$ and $S_P^{th} = 0.8$. The numerical experiments used to determine these values were involving idealized one-dimensional and fundamental three-dimensional shock / turbulence interactions (see section 4.3).

The smoothness evaluation of the density field is somehow more intricate. Typically, strong density discontinuities occur in shock regions (and are then detected by the pressure switch described above), and in mixing layers, at the interface between two fluids of different density/temperature (tip of an injector, flame fronts, Richtmyer-Meshkov instabilities). A strong density curvature causes numerical oscillations. However, the density field and its variations can play a major role in the dynamics of the flow mixing, and need to be resolved without excessive dissipation.

The experiments used to evaluate the parameters of the smoothness evaluation for the density field are based on the simulation of a shock / shear layer interaction problem (see section 4.4) and of a Richtmyer-Meshkov instability resolution, hereafter described. Larger variations of the density field are admissible as they do not have a self steepening property, and hence do not contaminate the flow resolution as pressure gradients do. The noise parameter $\epsilon_\rho = 0.1$ is found sufficient to capture strong gradients without dissipating the smooth variations in density of a compressible turbulent flow. The presence of strong gradients can, however, have a dramatic effect on the flow field, and $S_\rho^{th} = 0.25$ is used to ensure a good resolution of the density variations. The performance of the hybrid scheme in practical applications is hereafter illustrated.

3.6.2 Simulation of a Richtmyer-Meshkov Instability

Richtmyer-Meshkov instabilities (RMI) involve the impulsive acceleration of a density interface. The initial instability gives rise to a linear growth of the initial perturbations. This regime is followed by a nonlinear interaction, where the deterministic structures emerging from the initial discontinuity break down into smaller scale fluctuations, eventually leading to a fully turbulent mixing region. This transition to turbulent states is enhanced if the once-shocked interface is *re-shocked* (by a secondary shock following the primary shock, or, more likely from an experimental standpoint, from the primary shock reflection at the back wall of the wind-tunnel). The present simulation focuses on the experimental study of re-shocked RMI conducted by Vetter and Sturtevant [1995]. An interface air and SF_6 at room temperature is located at 0.62 m from the back end of a wind tunnel, and is shocked by a $M = 1.5$ shock. Reshocking is obtained from back-wall reflection of the travelling shock. A schematic of the configuration is presented in Fig. 3.20.

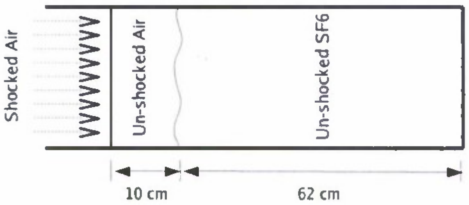

Figure 3.20: Schematic of the Richtmyer-Meshkov Instability problem.

A physical domain of $0.72 \times 0.135m \times 0.135m$ is discretized using $746 \times 140 \times 140$ grid cells, Periodic conditions are enforced in the transverse directions. In the axial direction, the left boundary uses supersonic inflow conditions and the right boundary is a no-slip wall. The initial interface perturbation is imposed following the model of

Hill et al. [2006]:

$$x_I(y,z) = a_0 \left|\sin(\pi y/\lambda)\sin(\pi z/\lambda)\right| + a_1 h(y,z)$$

where h(y,z) is a random function which perturbs the initial interface profile to break the symmetry and enhance the transition. $a_0 = 0.25\ cm$, $a_1 = 0.025\ cm$ and $\lambda = 0.27/14\ cm$ were assumed.

At the initial stage of the interaction, the shaped interface evolves and leads to the formation of finger-like structures of air that penetrate the SF_6 region, and the fluids start mixing, as presented in Fig. 3.21(b) and 3.21(b). These structures result from the hydrodynamic instability of the flow, and a good discontinuity capturing method is needed to capture the interface growth with limited dispersion. Figure 3.21(c) shows the regions of average switching $(1/3(\lambda_{i+1/2,j,k} + \lambda_{i,j+1/2,k} + \lambda_{i,j,k+1/2}))$ for this initial stage. The normal shock is captured with the shock capturing, as visible on the right side of the picture. Figure 3.21(b) shows the contours of the product of mass fractions, $Y_{air} \times Y_{SF_6}$, and highlights the regions where mixing is occurring. The regions where mixing occurs are resolved using the central scheme, hence achieving a proper resolution of the process. The neighboring zone, where the gradients with the unmixed fluids are still high are resolved with the shock-capturing scheme.

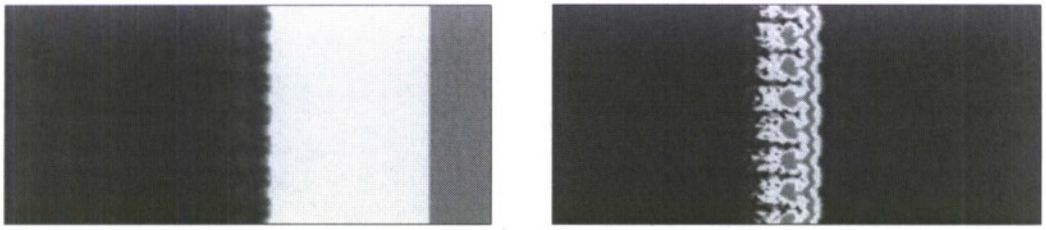

(a) Density Field (b) $Y_{air}Y_{SF_6}$

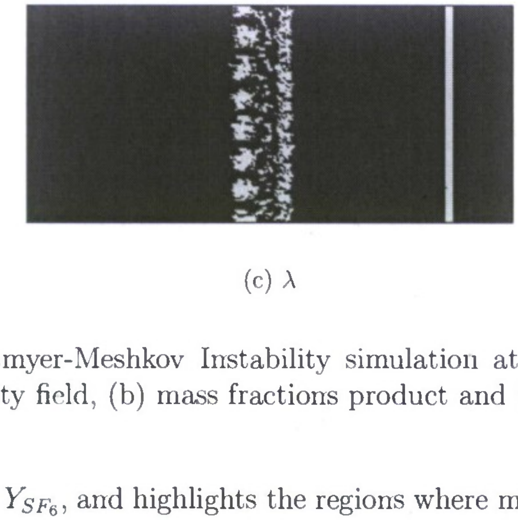

(c) λ

Figure 3.21: Richtmyer-Meshkov Instability simulation at an early stage of the interaction. (a) density field, (b) mass fractions product and (c) switch function.

After reshock, the transition to turbulence of the mixing region is enhanced. Figures 3.22(a) and 3.22(b) show the density field and the $Y_{air} \times Y_{SF_6}$ field after turbulent

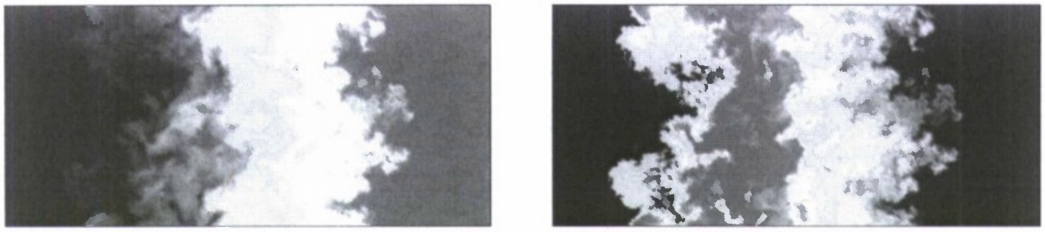

(a) Density Field

(b) $Y_{air} Y_{SF_6}$

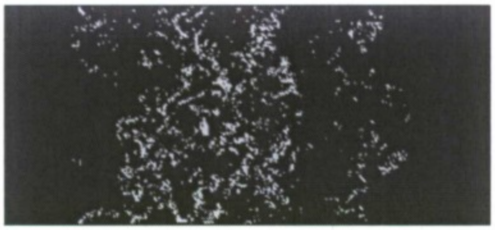

(c) λ

Figure 3.22: Richtmyer-Meshkov Instability simulation at a late stage of the interaction. (a) density field, (b) mass fractions product and (c) switch function.

transition. The presence of density gradients in the mixing region is clearly visible, although these features are not as sharp as during the initial stages. Rather, they show the boundaries of large scale vortical structures that entrain the fluids into the mixing region, and correspond to the interfaces between mixed and fresh fluids. In the mixing zone, large scale vortices coexist with smaller scale turbulent eddies, and the variations in density are more diffuse. The shock capturing scheme is employed in the regions of strong density variations, but overall, the turbulent zone is mostly resolved using the central scheme.

3.6.3 Shu-Osher Interaction

The Shu-Osher problem (Shu and Osher [1989]) consists in a one-dimensional shock front propagating into a sinusoidal density distribution. As the shock passes through, it is immediately followed by a region of rapid, high amplitude oscillations. These short wavelengths oscillations decay further downstream of the shock, forming a region of longer wavelength oscillations which steepen into shocks, forming an N-wave pattern. A complete resolution of the entire phenomenon and all wavelengths requires a fairly high resolution. Furthermore, an accurate computation of shock propagation, at the right speed, and a smooth capture of the short-wavelength variations that form in the post-shock region is needed to resolve all the physical features of this flow. This makes this simple test particularly relevant to the problem of shock / turbulence interaction.

The initial conditions for this problem are as follows: a shock initially located at $x = 2$ propagates in the $x > 2$ direction. The density profile is given by:

$$\rho(x) = \begin{cases} 3.857142 & x < 2 \\ 1 - 0.2\sin(5x) & x \geq 2 \end{cases} . \tag{3.69}$$

while pre-shock pressure and velocity are 1 and 0, respectively. The post-shock values for pressure and velocity are constant and equal to 10.333333 and 2.629369, respectively. The domain extends from $x = 0$ to $x = 10$. The left boundary is treated as a supersonic inflow, and the right boundary is an outflow. The gas obeys a calorically perfect gas equation of state with an adiabatic index γ of 1.4. The simulation is finalized at a time of 1.872. Uniform one-dimensional grids are used for these computations. The reference converged solution is classically obtained by performing a highly resolved simulation of this same configuration (noted Ref in the figures).

The purely upwind approach cannot capture to short wavelength oscillations when 200 grid cells are employed (figure 3.23), and in this region, the dominant wavenumber of the N-wave pattern appears as the smallest resolved wavenumber. A simulation using exclusively the smooth flow solver did not converge for the present resolution. The oscillations around the shock front generate unphysical values for the energy. The hybrid method leads to a crisp capture of the shock front using the upwind scheme, while the smooth flow solver is used to resolve the post-shock region. As a consequence, despite the fact that the full amplitude of the oscillations is not totally recovered, the short wavelengths are obtained in the post-shock region at this low-resolution simulation.

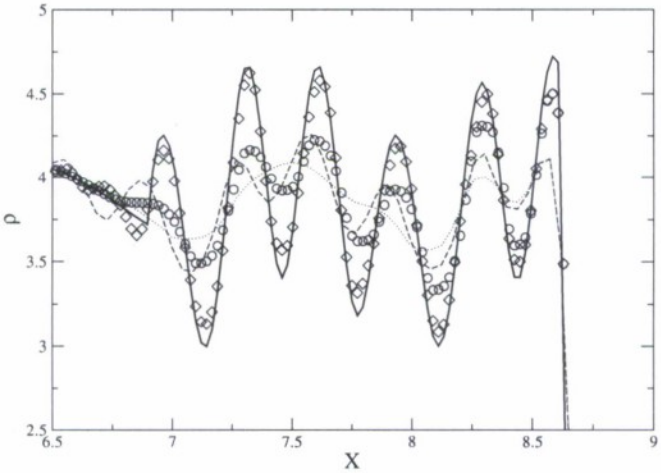

Figure 3.23: Density profile at the final time for the Shu-Osher shock / entropy Wave interaction. Ref —, Hybrid method (N=200)- - -, pure upwind (N=200) · · ·, Hybrid method (N=400) ◇, pure upwind (N=400) ○ .

As the resolution is increased to 400 grid cells (Fig. 3.23, 3.24), the simulation based on a purely upwind approach captures all the wavelengths of the problem, but the inherent dissipation of the scheme prevents this approach from capturing the oscillations amplitude. A purely central scheme simulation converges at this resolution, although, in the course of the simulation, pressure and density fields reach very small values. The non-physical oscillations formed around the shock front, modify the behavior of the post-shock region, but permit a capture of the oscillations. The self-steepening waves, however, are not correctly captured, and lead to the formation of numerical oscillations. The hybrid approach combines the advantages of both schemes, leading to a proper capture of the main shock, and a very good resolution of the post-shock oscillations. Furthermore, the oscillations around the N-wave pattern are rather small and do not amplify.

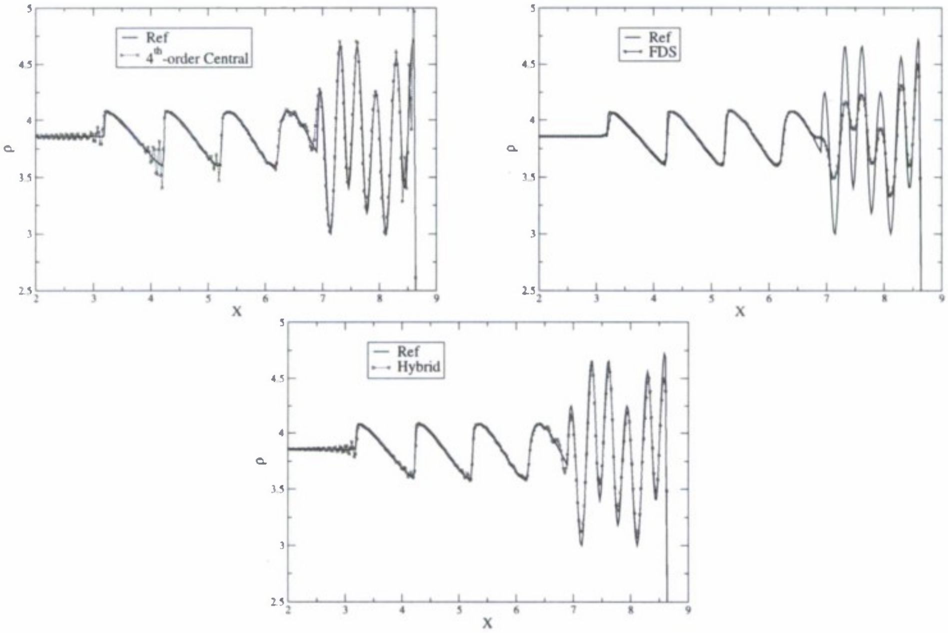

Figure 3.24: Density profile at the final time for the Shu-Osher shock / entropy Wave interaction using the central, upwind and hybrid schemes.

The observations made for a resolution of 400 grid cells are still valid for an extension to a resolution of 800 grid cells, presented in Fig. 3.25. The hybrid scheme captures the physical phenomenon with limited dissipation. The main front is captured at the right propagation speed, and the formation of the short wavelength oscillations is well simulated with the hybrid approach. Again, the N-wave pattern formed by the self-steepening pressure gradients, is initially resolved with the smooth flow solver. Small amplitude oscillations are formed around the discontinuities, which remain small throughout the simulation. Overall, the hybrid scheme shows good capture of this one-dimensional shock / turbulence interaction.

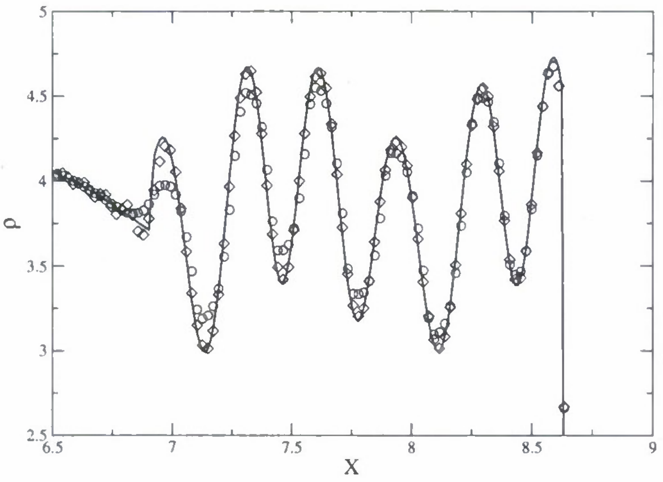

Figure 3.25: Density profile at the final time for the Shu-Osher shock / entropy Wave interaction. Ref —, Hybrid method (N=800) ⋄, pure upwind (N=800) ○ .

3.6.4 Shock / Vortex Interaction

The passage of a vortex through a shock wave is a problem of fundamental interest. It has been extensively studied experimentally (*e.g.* Dosanjh and Weeks [1965], Cattafesta and Settles [1992], Chang et al. [2004]), analytically (Ribner [1954a, 1985], Mahesh et al. [1997]) and numerically (Ellzey et al. [1995], Inoue and Hattori [1999], Dexun and Yanwen [2001]), with a particular emphasis on the noise production through the interaction. The passage of large coherent vortices through compression wave contributes significantly to the *shock-associated* noise that is found in jet engines. Experimental observations and numerical simulations have permitted to identify the physical mechanisms involved in the sound generation during the interaction. The shock deformation and the subsequent localized compressions and expansions lead to the formation of a series of acoustic waves which propagate radially from the point of interaction. Their strength is a function of the angle. The first wave generated is referred to as the precursor directly followed by the second sound wave. The shock wave distortion and its relaxation to the undisturbed position often lead to the formation of third and more waves.

The ability of the present numerical approach to capture shock / vortex interaction and the sound generation is hereafter tested. The numerical set-up used here is similar to that of Inoue and Hattori Inoue and Hattori [1999]. A standing normal shock, corresponding to a free-stream Mach number M_s is initialized at a location $x = 0$. The un-shocked fluid at $x > 0$ has a static pressure and temperature P_u and T_u respectively. The right boundary is treated as an inflow with constant properties. The shocked flow is on the left side of the interface and has pressure and temperature P_s and T_s. The left, top and bottom boundaries are subsonic outflows. Noting R the radius of maximum velocity in the initial vortex, the domain extends from $-20R$ to $8R$ in the x-direction, and from $-12R$ to $12R$ in the y-direction. A vortex is initialized

$x = 2R$, $y = 0$, with a velocity profile prescribed as:

$$v_\theta(r) = v_{max}\frac{r}{R}e^{\frac{1}{2}\left(1-\frac{r^2}{R^2}\right)}$$

The pressure within the vortex is obtained from the relation:

$$\frac{dP}{dr} = \frac{\rho v_\theta^2}{r} \tag{3.70}$$

Defining the vortex Mach number M_v as the ratio between v_{max} and the free-stream un-shocked speed of sound a_u, the integration of the previous equation for an isentropic flow gives:

$$P(r) = P_u\left(1 - \frac{\gamma-1}{2}M_v^2 e^{1-\frac{r^2}{R^2}}\right)^{\frac{\gamma}{\gamma-1}}$$

$$T(r) = T_u\left(1 - \frac{\gamma-1}{2}M_v^2 e^{1-\frac{r^2}{R^2}}\right)$$

The simulation conducted for the present study is based on the experimental study of Dosanjh and Weeks Dosanjh and Weeks [1965]. The mean flow Mach number is $M_s = 1.29$, and the vortex Mach number is $M_v = 0.39$. Following the study of Inoue and Hattori Inoue and Hattori [1999], the Reynolds number based on the un-shocked density, velocity and viscosity, and on the vortex radius is set to $Re = 800$. Figure 3.26(a) represents the density field at a time $T = 10.3R/a_u$. This field shows the structure of the waves generated from the interaction in the shocked region. Two reflected shocks are formed, that propagate outwards, and the triple points that result from the main shock / reflected shocks interaction lead to the formation of slip-lines, that *connect* the vortex to the triple points. The circumferential pressure distribution at this time is collected for the precursor ($P_p(\theta)$ at $r/R = 10.3$) and for the second sound wave ($P_2(\theta)$ at $r/R = 8.3$), where θ is the angle from the horizontal, taking the vortex as the origin. Their behavior is typical of the quadrupolar nature of the phenomenon. The angular variations of the normalized pressure difference $(P_2 - P_p)/P_s)$ is then computed and compared to experimental and other numerical (Ellzey et al. [1995], Inoue and Hattori [1999])

The domain has been discretized using uniform Cartesian grids, and two resolutions have been studied. A first simulation is conducted with a grid resolution of 560×480 grid cells. The resolution is decreased to 280×240 for the second simulation. Figure 3.26(b) shows the normalized pressure difference. The behavior of the pressure fields reproduces the physical phenomena observed in the experiments. Moreover, both simulations are in excellent agreement with the results of previous, more refined, numerical simulations. The lower resolution study reproduces the sound generation with good accuracy. Small oscillations start appearing at this resolution for very negative angles ($\theta < -120°$), but do not contaminate the solution, and the physical features remain properly resolved. The shock-capturing scheme is used in the main flow direction within the shock thickness which extends over two cells, and up to three cells during the interaction. The shock-capturing scheme is also activated

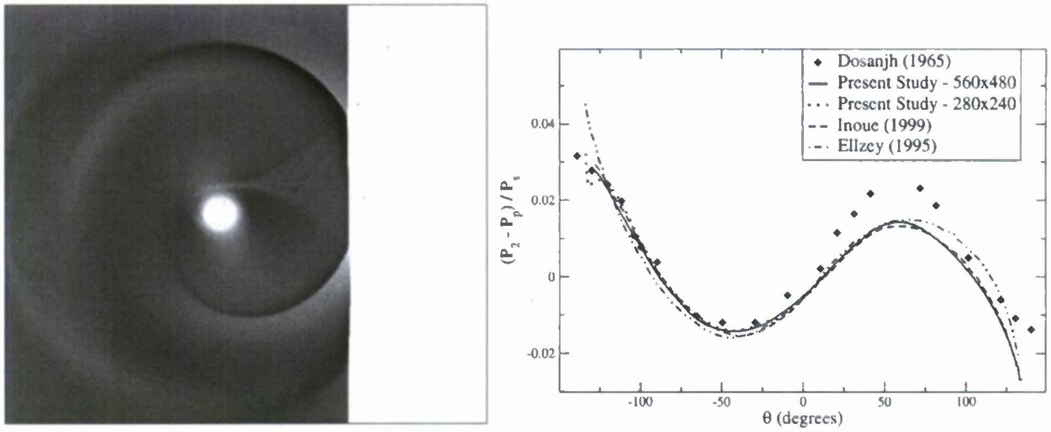

(a) Density Field

(b) precursor to secondary acoustic wave pressure difference

Figure 3.26: (a) Instantaneous density field showing precursor and second sound waves and (b) angular variations of the normalized pressure difference between precursor and second acoustic waves for the shock / vortex interaction problem - comparison with experiments Dosanjh and Weeks [1965] and other numerical methods (Ellzey et al. [1995], Inoue and Hattori [1999]).

in the transverse direction when the vortex distorts the shock front. The vortex core and the acoustic pulses are entirely resolved with the smooth flow solver.

The present switch formulation is based on the evaluation of the curvature of the pressure and density fields, as described earlier. This approach is found to permit a good capture of the problems considered in the present study. The set of parameters employed in the present formulation cannot, however, be considered universal. Their range of applicability is limited to supersonic flows with moderate density gradients. Their applicability to hypersonic configurations or flows with very large variations in the density field should be assessed. Furthermore, these parameters are flow-dependent by definition, and a dynamic evaluation of the parameters as a function of the flow field could be considered as an extension to the present hybrid methodology.

3.7 Other Computational Issues

3.7.1 Viscous Fluxes

The overall scheme for the convective and pressure forces resolution is fourth-order accurate away from the discontinuities, and switches to the upwind scheme in regions of discontinuity. There, the accuracy is flow dependent, and can vary between third and first order accuracy, depending on the smoothness of the flow. The evaluation of the viscous fluxes, subgrid terms and source terms for the k^{sgs} evolution requires the evaluation of first derivatives. A standard finite difference methodology is used for those evaluations, with second-order spatial accuracy for first derivatives, and overall fourth-order accurate resolution of the second derivative of the diffusion equation. Calling (ξ, η, ζ) the standard computational directions of increasing i, j and k, respectively, the physical derivatives are obtained from:

$$\frac{\partial u}{\partial x_i} = \frac{\partial u}{\partial \xi}\frac{\partial \xi}{\partial x_i} + \frac{\partial u}{\partial \eta}\frac{\partial \eta}{\partial x_i} + \frac{\partial u}{\partial \zeta}\frac{\partial \zeta}{\partial x_i} \tag{3.71}$$

where $\partial\xi/\partial x_i$, $\partial\eta/\partial x_i$ and $\partial\zeta/\partial x_i$ are computed from the grid directly, and are fixed in the course of the simulation. $\partial u/\partial\xi$ is obtained from the flow variables as follows: derivatives evaluated at the cell centers are computed as:

$$\left(\frac{\partial u}{\partial \xi}\right)_{i,j,k} = \frac{1}{12}\left(-u_{i+2,j,k} + 8u_{i+1,j,k} - 8u_{i-1,j,k} + u_{i-2,j,k}\right) \tag{3.72}$$

$\xi-$derivatives at an $i + 1/2$ interface will be obtained from:

$$\left(\frac{\partial u}{\partial \xi}\right)_{i+1/2,j,k} = \frac{1}{12}\left(-u_{i+2,j,k} + 15u_{i+1,j,k} - 15u_{i,j,k} + u_{i-1,j,k}\right) \tag{3.73}$$

The $\xi-$derivative evaluated at a $j+1/2$ interface is based on the extrapolated variables (Eqn. 3.17), and reads:

$$\left(\frac{\partial u}{\partial \xi}\right)_{i,j+1/2,k} = \frac{1}{12}\left(-u^{\pm}_{i,j+2,k} + 8u^{\pm}_{i,j+1,k} - 8u^{\pm}_{i,j-1,k} + u^{\pm}_{i,j-2,k}\right) \tag{3.74}$$

An identical formulation is used to compute a $\xi-$derivative at a $k+1/2$ interface. Furthermore, it is straightforward to extend the formulation given here for $\xi-$derivatives to the $\eta-$ and $\zeta-$ directions.

3.7.2 Time-Step Determination

Convection and viscous forces both contribute to the propagation of the information from one cell to its neighbors. The maximum characteristic speed for the convection is given by $|u| + c$, the viscous diffusion speed is $2\nu/\Delta x$, where ν is the kinematic viscosity, $\nu = \mu/\rho$, and the thermal diffusion speed is $2\kappa/(\rho c_v \Delta x) = 2\gamma\nu/(Pr\Delta x)$. The propagation time can be defined for each cell in the domain as:

$$\Delta t^p_{ijk} = \frac{V}{u_i\Sigma_i + c\overline{\Sigma} + \frac{2\gamma\nu}{Pr}\frac{\overline{\Sigma}^2}{V}} \tag{3.75}$$

where $\overline{\Sigma}$ is the average surface of the cell boundaries, and the viscous diffusion speed has been neglected to the thermal diffusion speed ($\gamma > 1$, $Pr < 1$). In order to get a time-explicit method, the most restrictive propagation time of all cells, $\overline{\Delta t}^p$, is obtained

$$\overline{\Delta t}^p = \min_{i,j,k}\left(\Delta t^p_{ijk}\right) \tag{3.76}$$

The actual time-step imposed for the time integration of the governing equation is determined from stability considerations as:

$$\Delta t = N_{CFL}\ \overline{\Delta t}^{p} \tag{3.77}$$

The CFL number, N_{CFL}, is used to ensure the stability of the computation, and is scheme-dependent. In the current approach, a CFL number $N_{CFL} = 0.25$ is imposed.

3.7.3 Boundary Conditions

Typically, temporally evolving problems are configurations with at least one, and often up to three directions of homogeneity. The use of periodic boundary conditions in these directions is a rather standard approach. Other boundary conditions for temporal problems include no-slip walls and symmetry boundaries. Spatial problems, on the other hand, require the integration of inflow and outflow boundary conditions into the problem. In the present study, both temporal and spatial problems are considered. Each boundary condition type is independently addressed in the following paragraphs.

- Periodic BC

Periodic BCs are used for simulating flows that have at least one direction of homogeneity. In a homogeneous flow, the evolution of a characteristic volume of fluid is statistically identical to the evolution of a neighboring volume of fluid. It can then be assumed that, for simplicity, the neighboring volume of fluid evolves exactly as the considered volume.

Under this assumption, the periodicity of the solution is used to reproduce the interior of the domain at the boundaries, at the end of every integration sub-step (predictor and corrector). This operation is not computational, but rather a copy handled by communication.

- Inflows

In supersonic flows, the flow velocity is greater than the local speed of sound, and no characteristic can propagate upstream of the flow. Hence, all the flow properties are prescribed for supersonic inflows.

The superposition of turbulent fields on the average inflow profiles is performed assuming that the Taylor hypothesis can be used, that is, that the spatial location of a turbulent field obtained from a temporal simulation can be converted into a time-varying profile at the inflow of a spatial problem. The instantaneous velocity field at the inflow $x = 0$ of a spatial problem is then the superposition of a mean profile $\bar{U}_i(y, z)$ and of a fluctuating field u'_i, obtained from a frozen turbulent field following:

$$U_i(x = 0, y, z, t) = \bar{U}_i(y, z) + u'_i(x = -U_c t, y, z) \tag{3.78}$$

This assumption is valid in the studies presented here, as the turbulent intensities encountered are relatively small, and mostly solenoidal (Lee et al. [1992]).

This approach cannot be used for simulations involving wall-bounded supersonic flows, and alternate inflow approaches need to be used. In the current study, a *recycling rescaling* methodology (RRM) is used to generate the turbulent inflow. Originally proposed by Lund [1998] for incompressible flows, this method uses the similarity in the turbulent structures at different downstream locations of a boundary layer to construct a self-developing turbulent inflow. While a boundary layer cannot be treated as a homogeneous flow in the direction of propagation, the scaling laws of the inner and outer layers of the boundary layer are used to rescale these turbulent fluctuations. This method has later been extended to compressible flows by several researchers. A review of the most commonly used RRM is given in Knight [2006]. In the present study, the RRM technique of Stolz and Adams [2003] is chosen for its simplicity and good convergence (Knight [2006]).

Let γ be the ratio of inflow and recycling friction velocities, $\gamma = u_{\tau,in}/u_{\tau,rec}$, it is assumed that the friction velocity depends on the boundary layer thickness as $u_\tau \propto \delta^{1/8}$. Given the classical scaling laws of the boundary layer, $\bar{U}/u_\tau$ is a function of $y^+ = yu_\tau/\nu$ in the inner layer, and $(U_\infty - \bar{U})/u_\tau$ a function of $\eta = y/\delta$ in outer layer. Extending this scaling to the fluctuating velocities u'/u_τ, v'/u_τ and w'/u_τ, the relation between inflow plane and recycling plane in the inner layer of the boundary is given by:

$$\frac{u'_{in}(y_{in}u_{\tau,in}/\nu)}{u_{\tau,in}} = \frac{u'_{rec}(y_{rec}u_{\tau,rec}/\nu)}{u_{\tau,rec}} \quad \text{where} \quad y_{in}u_{\tau,in}/\nu = y_{rec}u_{\tau,rec}/\nu \tag{3.79}$$

so that:

$$u'_{in}(y_{in}) = \gamma u'_{rec}(\gamma y_{in}) \tag{3.80}$$

In the outer layer, the scaling reads:

$$\frac{u'_{in}(y_{in}/\delta_{in})}{u_{\tau,in}} = \frac{u'_{rec}(y_{rec}/\delta_{rec})}{u_{\tau,rec}} \quad \text{where} \quad y_{in}/\delta_{in} = y_{rec}/\delta_{rec} \tag{3.81}$$

and:

$$u'_{in}(y_{in}) = \gamma u'_{rec}(\gamma^8 y_{in}) \tag{3.82}$$

The scaling obtained for the mean value of the axial velocity $\bar{U}$ is similar. The averaged variables are estimated using a Butterworth filter to obtain sliding time averaged quantities, similar to Stolz and Adams [2003].

These relations hold for the velocity fluctuations and the mean axial velocity. The mean transverse velocity, along with the mean and fluctuating thermodynamics variables are assumed to have universal scaling laws independent of the friction velocity, and solely functions of their freestream value $(V_\infty, T_\infty, \rho_\infty)$, of y^+ and *eta*. For instance, the temperature field is rescaled using $T'/T_\infty = f(y^+)$ so that $T'_{in}(y_{in}) = T'_{rec}(\gamma y_{in})$ in the inner layer, and $T'/T_\infty = f(\eta)$, and $T'_{in}(y_{in}) = T'_{rec}(\gamma^8 y_{in})$ in the outer layer.

The scalings described above are valid in their respective layer, and a blending is necessary to transition from one rescaling approach to the next. The weighting function $W(\eta)$ given by:

$$W(\eta) = \frac{1}{2}\left(1 + \tanh\left(\frac{\alpha(\eta - b)}{(1-2b)\eta + b}\right) / \tanh(\alpha)\right) \tag{3.83}$$

where $\alpha = 4$ and $b = 0.2$, is used to blend these two scalings, and, noting $\beta = W(\gamma^8 y/\delta_{rec})$, the field at the inflow of the spatial problem is obtained following:

$$\begin{array}{rcl}
u_{in}(y,z,t) = & \beta & [\gamma u_{rec}(\gamma^8 y, z, t) + (1-\gamma)U_\infty] \\
 & (1-\beta) & [\gamma u_{rec}(\gamma y, z, t)] \\
v_{in}(y,z,t) = & \beta & [\gamma v_{rec}(\gamma^8 y, z, t) + (1-\gamma)\bar{V}(\gamma^8 y, t)] \\
 & (1-\beta) & [\gamma v_{rec}(\gamma y, z, t) + (1-\gamma)\bar{V}(\gamma y, t)] \\
w_{in}(y,z,t) = & \beta & [\gamma w_{rec}(\gamma^8 y, z, t)] \\
 & (1-\beta) & [\gamma w_{rec}(\gamma y, z, t)] \\
T_{in}(y,z,t) = & \beta & [T_{rec}(\gamma^8 y, z, t)] \\
 & (1-\beta) & [T_{rec}(\gamma y, z, t)] \\
\rho_{in}(y,z,t) = & \beta & [\rho_{rec}(\gamma^8 y, z, t)] \\
 & (1-\beta) & [\rho_{rec}(\gamma y, z, t)]
\end{array} \tag{3.84}$$

- Outflows

Outflow boundary conditions are imposed using a standard extrapolation method for supersonic flows. Again, in supersonic flows, the characteristics are all out-going, and all the properties in the boundary cells can be imposed from the interior of the domain. For subsonic outflows, a characteristics-based formulation is used (Poinsot and Lele [1992]). In the cases considered in the present studies, perfectly absorbing outflows are used, as the acoustic coupling between the flows and the exits should be avoided. The use of a *sponge* layer before the outflow, similar to the numerical method of Mahesh et al. [1997], is used for the fundamental study of shock / isotropic turbulence interaction, in order to dampen the large velocity and thermodynamics fluctuations created by the interaction. This method consists in modifying the governing equations of motion in a small layer at the outflow of the domain, in order to add a relaxation to the fluctuating field. The governing equations read then:

$$\frac{\partial Q}{\partial t} = -\frac{\partial F_i}{\partial x_i} + S - \sigma(x_1)\left(Q - Q_{ref}\right) \tag{3.85}$$

where X_1 is the mean flow direction, and Q_{ref} are the flow properties in the absence of turbulent structures. $\sigma(x_1)$ is a damping factor, and varies as:

$$\sigma(x_1) = \begin{cases} A_s \frac{c_{ref}^2}{\nu_{ref}} \left(\frac{x_1 - x_s}{L_x - x_s}\right)^n & \text{if } x_1 \geq x_s \\ 0 & \text{otherwise} \end{cases} \tag{3.86}$$

where c_{ref} and ν_{ref} are reference values of the speed of sound and dynamic viscosities, L_x is the domain length, and A_s, x_s and n are parameters of the sponge layer method.

- Walls

No-slip walls are modeled as adiabatic, no-slip, acoustically reflecting boundaries. This ensures that the interpolated velocity vector is zero at the boundary, and that the gradients in pressure, density and species mass fractions are zero at the boundary.

Very fine resolutions are needed close to walls to capture the turbulent statistics in the turbulent boundary layers and often, when the resolution of the turbulent statistics in the boundary layer is found not to be critical to the overall flow evolution, *slip walls*, or symmetry boundaries, are used. These boundaries are adiabatic, acoustically reflecting. The conditions of non-penetration and of conservation of the tangential momentum are applied to the velocity field.

3.7.4 Parallelization

The developments presented here have been integrated in a parallel solver. Parallel communication is implemented using a standardized Message-Passing Interface (MPI) protocol. The resulting numerical code is portable and has been used on multiple platforms with different architectures (Intel PC linux cluster, Cray XT4, IBM SP4 clusters, ...). The performance of the implementation on parallel clusters depends on the domain decomposition, and the amount of *switching* between numerical schemes inside a given domain. The implementation of both the upwind and central schemes independently have been found to scale well, almost linearly, for up to 1024 processors, on multiple architectures (Masquelet et al. [2008]).

The stencil of the central scheme considered here extends over two cells on each side of the interface. The MUSCL reconstruction of the shock-capturing requires two levels of information on each side of the interface as well. The flattening method, on the other hand, requires the evaluation of the shock thickness at the cell centers within two cells from every interface, and has a stencil of two, yielding a total of four levels of communication. Finally, the computation of the filtered rate of strain, needed for the dynamic closure model, imposes three levels of communication. Overall, four levels of communication are necessary for the current methodology.

CHAPTER IV

SIMULATION OF SHOCK / TURBULENCE INTERACTION

The shock / turbulence interaction problem is of fundamental importance. The presence of shock waves in high speed flows cannot be avoided, and a correct treatment of their impact on turbulence evolution is critical in the development of this LES methodology for compressible flows. Three cases of shock / isotropic turbulence have been chosen in the present study, representative of the different regimes of the interaction: as reviewed earlier, the interaction of a field of homogeneous turbulence with a normal shock wave leads to different behaviors depending on the incoming Mach number. An increase in the turbulent intensity is observed through the interaction, that increases as the Mach number is increased, and saturates for a Mach number above 3. The amplification of the streamwise velocity fluctuations increases until a Mach number $M \approx 2$, decreases afterward, and saturates at $M = 3$.

An $M = 1.29$ interaction is studied first, similar to the case '1.29A' of Mahesh et al. [1997]. The other two cases are for Mach numbers of 2 and 3, and are similar to the configurations denoted 'B' and 'C' in Lee et al. [1997]. These three cases are simulated first in direct simulations. Though an exact match with the reference data cannot be expected, due to differences in numerical schemes and actual initial conditions, these simulations are used to verify the capability of the present hybrid methodology in reproducing the physical features of the interaction with minimal dissipation, and should reproduce the qualitative and, to a large extent, the quantitative characteristics of the interaction.

Direct simulations are performed in two stages. First, a field of isotropic turbulence is generated. A field of velocity fluctuations is initialized according to a fixed energy spectrum, and a simulation of isotropic turbulence decay is conducted, so that the artificial initial field gains physical correlations. This procedure will be described first. This turbulent field is used at the inflow of a spatial problem of shock / turbulence interaction. The domain of computation is attached to the shock front, and a statistical study of the interaction is obtained. Comparison of the present simulations with other reference DNS data shows the correct capture of the physical phenomena associated with this type of interactions at all regimes. These direct simulations are used to perform an *a-priori* study of the LDKM closure model for this interaction, followed by an LES of this canonical test case, to assess the performance of the closure model in *a-posteriori* analyses.

4.1 Initial Field of Isotropic Turbulence

The generation of an initial field is performed following the procedure given in Knight et al. [1998]. The steps of this initialization are:

- Generate a random field of velocity fluctuations and compute its Fourier transform,
- Subtract the divergent part of the field,
- Compute the energy spectrum in Fourier space associated with these initial random fluctuations,
- Scale all Fourier coefficients, using the ratio between expected and actual energy in the wavenumber mode this coefficient contributes to,
- Re-construct the velocity field using inverse Fourier transform.

This procedure initializes a field of isotropic, dilatational-free turbulence according to a given energy density spectrum. It should be noted that the velocity field only is initialized with this method. All thermodynamics variables are assumed constant. In the context of compressible turbulence studies, more realistic field generation initialize the thermodynamics fluctuations associated with the velocity field (see, e.g., Ristorcelli and Blaisdell [1997]). In the scope of the present study however, the field of turbulence is free of thermodynamics fluctuations, similar to the reference studies to which this study compares.

In the initial spectrum, two parameters can be chosen independently, namely the energy density and the rate of dissipation, through the following relations:

$$\begin{array}{c} \int_0^\infty E(\kappa)d\kappa = k \\ \int_0^\infty 2\nu\kappa^2 E(\kappa)d\kappa = \epsilon \end{array} \tag{4.1}$$

The Reynolds number of the initial field is related to these two parameters through the relation:

$$R_\lambda = \sqrt{\frac{20}{3}}\frac{k}{\sqrt{\nu\epsilon}} \tag{4.2}$$

Several analytic model spectra exist that mimic some features of real turbulent spectra. The Pao spectrum is often used for high Reynolds numbers flows. Its formulation explicitly includes an inertial range with a $-5/3$ law, and both the energy containing and dissipative ranges. This model spectrum is however a poor representation for low Reynolds number flows, and the following von Karman model spectrum is often preferred (see, *e.g.* Lee et al. [1997]):

$$E(\kappa) = \frac{32}{3}\sqrt{\frac{2}{\pi}}\frac{k}{\kappa_0}\left(\frac{\kappa}{\kappa_0}\right)^4 exp\left[-2\left(\frac{\kappa}{\kappa_0}\right)^2\right] \tag{4.3}$$

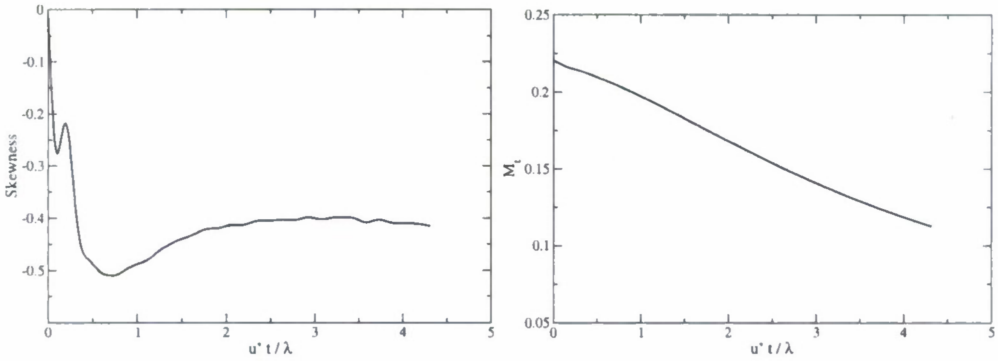

(a) Skewness of the isotropic turbulence (b) Turbulent Mach number evolution

Figure 4.1: Temporal evolution of the velocity skewness (left) and turbulent Mach number (right) in the simulation of isotropic decaying turbulence.

where κ_0 is the most energetic wavelength. It is straightforward to show, using the second relation in Eqn. 4.1 that this most energetic wavelength is related to the Taylor micro-scale through the relation:

$$\kappa_0 \lambda = 2 \tag{4.4}$$

Following the work of Mahesh et al. [1997], the initial energy spectrum follows the model spectrum given in Eqn. 4.3. The initial turbulent Mach number is $M_t = 0.22$ and $R_\lambda = 39.5$. The most energetic wavelength is given by $k_0 = 6$. The domain of dimensions $6\pi \times 2\pi \times 2\pi$ is discretized using $243 \times 81 \times 81$ grid cells with uniform spacing. Periodic BCs are applied on all sides of the domain. The simulation is performed using the hybrid methodology, but no switching occurs during the computation, entirely resolved with the fourth-order central scheme.

The simulation of turbulent decay is conducted until a $R_\lambda = 19.1$ is obtained. This corresponds to a non-dimensional time of $tu'/\lambda = 3.2$, where $u' = u_{rms}/\sqrt{3}$ is the amplitude of the initial velocity fluctuations. The skewness S_i of the $i-$component of the velocity field is an indicator of the coherence of the turbulence.

$$S_i = \frac{\overline{\frac{\partial u_i}{\partial x_i}^3}}{\overline{\frac{\partial u_i}{\partial x_i}^2}^{3/2}} \tag{4.5}$$

As reported in Mahesh et al. [1997], a skewness $-0.6 < S_i < -0.4$ indicates a well-developed turbulent field. The temporal evolution of the average velocity skewness S and of the turbulent Mach number during the course of the isotropic turbulence decay is shown in Fig. 4.1. At the end of this simulation, the turbulent Mach number has decayed to $M_t = 0.14$. The initially constant thermodynamics field evolves in the course of the simulation, and small temperature and density fluctuations

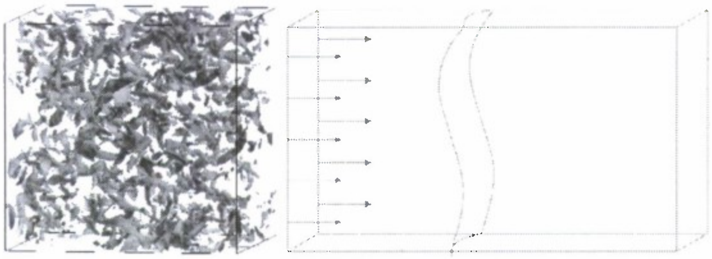

Figure 4.2: Schematic of the shock / Isotropic turbulence interaction configuration.

are present in the flow ($\rho_{rms}/\overline{\rho} \approx 0.01$). This initial field is used at the inflow of the shock / turbulence interaction problem of $M = 1.29$ described hereafter. A similar procedure is performed to generate the initial turbulent field for the two other interactions. The final fields have a Reynolds number of $R_\lambda = 20$, and $M_t = 0.11$.

4.2 Direct Simulations of Shock / Isotropic Turbulence Interaction

The fields of well-developed turbulence are superposed on a mean velocity at the inflow of a spatial problem. Figure 4.2 shows a sketch of the shock / isotropic turbulence interaction studied here. In the first simulation, a $M = 1.29$ standing shock is initialized at $x = \pi/2$ from the Rankine-Hugoniot relations based on the mean incoming thermodynamic state. The spatial problem extends over $4\pi \times 2\pi \times 2\pi$, and $231 \times 81 \times 81$ grid cells are used to discretize this configuration. The grid generation is performed following the stretching function given by Mahesh et al. [1997] for the same problem, so that a refined grid is obtained around the mean location of the shock front. The two high Mach number cases are solved with the same resolution, $231 \times 81 \times 81$ grid cells. The physical domain dimensions are $(2\pi + 1) \times 2\pi \times 2\pi$. The grid is clustered close to $x = \pi$, mean location of the shock.

For all three cases, the coordinate system of reference is attached to the mean shock location, and supersonic inflow and characteristic outflows are used. Periodicity is imposed in the transverse directions. A sponge layer method is applied before the outflow of the domain in order to damp the turbulent oscillations. This method is described in section 3.7.3, and the values of the parameters in this method follow the study of Mahesh et al. [1997], $A_s = 5$, $n = 3$ and $(L_x - x_s)/L_x = 0.14$.

The coordinate system of reference is attached to the mean shock location. Supersonic inflow and non-reflecting characteristic-based outflow conditions (Poinsot and Lele [1992]) are applied. All cases are simulated by solving the non-filtered Navier-Stokes equations, since the resolution permits a capture of all the physical scales involved in the problem, except within the shock. Using a shock-capturing methodology leads to a shock with a finite thickness. The computation of the viscous terms within this thickness being questionable, only the inviscid part of the governing equations have been solved within this region, both for the present DNS calculations and for the LES computations presented later in this study.

Statistics are collected for two flow-through-times, after the first two flow-through-times have been discarded to wash out initial transients. The profiles of statistically averaged Reynolds stresses in the normal and transverse directions are plotted in Fig. 4.3(a), 4.3(b) and 4.3(c), and compared to their respective reference DNS simulations. It should be noted that the profiles for the Reynolds stresses in the transverse directions show slight differences between u_2 and u_3 statistics, similar in amplitude to that reported by Lee et al. [1997] for the same cases. Hence, for clarity, the averages of those two profiles are plotted each time. The statistics in the shock region are strongly perturbed by the shock oscillations, and a high value is obtained for the axial Reynolds stress from the temporal averaging operation. These velocity fluctuations are not of turbulent nature, and this region should be disregarded for all physical interpretations, as also noted by other authors, e.g. Mahesh et al. [1997], Lee et al. [1997].

It is known from previous studies that the interaction of a shock wave with a turbulent field leads to a corrugation of the front which, through its oscillations and the formation of localized compressions and expansions, generates acoustic energy (Ribner [1954b]). Downstream of the shock, the evanescent acoustic waves transfer the acoustic energy into turbulent kinetic energy, hence leading to an overall amplification of the turbulence levels. It is inferred from the capture of the Reynolds stresses behavior that this energy transfer is correctly captured by the present DNS study.

Analysis of the behavior of the hybrid algorithm shows that the upwind scheme is used for less than 3% of the normal flux evaluations and less than 2% of the transverse flux evaluations. The turbulent features are then mostly resolved using the smooth flow solver. The flux difference splitting shows a good capture of the shock front and of its corrugation. The acoustic energy generation as well as the transmitted turbulent kinetic energy are correctly simulated by the hybrid method. Good agreement with the reference DNS data is obtained, with less than 5% differences in the amplitude of the Reynolds stresses profiles.

The relevance of the hybrid methodology is assessed in these direct simulations. The inadequacy of upwind methods for turbulent simulations was noted by Lee et al. [1997], who reported a significant dissipation of the turbulent field in shock / isotropic turbulence interactions, resolved with a $6^{th}-$order ENO scheme. This is illustrated in the present study of shock / turbulence interaction through the resolution of the same problems, using purely upwind schemes. The flux-difference splitting method developed in the context of the present hybrid method (noted FDS in the following) is employed first. Also, an alternate higher-order upwind method has been used: the Piecewise Parabolic Method (PPM, Colella and Woodward [1984]) is a higher-order flux difference splitting scheme, commonly used in astrophysical simulations, and previously employed for DNS studies (Mirin et al. [1999]). The implementation used for the present calculations is identical to that of the FLASH code (Fryxell et al. [2000]), except no artificial dissipation was employed for these simulations, in order to reduce the numerical dissipation. The contours of Reynolds stresses for the three Mach number flows considered here are presented in Fig. 4.4. These profiles are compared to the hybrid scheme simulations, since this approach performed well

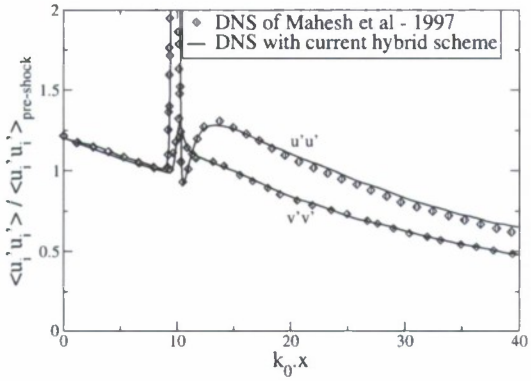

(a) M=1.29

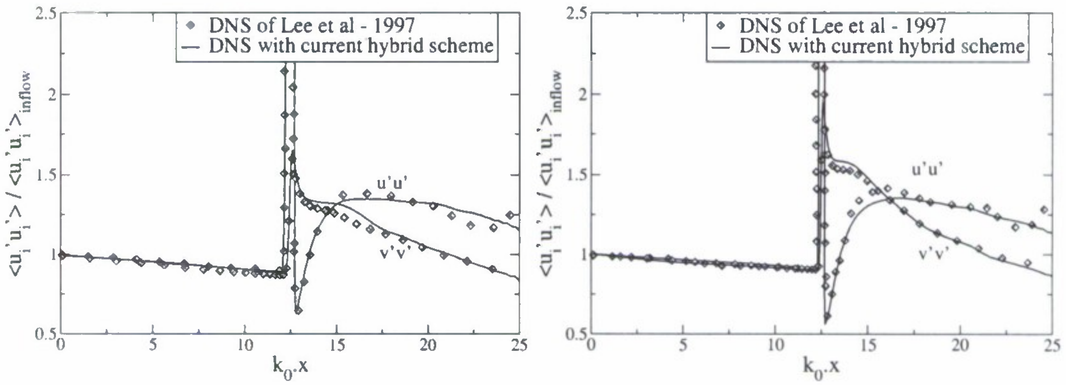

(b) M=2.0

(c) M=3.0

Figure 4.3: Longitudinal and transverse Reynolds stress profile in the direct simulation of the shock / isotropic turbulence interaction problems, with normal Mach numbers of 1.29, 2.0 and 3.0.

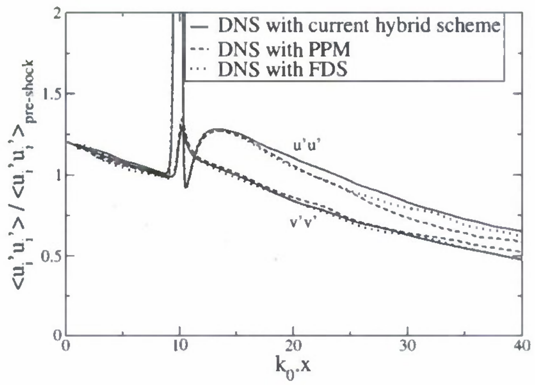

(a) M=1.29

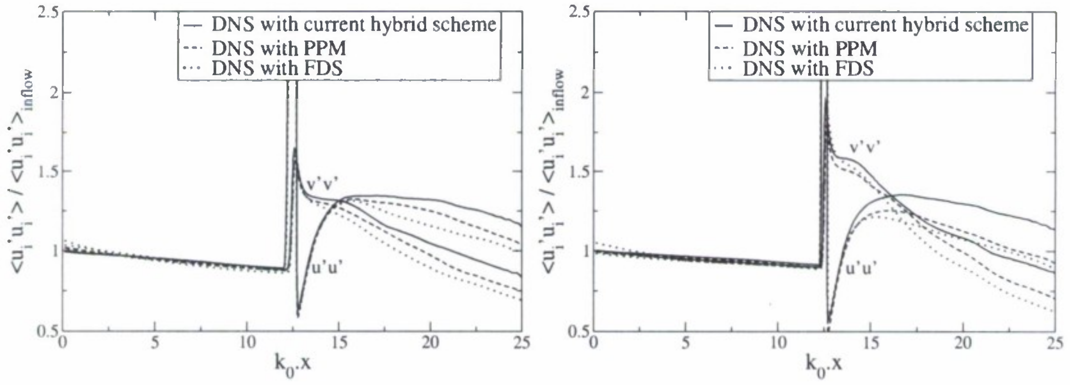

(b) M=2.0

(c) M=3.0

Figure 4.4: Longitudinal and transverse Reynolds stress profile in the direct simulation of the shock / isotropic turbulence interaction problems using the hybrid methodology, the flux-difference splitting and the Piecewise Parabolic Method, for normal Mach numbers of 1.29, 2.0 and 3.0.

for the resolution of the shock / turbulence interaction problems, and showed a good capture of the turbulent statistics. The initial turbulent decay in the pre-shock region is correctly captured by the upwind methods, but the statistics in the post-shock region do not represent the turbulence evolution correctly. The transfer from acoustic to kinetic energies is reproduced for the lowest Mach number, where both upwind methods show a reasonable resolution of the turbulent statistics. For higher Mach number cases, however, the rates of decay are strongly over-predicted. The amplification of the turbulent levels due to the acoustic energy transfer is better predicted using the PPM approach, but the subsequent excessive decays are similar for both upwind methods. As a consequence, the physical behavior of the configurations is not captured correctly, and the upwind methods are found unadapted to the resolution of such problems. The following analysis focuses on the results obtained with the hybrid methodology only.

The flow being homogeneous in the $y-$ and $z-$ directions, a spectral analysis is performed in the *radial* direction. The energy density spectrum of a given variable f at the transverse wavenumber $k_t = \sqrt{{k_y}^2 + {k_z}^2}$ is computed as:

$$E_{f^2}(k_t) = \sum_{k_y,k_z} \frac{1}{2}\hat{f}(k_y,k_z)\hat{f}^{\star}(k_y,k_z) \quad \text{for } \sqrt{{k_y}^2 + {k_z}^2} = k_t^2 \tag{4.6}$$

where $\hat{f}(k_y,k_z)$ is the discrete Fourier transform of the variable f, and $\hat{f}^{\star}(k_y,k_z)$ its conjugate. Figure 4.5 represents the energy spectra for the axial (E_{u^2}) and transverse (E_{v^2,w^2}) velocities, for all three Mach number configurations, at three locations: just before the shock ($k_0x = 8.5$ for $M = 1.29$, $k_0x = 11.5$ for $M = 2.0$ and $M = 3.0$), at the location of minimum longitudinal Reynolds stress behind the shock ($k_0x = 10.5$ and $k_0x = 13$), and at the peak of longitudinal Reynolds stress ($k_0x = 13.5$ and $k_0x = 17$). It is observed in Fig. 4.5(e) that the compression exerted by the shock reduces the fluctuations of axial velocity in the low wavenumbers, but enhances the fluctuations at higher wavenumbers. The amplification of the stress further downstream is known to be the result of evanescent acoustic waves formed by the shock oscillations. Those act mostly on the low wavenumbers. The global budget for the longitudinal fluctuations is an increase in the level of turbulence, more pronounced at high wavenumbers. The spectra for the transverse velocities, shown in Fig. 4.5(f), are globally amplified between $k_0x = 11.5$ and $k_0x = 13$. Further downstream, the transverse fluctuations are reduced at low wavenumbers and amplified at higher wavenumbers. Overall, the amplification is more pronounced at higher wavenumbers. This is in accordance with the findings of previous DNS simulations, where a decrease in most characteristic length-scales of turbulence was observed (Lee et al. [1997]).

The results of these direct numerical simulations are filtered in order to evaluate the driving terms in the evolution of the subgrid turbulent kinetic energy in the context of shock / turbulence interaction. A *coarser* grid is generated: $106 \times 32 \times 32$ grid cells are used to resolve the same computational domains. Following the study of Garnier et al. [2001], the grid spacing in the shock normal direction is refined at the mean shock front to recover the minimum spacing of the DNS study. Fig. 4.6 shows the profile of volume ratios between DNS cells and LES cells for the $M = 2.0$ and

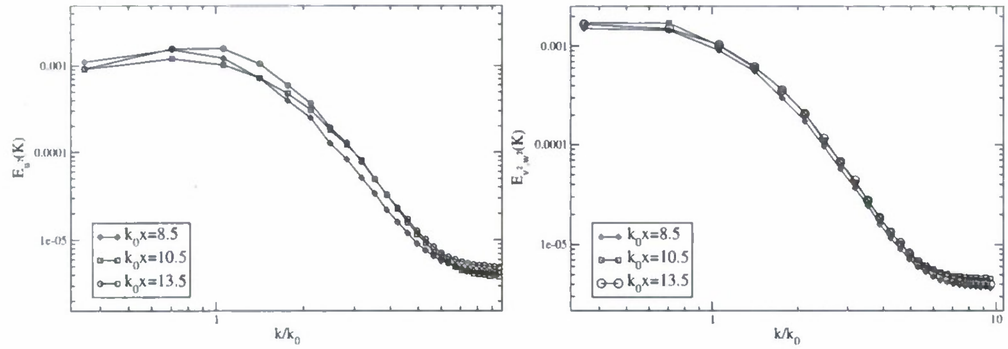

(a) Axial velocity spectrum for $M = 1.29$ (b) Transverse velocity spectrum for $M = 1.29$

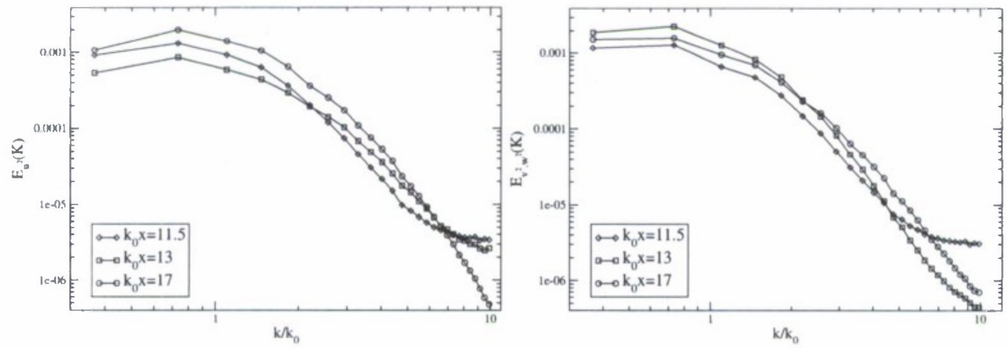

(c) Axial velocity spectrum for $M = 2.0$ (d) Transverse velocity spectrum for $M = 2.0$

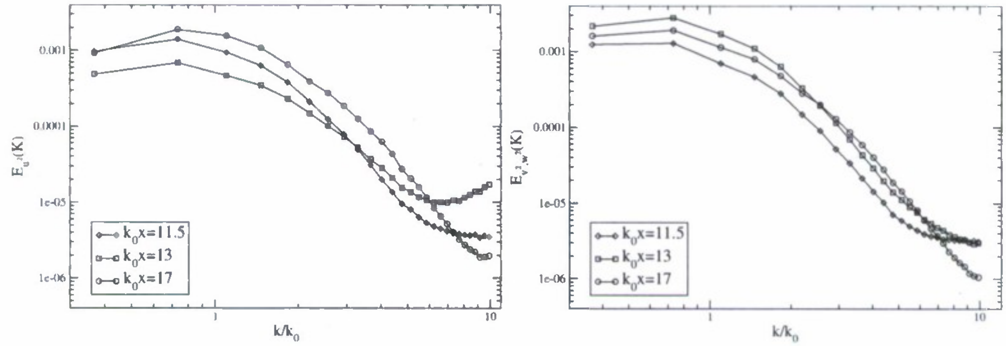

(e) Axial velocity spectrum for $M = 3.0$ (f) Transverse velocity spectrum for $M = 3.0$

Figure 4.5: Velocity spectra for the $M = 1.29$, $M = 2.0$ and $M = 3.0$ shock / isotropic turbulence interaction.

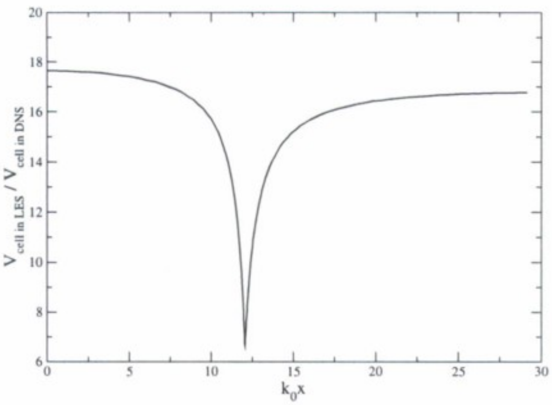

Figure 4.6: Ratios of the grid cell volumes between LES cells and DNS grids for the $M = 2.0$ and $M = 3.0$ shock / isotropic turbulence cases.

$M = 3.0$ cases. The coarsening results in volume ratios greater than 16 everywhere but in the shock region, where it is decreased to around 6.5. Fields from the direct simulation are filtered onto the LES grid using a top-hat filter.

A statistical average of the filtered field (taken over 40 instantaneous realizations) is obtained and used to study the behavior of the closure model for this configuration. Also, the dynamic Smagorinsky model (DSM) is analyzed during this $a - priori$ study. The DSM closure has been found to perform well in many fundamental studies of turbulence. In particular, this closure was found by Garnier et al. [2002] to reproduce the physics of the shock / turbulence interaction in LES studies. It is used in the present fundamental study for comparison purpose, but it should noted that the application of the DSM for practical flows is rather limited, as the formulation is ill-posed, and requires an averaging of the closure coefficient, over homogeneous directions or in a Lagrangian sense, in order to yield stable resolution.

As noted by Dubois et al. [2002], a high correlation between exact and modeled turbulent features in *a priori* studies does not necessarily imply superior performance by the model in *a posteriori* studies, but rather shows that the model is able to mimic some of the physical features of the turbulent flow. Typical profiles of the correlation coefficient for the subgrid stresses using the LDKM and the DSM closure approaches are shown in Fig. 4.7 for the different shock / turbulence interaction cases. The DSM approach is known to have poor correlations in $a - priori$ studies of turbulence, and also observed in Fig. 4.7. The *a priori* behavior of the LDKM for the subgrid stress shows a good correlation with the exact stress. Furthermore, the production of k^{sgs} using LDKM has a correlation coefficient above 0.8 almost everywhere.

The main terms of the exact governing equation for the subgrid turbulent kinetic energy are computed from the filtered DNS field, and their profiles are represented in Fig. 4.8. The convection of k^{sgs} is balanced everywhere by the production and the dissipation, except in the post-shock region close to the shock front. Very close to the shock front the pressure dilatation correlation plays a role in re-distributing the thermal energy into fluctuating energy. This region is localized, adjacent to the

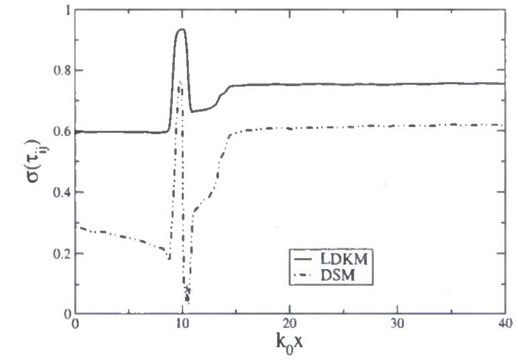

(a) $M = 1.29$

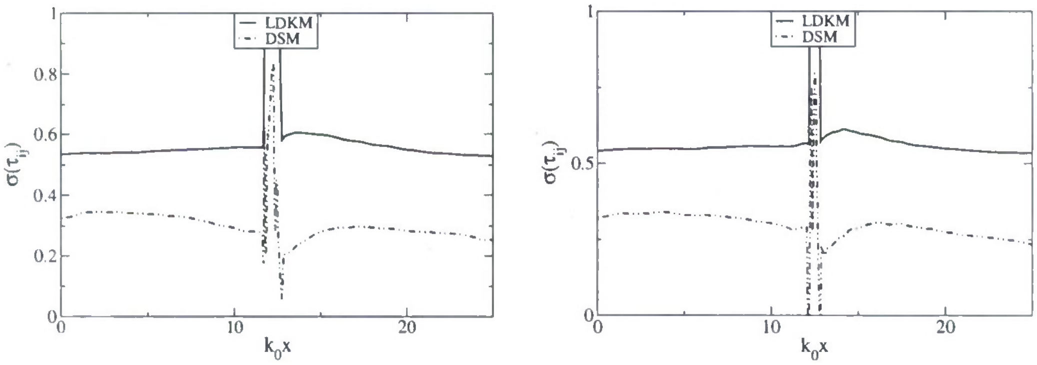

(b) $M = 2.0$

(c) $M = 3.0$

Figure 4.7: $a - priori$ correlation coefficients profiles for the subgrid stresses with LDKM and DSM models of the $M = 1.29$, $M = 2.0$ and $M = 3.0$ shock / isotropic turbulence interaction cases.

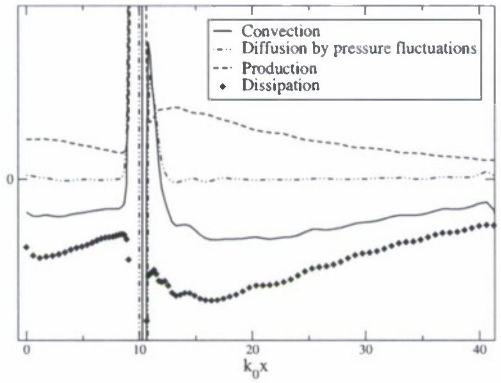

(a) $M = 1.29$

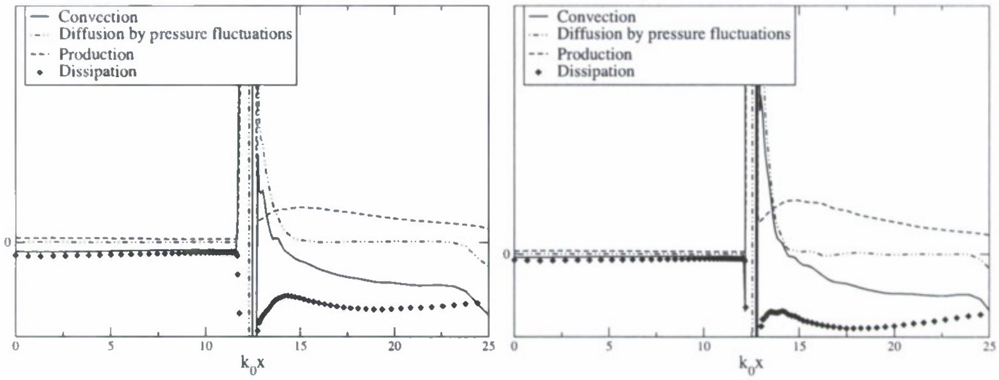

(b) $M = 2.0$ (c) $M = 3.0$

Figure 4.8: Profiles of the k^{sgs} budget in $M = 1.29$ and $M = 3.0$ shock / isotropic turbulence interactions

shock average location, and its overall impact is small compared to the diffusion of k^{sgs} due to pressure fluctuations, which plays a more important role over a broad region. This latter term is often neglected in the modeling of the governing equation for the subgrid kinetic energy and is explicitly modeled in the LDKM formulation given in Chap. 2. Furthermore, the turbulent Prandtl number, the closure coefficient for the diffusion due to subgrid pressure fluctuations, is computed dynamically, as shown in Sec. 2. The other terms in the governing equation for k^{sgs} that arise from compressibility effects, the pressure-dilatation correlation and the compressible turbulence, were found negligibly small for these cases, and are thus neglected in the current modeling approach.

4.3 LES of Shock / Isotropic Turbulence Interaction

The three cases of shock / turbulence interaction studied by direct simulations are repeated in the context of LES. The resolutions and grids for these studies are identical to that used in the $a-priori$ analysis described above. Three different modeling approaches have been tested: $under-resolved$ simulations are performed first, that is, simulations without any closure model. Next the LDKM closure model presented earlier is employed. Finally, the dynamic Smagorinsky model (DSM) is used. The implementation followed the formulation given in Moin et al. [1991]. A dynamic evaluation of Pr_t is used along with that model as well, with an averaging procedure over the homogeneous directions of the computation to maintain stability. However, the LDKM model does not require any averaging in all the reported results. A filtered instantaneous field from the DNS simulation is used to provide the initial condition for the LES simulations. Also, the field of isotropic turbulence used at the inflow plane is filtered onto a grid of uniform spacings. The problem is simulated for one flow through time, and statistics are collected for another two flow through times.

Figures 4.9(a), 4.9(c) and 4.9(e) represent the Reynolds stresses in the shock-normal direction for the three LES, along with the results from the filtered DNS data. The under-resolved simulations do not capture the rate of decay of the resolved turbulent energy in the pre-shock region, and lead to an over-estimation of the level of turbulence in the post-shock region. The closure of the subgrid terms should mimic the energy dissipation that occurs in the high wavenumbers of the energy spectrum. In the absence of subgrid scale models, the only source of extra dissipation can be the numerical dissipation. In these LES computations, about 5% of the axial fluxes and 3% of the transverse fluxes are evaluated using the dissipative scheme. Those interfaces are localized within the mean shock thickness. Thus, it appears that the current solver's numerical dissipation has only a minimal effect on the turbulent decay in the pre- and post- shock regions. This is an important requirement for a LES solver to demonstrate without any subgrid model.

The peaks of normal Reynolds stresses are recovered by the under-resolved DNS simulations presented for $M = 1.29$ and $M = 2.0$, but not for $M = 3.0$. The location for this peak in the highest Mach number case is captured, but the amplitude is

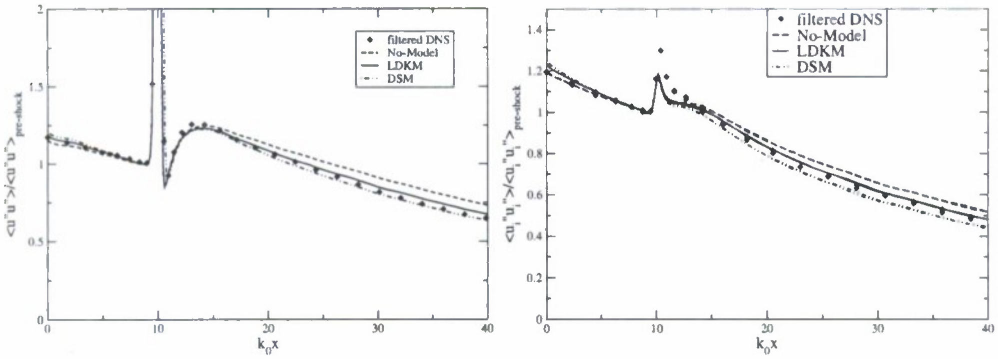

(a) Axial Reynolds stress profile, $M = 1.29$

(b) Transverse Reynolds stress profile, $M = 1.29$

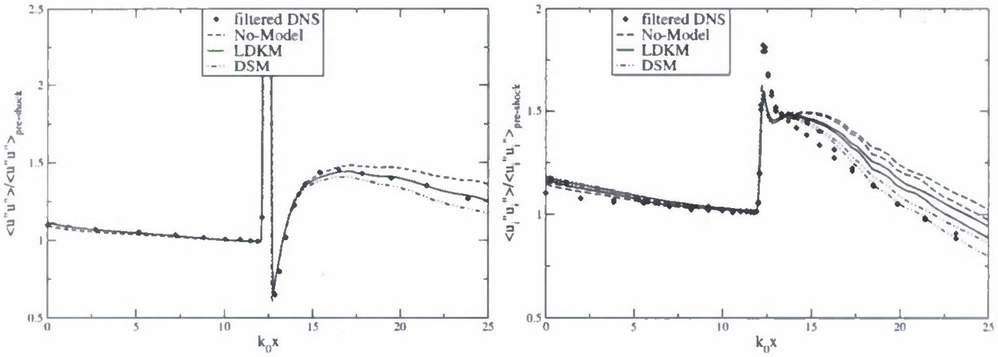

(c) Axial Reynolds stress profile, $M = 2.0$

(d) Transverse Reynolds stress profile, $M = 2.0$

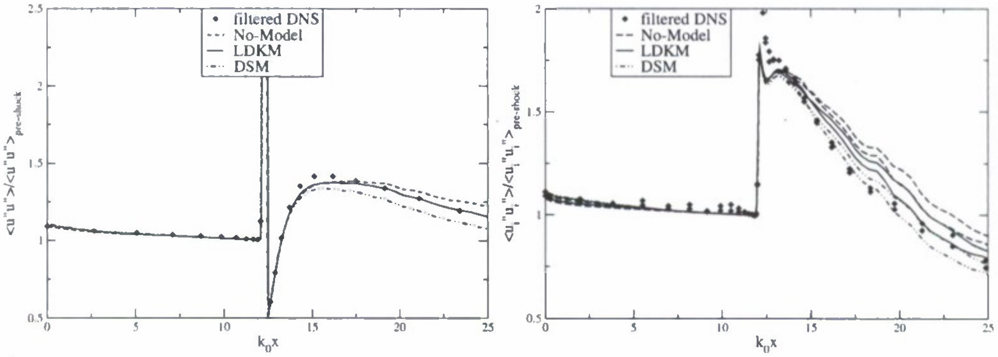

(e) Axial Reynolds stress profile, $M = 3.0$

(f) Transverse Reynolds stress profile, $M = 3.0$

Figure 4.9: Profiles of Reynolds stresses from the LES calculations, and comparisons with the filtered DNS fields, for the $M = 1.29$, $M = 2.0$ and $M = 3.0$ shock / isotropic turbulence cases.

under-predicted. This is attributed to the grid coarsening, and the subsequent *loss of corrugation*, already observed by Garnier et al. [2002]. This effect is more pronounced at higher Mach numbers, as the induced corrugation is reduced.

The closure models mimic the influence of the small, unresolved scales onto the resolved field, and this leads to a better capture of the resolved turbulent decay in both the pre- and post- shock regions. Figures 4.9(a), 4.9(c) and 4.9(e) show that both closure approaches perform well in the pre-shock regions, reproducing the pre-shock turbulent decay. In the post-shock regions, the peak of axial stresses is under-estimated by both methods. The LDKM closure however shows a better recovery of the turbulent fluctuations in that region, with a reduced dissipation compared to the DSM closure. Further downstream, it is noted that, independently of the absolute levels of turbulence, both closures give the right rate of decay of turbulence. The transverse fluxes are represented in Fig. 4.9(b), 4.9(d) and 4.9(f). Again, the under-resolved simulation does not capture the decay of resolved turbulence. The amplitudes in the post-shock regions are better simulated by the DSM approach for those quantities. However, both the LDKM and the DSM simulations show comparable results for the decay rates, which are correctly captured for all three cases. The energy spectra are computed from the LES field before the interaction ($k_0x = 8.5$ for $M = 1.29$, $k_0x = 11.5$ for the two other Mach numbers) and at the peak of Reynolds stresses in the post-shock region ($k_0x = 13.5$ and $k_0x = 17$). These spectra are shown in Fig. 4.10, along with the spectra computed from the filtered DNS fields. The physical processes are well captured by the LES simulations. The axial velocity fluctuations spectral distribution is significantly changed even at the smallest Mach number, and the small wavenumbers are reduced whereas the larger wavenumber fluctuations are amplified through the interaction. The transverse velocity fluctuations are amplified for the higher Mach number cases, and the amplification is uniform over the span of wavenumbers. The LES simulations show a slight over-prediction of the transverse velocity fluctuations at the small scales. This leads to an overestimation of the level of transverse fluctuations in the post-shock region, but does not affect the capture of the turbulent decay that follows.

Within the LDKM formulation, the closure coefficients are computed dynamically based on the resolved fields, and vary significantly in both space and time during the course of the simulations. The statistical averages profiles of c_ν and Pr_t are presented in Fig. 4.11 for the lowest and highest Mach numbers simulated here. The closure coefficient for the subgrid stresses varies spatially, and increases as the grid is clustered close to the mean shock locations to account for the reduced grid size. Consequently, the eddy viscosity decreases continuously as the flow approaches the shock. Downstream of the interaction, the subgrid stress coefficients vary spatially following the turbulence amplification and reach a constant value further downstream, as the turbulence reaches a state of homogeneity dominated by the turbulent decay. A slight decrease in the average value for c_ν is found as the mean Mach number is increased.

Similar to the behavior of c_ν, Pr_t decreases as the grid is refined close to the mean shock location, and reaches a stationary state downstream of the interaction. The values of this closure coefficients do not change significantly in the lowest Mach

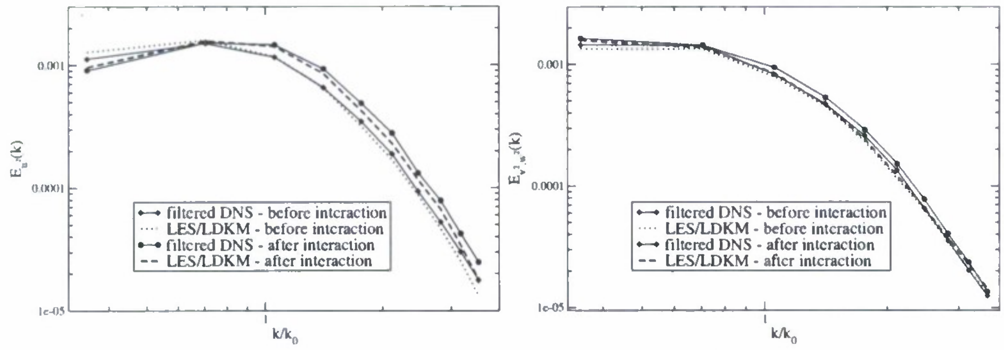

(a) Axial velocity spectrum (b) Transverse velocity spectrum

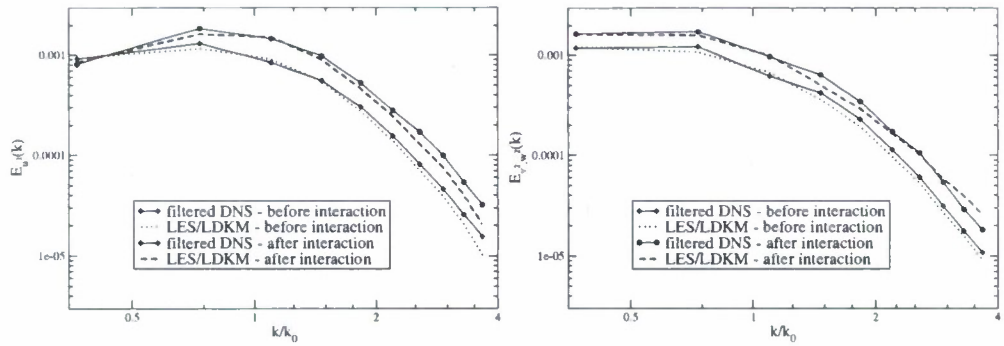

(c) Axial velocity spectrum (d) Transverse velocity spectrum

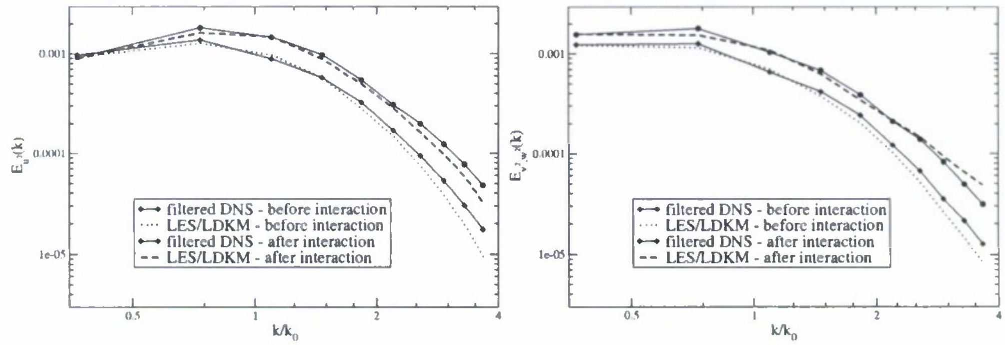

(e) Axial velocity spectrum (f) Transverse velocity spectrum

Figure 4.10: Velocity spectra of the filtered DNS field and of the LES field for the $M = 1.29$, $M = 2.0$ and $M = 3.0$ shock / isotropic turbulence cases.

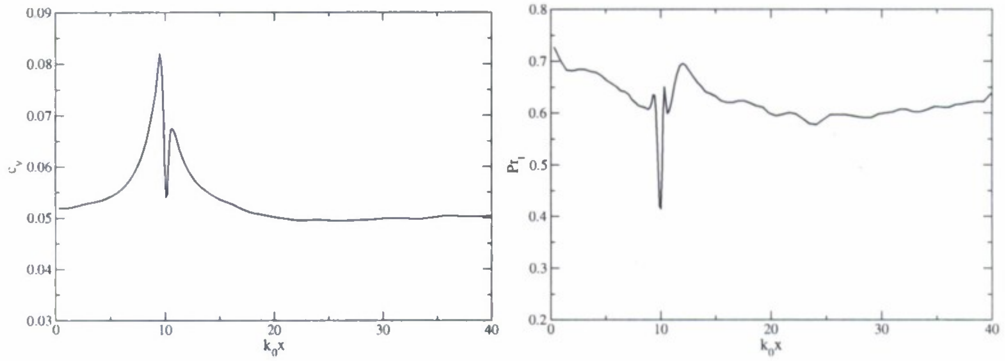

(a) c_ν for $M = 1.29$ (b) Pr_t for $M = 1.29$

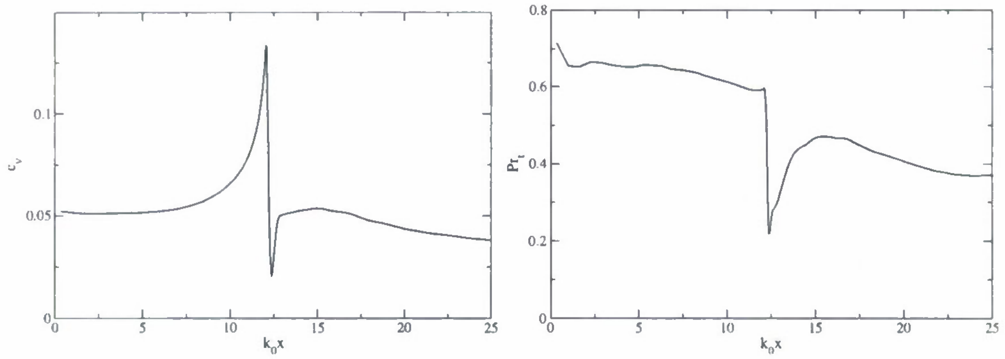

(c) c_ν for $M = 2.0$ (d) Pr_t for $M = 2.0$

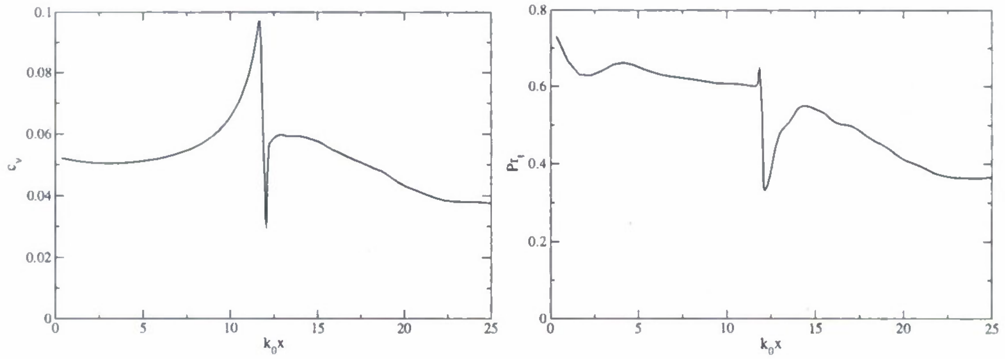

(e) c_ν for $M = 3.0$ (f) Pr_t for $M = 3.0$

Figure 4.11: Profiles of the closure coefficients c_ν and Pr_t for the shock / isotropic turbulence interaction for the $M = 1.29$ case (left), $M = 2.0$ case (center) and $M = 3.0$ case (right).

number case, but a stronger reduction in Pr_t is obtained for $M = 2.0$ and $M = 3.0$. Pr_t is close to 0.7 in all cases before the shock, and decreases to 0.4 in the region of homogeneous turbulence for the higher Mach number cases, leading to an enhanced diffusion of the energy. This effect is particularly important for the higher Mach number cases as the levels of temperature fluctuations are increased through the interaction with the stronger shock waves.

These conditions were found to be satisfied in more than 95% of the computational cells away from the shocks. Within the shock region, the fulfillment of these conditions dropped to 75%. Even when these realizability conditions were violated, the difference between the computed subgrid stress closure coefficient and the highest admissible value for c_ν remained small.

This fundamental study of shock / turbulence interaction has showed that the numerical scheme developed for the resolution of turbulence in supersonic fields permits the capture of both turbulent fields and discontinuity within one scheme, with minimal dissipation. Furthermore, the LDKM closure model is found to be well adapted to the modeling of the turbulent field in such configurations, showing a good reproduction of the turbulent statistics evolution across the interaction.

4.4 LES of Shock / Turbulent Shear Layer Interaction

The interaction of a shock with a shear layer is a very common flow feature in supersonic flows. Sonic and supersonic jets give rise to a complex cellular structure, where shocks and expansions interact with the turbulent outer shear layer. Shock waves are inherently present in scramjet intakes and combustors, and interact with the shear layers formed from the injection systems. Occurrence of shock waves in supersonic combustors induces pressure losses that cannot be avoided. However, the impact of shock interactions with mixing regions is of considerable importance and needs to be understood.Past studies show that mixing is significantly reduced in free shears as the convective Mach number is increased. This consideration led Drummond and Mukunda [1989] to study the gain in mixing and combustion efficiency obtained by simulating a dual shock interaction with a reacting free shear layer, but observed moderate improvements only. This configuration was later considered analytically by Buttsworth [1996] who estimated the vorticity gain through the interaction to be only about 16%. The original study of Drummond and Mukunda [1989] was a two-dimensional simulation, and the shocks impacted the shear layer before it had developed a fully unstable and self-similar state. Also, the analytical method treated the flow in the laminar limit, so that the turbulence amplification that occurs during the interaction was not included. This configuration is revisited in the present three-dimensional LES study, with a particular focus on the turbulence evolution during and after interaction with the shock waves.

The geometry and flow conditions for the present configuration are hereafter described and represented in Fig. 4.12. A primary grid of $250 \times 80 \times 40$ cells is used to discretize the domain of 17 $cm \times 10$ $cm \times 3$ cm. The grid is clustered towards

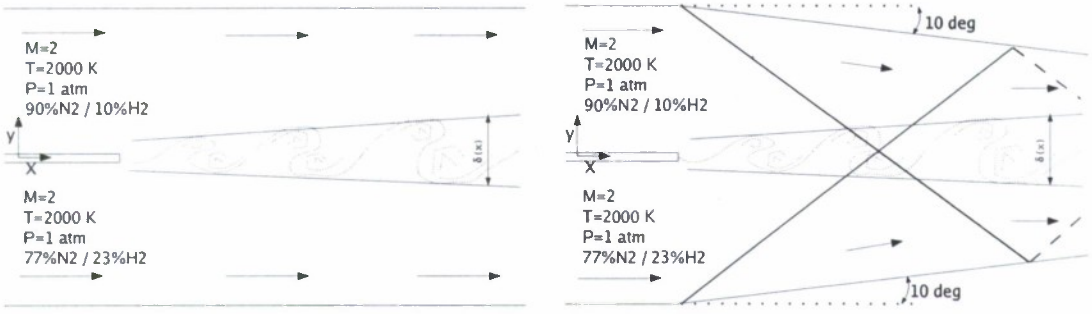

(a) Configuration of the base mixing layer

(b) Configuration of the shocked mixing layer

Figure 4.12: Schematic of the base Mixing layer configuration.

the centerline, to provide a proper resolution of the mixing layer, with a minimum spacing in the vertical direction of 0.1 mm, following the spatial resolution reported in the numerical simulation of Drummond and Mukunda [1989]. A refined simulation is performed to assess the accuracy of the coarser resolution. This secondary grid has a resolution of 400 × 140 × 60 cells, reaching a minimum spacing of 0.04 mm at the centerline.

The upper stream (hereafter denoted with a subscript u) is a mixture of N_2/H_2, with 10% hydrogen in mass, a static temperature of $2000K$ and a static pressure of 1 atm, flowing at Mach 2.0 (that is, a velocity of 2672 m/s with the thermally perfect gas EOS employed for this simulation). The lower stream (hereafter denoted with a subscript l) is an airflow with static temperature and pressure set to match that of the upper stream. The Mach number is also set to 2.0, which corresponds to a velocity of 1729 m/s. The convective velocity for this flow is about $U_c = 2100\ m/s$. The mean velocity profile at the inflow of the domain is given by a hyperbolic tangent:

$$\bar{U}(y) = \frac{U_u + U_l}{2} + \frac{U_u - U_l}{2} \tanh\left(2\frac{y}{\delta_\omega^0}\right), \qquad \bar{V}(y) = \bar{W}(y) = 0 \tag{4.7}$$

where δ_ω^0 is the initial vorticity thickness for the profile, here set to $\delta_\omega^0 = 0.4\ mm$. The temperature profile at the inflow is set as a function of the imposed velocity profile following the Crocco-Busemann relation (Vreman [1997], Doris et al. [2000]).

$$\begin{aligned} T(y) &= \tfrac{1}{2C_p}\left(U(y)^2 - U_u U_l + U(y)(U_u + U_l)\right) \\ &\quad + (T_u - T_l)\tfrac{U(y)}{U_u - U_l} + \tfrac{T_l U_u - T_u U_l}{U_u - U_l} \end{aligned} \tag{4.8}$$

The convective Mach number for the flow under consideration is $M_c = 0.43$, which makes it moderately compressible, with turbulent structures that still resemble those of the incompressible mixing layer.

In order to trigger transition, a velocity perturbation is added to this mean profile (Fortuné et al. [2004], Fu and Li [2006]). The fluctuating velocity field has an energy spectrum that follows eqn 4.3. The most energetic wavelength for this spectrum is chosen such that $\kappa_0 \delta_\omega^0 = 2$, and the amplitude of the fluctuations is such that u_{rms} represents 4% of the convective velocity for the current problem. The forcing described above is applied in the region of the mixing layer only, according to:

$$U(x=0,y,z,t) = \bar{U}(y) + u'(x=-U_c t, y, z) exp\left(-\left(\frac{y}{\delta_\omega^0}\right)^2\right) \tag{4.9}$$

The top and bottom boundaries are treated as subsonic outflows for the reference un-shocked mixing layer. For the shocked mixing layer, shocks corresponding to a 10° turning angle are imposed numerically by setting appropriate inflow conditions to the upper and lower boundaries. The right boundary is a supersonic outflow, and periodicity is imposed in the spanwise direction. After allowing five flow-through-times of initial simulation, statistics are collected for another five flow-through-times.

The incompressible mixing length growth rate is often given by the spatial-growth model of Dimotakis Dimotakis [1986]:

$$\delta' \approx c_\delta \frac{(1-r)}{1+r\sqrt{s}} \left(1 + \sqrt{s} - \frac{1-\sqrt{s}}{1+2.9(1+r)/(1-r)}\right) \tag{4.10}$$

where ϵ is a constant independent of the velocity ratio ($r = U_u/U_l$) and of the density ratio ($s = \rho_u/\rho_l$), with $c_\delta \approx 0.36$ Slessor et al. [2000] (although empirical correlations and curve-fits suggest $0.25 < c_\delta < 0.45$). This coefficient diminishes as the compressibility within the mixing layer increases. A mixing layer compressibility is often quantified solely based on the convective Mach number (Papamoschou and Roshko [1988]), though some modified parameters have been suggested (Π_c in Slessor et al. [2000] is a modification to M_c for varying γ flows). Goebel and Dutton Goebel and Dutton [1991] studied a $M_c = 0.453$ mixing layer, and the growth rate parameter was estimated to be $c_\delta = 0.21$ (Slessor et al. [2000]). In the present simulation, where $r = 0.647$, $s = 2.370$ and the convective Mach number is $M_c = 0.43$, the mixing growth rate is found to follow $\delta' = 0.228 c_\delta$, and the value for the coefficient found from the vorticity thickness evolution $c_{\delta,\omega} = 0.206$, which closely matches the experimental value.

The turning angle imposed at the top and bottom boundaries induce shocks with very similar properties (shock angles, pressure ratios across the shocks, density ratios across the shocks, etc...). They intersect on the centerline at an axial location of $X = 6.2\ cm$. The velocities in the post-shock region are then found to be essentially horizontal, $U = 2030\ m/s$, $M = 1.35$ in the upper stream, and $U = 1310\ m/s$, $M = 1.35$ in the lower stream. The velocity and density ratios across the mixing layer are almost unchanged ($r = 0.645$, $s = 2.40$). The post-shock convective Mach number is $M_{c,ps} = 0.29$.

In the early stage, the development of the mixing layer differs between coarse and fine resolutions simulations, but stabilizes within a few centimeters from the inflow. The flow evolution and turbulent statistics obtained from the coarser grid simulations were found to match closely those obtained with the refined grid. All results given hereafter are based on the coarser grid simulation.

Figure 4.13 shows a top view of the iso-surfaces of the $Q-$criterion for the base mixing layer and its shocked counter-part. This variable is defined as the second invariant of the velocity gradient tensor and is well-suited to vortical fields identification (Dubief and Delcayre [2000]). Those snapshots are taken at the same physical time, after 10 flow-trough-times have elapsed. The forcing imposed on the mean profile at the inflow of the spatial simulation leads to a fast transition to turbulence. The spanwise vortices develop early, and the ribs structures connecting the different rollers show the three-dimensionality of the configuration. The vortical structures that pass through the shocks are being compressed, and the post-shock structures resemble more two-dimensional rollers than the un-shocked mixing layer structures. Later downstream, those structures re-develop a strong three-dimensionality. The fast growth of the structures after the interaction affects the mixing layer growth rate. The thickness based on the 90%-H_2 mass fraction is shown in Fig. 4.14(a) for the reference mixing layer along with that of the shocked shear layer. A reduction of the thickness is observed as the shocks interact with the mixing region. This evolution is due to the spatial compression of the mixing region by the two shocks, and is not related a reduction in mixing efficiency. On the contrary, the growth rate of the shocked layer is significantly increased right after the interaction. This observation is confirmed by the profile of mass entrained by the mixing layer, showed in 4.14(b). In this figure, the results of both resolution studies are represented, showing the essentially grid-independent flow evolution after the interaction. The rate of momentum exchange between the two layers is significantly increased due to the shock / shear interaction. Within 6 *cm* from the location of the interaction, the growth rate steadies out at the level of the undisturbed mixing layer growth for that convective Mach

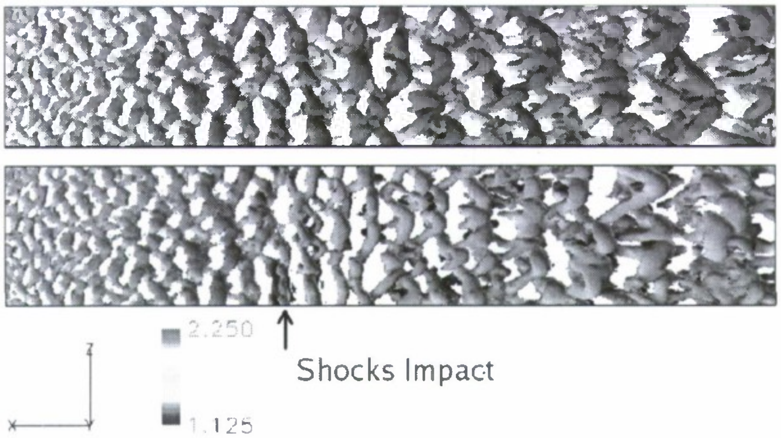

Figure 4.13: Iso-surface of the Q-criterion ($Q = 10^9 s^{-2}$) for the base mixing layer (top) and the shocked mixing layer (bottom), colored by the local Mach number – flow is from left to right.

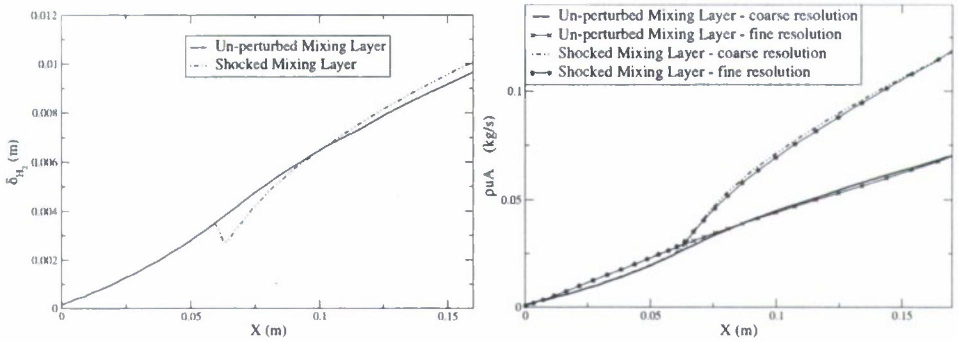

(a) Mixing layer thickness

(b) Mass entrainment in the mixing layer

Figure 4.14: Mixing Layers growth rate based on a 90% H_2 mass fraction, and mass entrainment within the mixing layer thickness.

number. It should be noted that this growth rate is 6% higher than its unshocked counter-part, as the decrease in convective Mach number associated with the shocks leads to a reduction in compressibility effects. The forcing imposed on the velocity and temperature profiles at the inflow of the simulation enhance the transition to a fully turbulent shear layer. Statistically averaged velocity correlation have been collected at several downstream locations along the domain. Figures 4.15(a) and 4.15(d) show the normalized statistics of u_{rms} and $< u'v' >$ respectively, showing that self-similarity is reached from $x = 8$ *cm* on. The normalized profiles of v_{rms} and w_{rms} show some small variations with downstream locations, essentially recovering the self-similar state.

The shocks impact increases the relative levels of turbulence in the shear layer. Figure 4.16 shows the profiles of turbulent velocity correlations downstream of the interaction. The axial and cross-wise autocorrelations are amplified by the shocks close to the point of interaction. Figures 4.16(a) and 4.16(c) show that their relaxation to the undisturbed, self-similar states is achieved over a very short distance, less than 3 *cm*. A more significant increase in the level of turbulence is observed for the transverse velocity fluctuations. This gain persists over a larger distance, and relaxes to the stable level 7 *cm* downstream of the point of interaction. The Reynolds stress $< u'v' >$ also shows this trend: largely amplified by the waves, it relaxes to its undisturbed level within a distance from the interaction that is greater than that for u_{rms}. The turbulence evolution in the shock / shear interaction is found to be mostly affected by two competing phenomena. The initial amplification of the turbulent levels is similar to the shock / isotropic turbulence interaction studied earlier. The turbulent eddies corrugate the shock fronts, and generate local compressions and/or expansions. Furthermore, the large scale coherent structures of the shear layer contribute to the shock oscillations. The shock corrugation and its motion lead to the

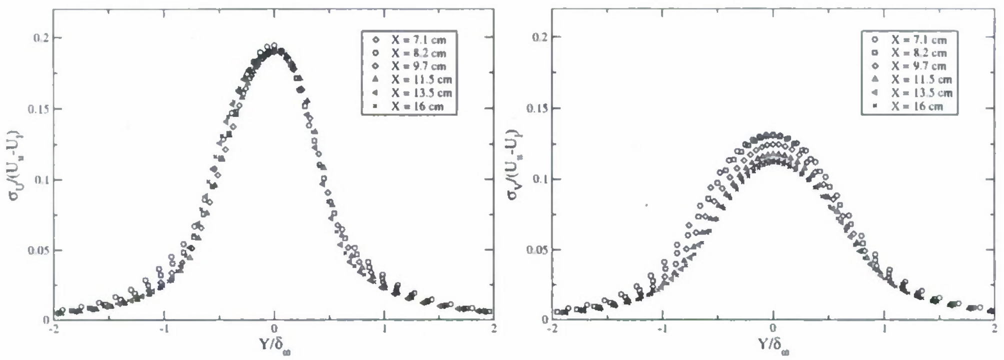

(a) $u_{rms}/\Delta U$ (b) $v_{rms}/\Delta U$

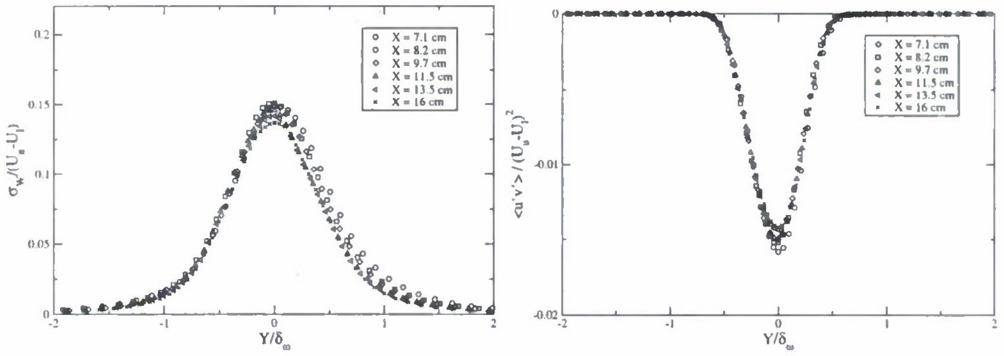

(c) $w_{rms}/\Delta U$ (d) $< u'v' > /(\Delta U)^2$

Figure 4.15: Normalized profiles of turbulent statistics (u_{rms} and $< u'v' >$) at several locations along the reference mixing layer.

formation of local acoustic waves, and evanescent pressure waves transfer the acoustic energy into kinetic energy. The motions of the two shocks, while traversing the mixing layer, are to a large extent dictated by the large scales of the flow, and are then out of phase. As a consequence, the levels of v_{rms} and $< u'v' >$ are particularly increased by the interaction.

The level of vorticity is increased by the compression of the mixing layer. A laminar calculation for this case showed a 25% increase in vorticity across the shocks, in relatively good agreement with the analytical predictions of Buttsworth Buttsworth [1996], where a 16% increase was predicted. The three-dimensional turbulent calculation shows only a 11% gain in mean vorticity. The presence of turbulence and large-scale coherent structures does not modify the overall vorticity budget significantly for the interaction. Despite the gain in vorticity, the fast growth of the mixing layer decreases the mean rate of strain across the mixing layer and consequently reduces the mean production of turbulence across the mixing layer. The high levels

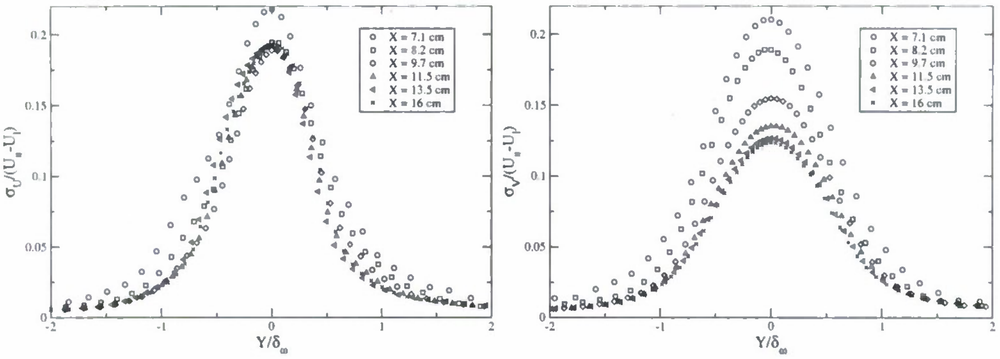

(a) $u_{rms}/\Delta U$ (b) $v_{rms}/\Delta U$

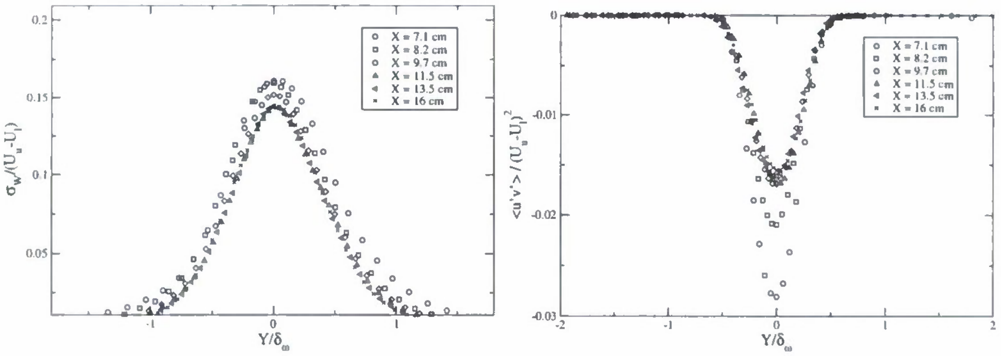

(c) $w_{rms}/\Delta U$ (d) $< u'v' > /(\Delta U)^2$

Figure 4.16: Normalized profiles of turbulent statistics (u_{rms}, v_{rms}, w_{rms} and $< u'v' >$) at several locations along the shocked mixing layer.

of fluctuations are not maintained by the external flow. The normalized turbulent statistics, $v_{rms}/\Delta U$ and $u'v'/\Delta U^2$ shown in Fig. 4.16(b) and 4.16(d), relax to the self-similar profiles. The reduced convective Mach number leads to higher values of the turbulent correlations once stationary state is reached, compared to the un-shocked case. The compressibility effects are significantly reduced, and the statistics across the layer show a behavior close to incompressible mixing layers.

Overall, the mixing improvement obtained from the shock / shear interaction is localized, but high. Furthermore, the increase in static temperature associated with this method can be beneficial to the combustion efficiency as well. Pressure losses are however induced by the shocks, and their interaction with the shear layer. The stagnation pressure is easily obtained in this thermally perfect gas flow by integration of the isentropic condition:

$$dS = -R\frac{dP}{P} + c_P\frac{dT}{T} = 0 \tag{4.11}$$

between static and stagnation temperatures and pressures. It is found that the interaction between the shocks and the mixing layer has a very little contribution to these losses. A 2.5% total pressure loss is induced by the two shocks, in the free-streams, as seen in Fig. 4.17. The amplification of the losses through the interaction is very small compared to the losses solely due to the shocks alone.

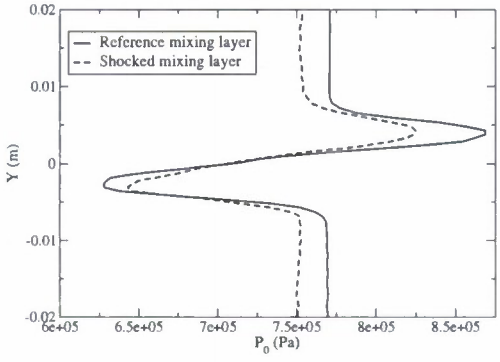

Figure 4.17: Profiles of total pressure before the outflow.

The statistically averaged model coefficients profiles across the mixing layers for the reference and shocked mixing layers are presented in Fig. 4.18 and 4.19 respectively. They exhibit a self-similar-like behavior. The closure coefficient for the subgrid stresses peaks at the mixing layer centerline and decreases towards the edges, consistent with the peaks of Reynolds stresses at the centerline observed in Fig. 4.15(a) and 4.15(d). The coefficient for the subgrid dissipation peaks at the edges of the mixing layer, where the value of k^{sgs} is smaller. The turbulent Prandtl number profiles follow the trends of the subgrid stress closure coefficient, peaking at the centerline, and decreasing towards the edges. The turbulent diffusion of energy at the centerline is associated with the coherent vortices of the mixing layer, and the subgrid contribution is found relatively weak, with a higher Pr_t. Closer to the edges of the layer, the subgrid contribution to the energy budget is more important, as the turbulent Prandtl number decreases significantly.

The interaction with the shock wave induces a scattering of the closure coefficients at the edges of the mixing layer, where the turbulent motions are lesser. Within the layer thickness however, their behavior is not strongly modified, showing essentially the same variations and the same amplitude as in the reference mixing layer case. In these computations again, the realizability constraints were found satisfied in more than 95% of the computational cells away from the shocks. Within the shock region, the fulfillment of these conditions dropped to about 80%.

The present study has showed that the shock / shear layer interaction leads to a turbulent amplification in the post-shock region, which can significantly enhance the mixing rate and/or the combustion efficiency. The gain in mean vorticity due to the interaction is found to follow the analytical prediction (Buttsworth [1996]) to a good extent, despite its limitation to laminar flows with mean shear. The coherent structures and turbulent fluctuations strongly affect the growth of the layer, but have

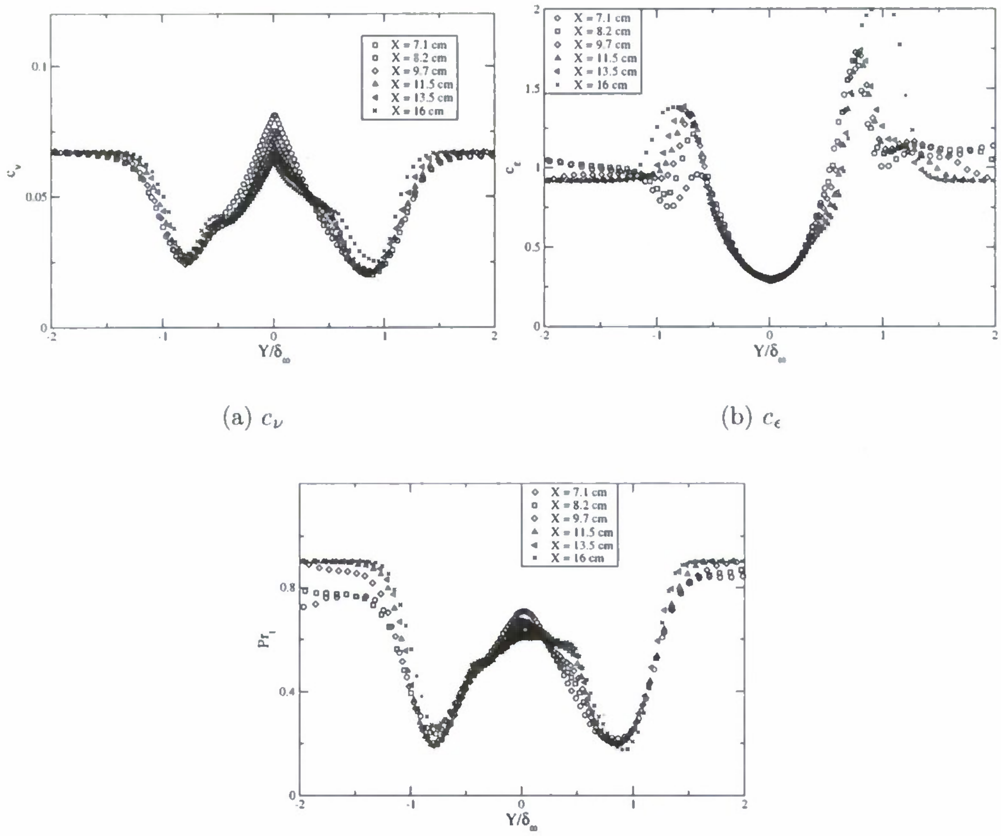

(a) c_ν

(b) c_ϵ

(c) Pr_t

Figure 4.18: Profiles of the LDKM closure coefficients for the reference mixing layer.

a limited influence on the average vorticity. The evolution of the turbulent shear layer downstream of the interaction is dictated by a relaxation process to the self-similar state of the *new* mixing layer. In particular, the reduction in velocity difference across the layer leads to a reduced mean production, and the levels of turbulence decrease with downstream location.

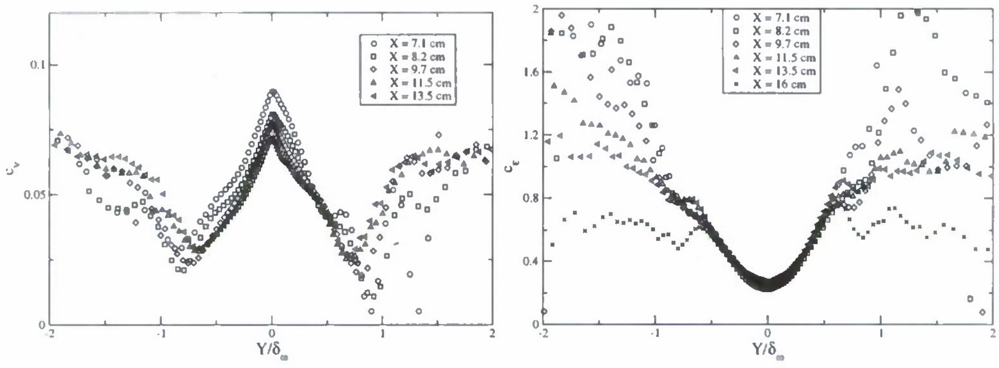

(a) c_ν (b) c_ϵ

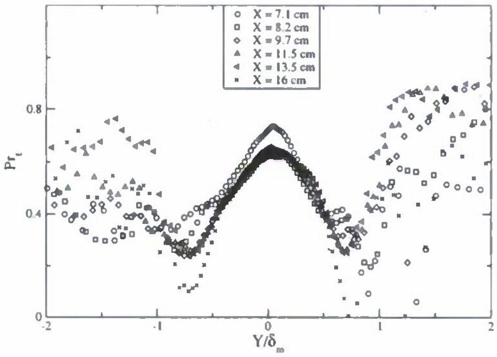

(c) Pr_t

Figure 4.19: Profiles of the LDKM closure coefficients for the shocked mixing layer.

CHAPTER V

SONIC JET IN SUPERSONIC CROSS-FLOW

A fast and efficient mixing of fuel and oxidizer is a requirement in most operational non-premixed combustion systems. This is of primary importance, and one of the biggest design challenges, especially in supersonic combustion systems, where the residence in the combustion chamber is very short. To achieve this goal, a good penetration of the fuel into the free-stream and high levels of mixing are required. Furthermore, in order to sustain and stabilize a flame, efficient re-circulation of hot products is needed to anchor and to continuously initiate the reaction in the mixed fluids. Several injector designs have been studied experimentally that generate high levels of mixing, sustain the flame, and minimize pressure losses throughout the process. Cavity-based (Gruber et al. [1999]) or strut-based (Waidmann et al. [1995]) injections, swept ramp injectors (Gruber et al. [2000]) and wall-normal injection (Ben-Yakar and Hanson [1998]) are some of the well studied designs.

Probably the simplest among all the injection designs, the jet in cross-flow (JICF) is an efficient method for supersonic mixing of fuel and oxidizer and for supersonic combustion, as it allies all the properties required in an efficient injector. A schematic of the JICF shown in Fig. 5.1 highlights some of the features observed during the interaction (Gruber et al. [1996], Dickmann and Lu [2006]). A blockage of the free-stream flow is induced by the transverse momentum of the jet, and a bow shock is formed ahead of it. Under the influence of the shock, the incoming turbulent boundary layer separates, and the thickening of the boundary layer in the near-jet region creates a $\lambda-$shock pattern, and leads to the separation of the incoming layer and the formation of a re-circulation region. In reacting flows, these regions can trap hot radicals and products, hence anchoring the flame. The under-expanded jet expands suddenly as it penetrates into the low pressure cross-stream and a high-speed shear layer is formed between the ambient air and the jet. Furthermore, as the expansion fan generated at the edges of the injector interacts with the shear layers, the boundaries of the jet are deflected inwards, and compression waves from these shear layers deflection form the barrel shocks. Finally, a Mach disk normal to the jet flow compresses the injected fluid. As the jet penetrates into the free-stream, a high pressure region is created by the shock ahead of the jet (on the windward side), whereas downstream, a low pressure region exists at the base of the jet as a result of the jet expansion.

Instantaneous flow fields and vortical structures of JICF in lower-speed flows have been the topic of many experimental and numerical studies (see, *e.g.* Andreopoulos [1985], Yuan et al. [1999], Lim et al. [2001], New et al. [2003]). Past experimental studies of JICF in supersonic crossflows have suggested that some of these vortical structures were also observed in supersonic JICF (VanLerberghe et al. [2000], Ben-Yakar et al. [2006]). The jet shear layer is at the interface between the high-speed jet

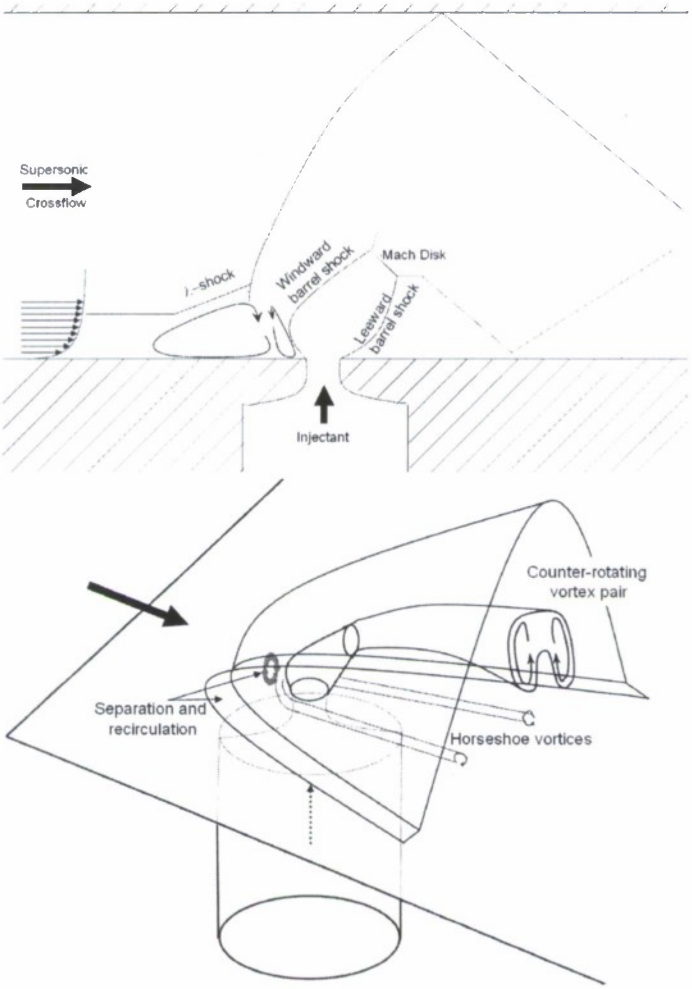
Supersonic
Crossflow
λ-shock
Windward barrel shock
Mach Disk
Leeward barrel shock
Injectant
Counter-rotating vortex pair
Separation and recirculation
Horseshoe vortices

Figure 5.1: Schematics of the supersonic JICF interaction.

and the low-velocity re-circulation on the windward side, and the separated region on the leeward side. Kelvin-Helmholtz instabilities (KHI) are generated, due to the high levels of shear, evolve into large-scale vortices that propagate along the jet boundaries, and contribute to the mixing process. Furthermore, a pair of counter-rotating axial vortices is formed in the plume region. These vortical features are regarded as the main phenomena for mixing the fluids in JICF. Horseshoe vortices are generated by the interaction between the incoming boundary layer and the jet, and remain close to the wall of injection. These vortices do not interact with the jet, and do not participate in the mixing process. Finally, vertical wake vortices form between the wall boundary layer and the jet plume, downstream of the injection. Their contribution to the mixing process is uncertain (Gruber et al. [1997]). Although simple from a conceptual point of view, it can be inferred from the above observations that this injection methodology leads to a rather complex flow pattern.

The jet shear vortices, the counter-rotating vortex pair and the wake vortices have clearly been identified in actual supersonic JICF experiments (VanLerberghe et al. [2000], Ben-Yakar et al. [2006]). However, a detailed capture of all the physical features of the flow is difficult, due to the intense fluctuations, the high levels of unsteadiness, and the flow speed. RANS, LES and hybrid RANS/LES simulations, on the other hand, have been used to isolate some of the key average and instantaneous features of this interaction (*e.g.*, Tam et al. [1999], Dickmann and Lu [2006], Peterson et al. [2006], Sriram and Mathew [2008], Kawai and Lele [2008]). In particular, some vortical structures typical of the high-speed interaction have been highlighted in these studies. Shock induced separations and horseshoe vortices have been identified. Some studies (Peterson et al. [2006], Kawai and Lele [2008]) have shown the particular nature of the KHI in supersonic JICF, related to the unsteady deformation of the barrel shock in response to the pressure oscillations within the incoming boundary layer (Kawai and Lele [2008]). All these phenomena add some complexity to the dynamics of the flow. Other vortical structures, such as the hanging vortices (Yuan et al. [1999]) or the windward vortex pairs (New et al. [2003]), found in subsonic JICF, have not been clearly identified in supersonic flows.

A LES of supersonic JICF is performed to resolve the time-averaged and unsteady features of this interaction. The present study focuses on the JICF configuration studied experimentally by Santiago [1995] and Santiago and Dutton [1997]. Detailed velocity fields have been obtained using LDV measurements, in the centerplane of the streamwise direction, and in two cross planes downstream of the injection. Mean velocities in the axial and transverse directions, and statistics of the fluctuating velocities are available for comparison. In addition to comparing with these experimental data, another focus of the present study is the investigation of the unsteady features of this interaction, and the impact of the free-stream Mach number and jet to free-stream momentum ratio on the flow dynamics.

5.1 Configuration and Parameters for the JICF Study

The present study focuses on the physics of a sonic jet injected into a supersonic crossflow. The configuration reproduces the experimental study presented in Santiago [1995], Santiago and Dutton [1997] and VanLerberghe et al. [2000], where time-averaged and fluctuating velocity profiles from LDV measurements, PLIF imaging and analysis of the mixing have been reported. The experimental conditions are as follows. Air is injected through a choked nozzle with an exit diameter $d = 4\ mm$ located at the bottom wall of a wind-tunnel. The free-stream in the wind tunnel is a $M = 1.6$ airflow. Stagnation conditions for the injector and the main stream are given in Tab. 5.1. The test section has a width of 76 mm and a height of 36 mm.

Table 5.1: Experimental parameters for the jet in cross flow experiment of Santiago and Dutton [1997].

Case A		
	free-stream	jet
Mach number	1.6	1.0
P_{stag} (kPa)	241	476
P_{static} (kPa)	57	251
$P_{norm\ shock}$ (kPa)	160	—
T_{stag} (K)	295	295
ρ_{static} (kg/m^3)	1.05	3.55
velocity (ms^{-1})	446	315
ρU^2 $(kg\ m^{-1}s^{-2})$	2.03 10^5	3.52 10^5
$J = (\rho U^2)_{jet} / (\rho U^2)_{\infty}$	1.73	
$PR = P_{t,jet}/P_{\infty}$	8	

Noting $(x, y, z) = (0, 0, 0)$ the center of the injection port, the computational domain used for the present study extends from $x = -16.5d$ to $x = 7d$ in the streamwise direction, and from $y = 0$ to $y = 9d$ in the transverse direction. The spanwise depth of the experimental facility has not been fully simulated for computational savings, and extends from $z = -6.3d$ to $z = 6.3d$. This domain extent is sufficient to capture all the physical processes, allows comparisons with the experimental data and prevents the wave reflections from the side of the domain from interacting with the regions of interest. Two grid resolutions have been used to resolve this configuration. A coarse grid consists of $300 \times 150 \times 100$ cells with grid stretching to refine the resolution close to the injector and close to the lower wall of the wind tunnel. The resulting resolution is finest at the tip of the injector, where $\Delta x/d = 0.023$, $\Delta y/d = 0.022$ and $\Delta z/d = 0.032$. Peterson et al. [2006] found that the inclusion of the injection plenum chamber in the domain of the simulation improved the jet flow rate, and therefore, this section is simulated and resolved using a $23 \times 60 \times 23$ grid. A finer grid is also used to assess grid independence of the reported simulations. This grid employed $600 \times 225 \times 200$ cells in the test-section, and $46 \times 90 \times 46$ grid cells in the injection chamber.

The test-section inflow conditions at $x = -16.5d$ are generated using the rescaling-recycling method described in Stolz and Adams [2003]. At every instant, the temporal fluctuations in velocity, temperature and density are extracted from the recycling plane located at $x = -5d$, rescaled, and reintroduced at the inflow plane, $x = -16.5d$. This method permits the self-generation of an inflow boundary layer with turbulent structures. The boundary layer displacement thickness at the recycling plane was constrained to match that obtained in the experimental study, $\delta^{\star} = 0.59\ mm$. The inflow in the plenum chamber uses a stagnation condition-based characteristic inflow. The outflow at $x = 7d$ is a standard supersonic extrapolation. The bottom boundary of the wind-tunnel, as well as the sides of the plenum chamber are treated as no-slip adiabatic walls, whereas symmetry conditions are applied to the top wall of the section. Periodicity conditions are used in the spanwise direction. After washing out the transients due to the initial conditions, statistics are collected for over 5 flow-through-times.

5.2 Comparisons with Experiments

The mean velocity profiles collected in the centerline plane at four different stations, $x/d = 2$, $x/d = 3$, $x/d = 4$ and $x/d = 5$ are compared to the experimental velocity fields in Fig. 5.2 for both grid resolutions. Similarly, profiles of velocity fluctuations are compared to the experimental profiles in Fig. 5.3. For both the second and last locations, velocity profiles have been acquired from centerplane measurements and from cross-plane acquisitions. Consequently, 3 sets of data for the axial velocity and 2 sets of data for the transverse velocity are available for these locations, and have all been used for comparison in the following plots. Some of the experimental uncertainty is highlighted in the scatter of the velocity fields obtained for different acquisitions. However, to a very good extent, the global behavior and the amplitude of the profiles are reproduced from one realization to the next. Note that the turbulent statistics in the free-stream do not go to 0 in the experimental data, probably due to some perturbations in the free-stream, and/or due to experimental noise.

The axial velocity predictions from the LES simulations show a fairly good agreement with the experiments, and the wake of the jet plume is correctly captured. The peak of vertical velocity is over-estimated at the first station, but decays quickly with downstream location and reaches amplitudes in good agreement with the experimental data. The velocity fluctuations are related to the boundary layer turbulence, to the wake of the jet and to the shear vortices (examined in more details later). The profiles and amplitude of u_{rms} match quite well the experimentally measured fluctuations. At the last station, a noticeable difference is seen with one set of experimental measurements. It should be noted, however, that the agreement with the other two sets of measurements is satisfactory. The transverse velocity fluctuations are overestimated in the near-jet region, but relax to the experimental profiles further downstream. For

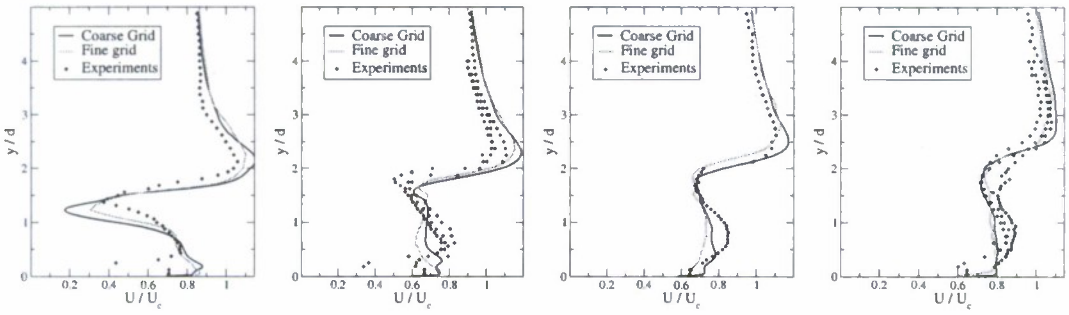

(a) U/U_c at $x/d =$ 2

(b) U/U_c at $x/d =$ 3

(c) U/U_c at $x/d =$ 4

(d) U/U_c at $x/d =$ 5

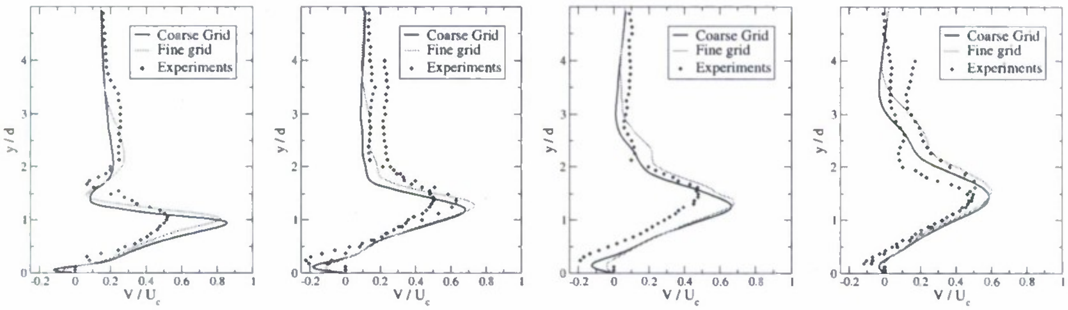

(e) V/U_c at $x/d =$ 2

(f) V/U_c at $x/d =$ 3

(g) V/U_c at $x/d =$ 4

(h) V/U_c at $x/d =$ 5

Figure 5.2: Profiles of mean axial and transverse velocities in the centerplane at four locations downstream of the injection. Comparison between numerical and experimental results (at $x/d = 3$ and $x/d = 5$, 3 sets of experimental data for U and 2 for V, 1 set of data otherwise - Santiago and Dutton [1997]).

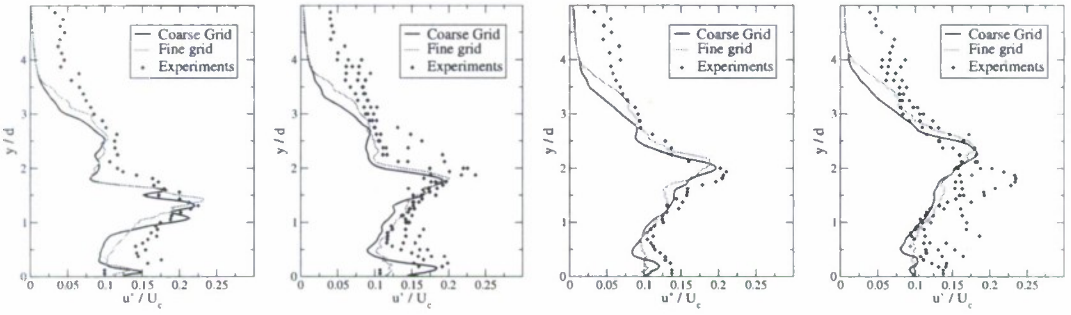

(a) u_{rms}/U_c at $x/d = 2$

(b) u_{rms}/U_c at $x/d = 3$

(c) u_{rms}/U_c at $x/d = 4$

(d) u_{rms}/U_c at $x/d = 5$

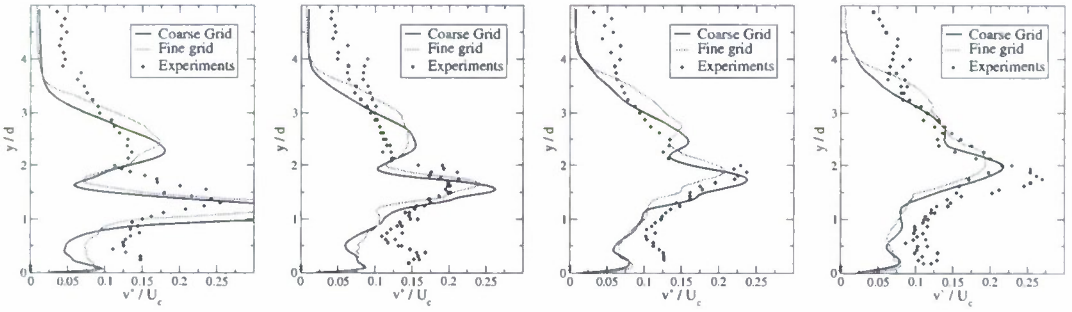

(e) v_{rms}/U_c at $x/d = 2$

(f) v_{rms}/U_c at $x/d = 3$

(g) v_{rms}/U_c at $x/d = 4$

(h) v_{rms}/U_c at $x/d = 5$

Figure 5.3: Profiles of fluctuating axial velocity statistics in the centerplane at four locations downstream of the injection. Comparison between numerical and experimental results (at $x/d = 3$ and $x/d = 5$, 3 sets of experimental data for u_{rms} and 2 for v_{rms}, 1 set of data otherwise - Santiago and Dutton [1997]).

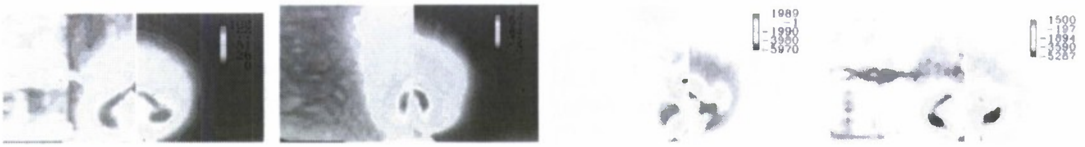

(a) u_{rms} at $x/d = 3$ (b) v_{rms} at $x/d = 3$ (c) $< u'v' >$ at $x/d = 3$ (d) $< u'w' >$ at $x/d = 3$

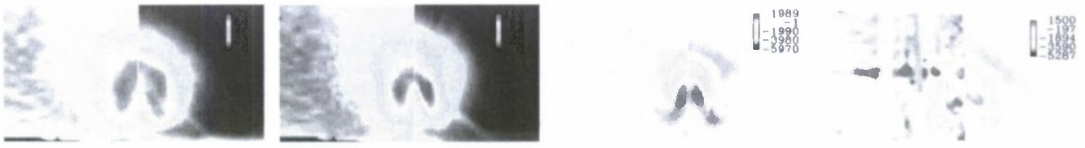

(e) u_{rms} at $x/d = 5$ (f) v_{rms} at $x/d = 5$ (g) $< u'v' >$ at $x/d = 5$ (h) $< u'w' >$ at $x/d = 5$

Figure 5.4: Contours of Reynolds stresses in two cross-planes downstream of the injection ($x/d = 3.0$ and $x/d = 5.0$). Comparison between experimental (left) and numerical (right) results.

v_{rms} again, a fair agreement with one set of data is obtained, whereas the agreement with the other experimental acquisition is less satisfactory.

As mentioned above, mean and fluctuating velocity profiles have been collected at two cross-sections downstream of the injector, at $x/d = 3$ and $x/d = 5$. A comparison of the contours obtained from experiments with the numerical result is presented in Fig. 5.4. The kidney-shaped vortices observed in the section of the counter rotating vortex pair (CVP) are highlighted in these plots The overall shape is correctly captured by the numerical simulation. At the first cross-plane, the width of the mixing region, estimated using the field of u_{rms}, is slightly over-estimated by approximately $0.2d$. The core of the CVP and the amplitude of the fluctuations are, however, in good agreement with the experimental field. At $x/d = 5$, the predictions on the jet plume extent and on the amplitude of fluctuations match the experimental observations.

The present simulation overall compares favorably to the experimental data. The statistics in mean and fluctuating velocities in the centerplane and at two different cross-sections show similar trends and amplitude, and the structures of the flow are recovered. A more systematic look at the time-averaged and instantaneous vortical structures developed in this interaction is examined next. The reference case described above (Case A) is complemented by two other cases: a sonic jet into an $M = 2$ crossflow (Case B) and a case where the jet to freestream momentum ratio, $J = (\rho U^2)_{jet}/(\rho U^2)_\infty$, is increased to $J = 5$ for a $M = 1.6$ crossflow (Case C), compared to $J = 1.6$ for Cases A and B. The stagnation conditions of Cases B and C are also given in table 5.1. The geometry is identical to the reference case and the boundary conditions are also kept identical for Case B. For Case C, an extrapolation boundary

Table 5.2: Numerical parameters for two jets in crossflow simulation: (a) free-stream Mach number $M = 2$ and (b) jet to freestream momentum ratio $J = 5$.

	Case B		Case C	
	free-stream	jet	free-stream	jet
Mach number	2.0	1.0	1.6	1.0
P_{stag} (kPa)	284	476	241	1428
P_{static}(kPa)	36	251	57	754
$P_{norm\ shock}$(kPa)	160	—	160	—
T_{stag} (K)	295	295	295	295
ρ_{static} (kg/m^3)	0.77	3.55	1.05	10.65
velocity (ms^{-1})	514	315	446	315
ρU^2 $(kg\ m^{-1}s^{-2})$	$2.03\ 10^5$	$3.52\ 10^5$	$2.03\ 10^5$	$10.56\ 10^5$
$J = (\rho U^2)_{jet} / (\rho U^2)_\infty$	1.73		5.20	
$PR = P_{t,jet}/P_\infty$	13		25	

condition is used at the top boundary, in order to prevent the stronger bow shock from reflecting and interacting with the jet mixing region.

The computational results for case A, shown in Figs. 5.2 and 5.3 demonstrate a good grid independent behavior and are in good agreement with experimental data. Furthermore, spectral analyses of the energy densities at some key locations, shown in Fig. 5.5, show an energy decay that scales with the inertial range scaling $\omega^{-5/3}$. Similar energy spectra are obtained from the finer resolution simulation, showing the appropriateness of the computational grid to the resolution of this turbulent problem. Based on this observation, and consistent with the LES philosophy of using as coarse a grid as possible to capture the features of interest, the coarser grid results are analyzed in more details in the next sections, and the coarser grid is employed for cases B and C listed in table 5.1.

5.3 Time-Averaged Flow Features

Some of the well documented time-averaged structures of JICF have been reviewed earlier, and are revisited here in the context of the present simulations. Figure 5.6 shows the pressure contours and some streamlines of the incoming flow for the three cases considered here. The mean flow blockage due to the jet leads to the formation of a primary strong shock wave ahead of the jet and induces a separation of the boundary layer. The weak shock generated by the subsequent thickening of the layer causes the formation of a $\lambda-$shock structure, as visible in Fig. 5.6. A primary recirculation region is formed ahead of the jet, centered at around $x/d = -1.31$, $y/d = 0.13$ for the reference case, in good agreement with the experimental observations $x/d = -1.25$ and $y/d = 0.13$. This region has a triangular shape, and interacts with the jet shear

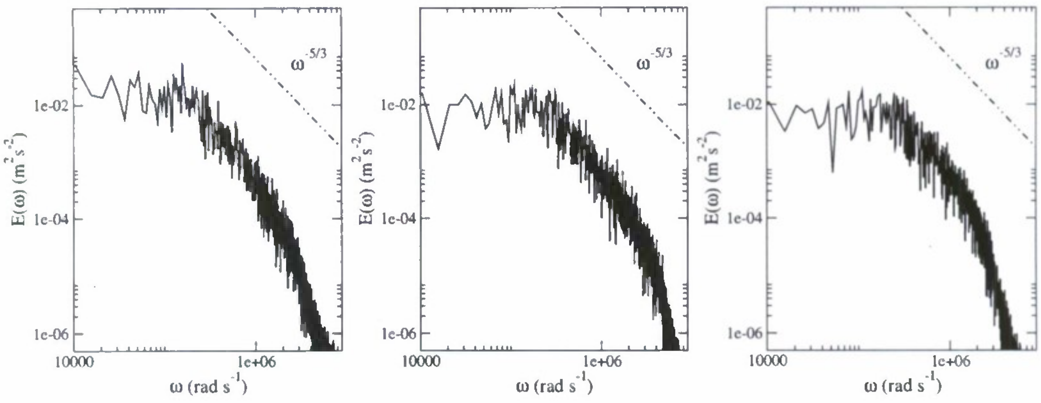

(a) (b) (c)

Figure 5.5: Energy spectra at three locations of the centerplane: (a) along the developing jet shear layer ($x/d = -0.83$, $y/d = 0.4$), (b) in the wake of the jet ($x/d = 2.35$, $y/d = 2.6$) and (c) further downstream in the jet wake ($x/d = 4$, $y/d = 2.7$).

layer from ($x/d = -0.5$, $y/d = 0$) to ($x/d = -0.67, y/d = 0.59$). A smaller anti-clockwise rotating recirculation is formed between the primary recirculation and the jet boundaries. As seen in Fig. 5.6(b), the bow shock in front of the jet is weaker than in the other two cases, and the boundary layer separation is weaker. As a consequence, the primary re-circulation is smaller, and its center is located at $x/d = -1.35$ and $y/d = 0.09$. Due to a higher momentum, the jet in case C penetrates further into the crossflow, and the bow shock is much stronger than in the two other cases. The boundary layer separation is moved upstream, and the recirculation region is located at $x/d = -1.9$, $y/d = 0.25$.

The expansion of the jet increases the Mach number of the injected gas, and a maximum velocity of 690 m/s is reached at a location $x/d = 1.2$, $y/d = 1.3$ for the reference case. Santiago and Dutton [1997] report a maximum velocity location of $x/d = 1.25$, $y/d = 1.38$, but estimated the maximum velocity to be 589 m/s. The penetration of the jet depends strongly on the momentum ratio, but also on the *effective back pressure* (Everett et al. [1998]). Despite an identical post normal-shock pressure of 160 kPa in the freestream for all three cases, the pressure increase through the $\lambda-$shock depends on both the strength of the separation and the jet pressure. As reported earlier, the bow shock for case B is weaker than in the other cases, and the effective back pressure is lower, leading to a greater penetration of the jet into the crossflow, leading to a greater penetration of the jet into the crossflow, and the maximum velocity is reached at $x/d = 1.52$, $y/d = 1.48$. The jet in case C penetrates further into the mean flow, and creates a stronger bow shock, leading to a higher effective back pressure and a higher pressure drag. The highest velocity for Case C occurs at $x/d = 1.88$, $y/d = 2.52$.

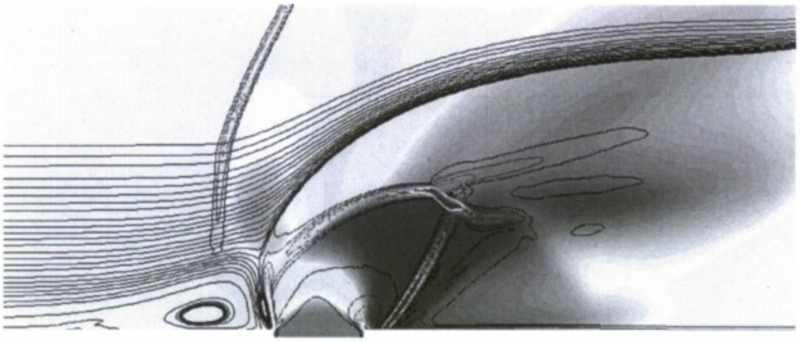

(a) $M = 1.6,\ J = 1.7$

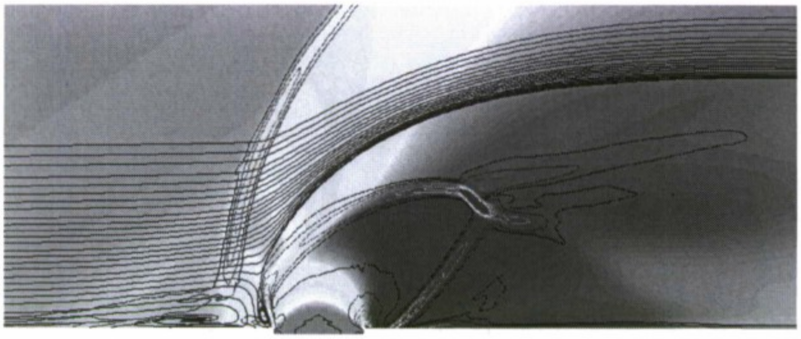

(b) $M = 2,\ J = 1.7$

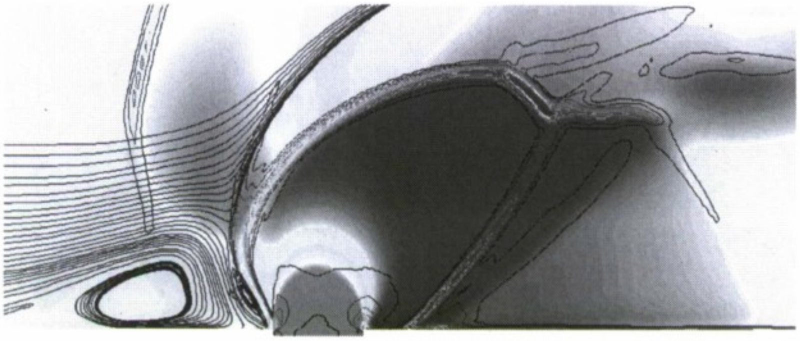

(c) $M = 1.6,\ J = 5$

Figure 5.6: Pressure field, temperature gradient contours and streamlines in the centerplane for the three JICF cases. The flow is from left to right.

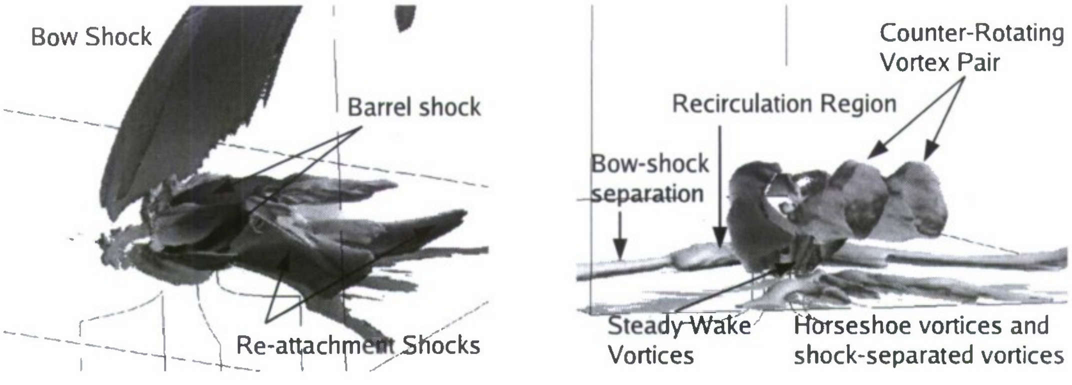

(a) Shear-dominated structures ; $Q = -8 \times 10^9 s^{-2}$

(b) Vorticity-dominated structures ; $Q = 7 \times 10^8 s^{-2}$

Figure 5.7: Vortical structures in the JICF configuration represented by the iso-contours of Q variable (Dubief and Delcayre [2000]). Flow is from left to right

For all cases, most of the injected fluid is found to pass through the windward and lateral barrel shocks, and across the Mach disk. A small amount only of jet fluid passes through the leeward barrel shock and remains over-expanded. As a consequence, two shocks are formed: a strong shock at the tip of the Mach disk compresses the jet fluid that passes through the leeward barrel shock and penetrates into the free-stream (most visible for case C pressure contours in Fig. 5.6). A weaker shock is generated from the re-attachment point at the wall, which propagates into the freestream.

The key observable three-dimensional structures in the JICF are illustrated in Fig. 5.7 for the reference case. Similar time-averaged features are observed for the other cases, and are not repeated here, for brevity. The second invariant of the velocity gradient tensor, often denoted Q, is well-suited to vortical fields identification (Dubief and Delcayre [2000]). An iso-surface of negative Q is shown first in Fig. 5.7(a), highlighting the shear-dominated regions of the average flow, and identifying the regions of high velocity gradients. The complex shock pattern in the centerplane discussed earlier leads to the formation of three-dimensional re-attachment shocks. These structures propagate outwards, interacting with the jet wake and the boundary layer.

An iso-surface of positive Q, highlighting the regions dominated by vorticity over strain (Q criterion), is shown in Fig. 5.7(b). The impact of the bow shock onto the boundary layer induces separation, and the vortical recirculation region follows the curved shock. Along the side of the jet, hanging vortices are formed by the skewed mixing layer between the streamwise flow and the vertical jet (Yuan et al. [1999]). The origin of the hanging vortices lies between the bottom wall and the boundaries of the laterally expanding jet, as shown in Fig. 5.8(a). The center of these vortices moves up with downstream location along the jet boundaries, as shown in the evolution from Fig. 5.8(a)-5.8(c). Although presented here for a statistically averaged field, it should be noted that these structures are observed to remain quasi-steady in the course of the simulations. Further downstream, a counter-rotating vortex pair is formed in the wake of the jet. In the present context of supersonic flows, the formation of this vortex pair is found to be the result of several simultaneous phenomena. The jet column is deformed by momentum, pressure of the crossflow at the windward side, and is sheared along the lateral edges, giving a kidney-shape to the initially circular jet cross-section, as visible in Fig. 5.9. After being deflected by the jet, the main stream expands along the sides of the jets and swerves back towards the centerplane of the wind tunnel. Actually, the circulation induced by the hanging vortices enhances this flow convergence towards the centerplane, as seen in Fig. 5.8(b)-5.8(c). As the flow converges, a higher pressure region is formed and the pressure increase leads to the formation of two outwards moving shocks, and of a strong upwash velocity which penetrates into the jet plume, and creates the circulation of the counter-rotating vortex pair (Chenault et al. [1999]). This phenomenon is illustrated in Fig. 5.8(d) and 5.8(e). On each side of the centerplane, hanging vortices and vortices of the CVP rotate in the same sense, and the hanging vortices quickly weaken. The CVP, on the other hand, is amplified in the plume of the jet, enhancing the mixing of free-stream and injected fluid.

Iso-surfaces of the Q variable are shown in Fig. 5.10 for all three JICF cases and case B and C show features similar to that of case A described above. Again, the hanging vortices formed on the side of the jets are clearly visible in the three results. For Case A, the centres of the hanging vortices form an angle of 18° with respect to the bottom wall. In the second case, the free-stream flow loses less momentum through the bow shock in front of the jet, and the skewed mixing layer is more inclined towards the streamwise direction. The angle formed between the centre of the hanging vortices and the bottom wall is decreased down to 14°. The opposite occurs in Case C, where the very high momentum of the jet creates a hanging vortex with a higher angle to the bottom wall, reaching 24°.

Another type of vortical structures is observed in these iso surfaces, present in all three cases but particularly visible for case C. A pair of vortices generated on the windward side of the jet, close to the point where the upper tip of the recirculation region ahead of the jet interacts with the shear layer, evolves along the side of the jet, above the hanging vortices, as visible in Fig. 5.10. These vortices closely resemble the Windward Vortex Pairs (WVPs) reported by New et al. [2003] in the studies of low-speed elliptical JICF. The under-expanded jet expands at the nozzle, and blocks a large portion of the incoming boundary layer. As a direct consequence, the recirculation zone formed ahead of the jet is large, and the pressure increase, significant. The windward side of the jet, initially circular, is deformed, leading to a concave warping of the jet boundary, and of the subsequent vortex sheet. The momentum impact of the recirculation region decreases at the spanwise location where the boundary layer flow gets around the jet core.

A bifurcation of the incoming streamlines occurs at $x/d = -0.6$, $y/d = 1.2$ and $z/d = \pm 0.75$, characterizing the separation between streamlines that get into the recirculation region ahead of the jet and streamlines that wrap around the jet. These locations, shown in Fig. 5.11, correspond to the location where windward vortices

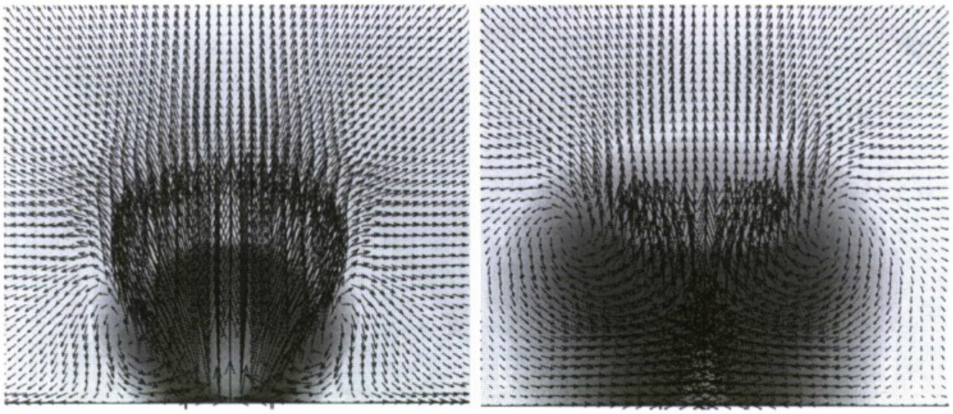

(a) $x/d = 0.5$ (b) $x/d = 1.5$

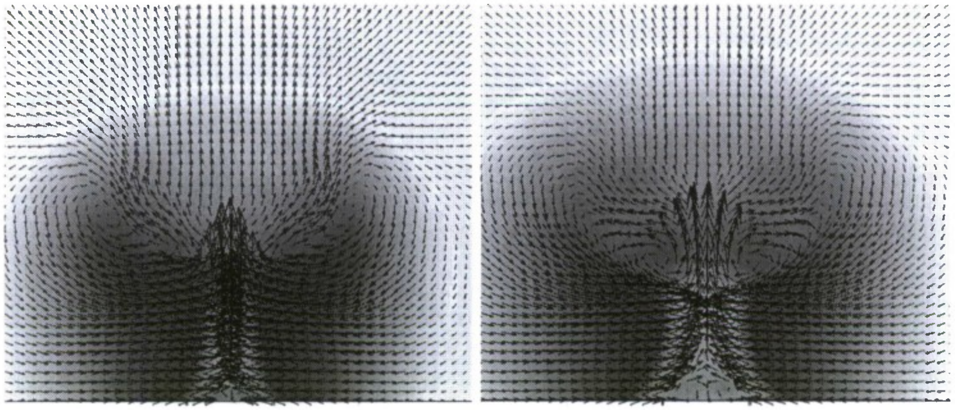

(c) $x/d = 2$ (d) $x/d = 2.5$

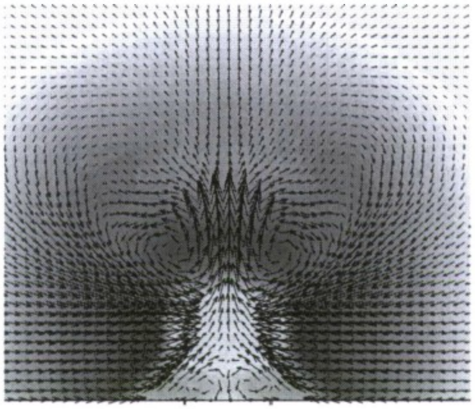

(e) $x/d = 3$

Figure 5.8: Average velocity vectors at five cross sections downstream of the injector for the reference JICF (background is the pressure field).

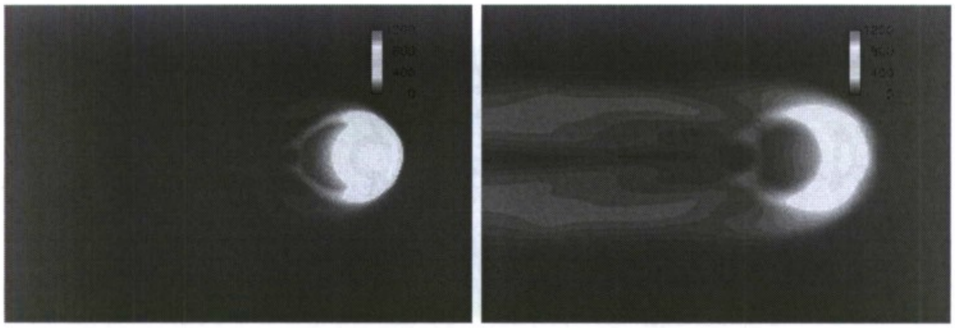

(a) $y/d = 0.5$

(b) $y/d = 1$

Figure 5.9: Contours of the average injected mass flux for two vertical planes for the reference JICF.

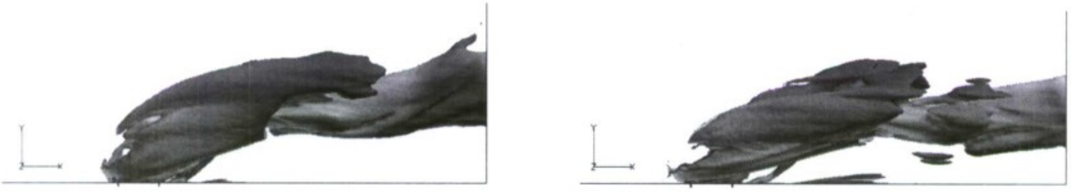

(a) Case A

(b) Case B

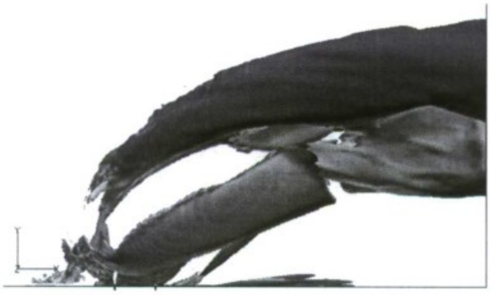

(c) Case C

Figure 5.10: Iso-surface of $Q = 10^8 s^{-2}$ highlighting the hanging vortices for the three JICF cases.

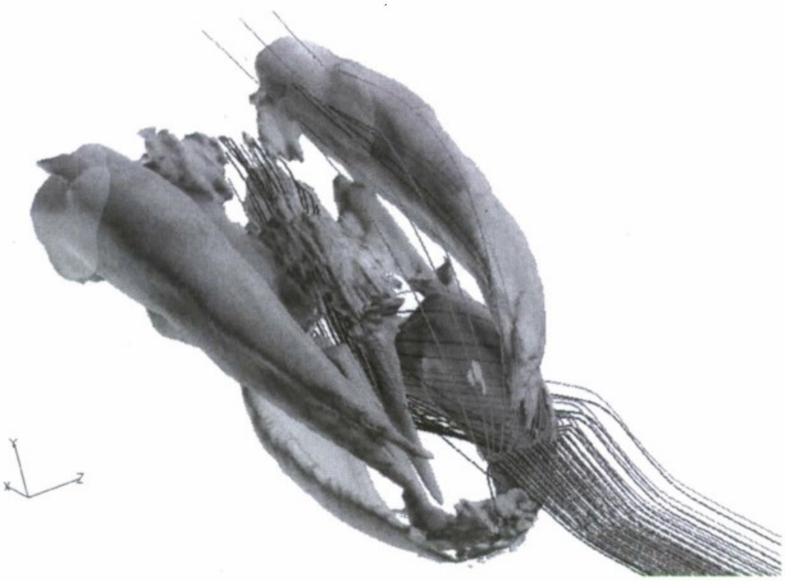

Figure 5.11: Iso-surface of $Q = 10^8 s^{-2}$ and streamlines from the upper boundary layer.

are formed. As these structures are convected downstream, they interact with the CVP and weaken. These vortices breakdown quickly for cases A and B. They evolve further away from the CVP for case C, hence survive longer.

The convergence of the freestream towards the centerplane downstream of the jet creates a circulation in the near wake region, and two steady wake vortices are generated. Also, horseshoe vortices are formed downstream of the injector, close to the wall in the wake of the jet. These vortices, also visible in Fig. 5.8(d) and 5.8(e) along the bottom wall, rotate in a direction opposite to the CVP above them. Again, in the cases of supersonic JICF presented here, and unlike the subsonic JICF, the formation of the horseshoe vortices is closely related to the outwards motion of the shock pair created in the centerplane and discussed earlier.

As expected, the averaged fields show a rather complex flow evolution in this JICF problem: many sources of vorticity have been identified, and could play a role in the overall mixing between jet and freestream. In order to gain understanding in the dynamics of this interaction, these *steady* features are revisited using the unsteady data from the simulations in the next section.

5.4 Unsteady Features and Flow Dynamics

Images of the injection region have been acquired using PLIF by VanLerberghe et al. [2000] in the same experimental facility, and under similar experimental conditions as the study of Santiago and Dutton. Large scale unsteady vortices generated on the windward side of the jet and convecting along the jet boundary and along the jet plume have been identified in this study. Some of the snapshots acquired in this

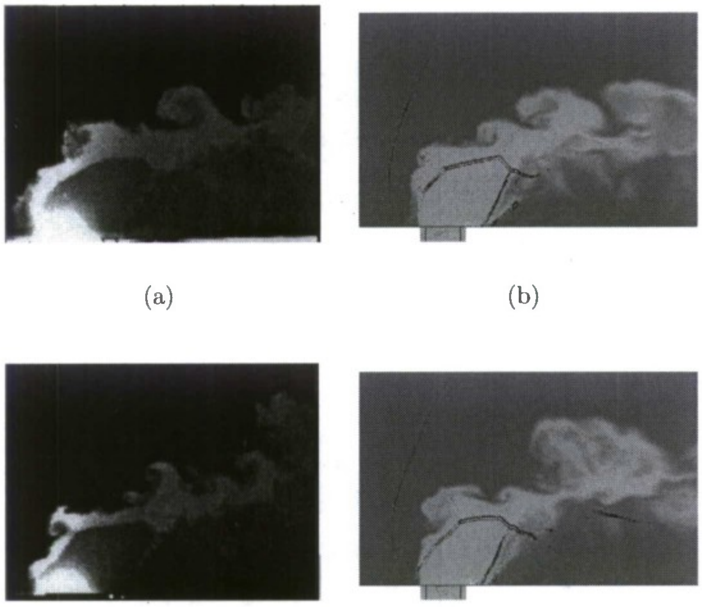

(a) (b)

(c) (d)

Figure 5.12: Large scale structures for the reference JICF, case A: (a) and (c) experimental observation by acetone PLIF of VanLerberghe et al. [2000], (b) and (d) numerical snapshots of the passive scalar field and density gradient contours.

experimental study are reproduced in Fig 5.12 along with some instantaneous contours obtained from the present simulation (case A). In these figures, the boundaries of the under-expanded jet are delimited by the contours of temperature gradients. Similar large scale structures are known to exist even in low-speed JICF due to Kelvin-Helmholtz instabilities (KHI) (Fric and Roshko [2004]) of the vortex sheet created at the jet nozzle. These KHI occur along the windward and the lateral sides of the jet, forming a circumferential vortical structure rather than a vortex ring, as originally thought (Lim et al. [2001]).

In high speed JICF, the large scale vortices are also observed in the centerplane, but their generation is more complex than in the low-speed case. Figure 5.13 represents a time-series of the temperature gradient magnitude in the centerplane of the reference case, showing the highly unsteady nature of the interaction. The phenomenon is enhanced in the present supersonic interaction by the unsteady deformation of the barrel shock illustrated in the time-series. The vortical structures and pressure fluctuations of the incoming boundary layer interact with the jet at the nozzle exit. The intensity of the pressure fluctuations inside the recirculation region reaches 13 kPa and unsteady compressions are generated within the jet flow. The formation of a compression is illustrated in Fig. 5.13 over a time interval of 8 μs. The wave steepens into a localized shock wave as it penetrates into the jet and propagates along jet

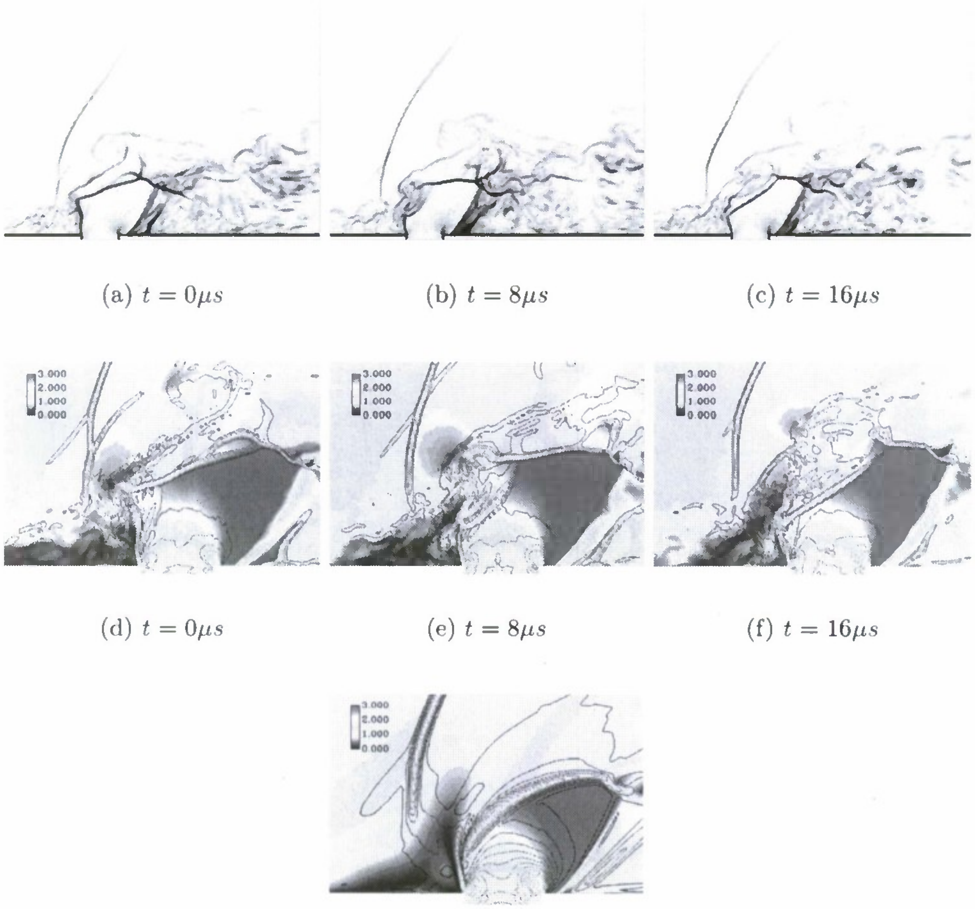

(a) $t = 0\mu s$ (b) $t = 8\mu s$ (c) $t = 16\mu s$

(d) $t = 0\mu s$ (e) $t = 8\mu s$ (f) $t = 16\mu s$

(g) Time-averaged field

Figure 5.13: Contours of the temperature gradients magnitude (a-c) and of the Mach number field with density gradient contours (d-f) at three consecutive instants. (g) time-averaged Mach number field.

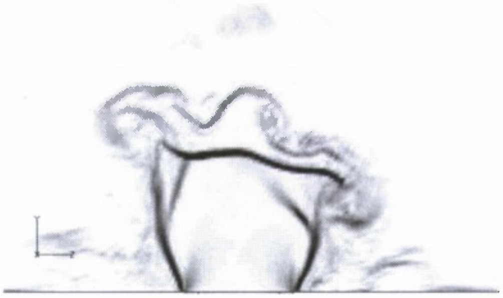

Figure 5.14: Contours of the temperature gradients magnitude in the $x/d = 0$ cross-plane at $t = 8\mu s$ of the reference JICF.

boundary. The moving shock finally reconnects the barrel shock further downstream of the injection and creates a kink in the jet boundary at the reattachment point , at $x/d = 0.75$, $y/d = 1.55$ (seen at $t = 16$ μs, Fig. 5.13(c)). A pocket of unshocked jet fluid is then detached from the jet.

Figures 5.13(d)-5.13(f) show close-up views of the jet windward jet boundary representing the Mach number field at the same three instants. The pockets of jet fluid formed by the unsteady shock motion within the jet leads to the ejection of high Mach number fluid that interacts with the recirculation region. The highly unsteady nature of the windward barrel shock impacts the time-averaged Mach number field (Fig. 5.13(g)), which shows a very diffuse windward-side barrel shock.

The pockets of jet fluid ejected through this process are submitted to high levels of shearing, and the vortical structures formed by KHI show intense levels of vorticity. Due to the higher vertical velocity of the jet fluid, the vortices formed through the interaction, and visible in Figs 5.13(a)-5.13(c), rotate counter-clockwise, are convected along the jet boundaries and break-down into smaller scale turbulence further downstream at the boundaries of the jet plume. Distortion of the windward barrel shock at the centerplane is also reported in the PLIF visualizations of VanLerberghe et al. [2000] (reproduced here in Fig. 5.12) where kinks in the upstream jet boundary are observed. Also, the unsteady formation of shock waves within the under-expanded jet, in the centerplane, was also observed and reported in other numerical study (Peterson et al. [2006], Kawai and Lele [2008]). This perturbation of the jet is found to be strongly three-dimensional. The unsteady compression is formed at the windward side, where the pressure fluctuations in the region ahead of the jet are the strongest, and extend along the jet boundary and to the lateral sides.

In Fig. 5.14, contours of temperature gradient in the cross-plane $x/d = 0$ are represented at the same instant as for Fig. 5.13(b), showing that the compression wave that propagates within the jet is actually curved. The pocket of unshocked fluid ejected through this process wraps around the jet, leading to the formation of a circumferential vortex due to KHI. The formation of unsteady compressions along the lateral sides of the jet is also observed during the unsteady evolution of the jet. The shocks that result from this interaction are found to be weaker than those due to windward compressions, and do not penetrate the jet significantly. As a consequence, these perturbations do not wrap around the jet, and KHI vortices are formed asymmetrically on the sides.

The deformations of the jet boundary due to the unsteady dynamic pressure of the incoming boundary layer is also observed for cases B and C. Despite an identical jet to freestream momentum ratio, the transverse jet in case B expands more at the nozzle exit, as reported earlier. The Jet Mach number along the boundaries is higher than in the reference case, and the penetration of the compression waves, lower. As a consequence, smaller pockets of fluid are ejected in case B. For the same reasons, the higher jet momentum of case C is less sensitive to the incoming perturbations in the boundary layer, and the penetration of the compression waves into the jet is smaller.

The jet distortion described above and the vortices formation generate strong acoustic waves that propagate upstream into the subsonic region and interact with the bow shock. The shock front appears wavy and unsteady, as observed in the temperature gradient snapshots, and in experimental Schlieren images (Gruber et al. [1995], Ben-Yakar et al. [2006]). The shock motion results in an unsteadiness of the boundary layer separation, and a deformation of the $\lambda-$shock structure ahead of the jet is observed in the present simulations. Pressure fluctuations are responsible for the jet boundary deformation, and this phenomenon could lead, through a self-exciting mechanism, to the periodic formation of shear layer vortices. Actually, in a recent study, Won et al. [2008] performed a Detached Eddy Simulation (DES) of a JICF and showed the very periodic formation of vortical structures from the jet front, probably a consequence of such a self-excitation mechanism. In the present calculations, no fundamental mode of excitation is found from the pressure and vorticity spectra computed ahead of the jet. It is likely that this difference in behavior comes from the levels of turbulence in the incoming boundary layer : very small amounts of turbulence in the incoming boundary layer was reported by Won et al. [2008] in their DES simulation, whereas the present calculations carry turbulent, and non periodic, structures in the incoming layer.

The vortices due to fluid ejection and/or by KHI are formed along the jet boundary. The three-dimensional evolution of these structures is highlighted through the iso-surface of the passive scalar (injected from the jet), as shown in Fig. 5.15 for the three cases. Figs. 5.15(a), 5.15(c) and 5.15(e) show large circumferential vortices that wrap around the jet and create a large roll up. These structures form symmetrically in a vertical plane. The windward part of the roll-up is convected upwards along the boundary of the jet, whereas the side vortices are carried along the jet plume. The initially planar structures tilt and fold around the jet. These structures engulf large amounts of freestream fluid, and a mixing of jet and free-stream fluids at the large scales is achieved at the periphery of the jet. Further downstream, these vortical structures break down into small scale turbulence, hence enhancing the mixing process.

The formation of vortices on the lateral sides of the jet is also observed, as illustrated in Figs. 5.15(b) and 5.15(d) for cases A and B, respectively. The higher

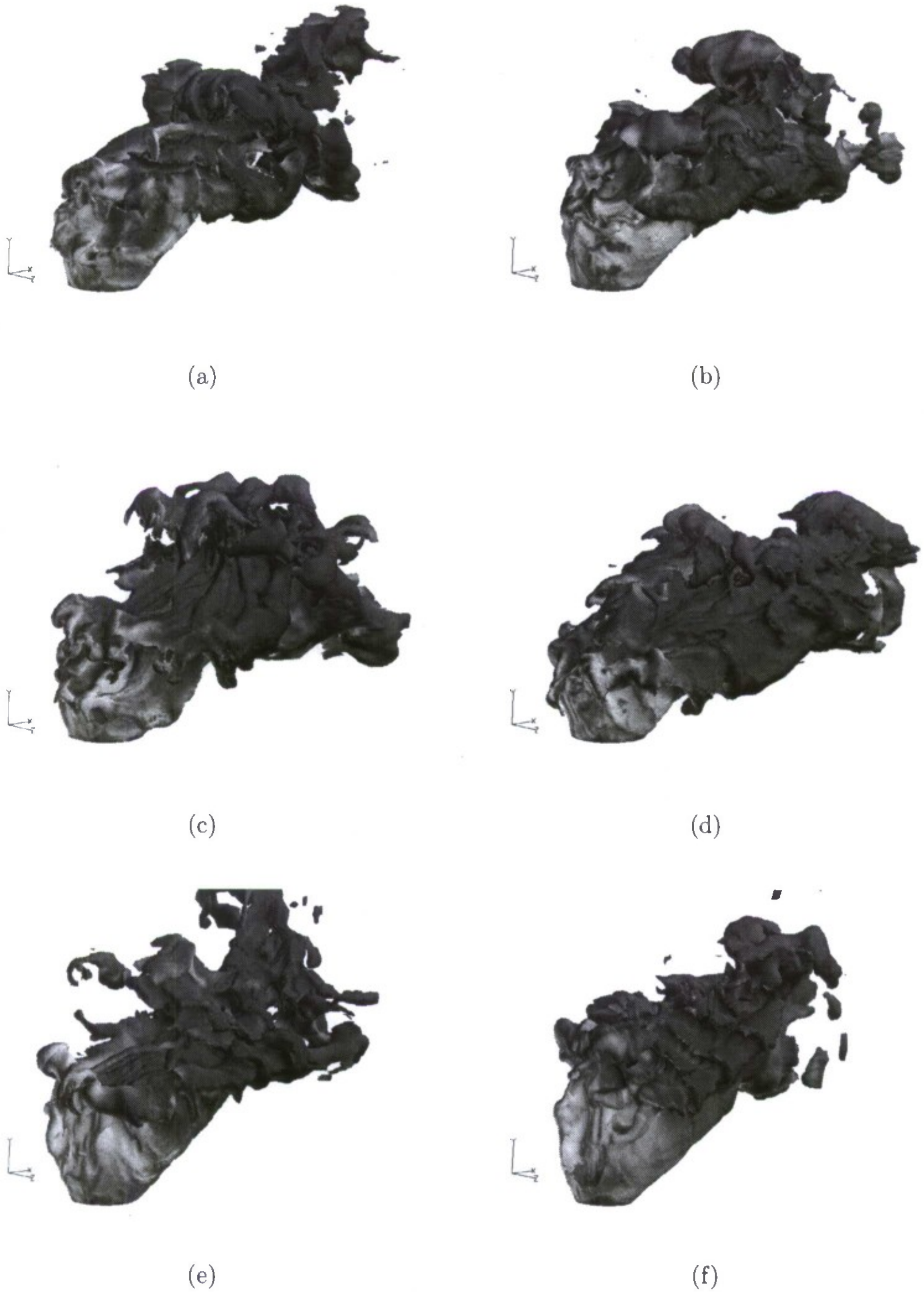

(a) (b)

(c) (d)

(e) (f)

Figure 5.15: Iso-surface of the passive scalar injected from the jet ($Y_2 = 0.3$) colored by the vorticity magnitude, highlighting the formation of vortical structures due to localized and/or circumferential Kelvin-Helmholtz instabilities: (a) and (b) case A, (c) and (d) case B, (e) and (f) case C.

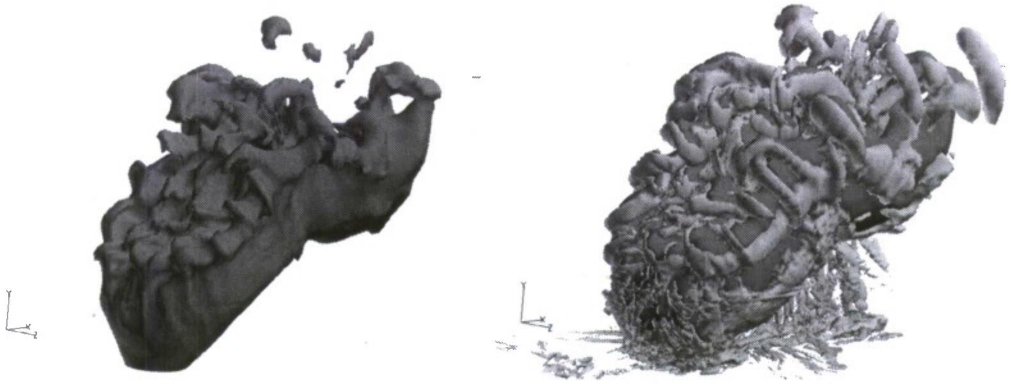
(a) (b)

Figure 5.16: Visualization of an instantaneous windward vortex. Iso-contour of the passive scalar, and superposition with an iso-surface of positive Q.

velocity of the jet leads to the formation of a roller with positive x-vorticity, and again, carries some of the freestream fluid towards the centerplane in the wake of the jet. These instabilities remain on the sides of the jet, and do not evolve circumferentially around it. Their generation is related to the lateral jet compression and to KHI along the skewed mixing layer. The impact of the quasi-steady hanging vortices in these regions is however difficult to assess. Such vortices are found in case C as well, but are less frequent and intense than in the other two cases. Windward vortices, on the other hand, can be clearly identified on the instantaneous flow structure of case C.

Figure 5.15(f) shows a vortical structure formed at the tip of the recirculation, at $x/d = -0.7$, $y/d = 1.25$ and $z/d = 0.75$. This feature extends along the jet boundary and is deflected towards the streamwise direction, tilting to a vortical structure with positive x-vorticity. Furthermore, the instabilities of the vortex sheet are observed along the path of this structure, as illustrated in Fig. 5.16. The wavy structure of the WVP is clearly visible in the iso-surface of passive scalar. The superposition of an iso-surface of Q shows that small vortex tubes wrap around the WVP, due to vortex sheet instability. Again, these WVP are found for all three cases, but have significant amplitude for case C only.

On the leeward side of the jet, the dynamics of the flow is much less coherent. Pressure fluctuations of the order of 4 kPa also induce barrel shock fluctuations, but the strong deformations that lead to the ejection of fluid pockets on the windward side are not observed here. Rather, small amplitude KHI vortices breakdown as they pass through the shock that is connected to the Mach disk. These structures induce high levels of velocity fluctuations in the jet plume, and do not influence the jet wake significantly.

A significant part of the injected fluid passes through the Mach disk of the under-expanded jet. This injected fluid does not carry a significant amount of turbulence.

However, the jet boundary unsteadiness provoke an oscillatory motion of the Mach disk, and velocity fluctuations are generated. Furthermore, the Mach disk induces a significant flow deceleration, as already observed in Fig. 5.2. The large coherent structures that develop along the jet boundary (circumferential, lateral and leeward KHI vortices, windward vortices) are strongly sheared as they propagate along the jet plume, and breakdown to smaller scale turbulence. Further downstream of the jet, mostly two types of coherent structures remain. The CVP creates a large scale circulation which mixes the freestream fluid with the injected fluid. Then, the turbulence in the wake region permits a good mixing at the molecular level. Also, intermittent wake vortices are formed and connect the CVP to the bottom wall boundary layer. A series of wake vortices is visible in fig. 5.16(b) for case C. These structures are formed on the lateral sides of the jet, and were found not to participate in the mixing process of this interaction, as they do not carry any of the jet fluid.

5.5 Computational Performance and Model Analysis

The simulations of JICF presented here have required about 10,000 single CPU hours of computation to wash out all the transients of the initialization, and the statistics have been collected over five flow through times, which have required around 15,000 hours for each coarse case. The finer resolution of the JICF case A required over 80,000 single CPU hours before to reach statistically stationary state, and to collect statistics. 8% of the streamwise fluxes and 5% of the spanwise and crosswise fluxes have required the use of upwinding. The switching of the hybrid method being localized, the upwind fluxes were evaluated when necessary only, and the computational overhead due to the hybrid scheme is rather limited.

The closure coefficients have been computed dynamically using the LDKM closure model described in section 2.3.2. These coefficients vary significantly in both space and time during the course of the simulations. This is illustrated in Fig. 5.17, where instantaneous and time-averaged fields of the subgrid turbulent kinetic energy and of the closure coefficients are presented.

On the instantaneous fields, it is clear that the jet shear layer is a region of intense turbulent activity. The model coefficients reach rather high values on both the windward and leeward sides, and peak significantly close to the Mach disk, due to the high levels of fluctuations of the jet boundary. The coefficients correlate with the coherent structures elsewhere in the flow. More particularly, c_ν reaches relatively high values in the plume and wake of the jet. The dissipation of k^{sgs} remains relatively small in these regions, and peaks very locally. The variations of c_ν/Pr_t show how the turbulent diffusion of total and turbulent energy is increased in the regions of shock waves, and along the jet shear layer, where high gradients of temperature are present.

Despite these high levels of unsteadiness, the dynamically computed model coefficients reach a statistically stationary behavior. As observed in the instantaneous fields, the levels of turbulence are quite high in the jet shear, and the closure coefficient for the subgrid stress and the dissipation of k^{sgs} reach relatively high values,

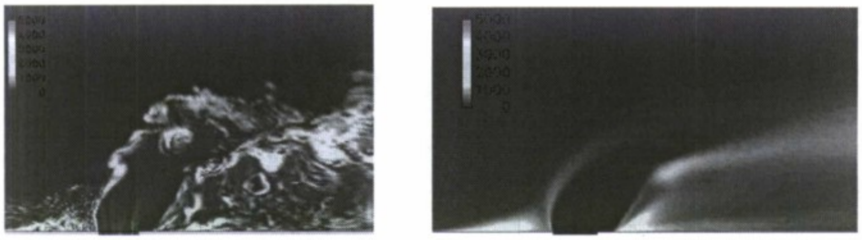

(a) Instantaneous k^{sgs} (b) Average k^{sgs}

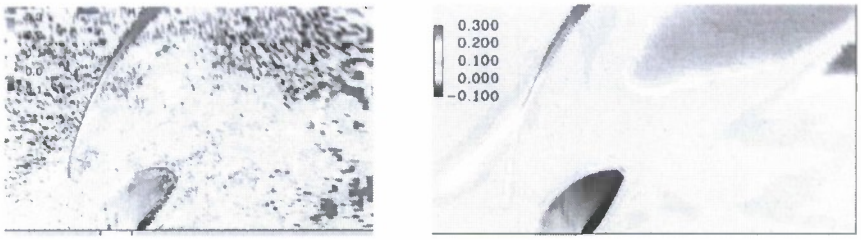

(c) Instantaneous c_ν (d) Average c_ν

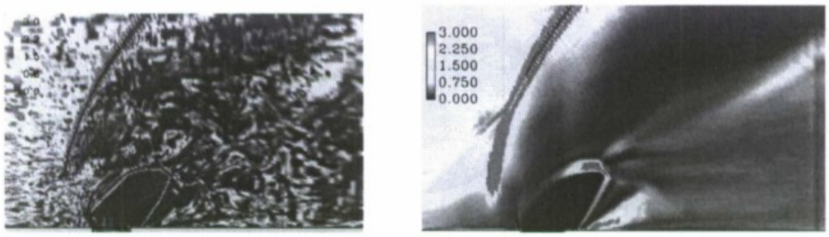

(e) Instantaneous c_ϵ (f) Average c_ϵ

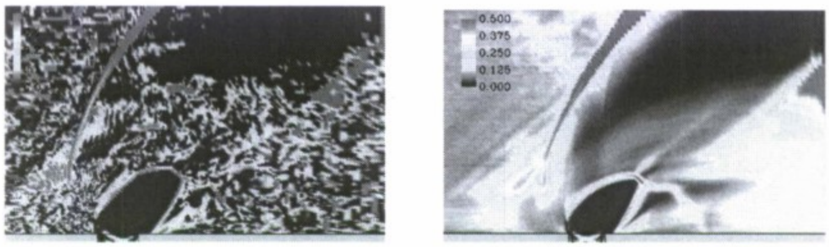

(g) Instantaneous c_ν/Pr_t (h) Average c_ν/Pr_t

Figure 5.17: Closure coefficient contours for case A of the JICF - Instantaneous and time-averaged fields.

c_ν approaching 0.15, and c_ϵ reaching its peak value above the Mach disk. The field of c_ν/Pr_t shows that the diffusion of energy is also important in the jet shear region. The average turbulent Prandtl number in this region varies between 0.45 and 0.7. In the separated boundary layer, a diminution of the dissipation coefficient is obtained. This region is a recirculation, where turbulent structures of the incoming boundary layer are being sheared by the upper boundary layer and the jet shear. Furthermore, diffusion of k^{sgs} due to pressure fluctuations is induced by the shock / boundary layer interaction. Overall, there is an accumulation of subgrid kinetic energy in this region which plays a fundamental role in the dynamics of the interaction.

In the present calculations, the closure for the pressure dilatation correlation was found to remain very small throughout the calculation, representing less than 1% of the dissipation everywhere except within the shock thickness. There the dilatational field is associated with the shock wave, and is not related to the compressible turbulent field. This term, like all viscous and k^{sgs} terms, is not explicitly computed within the shock thickness.

The impact of the closure on the flow evolution is assessed by repeating the simulation of Case A, performed as an under-resolved DNS (no-model simulation), and using the LDKM closure model without compressibility corrections (Following previous studies, the turbulent Prandtl is set to $Pr_t = 0.9$, and this closure is hereafter noted $LDKM_{NCC}$), and comparing these results to the simulation presented earlier (the closure model with compressibility corrections will be simply noted LDKM). The profiles of mean and fluctuating velocities for all cases are shown in Fig. 5.18 and 5.19, respectively. The predictions of the mean flow velocity profiles are not significantly affected by the closure model. All three simulations show similar captures of the velocity defect in the jet plume and in the wake. The differences are, however, clearly visible in the profiles of fluctuating velocities. The fluctuations in axial velocity at the first station are under-estimated by the no-model and $LDKM_{NCC}$ simulations, whereas the present LDKM approach correctly captures the peak in u_{rms} that occurs in the jet plume. Further downstream, the under-resolved simulation over-estimates the levels of fluctuations, and does not capture the turbulence evolution in the jet plume. The other numerical simulations recover the amplitude of the velocity fluctuations and compare well. It should be noted, however, that the turbulent statistics within the boundary layer are not captured by either model, but that the simulation using LDKM shows a peak in axial velocity fluctuations within the boundary layer, in agreement with the experimental observations.

The fluctuations in transverse velocities show a more significant impact of the closure model. At the first station, the simulation using LDKM over-predicts the peak in v_{rms} more significantly than the other numerical resolutions. The trend is however inverted further downstream, as the simulation with LDKM does recover the amplitude of v_{rms} in the jet plume, and shows a better capture of the transverse velocity fluctuations evolution than the other two approaches.

The differences between the LDKM and the no-model simulations can be easily conceived from the lack of dissipation in the under-resolved simulation. In this case, the rates of decay of the fluctuations is under-estimated, and the jet penetration is over-estimated. To assess the differences between $LDKM_{NCC}$ and LDKM, it is

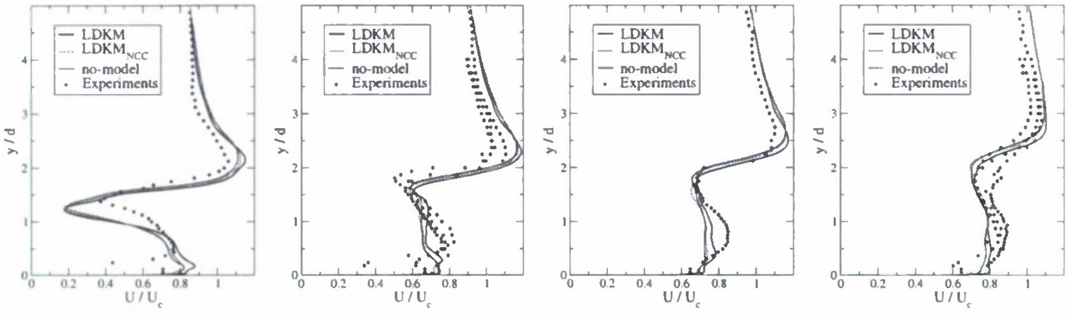

(a) U/U_c at $x/d =$ 2

(b) U/U_c at $x/d =$ 3

(c) U/U_c at $x/d =$ 4

(d) U/U_c at $x/d =$ 5

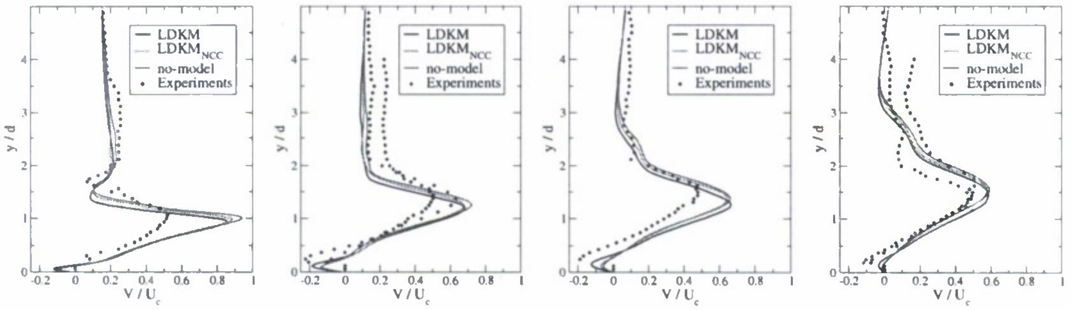

(e) V/U_c at $x/d =$ 2

(f) V/U_c at $x/d =$ 3

(g) V/U_c at $x/d =$ 4

(h) V/U_c at $x/d =$ 5

Figure 5.18: Profiles of mean axial and transverse velocities in the centerplane at four locations downstream of the injection. Comparison between no-model, classical LDKM (denoted $LDKM_{NCC}$) and the coarse grid results presented earlier.

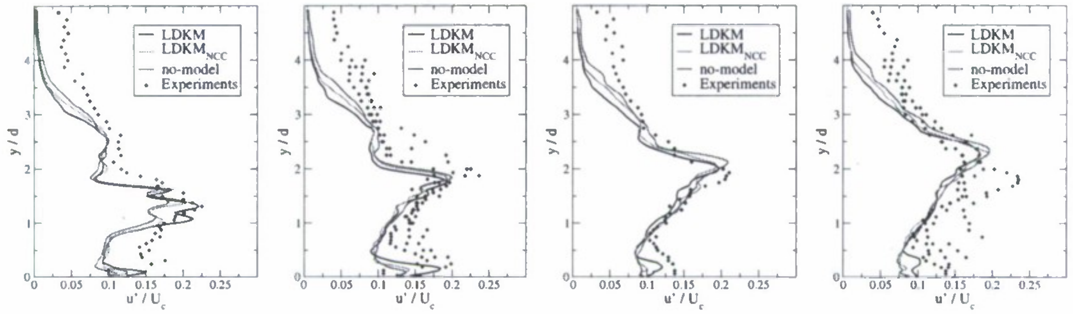

(a) u_{rms}/U_c at $x/d = 2$

(b) u_{rms}/U_c at $x/d = 3$

(c) u_{rms}/U_c at $x/d = 4$

(d) u_{rms}/U_c at $x/d = 5$

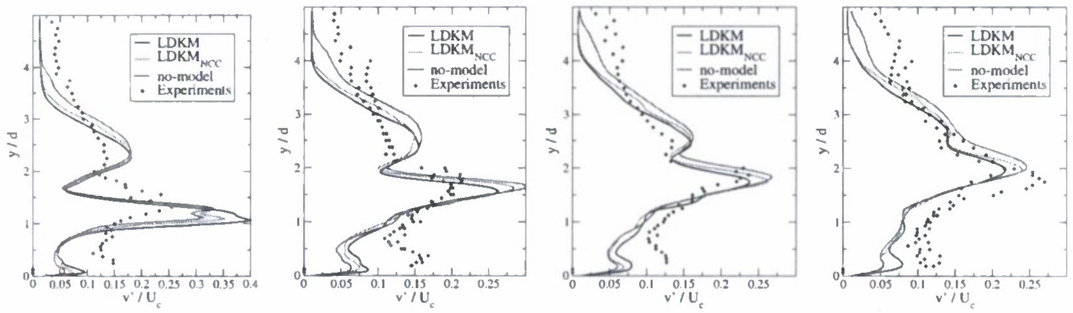

(e) v_{rms}/U_c at $x/d = 2$

(f) v_{rms}/U_c at $x/d = 3$

(g) v_{rms}/U_c at $x/d = 4$

(h) v_{rms}/U_c at $x/d = 5$

Figure 5.19: Profiles of fluctuating axial velocity statistics in the centerplane at four locations downstream of the injection. Comparison between no-model, classical LDKM (denoted $LDKM_{NCC}$) and the coarse grid results presented earlier.

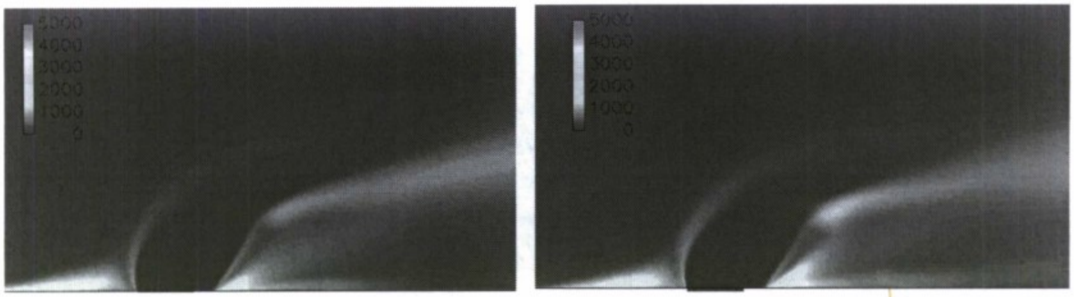

(a) $LDKM_{NCC}$ (b) LDKM

Figure 5.20: Contours of time averaged k^{sgs} for the simulation of Case A using $LDKM_{NCC}$ and LDKM.

interesting to compare the time averaged fields of k^{sgs} for the two simulations, shown in Fig. 5.20 The turbulent Prandtl number obtained through the dynamic procedure is smaller than in the classical LDKM approach, and leads to a higher diffusion of the energy across the shear layers. Furthermore, the diffusion of k^{sgs} due to pressure fluctuations can clearly be observed in Fig. 5.20, where the contours of subgrid kinetic energy in the mean barrel shock location are more diffuse. Furthermore, the intensity of k^{sgs} in the recirculation region at the windward side, and at the leeward boundary of the jet, is higher for the LDKM simulation. As a consequence, the LDKM closure model shows a better capture of the turbulent decay in the wake of the jet. Furthermore, despite the rather coarse resolution of the bottom wall, the LDKM simulation captures an increase in the levels of k^{sgs} in the near-wall region, whereas the $LDKM_{NCC}$ fails to capture that phenomenon.

5.6 Conclusion of the Jet in Crossflow Dynamical Study

The vortical structures of a sonic jet injected into a supersonic crossflow have been studied using a Large Eddy Simulation methodology, adapted to the resolution and modeling of turbulence in compressible flows. The present approach has been validated by comparisons with a series of experimental data (Santiago [1995], Santiago and Dutton [1997]) and the relevance of the grid resolution assessed. This base case has been complemented by two other operating conditions, designed to assess the impact of the free-stream Mach number and of the jet to momentum ratio on the flow average and dynamic vortical structures.

Six types of vortical structures have been identified in the time-averaged fields. The bow shock in from the jet provokes the separation of the boundary layer, and two recirculation regions are formed in the separated zone. This vortical structure is found at the bottom wall all along the bow shock trajectory in the spanwise direction. A pair of windward vortices is generated at the tip of the recirculation region, and extends along the upper jet boundary. This feature is present in all the cases considered in the present study, but is more clear for high jet to freestream momentum ratios. On the lateral sides of the jet, hanging vortices are formed along the expanding jet, and remain quasi-steady in the course of the interaction. On the leeward side of the jet, a pair of steady wake vortices is generated by the rapid re-centering of the mean flow towards the centerplane behind the jet. As the streams impact at the centerplane, a high pressure zone is created, which generates two outwards moving shocks and a strong upwash velocity. The shocks interact with the boundary layer and generate horseshoe vortices through local separation. The upwash velocity penetrates the jet plume, and generates the counter-rotating vortex pair in the wake of the jet.

The flow dynamics resembles the subsonic jet in cross flow behavior as large vortices are formed on the windward side of the jet due to Kelvin-Helmholtz instabilities. This phenomenon is however enhanced in the present supersonic flow. The flow expansion at the nozzle of the jet varies in response to the large pressure fluctuations of the separated boundary layer, and the intermittent formation of compression waves within the under-expanded jet occurs. These waves propagate into the jet and strengthen into shocks. Finally, after reconnecting to another portion of the barrel shock further downstream, large pockets of jet fluid are ejected, with a high vertical velocity, hence generating intense vortices along the jet boundary. These jet shocks are three-dimensional and the vortical structures generated by this phenomenon wrap around the jet. Similarly, unsteady compression waves form along the sides of the jet, hence generating lateral vortices. These structures also engulf large amounts of freestream fluid, and carry it in the jet plume and wake regions. Their strength is found weaker than their circumferential counterpart. Windward vortices are observed in the instantaneous fields, and are subject to vortex sheet instability, but do not initiate strong vorticity, and do not contribute significantly to the mixing occurring during the interaction.

The mixing of jet and freestream fluids is achieved in the wake and plume of the jet. The counter-rotating vortex pair creates a large circulation and efficiently induces mixing at the large scales. The unsteady vortices generated in the close-jet region breakdown into smaller scale turbulent as they interact with the low velocity jet plume and achieve a fine mixing at the molecular level. The unsteady wake vortices that connect the mixing region to the bottom wall boundary layer were found to play no role in the mixing process in the cases considered in the present study.

CHAPTER VI

CONCLUSION AND RECOMMENDATIONS

6.1 Conclusion

The focus of the present was the development of a Large Eddy Simulation methodology adapted to the resolution of supersonic turbulent flows in complex geometries. To achieve this goal, two key objectives have been identified and addressed.

The development of a numerical tool adapted to the resolution of turbulent structures on body-conforming structured grid in supersonic flows was considered first. The simulation of turbulent flows with explicit turbulence modeling usually relies on the use of numerical schemes with low levels of intrinsic dissipation. These schemes behave poorly in the presence of shock waves, contact surfaces and other discontinuities. Upwind and shock capturing schemes, on the other hand, are too dissipative to be used for the resolution of turbulent flows. A hybrid numerical scheme was designed to circumvent these limitations. In this hybrid framework, the resolution of the flow structures is performed using a fourth-order central scheme while flow discontinuities are captured using an upwind shock-capturing method. The reduced amount of numerical dissipation of the central scheme and its small stencil formulation make it an ideal candidate for simulating turbulent flows in complex geometries. The developed upwind shock-capturing method was carefully designed to reduce numerical instabilities and yet to yield accurate capture of shocks and contact surfaces. Furthermore, this upwind scheme is adapted to body-conforming grids and can thus be used in complex geometries. The hybrid formulation uses a smoothness sensor in order to identify the discontinuous regions of the flow. Numerical fluxes are evaluated using the fourth-order central scheme but locally revert to the shock capturing method when the smoothness constraint is violated.

The second development focused on the closure approach used to model the effect of subgrid turbulence on the resolved scales in compressible flows. The need for such development stemmed from the fact that closure models employed in compressible LES formulations have usually not been assessed for compressible turbulence, but rather have been calibrated in the incompressible flow limit. In the present work, the Localized Dynamic k^{sgs} Model (LDKM) is re-derived for compressible flows, and the dynamic formulation of the closure coefficients re-assessed. The model is extended to include the dynamic evaluation of the coefficient required for the closure of the energy equation, important in compressible flows. Finally, the turbulent diffusion associated with subgrid pressure fluctuations, which plays a major role during shock / turbulence interactions, and the pressure dilatation correlation are modeled and their closure coefficients are dynamically evaluated in the context of the LDKM closure.

The present study focuses on the resolution of turbulent flows in supersonic environment. The parameters used for the switch formulation of the hybrid methodology were designed to capture flow discontinuities locally in supersonic and hypersonic environments, and even though not *universal*, the present choice of switch parameter shows a satisfactory resolution of practical problems in supersonic flows. The modifications to the closure approach are based on analytical studies of turbulence states in compressible flows. The contribution of the dilatational mode of turbulence, the evaluation of the pressure dilatation correlation and the negligible contribution of the dilatational dissipation remain valid for small turbulent Mach numbers ($M_t < 0.3$), a condition satisfied in supersonic flows, but not necessarily for higher flow speeds. Based on these limitations, the present numerical methodology is applicable from low compressible to supersonic flows.

Direct numerical simulations of shock / isotropic turbulence interactions for low, intermediate and high Mach numbers have been conducted and show the good performance of the numerical scheme. The use of upwinding is limited to the regions of strong gradients whereas the turbulent structures are resolved with the central scheme. As a consequence, the characteristic evolution of the turbulent field is correctly captured. The resolution of these problems on a significantly coarser grid using the LDKM model with compressibility correction successfully reproduces the statistics of turbulence.

After validation in the fundamental configuration of shock / turbulence interactions, this LES methodology was employed to study problems of practical importance. In particular, two mixing techniques for high-speed flows have been investigated in this study. First, the efficiency of a shock / turbulent shear layer interaction as a mixing enhancement technique was investigated. It was found that the passage of large vortical structures and smaller vortical turbulence across the shocks significantly increases the levels of turbulence in the post-shocks region, resulting in an increase of the mixing growth rate. On the other hand, the turbulence production across the mixing layer remains rather low, and the increase in mixing and turbulent dynamics is not sustained downstream of the interaction. The improvements in mixing are thus very localized in space, and the mixing growth rate quickly decays to its undisturbed value.

The second case considered in the present work is that of a sonic jet injected normally into a supersonic crossflow. This injector design for scramjet applications shows a good penetration of the fuel into the cross stream, and an efficient mixing of the fluids is achieved due to the high levels of turbulence observed downstream of the jet. The numerical study of jet in crossflow presented in this report reproduce the velocity defect and high levels of turbulent fluctuations observed experimentally in the plume of the jet, and showed a fair agreement with the available experimental data. Having validated the LES approach for a given jet in crossflow, two other configurations were investigated to assess the impact of the free-stream Mach number and of the jet to free stream momentum ratios on the flow dynamics. In all the cases considered, the ejection of large pockets of unshocked jet fluids is identified, due to unsteady compressions and localized shock waves within the jet core. The vortical structures that result from this phenomenon show high levels of vorticity, and mix jet and freestream fluids at the large scale. Due to a higher jet expansion, the cases of higher momentum ratio and higher Mach number show a lower penetration of the shock waves into the jet core, and smaller pockets of unshocked fluid. The counter-rotating vortex pair formed in the wake of the jet also contributes to the large scale mixing. High levels of turbulence in the plume and wake of the jet permit mixing to occur at smaller scales. Finally, quasi-steady hanging vortices are formed during these high-speed interactions, and windward vortex pairs are clearly identified in the higher momentum ratio jet in crossflow. Their contribution to the mixing remains rather low.

All cases reported in this study demonstrate the accuracy and strength of the implemented approach. The use of an hybrid formulation provided the required methodology for the capture of shock waves and other discontinuities locally in space, while minimizing their impact on the turbulent field, as illustrated by the direct simulations of shock / turbulence interaction. The closure model explicitly accounts for two major terms that arise in turbulence of compressible flows, namely the subgrid pressure fluctuations and the pressure dilatation correlation, and the LES simulations of shock / turbulence interactions show a good capture of the flow physics. This methodology allowed for an in-depth study of shock / shear interaction and high-speed jet in crossflow configurations.

6.2 Recommendations for Future Work

In problems involving shock / turbulence interactions, turbulence enhancement is achieved in the post-shock region as a consequence of the shock deformation. The localized expansions and compressions formed by the shock corrugation increase the energy in the acoustic mode, and amplify the levels of turbulent stresses through an energy transfer. The capture of these phenomena requires a proper capture of the shock fronts and of their distortion. A good resolution of the shock fronts was possible for the configurations studied here. but this requirement might not always be easily satisfied for more complex and larger geometries, given that computational power remains limited. The implementation of a Local and Adaptive Mesh Refinement technique can be a useful complement to the developments presented here. In this method, the spatial resolution can be increased locally to resolve some parts of the flow that require higher grid refinements. The connectivity between blocks of different resolution is based on higher order interpolation techniques. The implementation of such a method in the context of LES is more intricate than for classical hydrodynamics problems. The flow variables are, by definition, spatially averaged, and a simple interpolation procedure might be insufficient. This is of particular importance for the k^{sgs} variable, which depends by definition on the local grid size, and cannot be simply interpolated. Nevertheless, the development and implementation of such a technique for LES would be beneficial, for the practical resolution of high-speed turbulent flows and for many more applications.

As reviewed earlier, the closure model developed during the present work aims at the resolution of turbulent compressible flows. Even though the mean flow might be compressible, it is stressed that turbulence is only weakly compressible in nature, and that compressible turbulence does not play a major role in most practical applications until hypersonic speeds are reached. For this reason, the current developments have solely focused on the modeling of turbulent diffusion due to pressure fluctuations and to the pressure dilatation correlation. In particular, the dilatational dissipation was neglected, as this phenomenon is important in low Reynolds number, high turbulent Mach number flows only. It can be expected that in hypersonic flows or in the study of post explosion turbulence, the amount of compressible turbulence might not be negligible anymore and may require a separate modeling approach. Furthermore, another source of turbulent dissipation comes from the presence of eddy shocklets. These small scales and localized shock waves, observed in experiments of very high speed shear layers, form in the presence of compressible turbulence and interact with both solenoidal and dilatational turbulence. A stochastic model to account for these phenomena might be needed as well.

Also, the present study has focused on the resolution and modeling of turbulence in high-speed, non-reacting flows. In the context of reacting flows, the treatment of the scalar fields requires particular attention, as the interaction between turbulence and flame fronts plays a fundamental role in the combustion processes and on the overall efficiency. Closure models for the subgrid species diffusion and filtered reaction rates are often valid in the incompressible limit, but might not be assessed for supersonic flows. Improvements on scalar closure models are a necessity to the future of scramjet simulations. The extension of the Linear Eddy Mixing model, for instance, to flows with significant variations in the pressure field would provide an efficient numerical tool for scramjet flow simulations.

Bibliography

N. A. Adams and K. Shariff. A high-resolution hybrid compact-ENO scheme for shock-turbulence interaction problems. *Journal of Computational Physics*, 127: 27–51, 1996.

V. Adumitroaie, J. R. Ristorcelli, and D. B. Taulbee. Progress in Favré-Reynolds stress closures for compressible flows. *Physics of Fluids*, 11(9):2696–2719, 1999.

J. H. Agui, G. Briassulis, and Y. Andreopoulos. Studies of interactions of a propagating shock wave with decaying grid turbulence: velocity and vorticity fields. *Journal of Fluid Mechanics*, 524:143–195, 2005.

J. D. Anderson. *Modern Compressible Flow (with historical perspective),* 3rd *Ed.* McGraw Hill Publishing Co.,, 2003.

J. Andreopoulos. On the structure of jets in a crossflow. *Journal of Fluid Mechanics*, 157:163–197, 1985.

Y. Andreopoulos, J. H. Agui, and G. Briassulis. Shock wave-turbulence interactions. *Annual Review of Fluid Mechanics*, 32:309–345, 2000.

M. F. Barone, W. L. Oberkampf, and F. G. Blottner. Validation case study: Prediction of compressible turbulent mixing layer growth rate. *AIAA Journal*, 44(7): 1488–1497, 2006.

S. Barre, D. Alem, and J. P. Bonnet. Experimental study of a normal shock/homogeneous turbulence interaction. *AIAA Journal*, 34(5):968–974, 1996.

F. Bataille, Y. Zhou, and J.-P. Bertoglio. Energy transfer and triadic interactions in compressible turbulence. *ICASE Report No. 97-62*, 1997.

P. Batten, N. Clarke, C. Lambert, and D. M. Causon. On the choice of wavespeeds for the HLLC Riemann solver. *SIAM Journal of Scientific Computing*, 18(6):1553–1570, 1997.

A. Ben-Yakar and R. K. Hanson. Experimental investigation of flame-holding capability of a transverse hydrogen jet in supersonic crossflows. *Proceedings of the Combustion Institute*, 27:2173–2180, 1998.

A. Ben-Yakar, M. G. Mungal, and R. K. Hanson. Time evolution and mixing characteristics of hydrogen and ethylene transverse jets in supersonic crossflows. *Physics of Fluids*, 18(026101), 2006.

C. Berthon. Stability of the MUSCL schemes for the euler equations. *Communications in Mathematical Sciences*, 3(2):133–157, 2005.

P. Bradshaw. Compressible turbulent shear layers. *Annual Review of Fluid Mechanics*, 9:33–54, 1977.

G. L. Brown. The entrainment and large structure in turbulent mixing layers. *Proceedings of the 5th Australasian conference on hydraulics and fluid dynamics*, pages 775–816, 1974.

D. R. Buttsworth. Interaction of oblique shock waves and planar mixing regions. *Journal of Fluid Mechanics*, 306:43–57, 1996.

W. H. Calhoon, K. W. Brinckman, J. Tomes, S. J. Mattick, and S. M. Dash. Scalar fluctuation and transport modeling for to high speed reacting flows. *AIAA paper 2006-1452*, 2006.

L. N. I. Cattafesta and G. S. Settles. Experiments on shock/vortex interactions. *AIAA Paper 92-0315*, 1992.

A. J. Chambers, R. A. Antonia, and L. Fulachier. Turbulent prandtl number and spectral characteristics of a turbulent mixing layer. *International Journal on Heat and Mass Transfer*, 28(8):1461–1468, 1985.

S.-M. Chang, K.-S. Chang, and S. Lee. Reflection and penetration of a shock wave interacting with a starting vortex. *AIAA Journal*, 42(4):796–805, 2004.

Y. Chauvat, J.-M. Moschetta, and J. Gressier. Shock wave numerical structure and the carbuncle phenomenon. *International Journal for Numerical Methods in Fluids*, 47:903–909, 2005.

C. F. Chenault, P. S. Beran, and R. D. W. Bowersox. Numerical investigation of supersonic injection using a Reynolds-stress turbulence model. *AIAA Journal*, 37 (10):1257–1269, 1999.

B.-T. Chu and L. S. G. Kovásznay. Non-linear interactions in a viscous heat-conducting compressible gas. *Journal of Fluid Mechanics*, 3:494–514, 1958.

P. Colella and P. Woodward. The piecewise-parabolic method for hydrodynamics. *Journal of Computational Physics*, 54:174–201, 1984.

A. W. Cook and W. H. Cabot. A high-wavenumber viscosity for high resolution numerical method. *Journal of Computational Physics*, 195:594–601, 2004.

E. T. Curran and S. N. B. Murthy. Scramjet propulsion. *Progress in Astronautics and Aeronautics*, 189:20–21, 2000.

S. F. Davis. Simplified second-order Godunov-type methods. *SIAM J. Sci. Stat. Comput.*, 9:445–473, 1988.

B. J. Delarue and S. J. Pope. Application of pdf methods to compressible turbulent flows. *Physics of Fluids*, 9:2704–2715, 1997.

F. Dexun and M. Yanwen. Analysis of super compact finite difference method and application to simulation of vortex-shock interaction. *International Journal for Numerical Methods in Fluids*, 36:773–805, 2001.

D. A. Dickmann and F. K. Lu. Jet in supersonic crossflow on a flat plate. *AIAA paper 2006–3451*, 2006.

P. E. Dimotakis. Two-dimensional shear-layer entrainment. *AIAA Journal*, 24:1791–1796, 1986.

L. Doris, C. Tenaud, and L. Ta Phuoc. LES of spatially developing 3d compressible mixing layer. *Comptes-rendus de l'Academie des Sciences de Paris, Série IIb*, 328 (7):567–573, 2000.

D. S. Dosanjh and T. M. Weeks. Interaction of a starting vortex as well as a vortex street with a traveling shock wave. *AIAA Journal*, 3(2):216–223, 1965.

J. P. Drummond and H. S. Mukunda. A numerical study of mixing enhancement in supersonic reacting flow fields. *AIAA 88-3260*, 1989.

Y. Dubief and F. Delcayre. On coherent-vortex identification in turbulence. *Journal of Turbulence*, 1:11, 2000.

T. Dubois, J. A. Domaradzki, and A. Honein. The subgrid-scale estimation model applied to large eddy simulations of compressible turbulence. *Physics of Fluids*, 14: 1781–1801, 2002.

F. Ducros, V. Ferrand, F. Nicoud, C. Weber, D. Darracq, C. Gacherieu, and T. Poinsot. Large eddy-simulation of the shock/turbulence interaction. *Journal of Computational Physics*, 152:517–549, 1999.

P. A. Durbin and O. Zeman. Rapid distortion theory for homogeneous compressed turbulence, with applications to modeling. *Journal of Fluid Mechanics*, 242:349, 1992.

J.-P. Dussauge. Compressible turbulence and energetic scales: What is known from experiments in supersonic flows? *Flow, Turbulence and Combustion*, 66:373–391, 2001.

J.-P. Dussauge. Compressible turbulence of supersonic flows: Actions and interactions. *Proceedings of the Symposium Turbulence and Interactions, Porquerolles, France, May 29-June 02*, 2006.

B. Einfeldt. On Godunov-type methods for gas dynamics. *SIAM J. Numer. Anal.*, 25(2):294–318, 1988.

B. Einfeldt, C. D. Munz, P. L. Roe, and B. Sjogreen. On Godunov-type methods near low densities. *Journal of Computational Physics*, 92:273–295, 1991.

A. M. El Baz. Modeling compressibility effects on free turbulent shear flows. *5th biennal Colloquium on Computational Fluid Dynamics*, 1992.

J. L. Ellzey, M. R. Henneke, J. M. Picone, and E. S. Oran. The interaction of a shock with a vortex: Shock distortion and the production of acoustic waves. *Physics of Fluids*, 7(1):172–184, 1995.

D. E. Everett, M. A. Woodmensee, J. C. Dutton, and M. J. Morris. Wall pressure measurements for a sonic jet injected transversely into a supersonic crossflow. *Journal of Propulsion and Power*, 14(6):861–868, 1998.

H. F. Fasel, D. A. von Terzi, and R. D. Sandberg. A methodology for simulating compressible turbulent flows. *Journal of Applied Mechanics*, 73(3):405–412, 2006.

G. Fauchet and J.-P. Bertoglio. An analytical expression for the spectrum of compressible turbulence in the low Mach number limit. *Advances in Turbulence VII*, pages 317–332, 1998.

G. Fauchet and J.-P. Bertoglio. Régimes pseudo-son et acoustique en turbulence compressible. *Comptes-rendus de l'Academie des Sciences de Paris, Série Ib*, 327: 665–671, 1999.

V. Fortuné, E. Lamballais, and Y. Gervais. Noise radiated by a non-isothermal, temporal mixing layer. part i: Direct computation and prediction using compressible DNS. *Theoretical and Computational Fluid Dynamics*, 18:61–81, 2004.

T. F. Fric and A. Roshko. Vortical structure in the wake of a transverse jet. *Journal of Fluid Mechanics*, 279:1–47, 2004.

R. Friedrich and F. P. Bertolotti. Compressibility effects due to turbulent fluctuations. *Applied Scientific Research*, 57:165–194, 1997.

B. Fryxell and S. Menon. Large-eddy simulation of Richtmyer-Meshkov instability. *AIAA Paper 2005-0314*, 2005.

B. Fryxell, E. Müller, and D. Arnett. Hydrodynamics and nuclear burning. *Max-Planck-Institute für Astrophysik Report 449*, 1989.

B. Fryxell, K. Olson, P. Ricker, F. X. Timmes, M. Zingale, D. Q. Lamb, P. MacNeice, R. Rosner, J. W. Truran, and H. Tufo. Flash: An adaptive mesh hydrodynamics code for modeling astrophysical thermonuclear flashes. *The Astrophysical Journal Supplement Series*, 131:273–334, 2000.

S. Fu and Q. Li. Numerical simulation of compressible mixing layers. *International Journal of Heat and Fluid Flow*, 27:895–901, 2006.

C. Fureby and S. I. Moller. Large-eddy simulations of reacting flows applied to bluff-body stabilized flames. *AIAA Journal*, 33:2339, 1995.

E. Garnier, P. Sagaut, and M. Deville. A class of explicit ENO filters with application to unsteady flows. *Journal of Computational Physics*, 170:184–204, 2001.

E. Garnier, P. Sagaut, and M. Deville. Large eddy simulation of shock/homogeneous turbulence interaction. *Computers & Fluids*, 31:245–268, 2002.

M. Germano, P. Piomelli, U. Moin, and W. H. Cabot. A dynamic sub-grid scale eddy viscosity model. *Center for Turbulence Research, Proceedings of the Summer Program*, pages 5–17, 1990.

S. K. Godunov. A finite difference method for the computation of discontinuous solutions of the equations of fluid dynamics. *Mat. Sbornik*, 47:357–393, 1959.

S. G. Goebel and J. C. Dutton. Experimental study of compressible turbulent mixing layers. *AIAA Journal*, 29:538–546, 1991.

S. Gordon and B. J. McBride. Computer program for calculation of complex chemical equilibrium compositions and applications. NASA Reference Publication 1311, NASA, 1994.

D. Gottlieb and E. Turkel. Dissipative two-four methods for time-dependent problems. *Mathematics of Computation*, 30(136):703–723, 1976.

M. Gruber, R. Baurle, T. Mathur, and K.-Y. Hsu. Fundamental studies of cavity-based flameholder concepts for supersonic combustors. *AIAA Paper 99-2248*, 1999.

M. Gruber, J. Donbar, T. Jackson, T. Mathur, D. Eklund, and F. Billig. Performance of an aerodynamic ramp fuel injector in a scramjet combustor. *AIAA Paper 2000-3708*, 2000.

M. R. Gruber, A. S. Nejad, T. H. Chen, and J. C. Dutton. Mixing and penetration studies of sonic jets in a Mach 2 freestream. *Journal of Propulsion and Power*, 11 (2):315–323, 1995.

M. R. Gruber, A. S. Nejad, T. H. Chen, and J. C. Dutton. Compressibility effects in supersonic transverse injection flowfields. *Physics of fluids*, 9(5):1448–1461, 1997.

M. R. Gruber, A. S. Nejad, and J. C. Dutton. An experimental investigation of transverse injection from circular and elliptical nozzles into a supersonic crossflow. *Wright Lab Technical Report WL-TR-96-2102*, 1996.

K. F. Gurski. An HLLC-type approximate Riemann solver for ideal magnetohydrodynamics. *SIAM J. Sci. Comput.*, 25:2165, 2005.

F. Hamba. Modeling of inhomogeneous compressible turbulence using a two-scale statistical theory. *Center for Turbulence Research, Annual Research Briefs-1996*, pages 53–66, 1996.

R. Hannappel and R. Friedrich. Direct numerical simulation of a Mach 2 shock interacting with isotropic turbulence. *Applied Scientific Research*, 54:205–221, 1995.

A. Harten. The artificial compression method for computation of shocks and contact discontinuities: III. self-adjusting hybrid schemes. *Mathematics of Computation*, 32:363–389, 1978.

A. Harten. High resolution schemes for hyperbolic conservations laws. *Journal of Computational physics*, 49:357–393, 1983.

A. Harten, B. Engquist, S. Osher, and S. R. Chakravarthy. Uniformly high order accurate essentially non-oscillatory schemes iii. *Journal of Computational Physics*, 71:231–303, 1987.

A. Harten, P. D. Lax, and B. van Leer. On upstream differencing and Godunov-type schemes for hyperbolic conservation laws. *SIAM Review*, 25:35–61, 1983.

A. Harten and G. Zwas. Self-adjusting hybrid schemes for shock computations. *Journal of Computational Physics*, 9:568–583, 1972.

D. J. Hill, C. Pantano, and D. I. Pullin. Large-eddy simulation and multiscale modelling of a Richtmyer-Meshkov instability with reshock. *Journal of Fluid Mechanics*, 557:29–61, 2006.

D. J. Hill and D. I. Pullin. Hybrid tuned center-difference-WENO method for large eddy simulations in the presence of strong shocks. *Journal of Computational Physics*, 194:435–450, 2004.

C. Hirsch. *Numerical computation of internal and external flows*, volume 2. John-Wiley and Sons, Inc., 1997.

A. Honkan and J. Andreopoulos. Rapid compression of grid-generated turbulence by a moving shock wave. *Physics of Fluids A*, 4:2562–2572, 1992.

O. Inoue and Y. Hattori. Sound generated by shock-vortex interactions. *Journal of Fluid Mechanics*, 380:81–116, 1999.

L. Jacquin, C. Cambon, and E. Blin. Turbulence amplification by a shock wave and rapid distortion theory. *Physics of Fluids A*, 5:2539–2550, 1993.

A. Jameson and T. J. Baker. Solution of the euler equations for complex configurations. *AIAA 83-1929*, 1983.

A. Jameson, W. Schmidt, and E. Turkel. Numerical solution of the euler equations by finite volume methods using runge-kutta time stepping schemes. *AIAA 81-1259*, 1981.

S. Jamme, J. Cazalbou, F. Torres, and P. Chassaing. Direct numerical simulation of the interaction between a shock wave and various types of isotropic turbulence. *Flow, Turbulence and Combustion*, 68(3):227–268, 2002.

S. Jamme, M. Crespo, and P. Chassaing. Direct numerical simulation of the interaction between a shock wave and anisotropic turbulence. *AIAA 2005-4886*, 2005.

Y. Kaneda, T. Ishihara, M. Yokokawa, K. Itakura, and A. Uno. Energy dissipation rate and energy spectrum in high resolution direct numerical simulations of turbulence in a periodic box. *Physics of Fluids*, 15(2):21–24, 2003.

S. Kawai and S. K. Lele. Mechanisms of jet mixing in a supersonic crossflow: A study using large-eddy simulation. *AIAA paper 2008-4575*, 2008.

M. J. Kermani and E. G. Plett. Modified entropy correction formula for the roe scheme. *AIAA-2001-0083*, 2001.

D. Kim and J. H. Kwon. A high-order accurate hybrid scheme using a central flux scheme and a WENO scheme for compressible flowfield analysis. *Journal of Computational Physics*, 210:554–583, 2005.

W.-W. Kim and S. Menon. A new dynamic one-equation subgrid-scale model for large-eddy simulations. *AIAA-95-0356*, 1995.

D. Knight, G. Zhou, N. Okong'o, and V. Shukla. Compressible large eddy simulation using unstructured grids. *AIAA-98-0535*, 1998.

D. D. Knight. Inflow boundary conditions for dns and les of compressible turbulent boundary layers. *AIAA-2006-498*, 2006.

L. S. G. Kovásznay. Turbulence in supersonic flow. *J. Aero. Sci.*, 20:657–682, 1953.

R. H. Kraichnan. Eddy viscosity in two and three dimensions. *Journal of Atmospheric Sciences*, 33:1521–1536, 1976.

F. Ladeinde, E. E. O'Brien, and X. D. Cai. A parallelized ENO procedure for direct numerical simulation of compressible turbulence. *Journal of scientific computing*, pages 179–205, 1996.

A. Lapidus. A detached shock calculation by second-order finite differences. *Journal of Computational Physics*, 2:154–177, 1967.

P. D. Lax. Hyperbolic systems of conservation laws and the mathematical theory of shock waves. *SIAM Regional Conference Series in Applied Mathematics*, 11, 1972.

S. Lee, S. K. Lele, and P. Moin. Simulation of spatially evolving turbulence and the applicability of Taylor's hypothesis in compressible flow. *Physics of Fluids*, 4:1521, 1992.

S. Lee, S. K. Lele, and P. Moin. Direct numerical simulation of isotropic turbulence interacting with a weak shock wave. *Journal of Fluid Mechanics*, 251:533–562, 1993.

S. Lee, S. K. Lele, and P. Moin. Interaction of isotropic turbulence with shock waves : Effect of shock strength. *Journal of Fluid Mechanics*, 340:225–247, 1997.

S. K. Lele. Compressibility effects on turbulence. *Annual Review of Fluid Mechanics*, 26:211–254, 1994.

M. Lesieur and O. Métais. New trends in large-eddy simulations of turbulence. *Annual Review of Fluid Mechanics*, 28:45–82, 1996.

D. K. Lilly. A proposed modification of the germano subgrid-scale closure method. *Physics of Fluids A*, 4(3):633–635, 1992.

T. T. Lim, T. H. New, and S. C. Luo. On the development of large-scale structures of a jet normal to a cross flow. *Physics of Fluids*, 13(3):770–775, 2001.

T. Linde. A practical, general-purpose, two-state HLL Riemann solver for hyperbolic conservation laws. *International Journal for Numerical Methods in Fluids*, 40:391–402, 2002.

M.-S. Liou and C. Steffen. A new flux splitting scheme. *Journal of Computational Physics*, 107:23–39, 1993.

R. Liska and B. Wendroff. Comparison of several difference schemes on 1D and 2D test problems for the euler equations. *SIAM J. Sci. Comput.*, 28(3):995–1017, 2003.

S. Liu, C. Meneveau, and J. Katz. On the properties of similarity subgrid-scale models as deduced from measurements in a turbulent jet. *Journal of Fluid Mechanics*, 275: 83–119, 1994a.

X. D. Liu, S. Osher, and T. Chan. Weighted essentially non oscillatory schemes. *Journal of Computational Physics*, 211:200–212, 1994b.

T. Lund. Generation of turbulent inflow data for spatially developing boundary layer simulations. *Journal of Computational Physics*, 140:233, 1998.

R. W. MacCormack. The effects of viscosity in hyper–velocity impact cratering. *AIAA Paper 69–354*, 1969.

K. Mahesh, S. K. Lele, and P. Moin. The influence of entropy fluctuations on the interaction of turbulence with a shock wave. *Journal of Fluid Mechanics*, 334: 353–379, 1997.

M. P. Martin. Mach number and wall temperature effects on turbulent boundary layers. *Conference - TI2006*, 2006.

M. Masquelet, F. Génin, and S. Menon. Update to the 107.leslie3d code for the SPEC MPI2007 benchmark. Technical Report 2008-004-1, Georgia Institute of Technology – Computational Combustion Laboratory, 2008.

R. Metcalfe, S. A. Orszag, M. A. Brachet, S. Menon, and J. Riley. Secondary instability of a temporally growing mixing layer. *Journal of Fluid Mechanics*, 194: 207–243, 1987.

A. Michalke. On the inviscid instability of the hyperbolic tangent velocity profile. *Journal of Fluid Mechanics*, 19:543–556, 1964.

A. A. Mirin, R. H. Cohen, B. C. Curtis, W. P. Dannevik, A. M. Dimits, M. A. Duchaineau, D. E. Eliason, D. R. Schikore, S. E. Anderson, D. H. Porter, P. R. Woodward, L. J. Shieh, and S. W. White. Very high resolution simulation of compressible turbulence on the ibm-sp system. *LLNL Report UCRL-JC-134237*, 1999.

T. Miyoshi and K. Kusano. A multi-state HLL approximate Riemann solver for ideal magnetohydrodynamics. *Journal of Computational Physics*, 208:315–344, 2005.

P. Moin, W. Squires, W. Cabot, and S. Lee. A dynamic sub-grid scale model for compressible turbulence and scalar transport. *Physics of Fluids*, 3(11):2746–2757, 1991.

M. V. Morkovin. Effects of compressibility on turbulent flows. *Mécanique de la Turbulence*, pages 367–380, 1962.

C. C. Nelson. *Simulations of spatially evolving compressible turbulence using a local dynamic subgrid model.* PhD thesis, Georgia Institute of Technology, Atlanta, GA, December 1997.

C. C. Nelson and S. Menon. Unsteady simulations of compressible spatial mixing layers. *AIAA paper 98-0786*, 1998.

T. H. New, T. T. Lim, and S. C. Luo. Elliptic jets in cross-flow. *Journal of Fluid Mechanics*, 494:119–140, 2003.

M. Oevermann. Numerical investigation of turbulent combustion in a scramjet using flamelet modeling. *Aerospace Science and Technology*, 4:463–480, 2000.

S. Osher and S. Chakravarthy. Upwind schemes and boundary conditions with applications to euler equations in general geometries. *Journal of Computational Physics*, 50:447–481, 1983.

M. Pandolfi and D. D'Ambrosio. Numerical instabilities in upwind methods: Analysis and cures for the carbuncle phenomenon. *Journal of Computational Physics*, 166: 271–301, 2001.

C. Pantano, R. Deiterding, J. H. Hill, and D. I. Pullin. A low numerical dissipation patch-based adaptive mesh refinement method for large-eddy simulation of compressible flows. *Journal of Computational Physics*, 221:63–87, 2007.

Y. H. Pao. Structure of turbulent velocity and scalar fields at large wave numbers. *Physics of Fluids*, 8:1063–1070, 1965.

D. Papamoschou and A. Roshko. The compressible turbulent shear layer:an experimental study. *Journal of Fluid Mechanics*, 197:453–477, 1988.

N. Park and K. Mahesh. Numerical and modeling issues in LES of compressible turbulence on unstructured grids. *AIAA paper 2007-722*, 2007.

D. M. Peterson, P. K. Subbareddy, and G. V. Candler. Assessment of synthetic inflow generation for simulating injection into a supersonic crossflow. *AIAA 2006-8128*, 2006.

M. V. Pham, F. Plourde, and K. S. Doan. Direct and large-eddy simulations of a pure thermal plume. *Physics of Fluids*, 19(125103), 2007.

R. T. Pierrehumbert and S. E. Widnall. The two- and three-dimensional instabilities of a spatially periodic shear layer. *Journal of Fluid Mechanics*, 114:59–82, 1982.

S. Pirozzoli. Conservative hybrid compact-WENO schemes for shock-turbulence interaction. *Journal of Computational Physics*, 178:81–117, 2002.

T. Plewa and E. Müller. The consistent multi-fluid advection method. *Astronomy and Physics*, 342:1790–191, 1999.

T. Poinsot and S. Lele. Boundary conditions for direct simulations of compressible viscous flow. *Journal of Computational Physics*, 101:104–129, 1992.

S. B. Pope. *Turbulent Flows*. Cambridge University Press, 2000.

J. J. Quirk. A contribution to the great Riemann solver debate. *International Journal for Numerical Methods in Fluids*, 18:555–574, 1994.

Y. X. Ren, M. Liu, and H. Zhang. A characteristic-wise hybrid compact-WENO scheme for solving hyperbolic conservation laws. *Journal of Computational Physics*, 192:365–386, 2003.

H. S. Ribner. Convection of a pattern of vorticity through a shock-wave. Technical Report 1164, NACA, 1954a.

H. S. Ribner. Shock-turbulence interaction and the generation of noise. Technical Report 1233, NACA, 1954b.

H. S. Ribner. Cylindrical sound wave generated by shock-vortex interaction. *AIAA Journal*, 23:1708–1715, 1985.

J. R. Ristorcelli. A pseudo-sound constitutive relationship for the dilatational covariances in compressible turbulence. *Journal of Fluid Mechanics*, 347:37–70, 1997.

J. R. Ristorcelli and G. A. Blaisdell. Consistent initial conditions for the DNS of compressible turbulence. *Physics of Fluids A*, 9(1):4–6, 1997.

D. P. Rizzetta, M. R. Visbal, and D. V. Gaitonde. Large-eddy simulation of superonic compression-ramp flow by a high-order method. *AIAA Journal*, 39(12):2283–2292, 2001.

P. L. Roe. Approximate Riemann solver, parameters vectors and difference schemes. *Journal of Computational Physics*, 43:357–371, 1981.

T. Rossmann, M. G. Mungal, and R. K. Hanson. Evolution and growth of large-scale structures in high compressibility mixing layers. *Journal of Turbulence*, 3(9), 2002.

N. D. Sandham and W. C. Reynolds. Three dimensional simulations of large eddies in the compressible mixing layer. *Journal of Fluid Mechanics*, 224:133–158, 1991.

J. G. Santiago. *An Experimental Study of the Velocity Field of a Transverse Jet Injected Into a Supersonic Crossflow.* PhD thesis, University of Illinois, Urbana-Champaign, 1995.

J. G. Santiago and J. C. Dutton. Velocity measurements of a jet injected into a supersonic crossflow. *Journal of Propulsion and Power*, 13(2):264–273, 1997.

S. Sarkar. Modeling the pressure-dilatation correlation. *ICASE Report No. 91-42*, 1991.

S. Sarkar. The pressure-dilatation correlation in compressible flows. *Physics of Fluids A*, 4(12):2674–2682, 1992.

S. Sarkar. The stabilizing effect of compressibility in turbulent shear flow. *Journal of Fluid Mechanics*, 282:163–183, 1995.

S. Sarkar, G. Erlebacher, M. Y. Hussaini, and H. O. Kreiss. The analysis and modeling of dilatational terms in compressible turbulence. *NASA - CR 181959*, 1989.

L. I. Sedov. Similarity and dimensional methods in mechanics. *Academic Press*, 1959.

J. Sesterhenn, J.-F. Dohogne, and R. Friedrich. Direct numerical simulation of the interaction of isotropic turbulence with a shock wave using shock-fitting. *Comptes Rendus de Mecanique*, 333:87–94, 2005.

L. Shao and J. P. Bertoglio. Large-eddy simulations of weakly compressible isotropic turbulence. In S. Gavrilakis, L. Machiels, and P. A. Monkewitz, editors, *Advances in turbulence VI*, pages 287–290. 1996.

C.-W. Shu and S. Osher. Efficient implementation of essentially non-oscillatory shock-capturing schemes. *Journal of Computational Physics*, 83:32, 1989.

A. Simone, G. N. Coleman, and C. Cambon. The effect of compressibility on turbulent shear flow: A rapid distortion theory and direct numerical simulation study. *Journal of Fluid Mechanics*, 330:307–338, 1997.

M. D. Slessor, M. Zhuang, and P. E. Dimotakis. Turbulent shear-layer mixing: growth-rate compressibility scaling. *Journal of Fluid Mechanics*, 414:35–45, 2000.

A. T. Sriram and J. Mathew. Numerical simulation of transverse injection of circular jets into turbulent supersonic streams. *Journal of Propulsion and Power*, 24(1): 45–54, 2008.

J. L. Steger and R. F. Warming. Flux vector splitting of the inviscid gas dynamics equations with application to finite difference methods. *Journal of Computational Physics*, 40:263–293, 1981.

S. Stolz and N. A. Adams. Large-eddy simulation of high-Reynolds-number supersonic boundary layers using the approximate deconvolution model and a rescaling and recycling technique. *Physics of Fluids*, 15(8):2398–2412, 2003.

V. Svetsov. Vortical regime of the flow behind the bow shock wave. *Shock Waves*, 11:229–244, 2001.

C.-J. Tam, R. A. Baurle, and M. R. Gruber. Numerical study of jet injection into a supersonic crossflow. *AIAA Paper 99-2254*, 1999.

J. C. Tannehill, D. A. Anderson, and R. H. Pletcher. *Computational Fluid Mechanics and Heat Transfer*. Taylor & Francis, 1997.

D. B. Taulbee and J. Van Osdol. Modeling compressible turbulent flows: The mass fluctuating velocity and squared density. *AIAA Paper 91-0524*, 1991.

E. F. Toro. *Riemann Solvers and Numerical Methods for Fluid Dynamics - A Practical Introduction*. Addison-Wesley Publishing Company, Inc., 1999.

E. F. Toro, M. Spruce, and W. Speares. Restoration of the contact surface in the HLL Riemann solver. *Shock Waves*, 4:25–34, 1994.

E. R. van Driest. Turbulent boundary layer in compressible fluids. *J. Aero. Sci.*, 18 (3):145–160, 1951.

B. van Leer. Towards the ultimate conservative difference scheme I. the quest for monotonicity. *Lecture Notes in Physics*, 18:163–168, 1973.

B. van Leer. Towards the ultimate conservative difference scheme II. monotonicity and conservation combined in a second-order scheme. *Journal of Computational Physics*, 14:361–370, 1974.

B. van Leer. Towards the ultimate conservative difference scheme V. A second order sequel to Godunov's method. *Journal of Computational Physics*, 32:101–136, 1979.

B. van Leer. Flux vector splitting of the euler equations. *Lecture Notes in Physics*, 70:507–512, 1982.

W. M. VanLerberghe, J. G. Santiago, J. C. Dutton, and R. P. Lucht. Mixing of a sonic transverse jet injected into a supersonic flow. *AIAA Journal*, 38(3):470–479, 2000.

M. Vetter and B. Sturtevant. Experiments on the Richtmyer-Meshkov instability. *Shock Wave*, 4:247–252, 1995.

D. Veynante and T. Poinsot. Reynolds averaged and large eddy simulation modelling for turbulent combustion. In O. Metais and J. Ferziger, editors, *New Tools in Turbulence Modelling.* Springer-Les Editions De Physique, 1996.

M. R. Visbal and D. V. Gaitonde. Shock capturing using compact-differencing-based methods. *AIAA Paper 2005-1265*, 2005.

B. Vreman. *Direct and large-eddy simulation of the compressible turbulent mixing layer.* PhD thesis, Universiteit Twente, 1997.

B. Vreman, B. Geurts, and H. Kuerten. Realizability conditions for the turbulent stress tensor in large-eddy simulations. *Journal of Fluid Mechanics*, 276:351–362, 1994.

W. Waidmann, F. Alff, M. Böhm, U. Brummund, W. Clauß, and M. Oschwald. Supersonic combustion of hydrogen/air in a scramjet combustion chamber. *Space Technology*, 15(6):421–429, 1995.

F. M. White. *Viscous Fluid Flow, Second Edition.* McGraw-Hill, 1991.

S.-H. Won, I.-S. Jeung, J.-R. Shin, D.-R. Cho, and J.-Y. Choi. Three-dimensional dynamic characteristics of transverse fuel injection into a supersonic crossflow. *AIAA paper 2008-2515*, 2008.

A. Yoshizawa. Simplified statistical approach to complex turbulent flows and ensemble-mean compressible turbulence modeling. *Physics of Fluids A*, 5:3302–3304, 1995.

L. L. Yuan, R. L. Street, and J. H. Ferziger. Large-eddy simulations of a round jet in crossflow. *Journal of Fluid Mechanics*, 379:71–104, 1999.

O. Zeman. Dilatational dissipation: the concept and application in modeling compressible mixing layers. *Physics of Fluids A*, 2(2):178–188, 1990.